NASA Contractor Report 158936

Northrop F-5F Shark Nose Development

O. R. EDWARDS

Northrop Corporation
Aircraft Group
Hawthorne, California 90250

NASA CONTRACT NAS1 15159
OCTOBER 1978

National Aeronautics and
Space Administration
Langley Research Center
Hampton, Virginia 23665

CONTENTS

SUMMARY

F-5F SHARK NOSE DEVELOPMENT

by O.R. EDWARDS

NORTHROP CORPORATION, AIRCRAFT GROUP
HAWTHORNE, CALIFORNIA

During spin susceptibility testing of the Northrop F-5F airplane, two erect spin entries were obtained from purely longitudinal control inputs at low speed. Post flight analysis of the data showed that the initial yaw departure occurred at zero sideslip and review of wind tunnel data showed significant yawing moments present at angles of attack well above stall. Further analysis of this wind tunnel data indicated that the yawing moments were being generated by the long slender nose of the airplane. Redesign of the nose was accomplished, resulting in a nose configuration which completely alleviated the asymmetric yawing moments.

This report documents the development of this new F-5F nose configuration from the initial identification of the importance of the nose region for high angle-of-attack flying qualities through the experimental studies in the Northrop low-speed wind tunnel and water tunnel to the flight testing of the finally developed nose configuration, the so-called "Shark nose."

The report draws on a unique data base of experimental wind tunnel and flight test data obtained by Northrop during the development of the F-5F aircraft.

INTRODUCTION

In recent years, much interest has been generated in the high angle-of-attack characteristics of military aircraft, particularly of fighters, where utilization of the maximum capabilities of the aircraft is so important in the air combat arena. Increasing maneuverability requires operation at higher angles of attack, which in turn leads to poor handling qualities due to the usual degradation in the effectiveness of lateral/directional control devices and stabilizing surfaces.

Identifying configuration features which provide the airplane with good inherent stability characteristics has been an important high angle-of-attack research task in recent years. This research has identified the long, slender fuselage forebody of several current configurations as being a major contributor to high angle-of-attack directional stability. Depending on the geometry of the forebody, both favorable and adverse effects can be produced and it is possible for significant improvements to be obtained in high angle-of-attack handling qualities by proper fuselage forebody design.

During the development flight tests of the F-5F airplane, it was determined that the high angle-of-attack flying qualities were largely dominated by asymmetric forces and yawing moments associated with the long forebody of the aircraft. These asymmetries had long been noted on the wind tunnel model, but this was the first indication that they existed in flight. Experience gained during previous experimental investigations, together with published studies by NASA and others, indicated that the fluid mechanic source of the asymmetries was a strong vortex system which originates from the nose. A concerted effort was made to develop a forebody modification to reduce the asymmetric forces and yawing moments. This study was undertaken using the low speed wind tunnel as the primary experimental tool, investigating various forebody modifications such as strakes of different size and location, and changes in nose angle and radius. Of all the changes made, the Shark nose provided the most dramatic benefits, essentially eliminating the asymmetry in the aerodynamic forces and moments and augmenting the stability characteristics of the aircraft as well. The symmetric formation of the forebody

vortex system caused by the Shark nose was confirmed by both surface oil flow studies in the wind tunnel and by flow field visualization in the water tunnel.

A full-scale Shark nose was constructed, and a flight test investigation of its effects was made using a production F-5F which was fitted with a modified leading edge extension (LEX), the low speed wind tunnel results having indicated that this was an additional benefit. The results of this flight program verified the analytical predictions which were based on the wind tunnel data, and confirmed that the nose vortex system had been stabilized, thus eliminating the asymmetric yawing moments previously experienced.

This report presents and discusses these recent advances which have been obtained in the field of high angle-of-attack aerodynamics.

SYMBOLS AND NOMENCLATURE

Airplane wind tunnel aerodynamic force and moment data were reduced to coefficient form in the body axis system of coordinates as defined in Figure 1. The moment center was located at the quarter chord of the MAC (mean aerodynamic chord), fuselage station 365.78, and the waterline of the aft fuselage reference plane.

In order to facilitate usage of data presented, dimensional quantities are presented both in the International System of Units (SI) and in the U.S. Customary Units. Measurements were made in the U.S. Customary Units, and equivalent dimensions were determined by using the conversion factors given in Reference 1.

ABBREVIATION	DEFINITION	UNITS
AOAB	Boom Angle of Attack	deg
AOAT	True Angle of Attack	deg
BETAB	Boom Angle of Sideslip	deg
BETA TRUE	True Angle of Sideslip	deg
cg	Center of Gravity position	% MAC
C_ℓ or CLLB	Rolling Moment Coefficient	———
C_{ℓ_β}	Dihedral Effect $\partial C_\ell / \partial \beta$	per deg
$C_{\ell_{\delta_a}}$	Aileron Effectiveness $\partial C_\ell / \partial \delta_a$	per deg
$C_{\ell_{\delta_r}}$	Rolling Moment Coefficient due to Rudder $\partial C_\ell / \partial \delta_r$	per deg
C_m	Pitching Moment Coefficient	———
C_n or CLNB	Yawing Moment Coefficient	———
C_{n_β}	Static Directional Stability Derivative $\partial C_n / \partial \beta$	per deg
$C_{n_{\beta_{dynamic}}}$	$C_{n_\beta} \cos \alpha - \frac{Iz}{Ix} \cdot C_{\ell_\beta} \sin \alpha$	per deg

ABBREVIATION	DEFINITION	UNITS
$C_{n_{\delta_a}}$	Yawing Moment Coefficient due to Aileron $\partial C_n/\partial \delta_a$	per deg
$C_{n_{\delta_r}}$	Rudder Effectiveness $\partial C_n/\partial \delta_r$	per deg
C_Y	Side Force Coefficient	———
δ_a	Aileron Deflection	deg
δ_F	T.E. Flap Deflection	deg
δ_H	Horizontal Stabilizer Deflection	deg
δ_n	L.E. Flap Deflection	deg
δ_N	Semi-apex Angle	deg
δ_R	Rudder Deflection	deg
HPC	Corrected Pressure Altitude	meters (ft)
I_x	Airplane Rolling Moment of Inertia	Newton-m^2 (slug-ft^2)
I_y	Airplane Pitching Moment of Inertia	Newton-m^2 (slug-ft^2)
I_z	Airplane Yawing Moment of Inertia	Newton-m^2 (slug-ft^2)
I_{xz}	Airplane Product of Inertia	Newton-m^2 (slug-ft^2)
FAS	Full Aft Stick	———
FRP	Fuselage Reference Plane	———
K	δ_r/δ_a	———
LCDP	$C_{n_\beta} - C_{\ell_\beta} \dfrac{C_{n_{\delta_a}} + KC_{n_{\delta_R}}}{C_{\ell_{\delta_a}} + KC_{\ell_{\delta_R}}}$	per deg
MAC	Mean Aerodynamic Chord	meters (ft)
MHB	Maximum Half Breadth	———
n_x	Load Factor along body X axis	g's
n_z	Load Factor along body Z axis	g's
ψ	Heading Angle	deg

ABBREVIATION	DEFINITION	UNITS
p	Roll Rate	deg/sec
PDOT	$\dot{p}$ - Roll Acceleration	deg/sec^2
PDOT I	$\dot{p}_I$ Inertia Contribution to Roll Acceleration	deg/sec^2
PDOT A	$\dot{p}_A$ Aerodynamic Contribution to Roll Acceleration	deg/sec^2
PDOT 1	$\left(\frac{I_y - I_z}{I_x}\right) qr$	deg/sec^2
PDOT 2	$\left(\frac{I_{xz}}{I_x}\right) \dot{r}$	deg/sec^2
PDOT 3	$\left(\frac{I_{xz}}{I_x}\right) pq$	deg/sec^2
q	Pitch Rate	deg/sec
QDOT	$\dot{q}$ Pitch Acceleration	deg/sec^2
QDOT I	$\dot{q}_I$ Inertia Contribution to Pitch Acceleration	deg/sec^2
QDOT A	$\dot{q}_A$ Aerodynamic contribution to Pitch Acceleration	deg/sec^2
QDOT 1	$\left(\frac{I_z - I_x}{I_y}\right) pr$	deg/sec^2
QDOT 2	$\left(\frac{I_{xz}}{I_y}\right) r^2$	deg/sec^2
QDOT 3	$\left(\frac{I_{xz}}{I_y}\right) p^2$	deg/sec^2
r	Yaw Rate	deg/sec
RDOT	$\dot{r}$ Yaw Acceleration	deg/sec^2
RDOT I	$\dot{r}_I$ Inertia Contribution to Yaw Acceleration	deg/sec^2

ABBREVIATION	DEFINITION	UNITS
RDOT A	$\dot{r}_A$ Aerodynamic Contribution to Yaw Acceleration	deg/sec^2
RDOT 1	$\left(\frac{I_x - I_y}{I_z}\right) pq$	deg/sec^2
RDOT 2	$\left(\frac{I_{xz}}{I_z}\right) \dot{p}$	deg/sec^2
RDOT 3	$\left(\frac{I_{xz}}{I_z}\right) qr$	deg/sec^2
θ	Pitch Angle	deg
V_{Cal}	Calibrated Airspeed	knots
W	Airplane Weight	Kilograms (lbs)
WUT	Wind Up Turn	———

DESCRIPTION OF AIRPLANES

While the subject of this report is the two place F-5F airplane, frequent reference is also made to the F-5E single place airplane. The F-5F contains all of the basic features of the F-5E, the only major external difference being the two place cockpit of the F-5F and hence the longer forebody.

The F-5E/F airplanes are supersonic, low wing tactical fighters powered by twin, afterburning, turbojet engines. Three-view drawings showing the general layout of the configurations are shown in Figures 2 and 3; the centerline fuel tank shown on the F-5E can also be carried by the F-5F. General geometric data for the airplanes are listed in Table 1 and the mass and inertia characteristics for the F-5F flight test airplane are presented in Table 2. Longitudinal control of the airplane is accomplished by means of an all-movable horizontal tail, and lateral control by conventional ailerons. The directional control system consists of a conventional rudder. Automatically-actuated maneuvering leading and trailing edge flaps provide increased turn rates for all combat conditions. Flap settings referred to in this report are either flaps up, flaps down or flaps maneuver, the latter setting being dependent on airspeed.

As shown in Figure 2, the basic configuration chosen for both F-5E and F-5F spin susceptibility testing was an operational air combat maneuver (ACM or clean loading) with no wing stores, empty tip launcher rails and an empty centerline pylon. Among the other store loadings tested, a number of flights were made with the centerline $1.04m^3$ (275 U.S. gallon) tank, Figure 3, F-5E shown, a configuration which is typical of operational and training configurations. The F-5F, clean and centerline tank configurations are the main subject of this report.

REVIEW OF FLIGHT TESTS

During 1975 and 1976 spin susceptibility flight test programs were conducted on both the F-5E and the F-5F airplanes. The tests were conducted following the guidelines specified by MIL-S-83691A, Stall/Post-Stall/Spin Flight Test Demonstration Requirements for Airplanes. The tests were limited to determination of the susceptibility to post-stall gyration (PSG) or spin entry and emphasis was placed on identifying spin avoidance techniques. Detailed reports on the results of these flight test programs can be found in References 2 and 3. The discussion which follows is intended only to summarize the highlights of these tests and to show the manner in which the yawing moment asymmetries became evident on the F-5F during flight tests.

A summary of both flight test programs is shown in Table 3. During this, and subsequent Shark nose testing, a departure was defined primarily as sustained, uncontrollable lateral/directional excursions. Both the F-5E and the F-5F were found to be highly resistant to departures and spins during tactical maneuvers performed with normal control inputs (not prolonged or adverse). Both airplanes could, however, be departed during accelerated stall entries. For the F-5F, which has a higher trim angle of attack capability than the F-5E, an additional departure region was found to exist at angles of attack above 35°. This result, as will be explained momentarily, was caused by large asymmetric yawing moments produced by the long forebody of the F-5F. Both airplanes were found capable of transitioning to a flat spin if allowed to remain at angles of attack above 50°. Finally both airplanes were found to be extremely susceptible to departure in the stall when carrying the standard centerline tank.

As just mentioned above, the F-5F was found to exhibit departures when flown above 35° angle of attack, even for simple symmetric, full-aft stick stall entries. This result was distinctly different from the F-5E experience. Two departures and spin entries were obtained on the F-5F from abrupt full-aft stick inputs made at 150-kts airspeed. The first departure (Figure 4) was generated from a stick snap where the horizontal stabilizer was input at maximum rate from 15° angle of attack. The aircraft was configured with flaps up and was at the aft c.g. limit. The second departure (Figure 5) came from an extended 1g stall where full aft stick was abruptly applied at the

stall angle of attack and held for 18 seconds. For this maneuver, the flaps were set at "maneuver" and, again, the c.g. was at the aft limit. In both instances, the angle of attack increased to around 40° in response to the stick input and then fell to 30° before increasing again. During this time, yaw rate was slowly increasing and subsequent application of recovery controls failed to reduce the angle of attack. Postflight analysis of the data showed that the initial yaw departure occurred at essentially zero sideslip, leading to the conclusion that a large asymmetric aerodynamic yawing moment was present at zero sideslip. Reevaluation of the wind tunnel data showed this to be correct with significant yawing moments present above 35° angle of attack. Above 42° angle of attack, the magnitude of the yawing moment coefficient was 0.1. This moment is significant, being equivalent to twice the rudder power available at low angles of attack. Review of previous wind tunnel data indicated that this asymmetric yawing moment at zero sideslip/high angle of attack also existed for the F-5E, but to a much lesser extent, and the F-5E spin susceptibility testing had shown that it was much less influential on the aircraft's behavior if full controls were applied and held as the airplane stalled near 24° angle of attack. Representative flight time histories showing the 1-g stall characteristics of the F-5E and the F-5F are presented in Figures 6 and 7, respectively. Additional time histories are presented in Figures 8 and 9 for the F-5E and F-5F, respectively, showing examples of the departures obtained in flight tests.

DEPARTURE PARAMETER ANALYSIS

Analysis of past wind tunnel data and correlation with flight test pilot's comments have shown a definite correlation between the minimum value of $C_{n_{\beta_{dynamic}}}$ and the response of the airplane in the stall angle-of-attack area. Examples of this type of correlation are shown in Reference 4 where ranges of minimum $C_{n_{\beta_{dynamic}}}$ correspond to various aircraft responses, i.e., solid stall, acceptable stall, random departure and severe yaw departure. For example, a solid stall could be expected with a minimum $C_{n_{\beta_{dynamic}}}$ value above .004.

Using the data from References 5 and 6, minimum $C_{n_{\beta_{dynamic}}}$ values were calculated for both airplanes for the clean and centerline tank configurations which were flight tested. These are shown in Figure 10 together with the departure classifications as obtained from the flight test program. In general, a good correlation is shown when compared with the various levels of minimum $C_{n_{\beta_{dynamic}}}$, substantiating the value of this criteria. However, this criteria is only applicable in the stall region and does not predict the departure susceptibility at higher angles of attack where other parameters such as aerodynamic asymmetries become dominant.

Again using the data of References 5 and 6, the lateral control departure parameter (LCDP) was calculated for different Mach numbers at stall and post-stall angles of attack. LCDP was calculated for both an aileron only input and for crossed controls and the results are shown plotted against calibrated airspeed at 10,670 meters (35,000 ft.) in Figures 11 and 12 for the F-5E and F-5F, respectively.

For the F-5E, LCDP is shown to be negative at angles of attack above 20-22^{O} for speeds between approximately 120-250 V_{Cal}, the cross control input showing the most negative values. For the F-5F, the same general trend is shown except that for angles of attack above 24^{O} the aileron only LCDP is positive, and can be attributed to the beneficial effect of the wing fences. This speed range for both the F-5E and F-5F coincides with that at which departure was generated with the most consistency.

SUMMARY OF FLIGHT TEST PROGRAMS

A summary of both spin susceptibility flight test programs is shown in Table 3. The main conclusions drawn from these tests for the clean configuration are:

- Both the F-5E and F-5F are highly departure/spin resistant from tactical maneuvers with normal control inputs.
- The F-5E/F departure/spin entry window is in the stall region with prolonged control inputs.

- The F-5F also has a departure/spin entry window at angles of attack above 35° due to large asymmetric yawing moments.
- Both aircraft can transition to a flat spin if allowed to remain at angles of attack above 50°.

For the centerline tank configuration:

- Both the F-5E and F-5F were extremely susceptible to departure if the stall angle of attack was exceeded.

ANALYSIS OF F-5E/F FLOW CHARACTERISTICS AT HIGH ANGLES OF ATTACK

As summarized in the previous section, the F-5F was found to be most prone to loss of control and possible spin entry at angles of attack above 35^{o} due to an onset of large yawing moments at zero sideslip. The F-5E, on the other hand, showed smaller asymmetric aerodynamic characteristics at high angles of attack. The primary geometric difference between the F-5E and F-5F is the length of the forebody of each aircraft. Figure 13 illustrates the increase in forebody fineness ratio of the F-5F over the F-5E. The convention for forebody fineness ratio used in this figure is taken from Reference 7. Figure 14 presents the results of previous wind tunnel tests on the F-5A, F-5E and F-5F and compares yawing moments at zero sideslip for these aircraft. Data from Figure 14 along with data on other F-5 derivative aircraft has been cross plotted in Figure 15 and shows the effect of forebody fineness ratio on the absolute magnitude of yawing moment measured at a constant angle of attack of 46^{o}. A significant increase in yawing moment at zero sideslip is indicated for l/d = 6.0 which corresponds to the F-5F forebody fineness ratio.

Experiments were carried out in the Northrop water tunnel on an F-5F scale model to develop an understanding of the flow characteristics around the forebody at high angles of attack. The fluid mechanism found to be responsible for the aerodynamic asymmetries was the growth of a strong vortex system originating from a feeding sheet along the side of the forebody. At high angles of the attack, this vortex system was observed to be asymmetric. This vortex pattern is schematically illustrated in Figure 16. A photograph of the vortex patterns observed in the water tunnel is shown in Figure 17.

PRIOR EXPERIMENTAL STUDIES

The review of low speed wind tunnel data discussed in the previous paragraphs identified the source of the asymmetric moments as being the forebody of the airplane. Existing literature was surveyed to seek possible methods of attenuating the asymmetries. The data of Reference 8 showed that yawing moment coefficients at zero sideslip and high angle of attack ranging between .08 and -.16 had been measured

on various scale models of the F-104, F-4 and F-111 airplanes. Much work has been done in the past few years on this problem following continual loss of many high performance aircraft. A good compilation of all the recent work in this field is covered in Reference 9. This work showed that the geometry of the forebody was the variable which affects the angle of attack, or onset angle, at which the side force due to the vortex asymmetry first occurs. The data for this correlation, Figure 18, came from many sources. In general, for circular forebodies, the onset angle of attack was found to be equal to twice the semiapex angle of the forebody. The onset angle was observed to be independent of Mach Number and Reynolds Number within the range tested. The side force also decreased to zero near an angle of attack of 70°, probably as a result of the forebody vortices weakening and the leeside flow becoming a turbulent wake.

Figure 19 is taken from Reference 9 and illustrates the effect of nose bluntness on side force for a pointed tangent ogive forebody with a fineness ratio of 3.5. As the nose radius increases, the side force variation with angle of attack is attenuated.

The data of Reference 7 compared side force and yawing moment coefficients for various nose fineness ratios for slender bodies with thin wings and tails. These comparisons were consistent with the data of Reference 10 for similar nose geometries and similar to the data of Reference 11 for the same noses with circular bodies. Also consistent with the data of References 7, 10 and 11 was the data of Reference 12, which was for simple winged bodies with pointed noses and no tail. It was concluded from these references that the undesirable side-force and yawing moment characteristics at zero sideslip occur when the forebody fineness ratio exceeds a critical value of approximately 3.5.

The data of Reference 7, which illustrate the relationship between onset angle of attack and fineness ratio are shown in Figure 20. Data for the F-5E and F-5F are compared with these data and a good correspondence is indicated.

NORTHROP EXPERIMENTAL STUDIES

Wind tunnel tests were conducted on a 1/10th scale model of a production F-5E clean configuration (with centerline pylon) in the Northrop 7 x 10-ft (2.3 x 3.3m) lowspeed facility with primary emphasis on high angle of attack

directional stability. Data were obtained on several radome configurations at a free-stream Mach number of 0.26 corresponding to a Reynolds number of 0.46×10^6/meter (1.5×10^6/ft.).

Preliminary studies were made on the clean F-5F configuration at angles of attack up to 65° in order to establish the magnitude and repeatibility of the zero sideslip forces and moments. Data obtained in References 13 and 14 are presented in Figure 21 which clearly illustrate the large asymmetric yawing moments in addition to the data nonrepeatibility associated with model nose assembly differences. The wind tunnel runs shown in Figure 21 were obtained at various times during the running of the tests. Because the nose section is removable, a certain amount of slop exists between it and the main model body when assembling for a particular run. This slop translates into a slight nose section roll-angle difference for each particular run. It should be noted that no roll-angle position of the removable nose section was found which eliminated the zero-sideslip forces. These results are in agreement with the data obtained in Reference 9, some results from which are shown in Figure 22.

While specific information about these data is contained in References 13 and 14, the following discussion will summarize some of the research highlights that illustrate the effect of nose angle, radius, ellipticity and forebody strakes on the lateral/directional and longitudinal stability of the F-5F.

Effect of Nose Angle

Studies were made to determine the effect of nose apex angle forward of station 17.5, where nose apex angle is defined in the profile view shown in Figure 23. It should be noted that the profile view and plan view nose apex angles differ due to the elliptical cross-section of the nose. The semi-apex angle, in the plan view, for the F-5F is 18°. The corresponding onset angle for asymmetries is 24° and is shown in Figure 24 along with data taken from Figure 18 for circular and elliptic forebodies. Results indicate that the F-5F correlates well with the elliptic forebodies, which exhibit, in general, lower onset angle relative to the circular forebodies for a given semi-apex angle.

Zero-sideslip lateral/directional data from the current tests are shown in Figures 25 and 26 and pitching moment data are presented in Figure 27. Lateral/directional asymmetries are evident for all nose angles considered (Figure 25) and onset angle is essentially independent of nose angle ($\alpha_{onset} \approx 24^{\circ} - 25^{\circ}$). These results indicate that the onset angles corresponding to the nose angles of 45° and 90° (32.5° and 56.5° semi-apex angles, respectively) fail to correlate with the relationships shown previously in Figure 24 for circular and elliptic forebodies, which suggests that these relationships are invalid for the large nose angles considered. The lack of correlation may also be due to the nose surface discontinuities introduced in creating these angles. The results of such a change to the nose tip might be expected to involve differences due to both nose apex angle changes and nose bluntness. Furthermore, the magnitude of the asymmetric yawing moment varies nonlinearly with nose angle, as shown in Figure 26, the lowest $|C_n|$ being obtained with a plan-view nose angle of 65°. The data presented in Figure 27 indicate that longitudinal stability is greatly improved relative to the production nose by increased nose angle.

Lateral/directional and longitudinal data are presented in Figures 28 and 29, respectively, for $\beta = -10^{\circ}$ and the yawing moment and pitching moment increments due to sideslip are shown in Figure 30. It should be noted that the increments presented in Figure 30, which were obtained between $\beta = 0^{\circ}$ and -10°, may be somewhat misleading due to the directional bias exhibited by the production configuration.

Results shown in Figure 30 indicate that directional stability is lost above angles of attack of 35° and 50° with nose angles of 90° and 45°, respectively, although the configuration with 45° nose angle results in a slight directional improvement relative to the base configuration at angles of attack between 28° and 32°. Any improvement in directional stability is accompanied by longitudinal instability, however, as indicated by the pitching moment increments in Figure 30.

Effect of Nose Radius

Blunting the tip of a tangent ogive forebody has been shown in Reference 9 to be an effective means of zero-sideslip side force alleviation and results from Reference 9 were shown previously in Figure 19 for a range of nose

bluntness. Based on these results, tests were conducted on the F-5F for the range of nose radii shown in Figure 31. The radius is measured in the profile view and results in a planview somewhat more blunt than a circular arc.

Lateral/directional and pitching moment data are presented in Figures 32-34 for $\beta = 0^{\circ}$. Increased nose radius delays to higher angles of attack the onset of the more significant asymmetric yawing moments (see Figure 32) and reduces in a nonlinear manner the magnitude of the yawing moments, as illustrated in Figure 33 for $\alpha = 46^{\circ}$. The more favorable conditions were obtained with a nose radius of 4 in. (10.2 cm) (full scale). Furthermore, all radii result in improved longitudinal stability which is illustrated in Figure 34.

Figures 35 and 36 show the effect of nose radius on the lateral/directional and pitching moment characteristics, respectively, for $\beta = -10^{\circ}$, and Figure 37 illustrates yawing moment and pitching moment increments due to sideslip. As discussed in the previous section, the data presented in Figure 37 should be viewed with discretion due to the directional bias exhibited by the production nose.

The data in Figure 37 indicate that the more favorable directional characteristics are obtained with a nose radius of 4 in. (10.2 cm) which results in post-stall directional stability up to $\alpha \approx 49^{\circ}$. Longitudinal stability is compromised, however, as indicated in Figures 36 and 37 by the pitch-up increments due to increased nose radius.

In summary to this point, results obtained for a range of nose angle and nose radius suggest that F-5F forebody tailoring can effectively reduce zero-sideslip forces and moments at high angles of attack.

Effect of Nose Ellipticity

Wind tunnel tests of the F-5E reconnaissance (RECCE) nose configuration have indicated a reduction in zero-sideslip asymmetries relative to the production nose configuration. A three-view drawing of the F-5E featuring the RECCE nose (F-5F configuration is similar) is shown in Figure 38 which illustrates the increase in nose broadness, nose radius, and nose angle in the plan view and the subsequent increased cross-sectional ellipticity. The RECCE nose thus incorporates nose features which effectively suppress zero

sideslip forces and moments. The elliptic cross-section produced by the oblique forward-looking window across the nearly circular body should produce a configuration which exhibits favorable zero sideslip characteristics.

Data were obtained on the F-5F RECCE nose configuration for an extended range of angle of attack and zero sideslip and these results are compared to the basic F-5F configuration in Figures 39-41. The RECCE nose configuration results in a significant reduction in the maximum zero-sideslip yawing moment, no erratic drifting relative to the basic configuration (see Figure 39), and an improvement in longitudinal stability at angles of attack of 40° to 53° (see Figure 40). Limited angle of attack data are available for the RECCE nose with sideslip angles greater than zero. Figures 42-44 show lateral/directional and longitudinal data for this configuration up to 40° angle of attack and -10° sideslip relative to the production nose and clearly indicate the improvement in directional stability and reduced pitch-up tendency at angles of attack above stall. These results confirm that nose geometry changes, as exemplified by the RECCE nose, result in significant reductions in the zero-sideslip forces and moments and improved directional and longitudinal stability at angles of attack above stall.

Effect of Strakes

Extensive studies were made to determine the effect of nose strakes on high angle-of-attack characteristics of the F-5F in an attempt to control the location of the formation of the primary nose vortex pair and to produce a symmetrical flow field at zero sideslip. It should be noted that Reference 15 has shown nose strakes to be detrimental to the directional stability of an F-5A-shaped nose. The current investigation was conducted, therefore, in order to determine a suitable strake configuration which retains the stabilizing characteristics while eliminating asymmetries.

Figures 45-52 illustrate the nose strakes, which can be classified as flat-plate (strakes M63, S7, S8, S9, and S10) and constant cross-section (strakes S11, S12, S13, and S14), which were tested on the F-5F model in the Northrop low speed wind tunnel. Within these classifications, strakes of similar size or location are compared with a baseline case. All strakes were tested with a production nose and pitot, except for M63, S8, and S9 which were tested with production nose only.

The effect of the production pitot relative to the pitot-off case, shown in Figures 53-55 for $\beta = 0^{\circ}$, is to change the sense of the asymmetry only. In addition, beyond $\alpha = 45^{\circ}$ the production pitot results in a pitch-up increment up to $\alpha = 53^{\circ}$ and a nose-down moment thereafter.

Results obtained for the strakes shown in Figures 45-52 are presented in Figures 56-90. Due to the large amount of data involved, Table 4 presents the highlights of the nose strake tests and compares each strake with base (production nose with pitot on/off) data.

The results summarized in Table 4 indicate that improvements in directional stability are usually accompanied by a corresponding loss in longitudinal stability at -10° sideslip. Only strakes S12, S13, and S14 could truly be called beneficial and, of those, the faired strake S14 was best. The fact that the faired strake, which results in a nose cross-section possessing a more elliptic profile, was most favorable corroborates the findings discussed previously in this report, namely, that nose broadness is an essential feature in alleviating zero-sideslip asymmetry and retaining stabilizing characteristics.

EVOLUTION OF THE SHARK NOSE

GEOMETRIC FEATURES AND APPLICABLE AERODYNAMIC DATA

The several geometric features which were found to alleviate zero-sideslip forces and moments were incorporated into one forebody shape, the geometric changes being confined to the radome section forward of fuselage station 47.5 due to practical considerations. The resulting blended nose, designated B29, is shown in Figure 91 which indicates that the geometric changes occur in the plan view only. The similarity of this forebody shape to a shark nose is obvious, hence the term "Shark nose" will be used when referring to this shape.

Figures 92-101 present the effect of the Shark nose on lateral/directional and longitudinal characteristics for a range of angle of attack and sideslip. For $\beta = 0^{\circ}$, the Shark nose results in a significant reduction in the asymmetric forces and moments relative to the production nose configuration (see Figure 92). Data obtained for a range of sideslip angles (Figures 93-95) indicate that lateral/directional stability is greatly improved above stall and that the strong directional bias exhibited by the production nose is eliminated. Furthermore, the angle of attack at which directional stability is regained is reduced from 28° to 26° and the region of instability at the stall is considerably reduced. As might be expected, this improvement in directional stability due to the Shark nose is accompanied by a longitudinal instability between stall and 44° angle of attack, as shown in Figures 96-101. Above 44°, the Shark nose exhibits improved longitudinal stability relative to the production nose, whereas below stall the longitudinal characteristics are unchanged.

Radar performance is an important consideration, therefore, radome contours were examined to maximize radar performance without compromising the aerodynamic benefits of the Shark nose. The majority of nose radomes employed on high-performance aircraft are electrically-tuned systems in which the electrical thickness of the radome corresponds to multiples of one-half wavelength in the dielectric, thereby maximizing transmission efficiency. This condition is best satisfied if the radome shape corresponds to a portion of a sphere, in which case the electrical path length through

the radome is the same for any pointing angle. When the radome contours diverge from the theoretical hemispheric shape, the electrical path length through the radome is a function of look angle, with subsequent increased reflection levels and reduced transmission efficiency.

The latter considerations resulted in the revised Shark nose shown in Figure 102, designated B30, which exhibits a blunter plan view relative to Shark nose B29 and an altered profile view, providing a blunter tip forward of approximately fuselage station 20.0. Test data were obtained for a range of sideslip angle and results are presented in Figures 103-105. Shark nose B30 resulted in a larger region of directional instability at the stall compared to Shark Nose B29, the angle of attack at which directional stability is regained being increased from 26° to 27.5°. There was a slight improvement in directional stability due to B30, however, between angles of attack of 27.5° and 49°. In addition, longitudinal stability exhibited by nose B30 was improved relative to nose B29, but it should be noted in Figure 105 that going from zero to -10° sideslip increases trim angle of attack from 42° to 58°.

The aerodynamic, structural, and electronic functions of the nose radome result in conflicting design requirements, which necessitated an alternate Shark nose shape. The contours of Shark nose B31, Figure 106, are essentially Shark nose B30 cross-sections rotated 180°. The resulting nose shape features more curved upper surface contours which are desirable for minimizing upper surface radar reflection, a prerequisite for clutter control on an air-to-ground mission.

Data obtained on Shark nose B31 are presented in Figures 107-109. Results shown in Figure 107 indicate that: the region of directional instability at the stall is comparable to that obtained with Shark nose B29 shown previously in Figure 94. B31 results in improved directional stability up to $\alpha = 49^{\circ}$; directional stability is regained at $\alpha = 26^{\circ}$; and longitudinal stability is slightly degraded between $\alpha = 32^{\circ}$ and 40° relative to nose B29 (see Figures 108 and 109).

Reviewing B31 relative to the original F-5F forebody, Figures 92 and 107, indicates that the zero sideslip yawing asymmetries are greatly reduced by B31. Longitudinal stability is decreased, Figures 96 and 109, with the trim

angle of attack increasing from 38° to 50°. At sideslip angles greater than zero, Figures 94 and 107, the lateral/directional characteristics are enhanced but there is a degradation in pitch characteristics; compare the production forebody with pitot boom data of Figure 89 and B31 of Figure 109, with trim angle of attack increasing from 43° to 61°. However, a review of Shark noses B29, B30 and B31 indicates that B31 might best satisfy radar requirements, while retaining aerodynamic benefits. Shark nose B31 was, therefore, chosen for full-scale flight testing.

A brief, concurrent water tunnel study was made in the Northrop facility using Shark and production nose models, which demonstrated qualitatively the aerodynamic benefits obtained with the Shark nose.

W44 LEADING-EDGE EXTENSION

The W44 LEX, illustrated in Figure 110 along with the production LEX W8, was shown in prior F-5E/F wind tunnel development tests to provide lateral/directional benefits, namely, to increase the angle of attack at which directional stability is lost in the critical stall region and to provide increased dihedral effect. It was desirable, therefore, to combine the W44 LEX with the Shark nose, since the latter was shown (Figure 107) to result in a reduction in the angle of attack at which directional stability is regained. Wind tunnel data for the Shark nose/W44 LEX configuration are shown in Figures 111-116 along with reference data obtained for the Shark nose/W8 LEX.

Results presented in Figures 111-113 for $\beta = 0^{\circ}$ indicate that lateral/directional characteristics are unchanged with the W44 LEX, maximum lift is increased; longitudinal stability is essentially unchanged. Figures 113-116 indicate that for $\beta = -10^{\circ}$, the W44 LEX results in virtual elimination of the "trough" in degraded directional stability exhibited by the Shark nose/W8 LEX around stall angle of attack. The W44 LEX also increases maximum lift and dihedral effect, and reduces longitudinal stability slightly at the stall. Furthermore, the data in Figure 114 indicate that the Shark nose/W44 LEX results in positive directional stability up to $\alpha = 50^{\circ}$.

FLIGHT TEST NOSE BOOM STUDY

The effect of the flight test nose boom, which has a 4-inch (10.2-cm) base diameter, on the aerodynamic benefits of the Shark nose was of critical concern. The flight test boom on the F-5F airplane is considerably larger than the production pitot and also carries the angle-of-attack and sideslip measurement vanes. Wind tunnel tests were, therefore, conducted with the flight test pitot and the results are shown compared to the pitot-off case in Figures 117-122. The flight test boom results in slightly reduced longitudinal stability at $\beta = 0^{\circ}$ (see Figure 119). For $\beta = -10^{\circ}$, directional stability is significantly reduced with flight test boom on throughout the range of angle of attack considered, although longitudinal stability is improved somewhat abo $\alpha = 50^{\circ}$ (see Figures 120-122).

Data were also obtained on the production nose/flight test boom configuration and are presented in Figures 123-125 and Figures 126-128 for $\beta = 0^{\circ}$ and $\beta = \pm 10^{\circ}$, respectively. For $\beta = 0^{\circ}$, the flight test boom results in large and oscillatory directional characteristics in contrast to the erratic drifting of the production nose/production pitot presented here and in Figure 21. Longitudinal stability is improved, however, between $\alpha = 38^{\circ}$ and 53°. For $\beta = \pm 10^{\circ}$, the directional stability is virtually eliminated above stall angle of attack with flight test boom on. The longitudinal stability was very erratic with areas of better and worse stability above $\alpha = 34^{\circ}$. This erratic behavior coincides with similar oscillations in the yawing moment coefficient indicating the total forebody force vector wanders randomly around the forebody as angle of attack changes.

These results suggest that the production nose flight test results with flight test boom on may not be representative of the production configuration characteristics. Similarly, the aerodynamic benefits of the Shark nose may be severely degraded with the installation of the flight test boom. Accordingly, wind tunnel tests were conducted on a Shark nose/production pitot configuration and the favorable zero-sideslip results, shown in Figures 129-131, resulted in approval of this configuration for flight testing.

SHARK NOSE FLIGHT TESTING

FLIGHT TEST EVALUATION

Following the completion of the experimental tests of the Shark nose in both the low-speed wind tunnel and the water tunnel, and due to the favorable results predicted from the analytical evaluation of the effect of the Shark nose on the high angle-of-attack characteristics of the F-5F, a ten-flight test program was conducted to substantiate these predictions. Prototypes of the Shark nose radome and the W44 LEX were fabricated and installed on the second production F-5F designated W-1002 (Figures 132-134). This aircraft had been used in the flight test evaluation of the spin susceptibility characteristics of the production F-5F and, therefore, was configured with an emergency spin chute recovery system, backup electrical and hydraulic systems, and special instrumentation. Flight tests on the production aircraft were made with a large nose boom fitted with vanes for measuring angle-of-attack and sideslip information as well as pitot static data. As previously discussed, this large nose boom was found to have a detrimental effect on the characteristics of the Shark nose at high angles of attack. For this reason, the Shark nose radome was fabricated with a small nose boom designed to have no effect on the flow characteristics of the nose but providing pitot-static data only. Angle-of-attack vanes were installed on the left and right wing-tip launcher rails and the sideslip vane was installed just aft of the radome on the lower centerline of the fuselage. Flight tests were conducted between 25 February and 29 March 1977 at the AFFTC, Edwards AFB, California.

The test maneuvers performed utilized a judicious buildup in both degree of control misapplication and the energy level of the entry. In addition, the majority of the maneuvers flown were designed to duplicate similar maneuvers performed in the spin testing of the production aircraft. The testing was done to allow a direct comparison of production and Shark nose characteristics. A total of ten Shark nose flights were flown, seven with the launcher-rail/centerline pylon (clean) configuration and three with the centerline 1.04 m^3-(275 U.S. gallon) tank. The center of gravity was varied between 12% and 16% MAC for the clean airplane while the centerline tank was only tested at 12% MAC.

A complete summary of the flight test maneuvers performed is shown in Table 5. These are tabulated in the chronological sequence in which they were performed but in the following discussion they are presented in a configuration sequence for easier understanding. Under the judicious buildup approach, for a given configuration, maneuvers were usually performed with flaps maneuver and then flaps up.

Clean Configuration (launcher rails, centerline pylon)

1. Forward c.g. (12%), Flaps maneuver.

Initial maneuvers flown with this configuration consisted of stalls and constant speed wind-up turns. Control inputs were limited to the longitudinal axis and the recoveries were initiated at an angle of attack of 40^{O} or prescribed duration of control input, whichever came first.

The initial results from these maneuvers were very encouraging and pilot comments indicated that the aircraft felt very solid and exhibited no tendency to depart from controlled flight. In addition, immediate positive response to forward stick inputs at high angles of attack was noted. During these maneuvers, wing rock gradually on-set above 28^{O} angle of attack with an increasing magnitude and frequency. Angles of attack up to 44^{O} were obtained.

Continuing the testing, a series of rudder reversals at full aft stick were performed followed by wings-level pull-ups. For these maneuvers the 40^{O} angle of attack restriction was removed. For the maneuvers involving rudder reversal, the prescribed control inputs were applied as the target angle of attack (20^{O}) was reached in either 2-g or 4-g turns. Wings-level pull-ups were initiated from both 150 and 160-knots. At no time during the execution of these maneuvers was there any indication of a departure.

2. Forward c.g. (12%), Flaps up.

Maneuvers flown with this configuration were the same as those performed with flaps maneuver, starting with 1-g stalls and progressing to constant speed wind-up turns, rudder reversals at full aft stick and finally a wings-level pull-up at 150-knots. Again, the control inputs on the stalls and

wind-up turns were limited to the longitudinal axis and angle of attack was limited to 40° or prescribed duration of control input. Wing rock on-set was the same as had been seen with flaps maneuver and immediate positive response to forward stick inputs at high angles of attack was noted. It should be remembered that large asymmetric yawing moments produced a departure from controlled flight which eventually developed into a flat spin, as shown in Figure 4, when the wings-level pull-up was initiated at 160-knots with flaps up on the unmodified aircraft during the F-5F spin susceptibility test. The initial conditions and control inputs of this maneuver were duplicated with the Shark nose and W44 LEX installed and no departure tendencies were evident. The complete time history for this maneuver is shown in Figure 135.

3. Aft c.g. (16%), Flaps maneuver.

The maneuvers for this configuration were designed to further aggravate critical control misapplications to test the resistance of the Shark nose/W44 LEX to departure. The control inputs for the first maneuver were identical to the control inputs of an extended 1-g stall which had departed and transitioned into a flat spin during the basic spin susceptibility testing. On this flight, aft stick was abruptly applied at 25° angle of attack and held for 32 seconds as seen in Figure 136. The angle of attack increased to 60°, fell to 32° and then increased to 60° again while yaw rate was oscillating between ±12°/sec. At no time were any departure tendencies evident.

The second maneuver was a wings-level pull-up from 150-knots, similar to that shown in Figure 135; however, full aft stick was held for 15 seconds rather than 3 seconds. Like the previous stall maneuver, the angle of attack rose to almost 60° and then dropped and oscillated around 40° as long as the stick was held aft. On releasing aft stick, reduction in angle of attack to below stall was immediate. Yaw rate throughout the maneuver never exceeded 20°/second.

The third maneuver was a level decelerating left turn with smooth full aft stick and full right rudder application at 20° angle of attack. Inputs were applied for 3 and 5 seconds, respectively. Maneuvers of this type had consistently departed both the F-5E and the unmodified F-5F. This Shark nose/W44 LEX maneuver proved very innocuous, with the aircraft rolling in an oscillatory manner out of the turn with a very stable response. An overlay

of this maneuver with the similar production nose maneuver is shown in Figure 137. Recovery was easily accomplished with neutral controls. The remainder of the maneuvers on this flight were devoted to higher energy, level decelerating turns with smooth aft stick and rudder inputs. No departures were noted.

Maneuvers one, two and three on the next flight were rudder rolls during 240-knot wind-up turns with full aft stick being applied when 180° of roll had been achieved. The intent here was to couple the rolling and yawing motion due to rudder into the pitch axis and thereby increase the angle of attack. A maneuver such as this one had generated a departure during the spin susceptibility testing of the unmodified F-5F but none was produced with the Shark nose. Angles of attack as high as 68° were obtained.

An inverted pitch maneuver was flown next. The airplane was rolled inverted at 160-knots and full forward stick was applied in an attempt to generate an inverted departure. This departure was accomplished after 28 seconds of full forward stick; the airplane oscillated in angle of attack between -30° and -70°. This was not as abrupt as was seen on the production aircraft with the unmodified nose.

A 310-knot left wind-up turn with full aft stick and right rudder applied at 20° angle of attack completed this flight card; no departure occurred. The angle of attack reached 44°. There was no comparable maneuver from the production nose spin susceptibility testing.

All of the remaining maneuvers flown were duplicates of maneuvers which had produced severe departures and spins during the testing of the F-5E or unmodified F-5F. These maneuvers included a 310-knot wind-up turn and higher energy 4-g high-pitch-attitude and level-attitude decelerations. Control aggravations for these maneuvers were full aft stick and rudder applied at 15° or 20° angle of attack for 1 or 3 seconds. No departures occurred, even when angles of attack as high as 70° were obtained. Recoveries from the extreme angles of attack reached in these maneuvers was positive and a typical time history is shown in Figure 138. The pilot stated that the airplane provided sufficient warning of this extreme motion in the form of severe wing rock involving extremely high roll rates and large amplitudes. Under normal circumstances a pilot flying these types of maneuvers would terminate the maneuver long before the duration of control misapplication applied during

these tests. These maneuvers demonstrated that the airplane has a large degree of departure resistance.

4. Aft c.g. (16%), Flaps up.

Six maneuvers were flown with this configuration, all being duplicates of maneuvers which had produced severe departures and spins during testing of the F-5E and unmodified F-5F. These maneuvers included an extended 1-g stall, a wings-level pull-up and a higher energy 2-g and 4-g decelerations and wind-up turns. Control inputs with the decelerations and wind-up turns consisted of full aft stick and rudder applied at 15° or 20° angle of attack for 1 or 3 seconds.

During the extended 1-g stall, aft stick was held for 21 seconds and the angle of attack peaked at 55° twice, due to the large sideslip oscillations and coupling. Yaw rate never exceeded 20°/second. The abrupt pull-up maneuver was flown at 150-knots and full aft stick was held for 3 seconds. Again a peak angle of attack of 55° was reached but there was no indication of a departure.

In general, the airplane motion with the aft stick and rudder inputs was the same for the decelerations and wind-up turns. The airplane would roll in an oscillatory manner with angle of attack increasing due to sideslip coupling. In the case of the 240-knot and 310-knot wind-up turns, the angle of attack began to reduce before aft stick was released. None of the maneuvers resulted in departures even though peak angles of attack of the order of 70° were reached. See Figure 139.

These maneuvers with flaps up further substantiated the conclusion obtained in the previous section, namely, that the airplane has a high degree of departure resistance.

Centerline Tank

1. Forward c.g. (12%), Flaps maneuver.

The majority of testing with the centerline tank was done in this configuration. Most maneuvers were flown with flaps selected "full down" ($24^{\circ}/20^{\circ}$), or "maneuver." Initially, stalls and wind-up turns were performed followed by level, decelerating, 3-g turns. Only aft stick control inputs of

3 seconds or less duration were applied. Analysis of the data from these maneuvers indicated a significant improvement in resistance to departure and spin.

As an indication of the improved characteristics with the centerline tank, an overlay of maneuvers flown with and without the Shark nose/W44 LEX maneuvers is shown in Figure 140. Initial conditions and control inputs were identical for both maneuvers. Uncommanded yaw oscillations are not present in the Shark nose maneuver even though full nose up stabilizer deflection was sustained longer.

Continuing the testing, a series of 1-g stalls and varying speed wind-up turns were flown. Aft stick and rudder misapplications were applied to aggravate the departure. No comparable maneuvers had been performed with the centerline tank loading during the spin testing of the unmodified aircraft since departures consistently were generated during low energy maneuvers without aggravated rudder misapplications. Maneuvers performed on this flight with the Shark nose/W44 LEX modification demonstrated a high level of resistance to loss of control similar to the departure resistance of the F-5E in a clean (no centerline store) configuration. A mild departure was experienced from a high energy decelerating wind-up turn; however, a repeat of this maneuver showed no departure tendency.

Higher energy maneuvers concluded testing with this configuration and these included high load factor level decelerating turns with flaps set at "maneuver." The first two maneuvers, the 3-g and 4-g level decelerating turns, performed with smooth full aft stick, had departed the production-nose airplane. With this Shark nose configuration, no departures occurred. The speed decreased with angle of attack not exceeding 35° and yaw rate not exceeding 12°/sec. An overlay of these two maneuvers compared with the corresponding production nose maneuvers is shown in Figures 141 and 142. These show angle of attack, yaw rate, and horizontal stabilizer position. Maneuver three was a repeat of maneuver two but with the turn direction to the right instead of to the left. This time a departure was experienced with the airplane nose slicing out of the turn at approximately 23° angle of attack. Full nose up horizontal stabilizer was never reached. Immediate recovery was obtained as aft stick was released. Maneuvers four and five were stick-fixed rudder rolls initiated from 15° and 20° angle of attack with no departures.

The peak angle of attack reached was 38° during maneuver five. A repeat of maneuver three again departed to the outside of the turn but was milder, with the peak angle of attack reaching 31°. The final maneuver, a repeat of the 20° angle of attack stick fixed rudder roll produced a departure and oscillatory one-turn spin. Recovery from the spin was rapid with forward stick and aileron in the spin direction.

2. Forward c.g. (12%), Flaps up.

Only two maneuvers were flown with this configuration and both resulted in mild departures. The first was a 1-g stall and the second a 2-g accelerated stall, both maneuvers being performed with smooth application of full aft stick for 3 seconds. Angles of attack of 43° and 34°, respectively, were obtained with mild uncommanded yaw rates developing.

FLIGHT TEST SUMMARY

The Shark nose configuration conclusively showed during flight testing that the asymmetric aerodynamic forces and moments generated by long, slender forebodies can be attenuated by proper forebody design. The most severe control misapplications which produced departures and spins during the F-5E and F-5F Spin Susceptibility Flight Test programs were repeated with the aircraft modified with the Shark nose, and only one oscillatory, one turn spin was obtained. This spin occurred with the centerline tank configuration during a high energy, stick-fixed rudder roll, a maneuver which could not be flown with the production nose configuration due to the almost 100% chance of spinning the airplane. A complete summary of those maneuvers which produced departures and spins from production nose and Shark nose testing is shown in Tables 6, 7, and 8. The tables are produced for the configurations and c.g.'s tested. Figure 143 illustrates the comparison between the flight test gross maneuver boundaries and the analytical two-turn spin entry boundary. The asymmetric nature of the production F-5F spin resistance seems to be confirmed by the flight test results as is the symmetric nature of the Shark nose data.

Highlights of the Shark nose flight test program are as follows:

Basic Configuration

- Increased departure/spin resistance
  (could not find spin entry window)
- Positive recovery from high angles of attack
  (always responds to forward stick)
- Improved inverted departure characteristics
  (departure milder than production nose configuration)
- Increased $C_{L_{max}}$ (W44 LEX)
- Enhanced "heads-out-of-cockpit" ACM capability
  (removes 29 unit angle of attack restriction)
- Lateral/directional characteristics above 20^{o} are
  comparable to the F-5A

C.L. Tank Configuration

- Increased departure/spin resistance
  (maneuver must be aggravated)
- Positive departure/spin recovery
  (better than basic F-5F)

CONCLUSIONS

A comprehensive investigation of the F-5F high angle-of-attack characteristics was conducted. This investigation included small scale, low-speed wind tunnel testing, an analytical prediction of the departure and spin resistance using nonlinear six degree of freedom simulation, and full-scale flight testing of the aircraft incorporating a modified forebody and LEX geometry. The following conclusions are the result of this investigation:

- Positive static directional stability at post-stall angles of attack on the F-5F is due to a unique orientation of the vortex patterns of the forebody when the aircraft is sideslipped. This unique orientation is a strong function of the forebody cross-sectional shape.
- At extreme post-stall angles of attack and at zero sideslip, this forebody vortex system becomes asymmetric and is responsible for large side forces and yawing moments at these conditions. These asymmetric forces and moments are aggravated by long slender forebodies and can become large enough to dominate the aircraft motion at high angles of attack.
- For a given forebody fineness ratio, nose geometry modifications can be designed to significantly attenuate asymmetric yawing moments while maintaining the unique vortex orientation at sideslip which is responsible for providing good, post-stall directional stability.
- Attenuation of the asymmetric yawing moments results in a significant improvement in the spin resistance and recovery characteristics of the F-5F.
- Longitudinal stability is sensitive to design changes in the airplane forebody and is highly dependent on the angle of attack region of interest. The Shark nose had no effect on longitudinal stability below approximately 25° angle of attack,

resulting in no change to normal flying qualities. Between 25° and 50° angle of attack, the Shark nose was destabilizing, resulting in an increase in trim angle of attack for full up elevator. Above 50° angle of attack, the Shark nose resulted in an improvement in longitudinal stability, contributing to the improved recovery capability from high angles of attack experienced in flight.

- The Shark nose was found to be compatible with radar performance requirements, resulting in a nominal reduction in lock-on range. Forebody cross-sectional shape is of secondary importance on the F-5F in its influence on the radar performance. Problems associated with incorporation of metal pitot heads and lightning protection devices into the radome tend to be of primary importance.
- The addition of a large nose boom to the forebody of an aircraft can significantly alter the forebody vortex system and, hence, the overall aerodynamics of the aircraft at high angles of attack.

REFERENCES

1. Mechtly, E. A., The International System of Units - Physical Constants and Conversion Factors. NASA SP-7012, 1973.

2. Edwards, O.R., Skow, A.M., F-5E Stall/Post Stall/Spin Susceptibility Flight Test. Northrop Corporation, Aircraft Group Report, NOR 77-90, April 1977.

3. Edwards, O.R., F-5F Stall/Post Stall/Spin Susceptibility Flight Test. Northrop Corporation, Aircraft Group Report, NOR 77-91, August 1977.

4. Skow, A.M., F-5E/F Yaw Departure Analysis. Northrop Aerodynamic Report AR 75-3, May 1975.

5. Bennett, G.B., Data Report of a Low Speed Wind Tunnel Test of a 10% Force Model of an F-5E in Deep Negative Pitch Attitudes and an F-5F with Wing Fence. Northrop Corporation, Aircraft Division, Report NOR 75-80, February 1975.

6. Bennett, G.B., Data Report of a Low Speed Wind Tunnel Test of a 10% Force Model of an F-5E at Spin Entry Attitudes and an F-5F in Post Stall Gyration Attitudes and with Nose-Wheel Lift-Off Devices. Northrop Corporation, Aircraft Division, Report NOR 75-79, August 1975.

7. Jorgensen, L.H., Nelson, E.R., Experimental Aerodynamic Characteristics for Slender Bodies with Thin Wings and Tail at Angles of Attack from 0° to 58° and Mach Number from 0.6 to 2.0. NASA TMX-3310, March 1976.

8. Chambers, J.R., Anglin, E.L., and Bowman, J.S., Effects of a Pointed Nose on Spin Characteristics of a Fighter Airplane Model Including Correlation with Theoretical Calculations. NASA TN D-5921, 1970.

9. Chapman, G.T., Keener, E.R., and Malcolm, G.N., Asymmetric Aerodynamic Forces on Aircraft at High Angles of Attack - Some Design Guides. AGARD Conference Proceedings No. 199, 18-21 Nov. 1975, Stall/Spin Problems of Military Aircraft.

10. Keener, E.R., Chapman, G.T., Onset of Aerodynamic Side Force at Zero Sideslip on Symmetric Forebodies at High Angles of Attack. AIAA Paper 74-770, 1974.

11. Jorgensen, L. H., Nelson, E. R., Experimental Aerodynamic Characteristics for a Cylindrical Body of Revolution with Various Noses at Angles of Attack from 0^{o} to 58^{o} and Mach Numbers from 0.6 to 2.0. NASA TMX-?128, 1974.

12. Jorgensen, L.H., Howell, M.H., Experimental Aerodynamic Characteristics for Slender Bodies with Thin Wings at Angles of Attack from 0^{o} to 58^{o} and Mach Numbers from 0.6 to 2.0, NASA TMX-3309, 1976.

13. Bennett, G.B., Data Report of a Low Speed Wind Tunnel Test of a 10% Force Model of an F-5F at High Attitudes with Various Nose Radome Configurations. Northrop Corporation, Aircraft Group Report NOR 76-212 (2 Vols.), May 1977.

14. Bennett, G.B., Data Report of a Low Speed Wind Tunnel Test of a 10% Force Model of an F-5F and F-5E at High Attitudes with Various Nose Radome Configurations. Northrop Corporation, Aircraft Group Report NOR 77-86 (2 Vols.), June 1977.

15. Grafton, S.B., Chambers, J.R., Coe, P.L., Wind Tunnel Free Flight Investigation of a Model of a Spin-Resistant Fighter Configuration. Langley Research Center, Technical Note NASA TN D-7716, June 1974.

TABLE 1. F-5E/F GEOMETRIC DATA

SECTION		
WING	AREA TOTAL (INCLUDING AILERONS, FLAPS, 5.34-m^2 OF FUSELAGE, AND EXPOSED LEADING EDGE EXTENSION)	18.06-m^2 (194.42-ft^2)
	AREA BASIC (REFERENCE) (INCLUDING AILERONS, FLAPS, 5.34-m^2 OF FUSELAGE BUT EXCLUDING LEADING EDGE EXTENSION)	17.30-m^2 (186.25-ft^2)
	TAPER RATIO - BASIC WING	0.19
	ASPECT RATIO - BASIC WING (SPAN: 8.13-m (26.66-ft)	3.82
	SWEEPBACK AT 25% CHORD	24°
	AIRFOIL SECTION	NACA 65A-004.8 MODIFIED
	FLAP AREA - TRAILING EDGE (TOTAL)	1.95-m^2 (21-ft^2)
	FLAP AREA - LEADING EDGE (TOTAL)	1.14-m^2 (12.3-ft^2)
	FLAP MOVEMENT:	
	LEADING EDGE (ROOT)	24° DOWN
	TRAILING EDGE	20° DOWN
	AILERON AREA - AFT OF HINGE - PER AILERON	0.43-m^2 (4.62-ft^2)
	AILERON MOVEMENT:	
	GEAR DOWN	35° UP, 25° DOWN
	GEAR UP	18.5° UP, 14° DOWN
HORIZONTAL TAIL	AREA TOTAL - INCLUDING 2.41-m^2 (25.97-ft^2) OF FUSELAGE	5.48-m^2 (59.0-ft^2)
	AREA EXPOSED	3.07-m^2 (33.03-ft^2)
	TAPER RATIO (EXPOSED)	0.33
	ASPECT RATIO (EXPOSED)	2.88
	SWEEPBACK AT 25% CHORD	25°
	AIRFOIL SECTION	NACA 65A-004
	SURFACE MOVEMENT TRAILING EDGE	F-5E 17° UP, 5° DOWN F-5F 20° UP, 5° DOWN
VERTICAL TAIL	AREA EXPOSED	3.85-m^2 (41.42-ft^2)
	TAPER RATIO (EXPOSED)	0.25
	ASPECT RATIO (EXPOSED)	1.22
	SWEEPBACK AT 25% CHORD	25°
	AIRFOIL SECTION	NACA 65A-004 MODIFIED
RUDDER	AREA - AFT OF HINGE	0.57-m^2 (6.10-ft^2)
	MOVEMENT (MAXIMUM)	30° RIGHT, 30° LEFT
SPEED BRAKE	AREA TOTAL	0.60-m^2 (6.42-ft^2)
	SURFACE POSITION (MAXIMUM DOWN)	45° (RELATIVE TO HPL)

TABLE 2. F-5F FLIGHT TEST AIRPLANE
MASS AND INERTIA CHARACTERISTICS

	CONFIGURATION	
	CLEAN	CENTERLINE TANK
WEIGHT kg (lbs)	5,874 (12,950)	5,976 (13,175)
ROLL INERTIA $kg\text{-}m^2$ ($slug\text{-}ft^2$)	6,295 (4,640)	6,376 (4,700)
PITCH INERTIA $kg\text{-}m^2$ ($slug\text{-}ft^2$)	73,937 (54,500)	74,208 (54,700)
YAW INERTIA $kg\text{-}m^2$ ($slug\text{-}ft^2$)	78,278 (57,700)	78,468 (57,840)
PRODUCT OF INERTIA $kg\text{-}m^2$ ($slug\text{-}ft^2$)	18 (13)	27 (20)
c.g. % $\bar{c}$	12.0	12.0
	or 16.0	

TABLE 3. F-5E/F SPIN TEST SUMMARY

			SPINS	
	MANEUVERS	DEPARTURES	ERECT	INVERTED
F-5E				
Clean Configuration	299	32	5	4
C.L. Tank	45	8	1	0
F-5F				
Clean Configuration	170	15	3	1
C.L. Tank	2	2	0	0

TABLE 4. SUMMARY OF F-5F NOSE STRAKE TESTS

STRAKE	ZERO-SIDESLIP ASYMMETRY	DIRECTIONAL STABILITY	LONGITUDINAL STABILITY	
			SIDESLIP = 0°	SIDESLIP = -10°
S7	SAME	BETTER 24°-52° AOA	WORSE 35°-55° AOA	WORSE BELOW 51° AOA
S8	SAME	WORSE	BETTER	BETTER
S9	SAME	WORSE	BETTER	BETTER
M 63	SLIGHTLY BETTER	SLIGHTLY WORSE	MUCH WORSE	MUCH WORSE
S11	WORSE	SLIGHTLY BETTER 29°-42° AOA	BETTER ABOVE 45° AOA	SAME UP TO 53° AOA
S10	BETTER	BETTER 24°-59° AOA	BETTER ABOVE 46° AOA	WORSE
S12	BETTER	BETTER 24°-44° AOA	BETTER ABOVE 46° AOA	WORSE
S13	BETTER	BETTER 24°-44° AOA	BETTER	SAME
S14	BETTER	BETTER THAN S13	BETTER	SAME

NOTE: Each strake is compared with base (production nose with pitot on/off) data.

TABLE 5. F-5F SHARK NOSE FLIGHT TEST PROGRAM

FLIGHT NO.	CONFIGURATION	C.G. $\frac{\bar{c}}{c}$	FLAP POSN	MANEUVER
421	CLEAN	12	MAN.	1-g STALL 3 SECS FAS
"	"	12	UP	1-g STALL 3 SECS FAS
"	"	12	MAN.	1-g STALL 15 SECS FAS
"	"	12	UP	1-g STALL 15 SECS FAS
422	CLEAN	12	MAN.	240-kt WUT 11 SECS SMOOTH FAS
"	"	12	UP	240-kt WUT 10 SECS SMOOTH FAS
"	"	12	MAN.	310-kt WUT 14 SECS SMOOTH FAS
"	"	12	UP	310-kt WUT 2½ SECS SMOOTH FAS
"	"	12	MAN.	1-g STALL 15 SECS FAS
423	CENTERLINE TANK	12	MAN.	1-g STALL 3 SECS FAS
"	" "	12	UP	1-g STALL 3 SECS FAS
"	" "	12	MAN.	2-g STALL 3 SECS FAS
"	" "	12	DOWN	240-kt WUT 3 SECS FAS
"	" "	12	MAN.	240-kt WUT 3 SECS FAS
"	" "	12	DOWN	3-g LEVEL DECEL 3 SECS FAS
"	" "	12	MAN.	3-g LEVEL DECEL 3 SECS FAS
"	" "	12	UP	2-g STALL 3 SECS FAS
425	CLEAN	12	MAN.	2-g LEVEL DECEL 5 SECS FAS & RUDDER FROM 20° AOA
"	"	12	UP	2-g LEVEL DECEL 3 SECS FAS & RUDDER FROM 20° AOA
"	"	12	MAN.	4-g LEVEL DECEL 3 SECS FAS & RUDDER FROM 20° AOA
"	"	12	UP	240-kt WUT 3 SECS FAS & RUDDER FROM 20° AOA
"	"	12	MAN.	PULL-UP ABRUPT FAS FROM 150-kts
"	"	12	MAN.	PULL-UP ABRUPT FAS FROM 160-kts
"	"	12	UP	PULL-UP ABRUPT FAS FROM 160-kts
426	CLEAN	16	MAN.	1-g STALL ABRUPT FAS AT 25° AOA 32 SECS
"	"	16	MAN.	PULL-UP ABRUPT FAS FROM 150-kts 15 SECS
"	"	16	MAN.	2-g LEVEL DECEL 3 SECS SMOOTH FAS & RUDDER FROM 20° AOA
"	"	16	MAN.	4-g LEVEL DECEL 1 SEC SMOOTH FAS & RUDDER FROM 20° AOA
"	"	16	DOWN	4-g LEVEL DECEL 3 SECS SMOOTH FAS & RUDDER FROM 20° AOA
"	"	16	MAN.	4-g LEVEL DECEL 3 SECS SMOOTH FAS & RUDDER FROM 20° AOA
427	CLEAN	16	MAN.	240-kt WUT RUDDER AT 15° AOA FAS AT 180° $\Delta\phi$ FOR 1 SEC
"	"	16	MAN.	240-kt WUT RUDDER AT 15° AOA FAS AT 180° $\Delta\phi$ FOR 1 SEC
"	"	16	MAN.	240-kt WUT RUDDER AT 15° AOA FAS AT 180° $\Delta\phi$ FOR 3 SECS
"	"	16	MAN.	INVERTED FLIGHT FULL FORWARD STICK
"	"	16	MAN.	310-kt WUT FAS & RUDDER AT 20° AOA FOR 1 SEC

TABLE 5. F-5F SHARK NOSE FLIGHT TEST PROGRAM (Continued)

FLIGHT NO.	CONFIGURATION	C.G. % $\bar{c}$	FLAP POS^N	MANEUVER
428	CENTERLINE TANK	12	MAN.	1-g STALL 5 SECS FAS
"	" "	12	MAN.	240-kt WUT 5 SECS FAS
"	" "	12	MAN.	240-kt WUT STICK FIXED RUDDER ROLL AT 15^O AOA
"	" "	12	MAN.	240-kt WUT STICK FIXED RUDDER ROLL AT 20^O AOA
"	" "	12	MAN.	280-kt WUT 5 SECS FAS
"	" "	12	MAN.	310-kt WUT 5 SECS FAS
"	" "	12	MAN.	280-kt WUT STICK FIXED RUDDER ROLL AT 20^O AOA
"	" "	12	MAN.	310-kt WUT 5 SECS FAS
429	CLEAN	16	UP	1-g STALL 21 SECS FAS
"	"	16	UP	PULL-UP ABRUPT FAS FROM 150-kts
"	"	16	MAN.	310-kt WUT FAS & RUDDER AT 20^O AOA FOR 3 SECS
"	"	16	MAN.	4-g DECEL 30^O PITCH.FAS & RUDDER AT 15^O AOA FOR 3 SECS
"	"	16	UP	2-g LEVEL DECEL FAS & RUDDER AT 20^O AOA FOR 3 SECS
"	"	16	MAN.	4-g DECEL 30^O PITCH.FAS & RUDDER AT 15^O AOA FOR 3 SECS
430	CENTERLINE TANK	12	MAN.	3-g LEVEL DECEL 6 SECS FAS
"	" "	12	MAN.	4-g LEVEL DECEL 6 SECS FAS
"	" "	12	MAN.	4-g LEVEL DECEL ½ SEC FAS
"	" "	12	MAN.	4-g LEVEL DECEL STICK FIXED RUDDER ROLL AT 15^O AOA
"	" "	12	MAN.	4-g LEVEL DECEL STICK FIXED RUDDER ROLL AT 20^O AOA
"	" "	12	MAN.	4-g LEVEL DECEL ½ SEC FAS
"	" "	12	MAN.	4-g LEVEL DECEL STICK FIXED RUDDER ROLL AT 20^O AOA
431	CLEAN	16	MAN.	4-g DECEL 30^O PITCH.FAS STICK & RUDDER AT 15^O AOA FOR 1 SEC
"	"	16	UP	4-g DECEL 30^O PITCH.FAS STICK & RUDDEF AT 15^O AOA FOR 1 SEC
"	"	16	MAN.	4-g LEVEL DECEL FAS & RUDDER AT 20^O AOA FOR 3 SECS
"	"	16	UP	240-kt WUT FAS & RUDDER AT 20^O AOA FOR 3 SECS
"	"	16	UP	310-kt WUT FAS & RUDDER AT 20^O AOA FOR 3 SECS

TABLE 6. F-5F SUMMARY OF DEPARTURE MANEUVERS. CLEAN CONFIGURATION 12% C.G.

PRODUCTION NOSE AND SHARK NOSE MANEUVER	MAXIMUM ANGLE OF ATTACK DEGREE		MAXIMUM ANGLE OF SIDESLIP DEGREE		MAXIMUM YAW RATE DEG/SEC		PRODUCTION DEPARTURE / SHARK DEPARTURE	
	PRODUCTION	SHARK	PRODUCTION	SHARK	PRODUCTION	SHARK	PRODUCTION	SHARK
310 Kt WUT flaps up 2-1/2 secs smooth FAS	--	42	--	22	--	26	--	Mild
240 Kt WUT flaps up FAS and rudder from 20° AOA 3 secs	41	44	32	20	40	18	Yes	No
Wings-level pullup, flaps up abrupt FAS from 160 kts	88	44	58	10	84	14	Yes + spin	No

TABLE 7. F-5F SUMMARY OF DEPARTURE MANEUVERS.CLEAN CONFIGURATION 16% C.G.

PRODUCTION NOSE AND SHARK NOSE MANEUVER	MAXIMUM ANGLE OF ATTACK DEGREE		MAXIMUM ANGLE OF SIDESLIP DEGREE		MAXIMUM YAW RATE DEG/SEC		PRODUCTION DEPARTURE / SHARK DEPARTURE	
	PRODUCTION	SHARK	PRODUCTION	SHARK	PRODUCTION	SHARK	PRODUCTION	SHARK
1g stall. flaps man abrupt FAS from 25° AOA 3 secs	88	60	62	26	72	18	Yes + Spin	No
Wings-level pullup flaps man Abrupt FAS from 160 kts. 15 secs	88	52	58	18	84	20	Yes + Spin	No
2g level decel. flaps man Smooth FAS and rudder from 20° AOA, 3 secs	54	51	38	24	32	24	Yes	No
240 kt WUT flaps man, rudder at 15° AOA FAS at 180° for 1 sec	57	64	21	38	34	36	Yes	No
Inverted pitch hangup. flaps man Full forward stick	-100	-85	100	36	52	32	Yes	Yes
1g stall flaps up FAS for 21 secs	88*	55	62*	26	72*	20	Yes* + Spin	No
Wings-level pullup, flaps up Abrupt FAS at 150 Kts	88	55	58	10	84	20	Yes + Spin	No
310 Kt WUT Flaps Man FAS and Rudder at 20° AOA. 3 secs	80	64	50	45	44	24	Yes	No
4g Decel. 30° pitch. flaps man. FAS and rudder at 15° AOA. 3 secs	64X	52	38X	20	42X	18	Yes	No
2g level decel flaps up FAS and rudder at 20° AOA. 3 secs	68X	60	43X	30	43X	21	Yes	No
4g decel 30° pitch flaps man. FAS and rudder at 15° AOA. 3 secs	64X	50	38X	28	42X	24	Yes	No
240 Kt WUT, flaps up. FAS and rudder at 20° AOA, 3 secs	44	68	32	50	40	23	Yes	No
310 Kt WUT, flaps up. FAS and rudder at 20° AOA, 3 secs	80*	73	50*	50	44*	24	Yes*	No

*Flaps maneuver

XF-5E departure maneuvers

TABLE 8. F-5F SUMMARY OF DEPARTURE MANEUVERS. CENTERLINE TANK CONFIGURATION 12% C.G.

PRODUCTION NOSE AND SHARK NOSE MANEUVER	MAXIMUM ANGLE OF ATTACK DEGREE	MAXIMUM ANGLE OF SIDESLIP DEGREE	MAXIMUM YAW RATE DEG/SEC	PRODUCTION DEPARTURE / SHARK DEPARTURE
	PRODUCTION / SHARK	PRODUCTION / SHARK	PRODUCTION / SHARK	
1g stall. flaps man. FAS, 3 secs	44[x] / 35	28[x] / 18	20[x] / 4	Yes (2) / No
2g stall flaps up. FAS 3 secs	-- / 34	-- / 16	-- / 24	-- / Mild
1g stall. flap. man. FAS 5 secs	44[x] / 44	28[x] / 20	20[x] / 4	Yes (2) / No
310 Kt WUT, flaps man. FAS 5 secs	-- / 40	-- / 18	-- / 32	-- / Mild
3g level decel. flaps man. FAS 6 secs	32 / 36	12 / 16	23 / 12	Yes / No
4g level decel (left). flaps man. FAS 6 secs	76 / 28	44 / 6	60 / 12	Yes / No
4g level decel (right). flaps man. Reached -16° stab for 1/2 sec	-- / 44	-- / 22	-- / 24	-- / Yes
4g level decel (right). flaps man. reached -15° stab for 1/2 sec	-- / 31	-- / 14	-- / 30	-- / Mild
4g level decel flaps man Stick fixed rudder roll at 20° AOA	-- / 67	-- / 43	-- / 44	-- / Yes + 1 Turn Spin

[x]With W44 LEX only configuration

POSITIVE FORCES & POSITIVE MOMENTS ARE SHOWN. CONTROL SURFACE DEFLECTIONS ARE MEASURED IN A PLANE PERPENDICULAR TO THE RESPECTIVE SURFACE HINGE LINE.

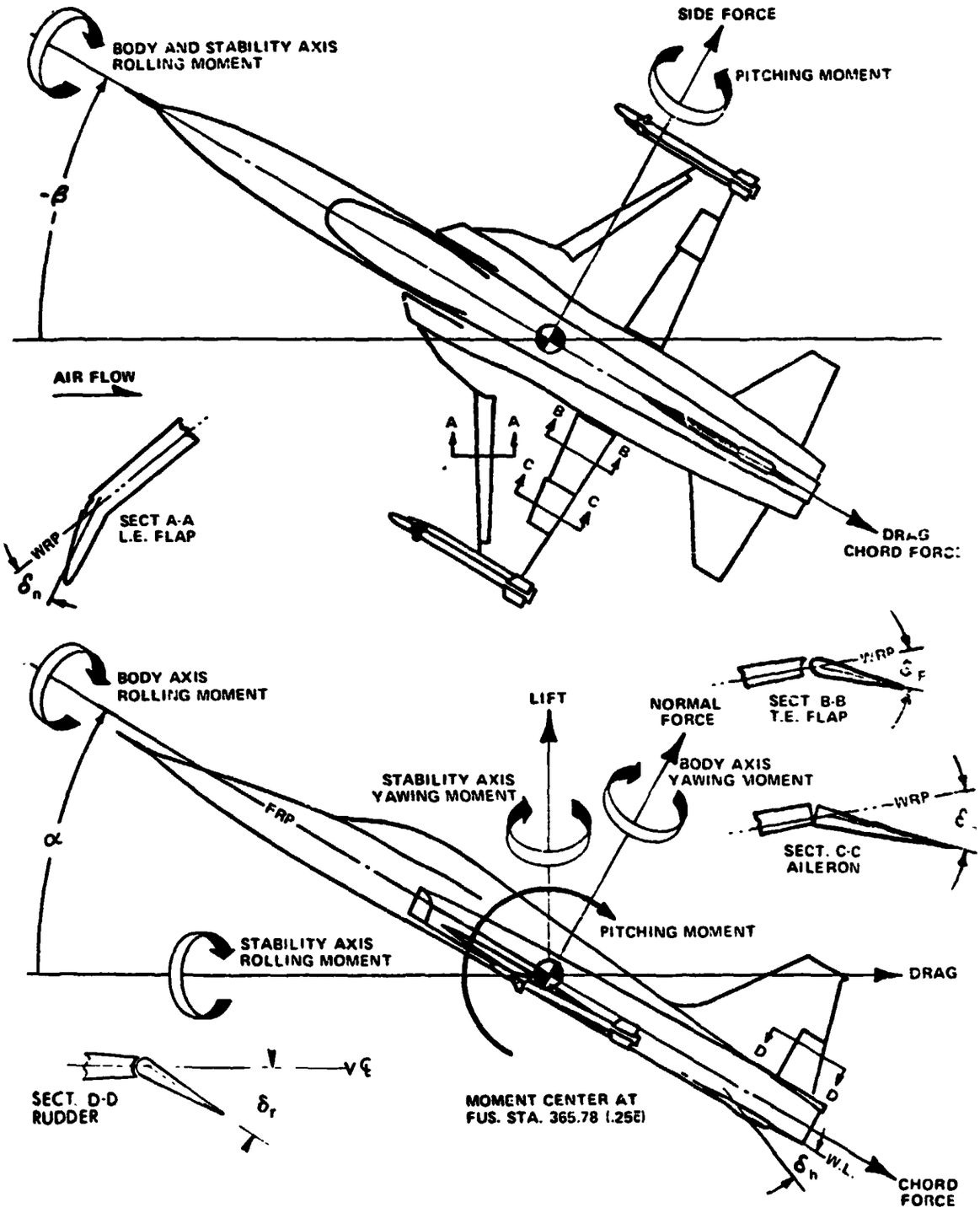

FIGURE 1. BODY AND STABILITY AXIS SYSTEMS AND POSITIVE SIGN CONVENTION

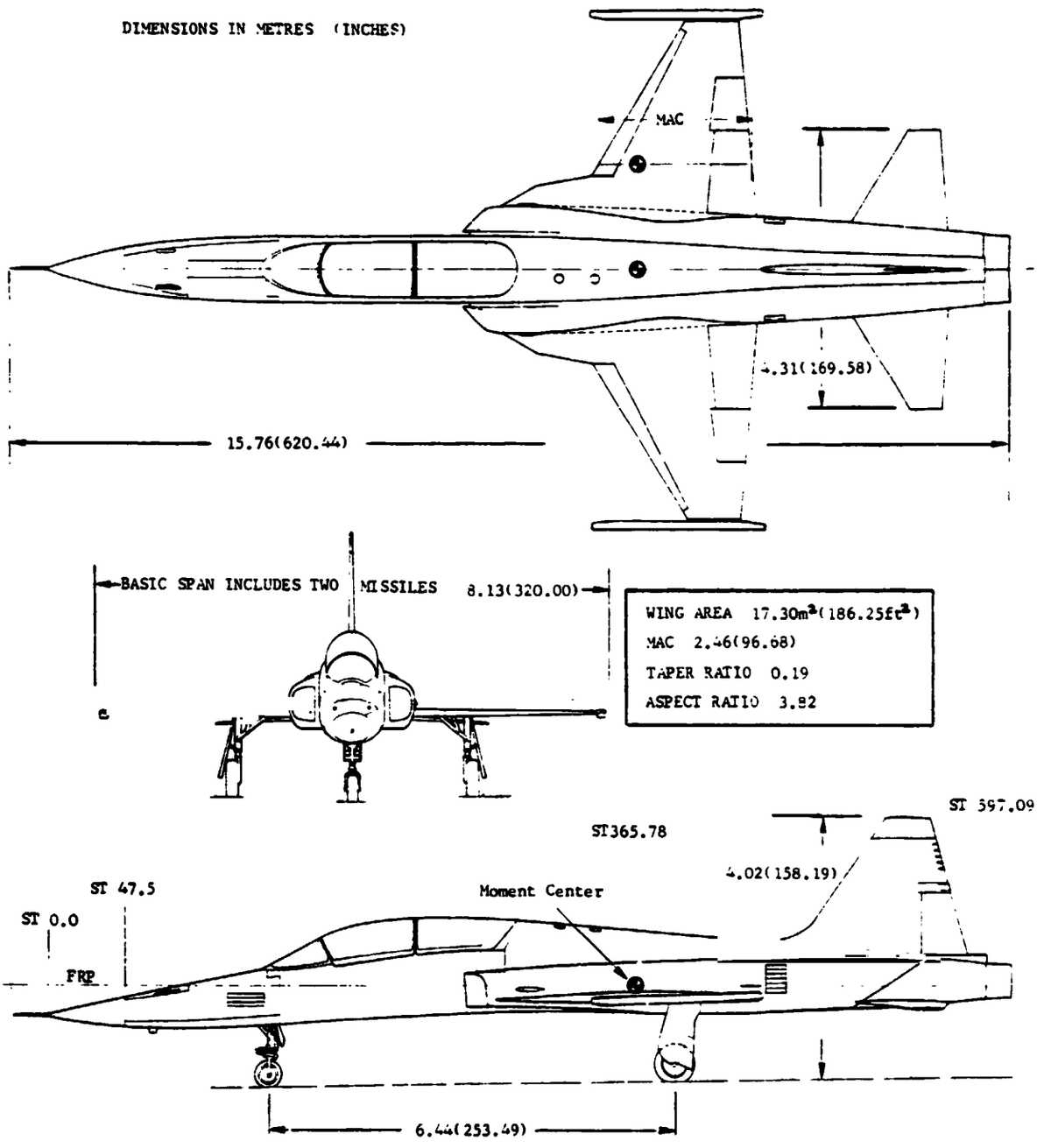

FIGURE 2. F-5F CLEAN CONFIGURATION

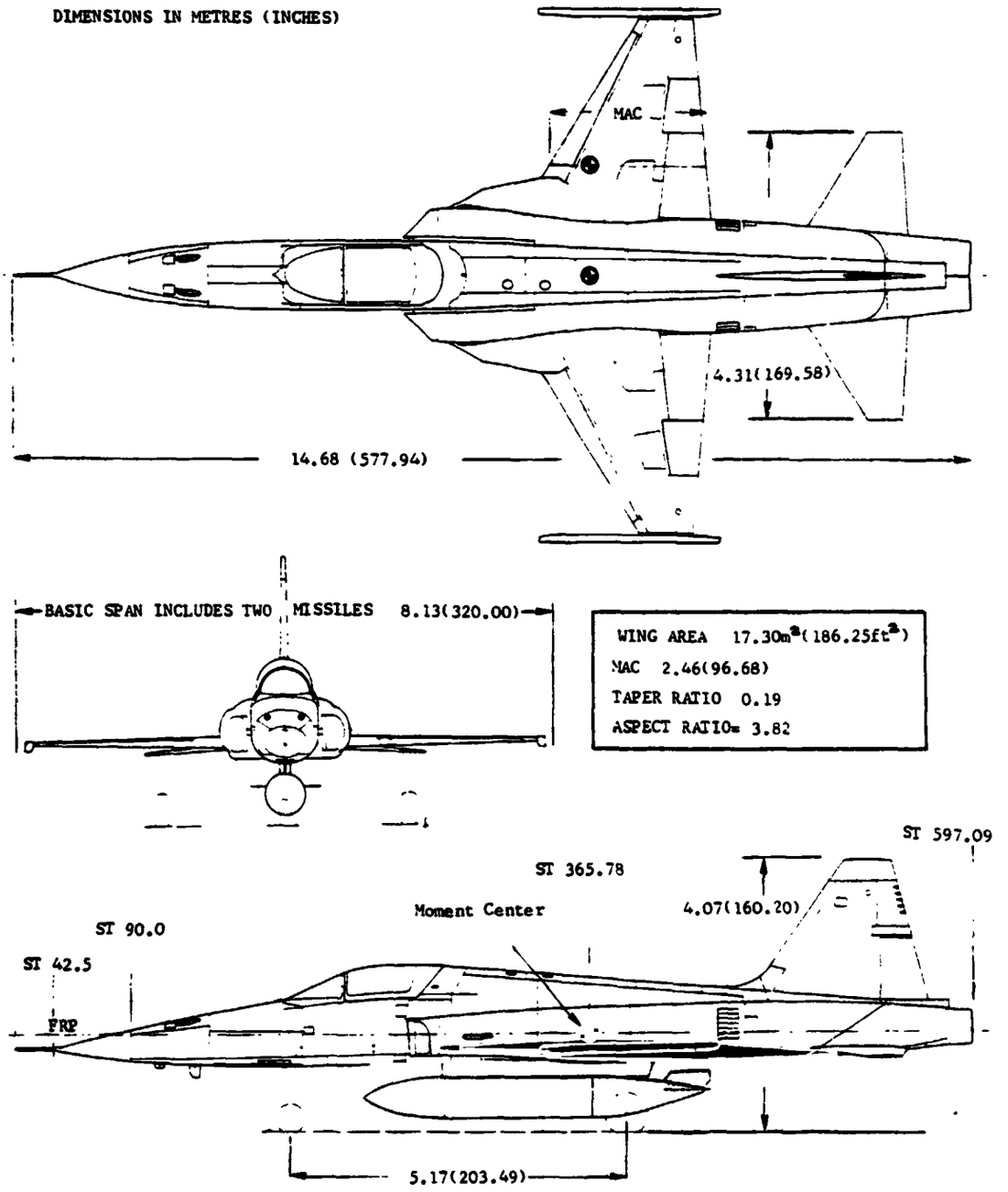

FIGURE 3. F-5E CENTERLINE TANK CONFIGURATION

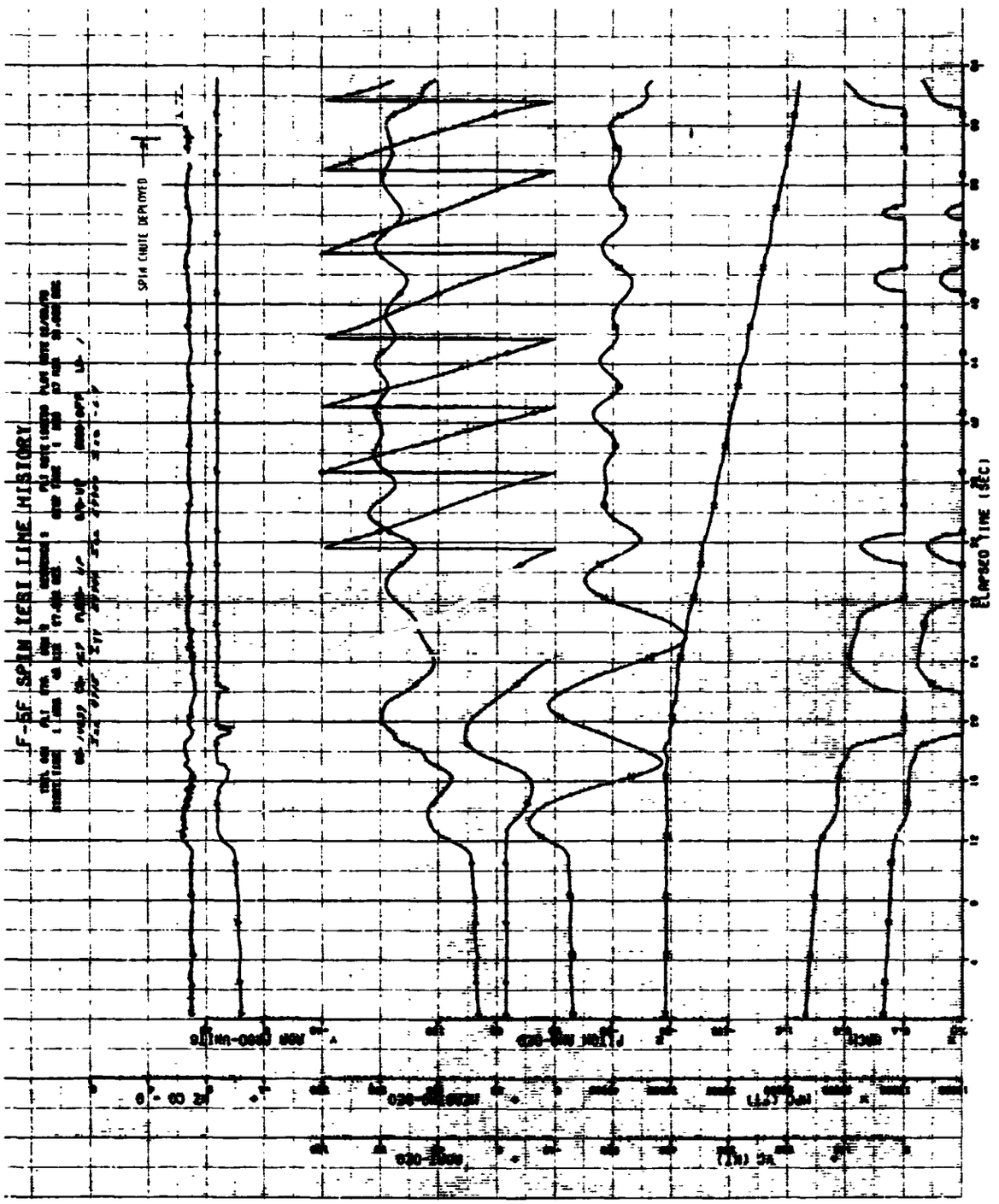

FIGURE 4. F-5F CLEAN CONFIGURATION. ABRUPT FULL AFT STICK, FLAPS UP (Sheet 1 of 4)

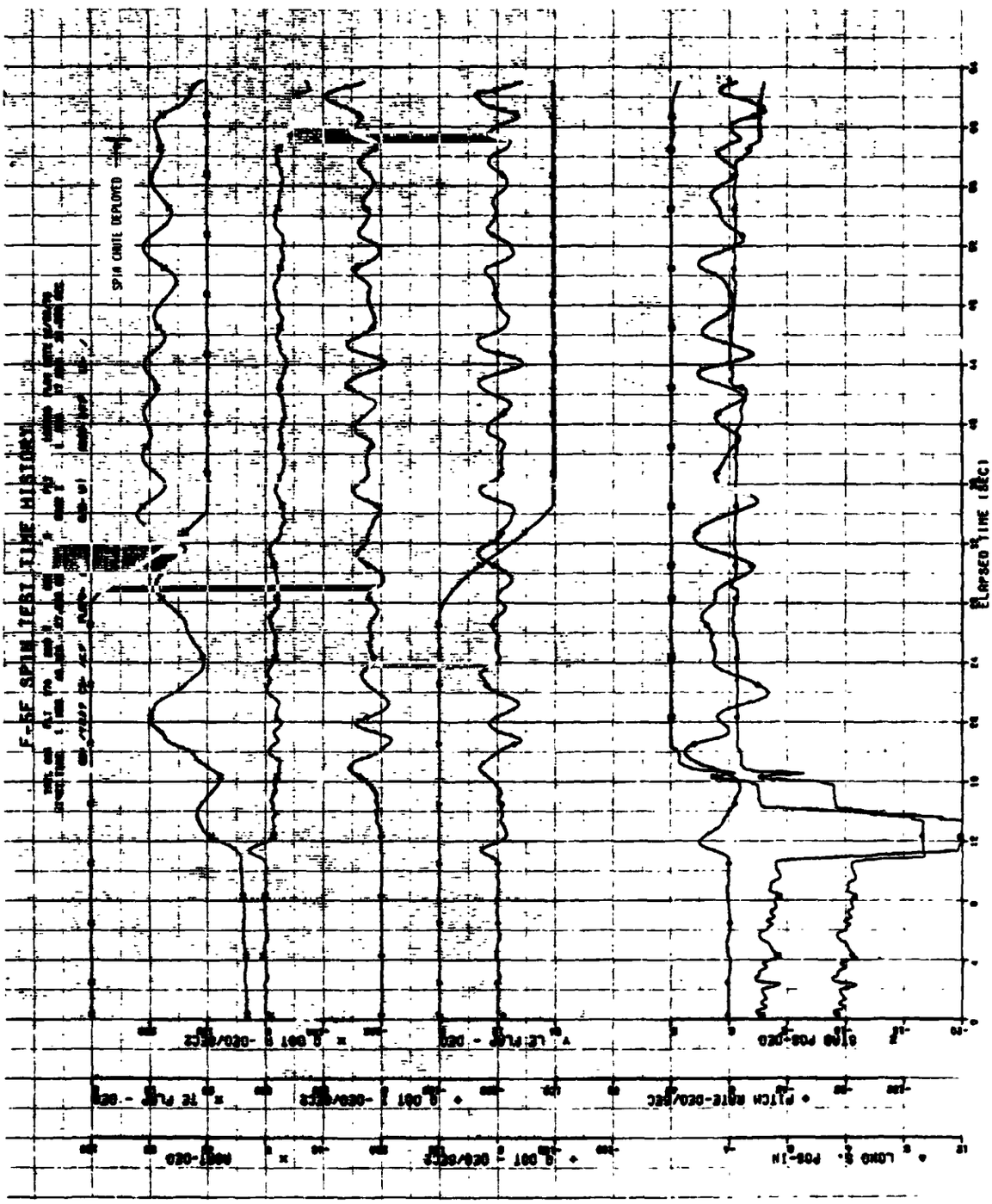

FIGURE 4. F-5F CLEAN CONFIGURATION.ABRUPT FULL AFT STICK, FLAPS UP (Sheet 2 of 4)

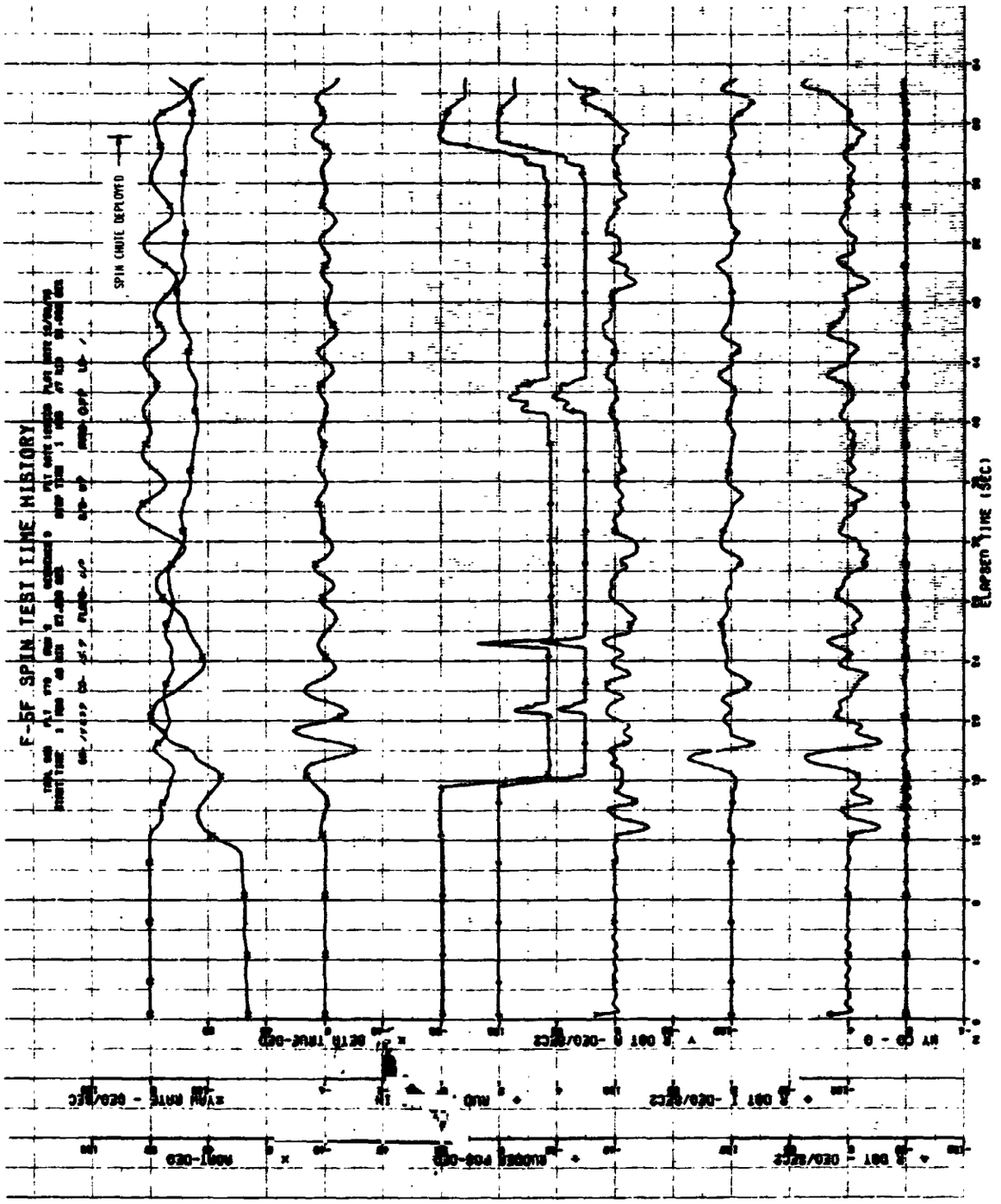

FIGURE 4. F-5F CLEAN CONFIGURATION. ABRUPT FULL AFT STICK, FLAPS UP (Sheet 3 of 4)

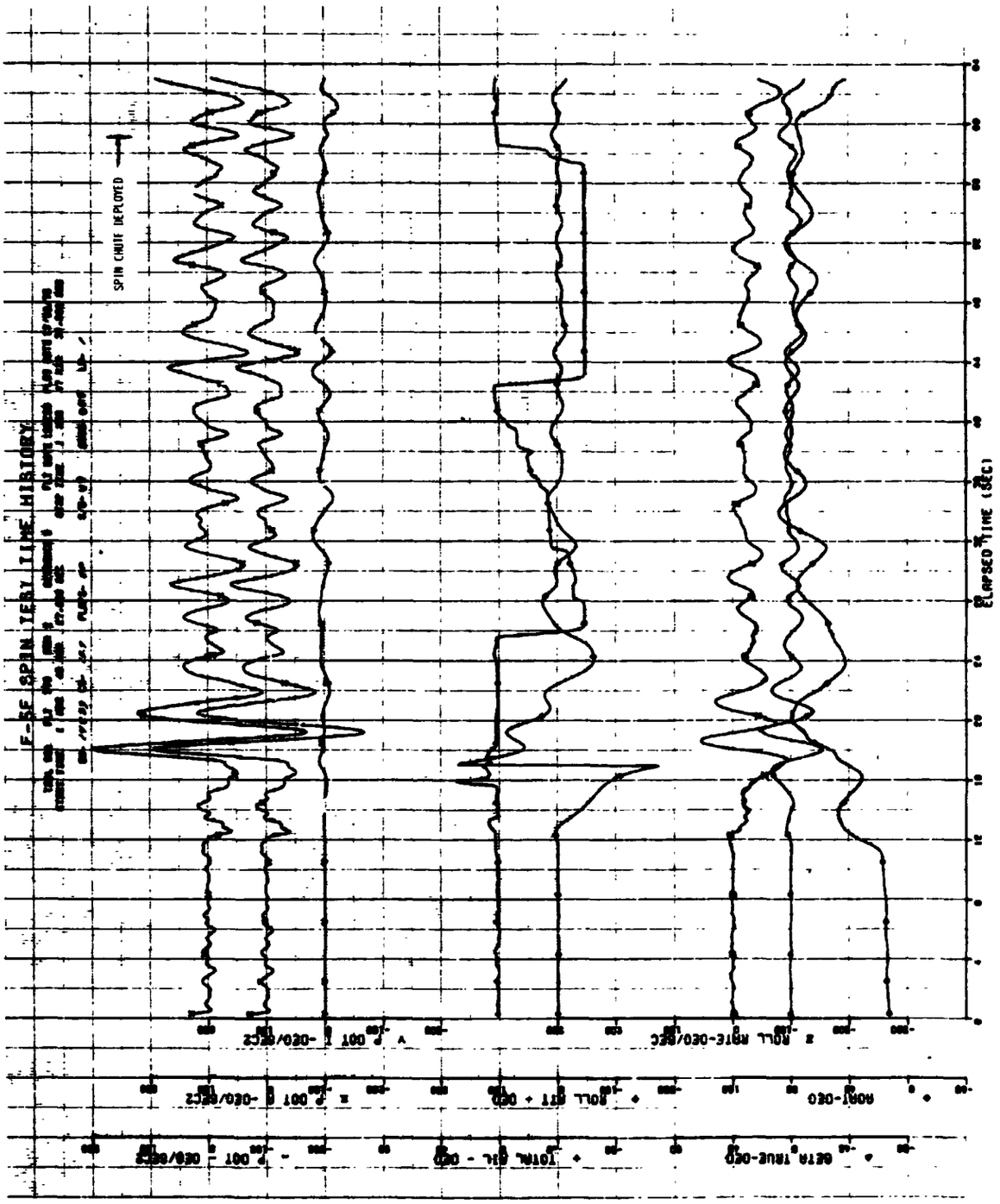

FIGURE 4. F-5F CLEAN CONFIGURATION, ABRUPT FULL AFT STICK, FLAPS UP (Sheet 4 of 4)

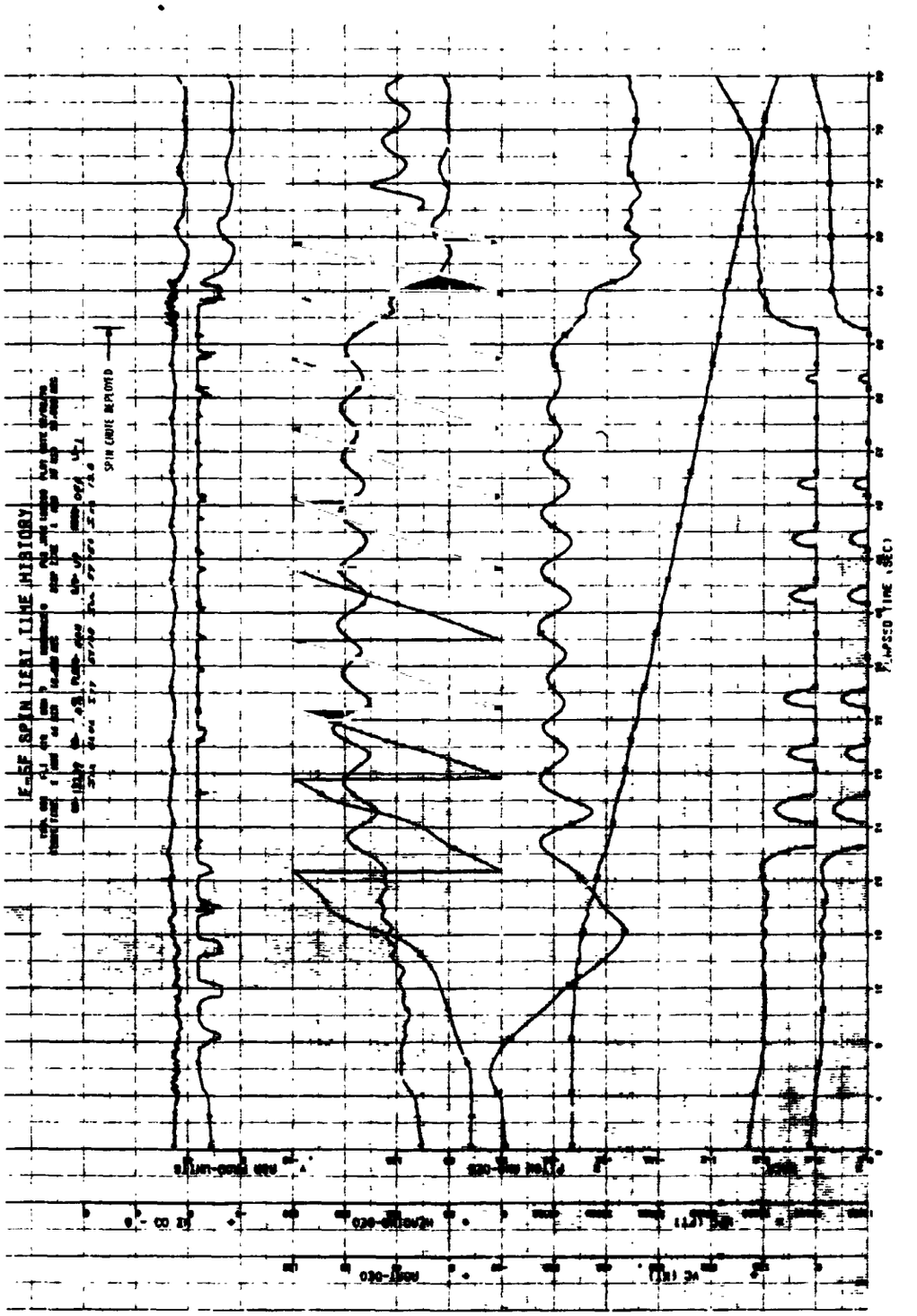

FIGURE 5. F-5F CLEAN CONFIGURATION. EXTENDED 1-g STALL, FLAPS MANEUVER (Sheet 1 of 4)

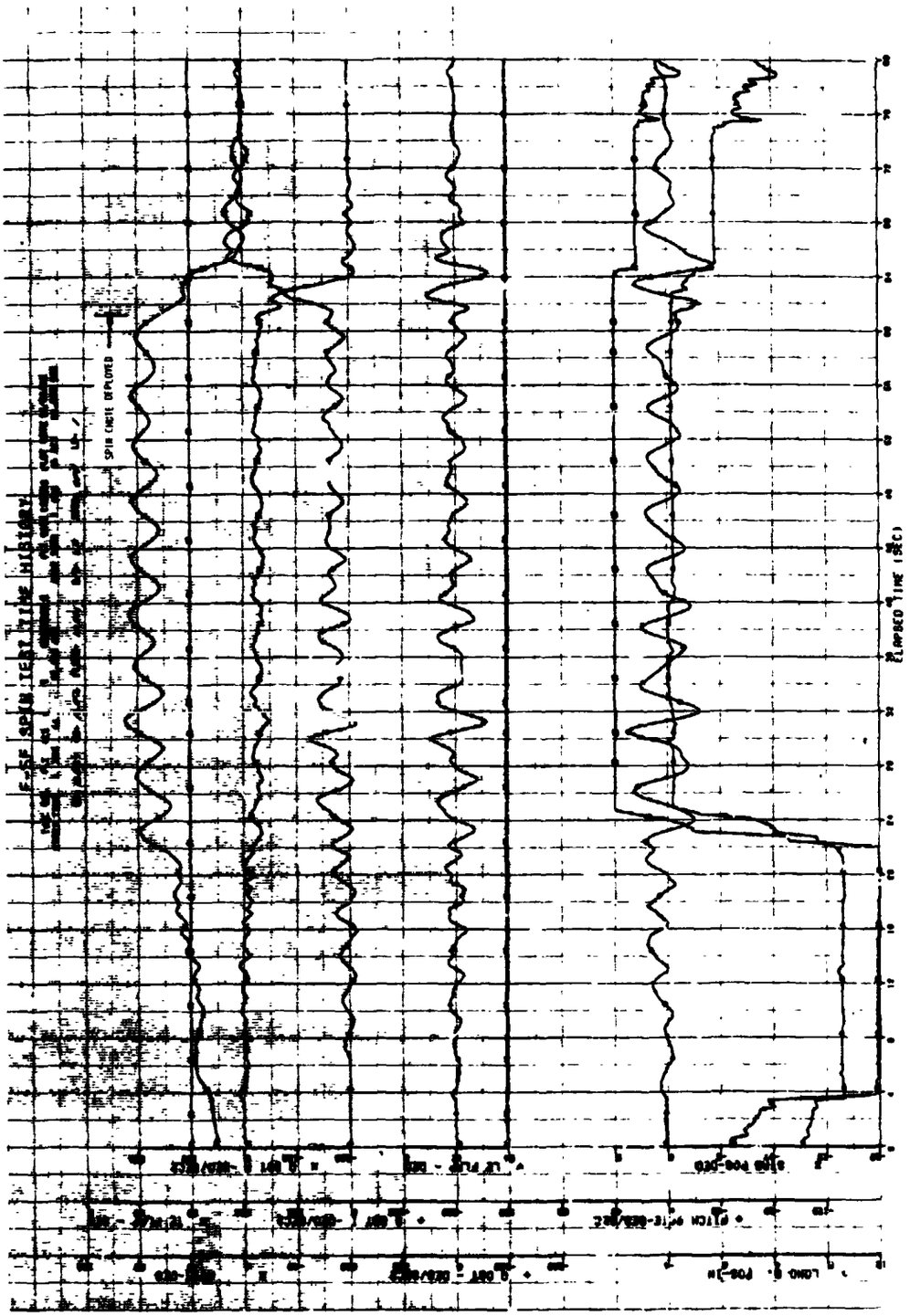

FIGURE 5. F-5F CLEAN CONFIGURATION. EXTENDED 1-g STALL, FLAPS MANEUVER (Sheet 2 of 4)

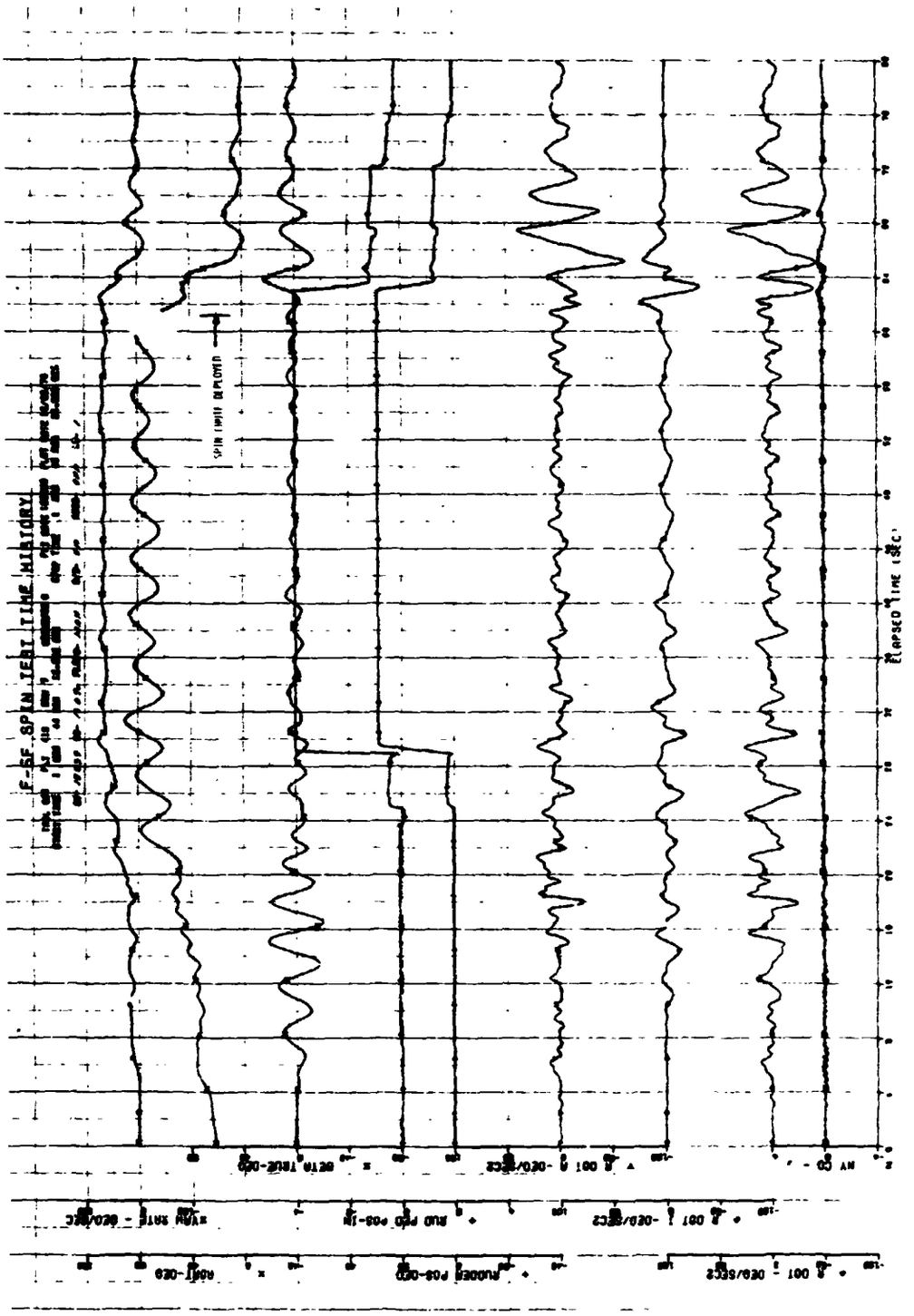

FIGURE 5. F-5F CLEAN CONFIGURATION. EXTENDED 1-g STALL, FLAPS MANEUVER (Sheet 3 of 4)

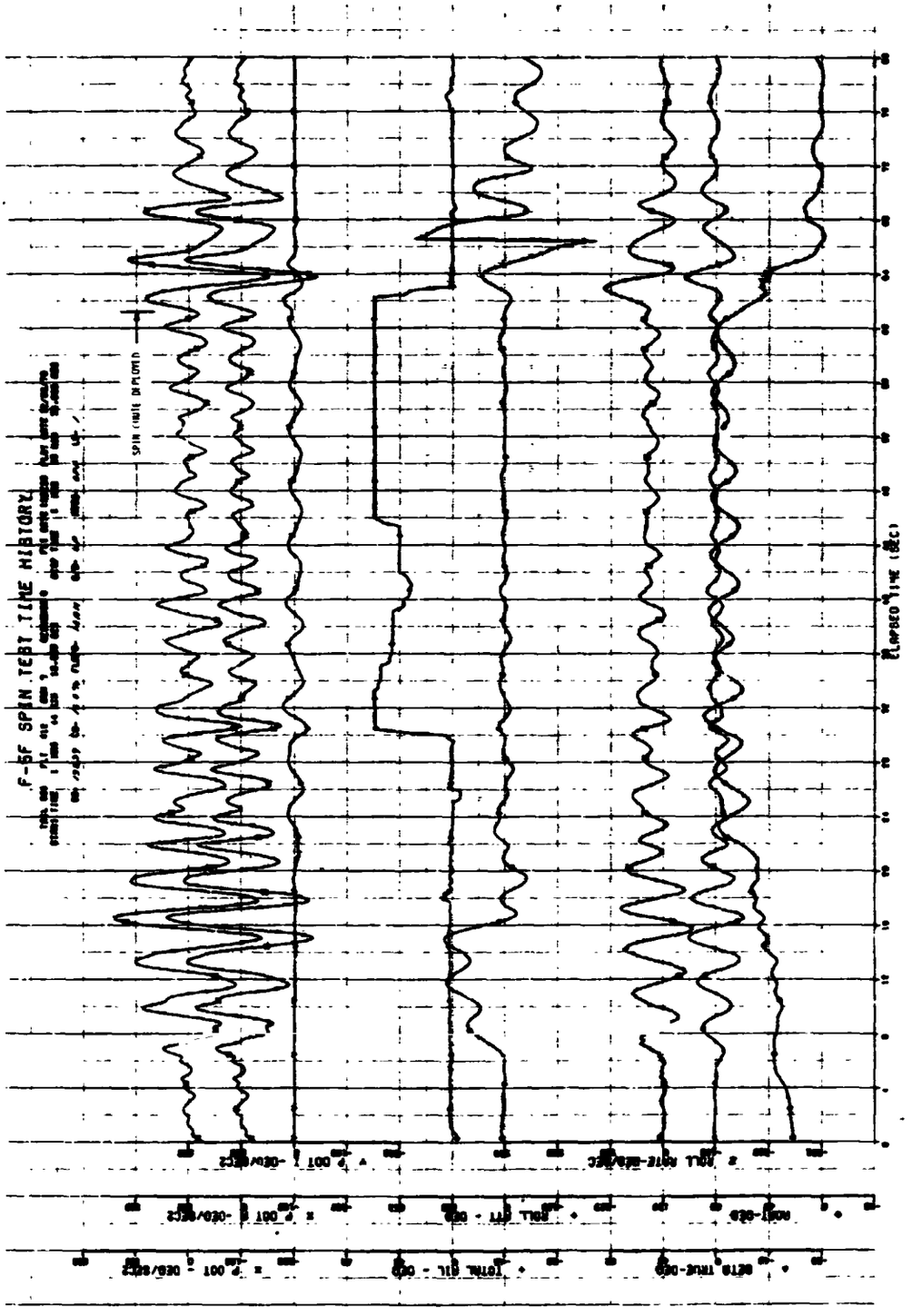

FIGURE 5. F-5F CLEAN CONFIGURATION. EXTENDED 1-g STALL, FLAPS MANEUVER (Sheet 4 of 4)

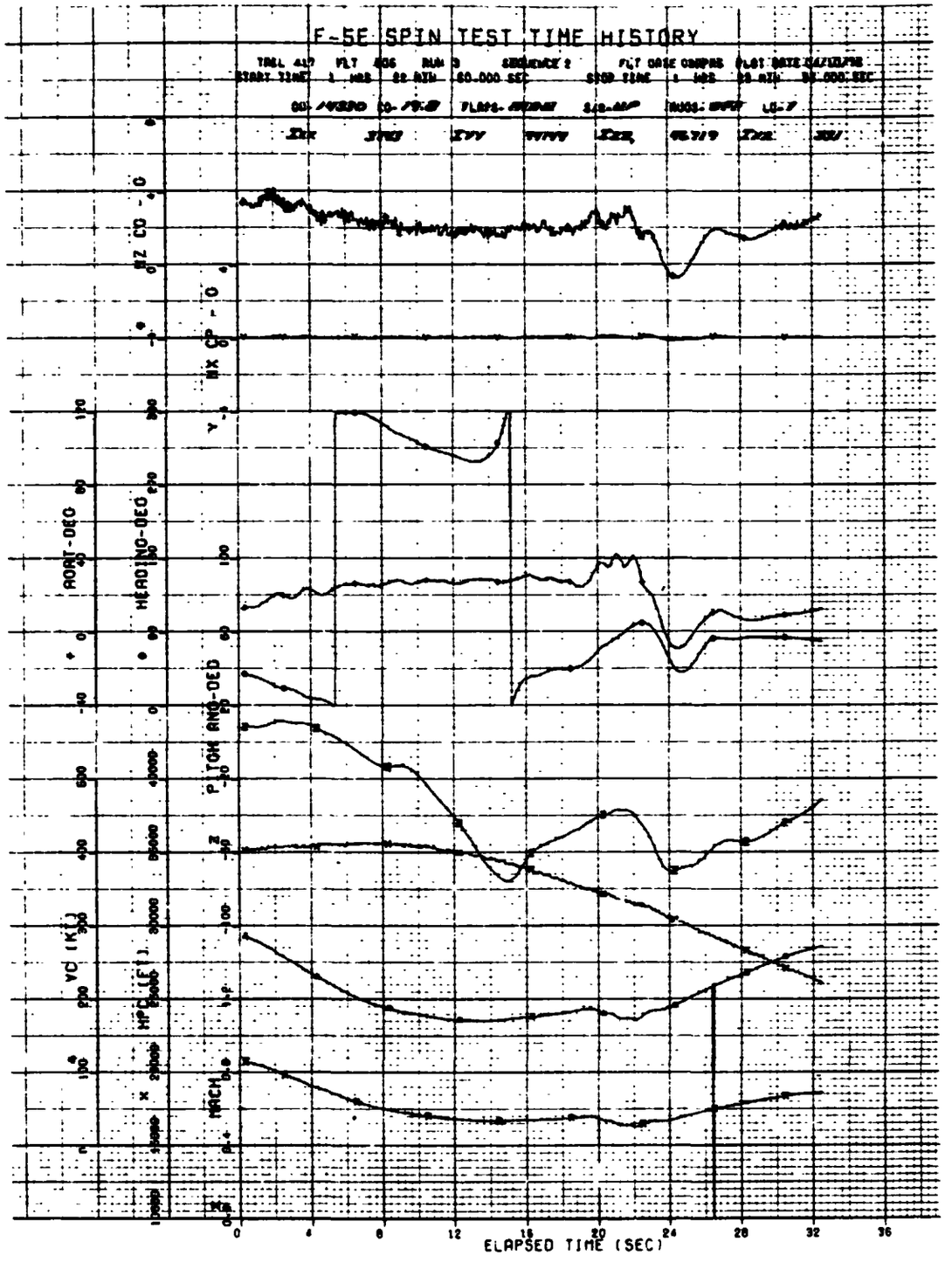

FIGURE 6. F-5E CLEAN CONFIGURATION. 1-g STALL, AFT STICK ALONE, FLAPS MANEUVER (Sheet 1 of 5)

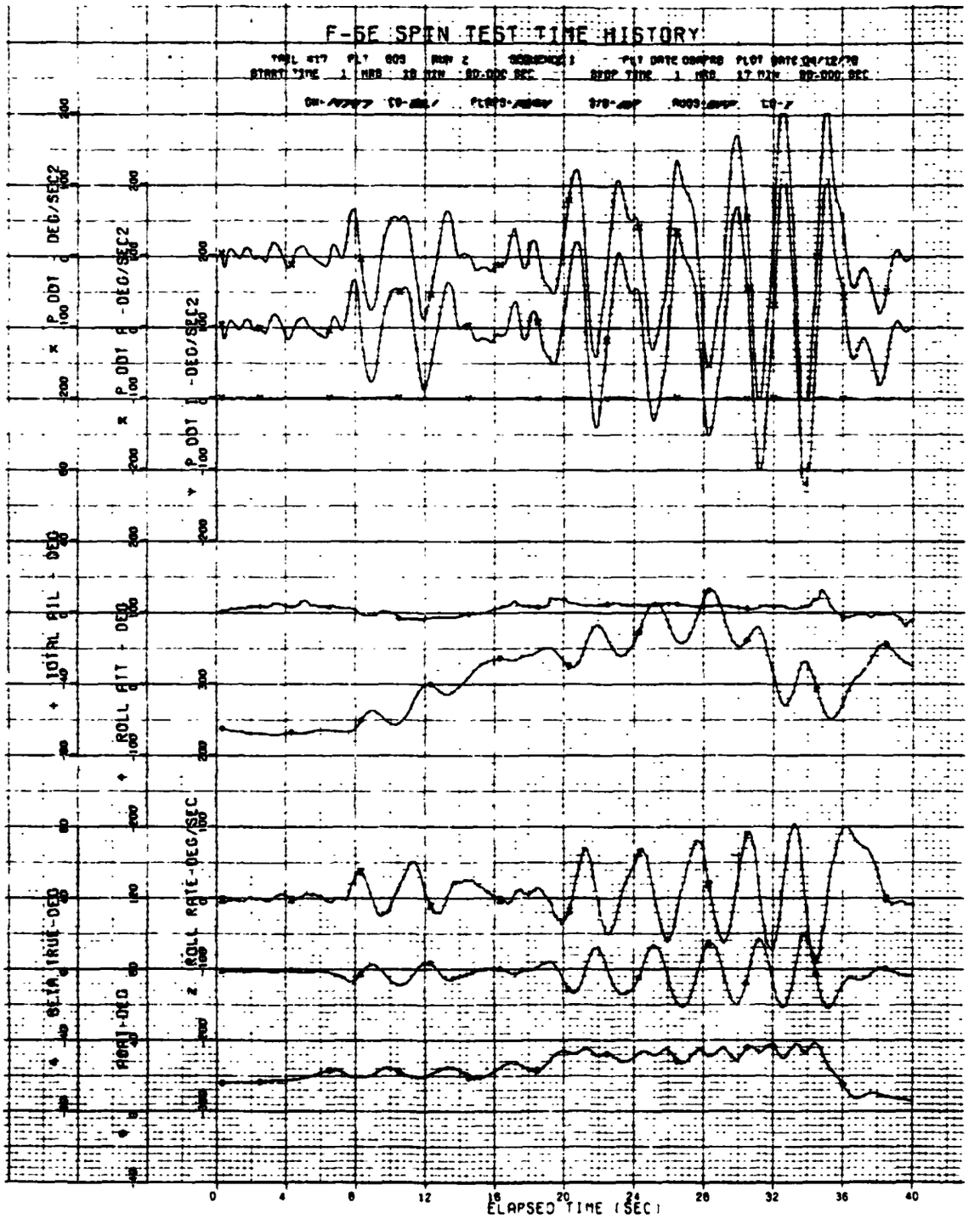

FIGURE 6. F-5E CLEAN CONFIGURATION. 1-g STALL, AFT STICK ALONE, FLAPS MANEUVER (Sheet 2 of 5)

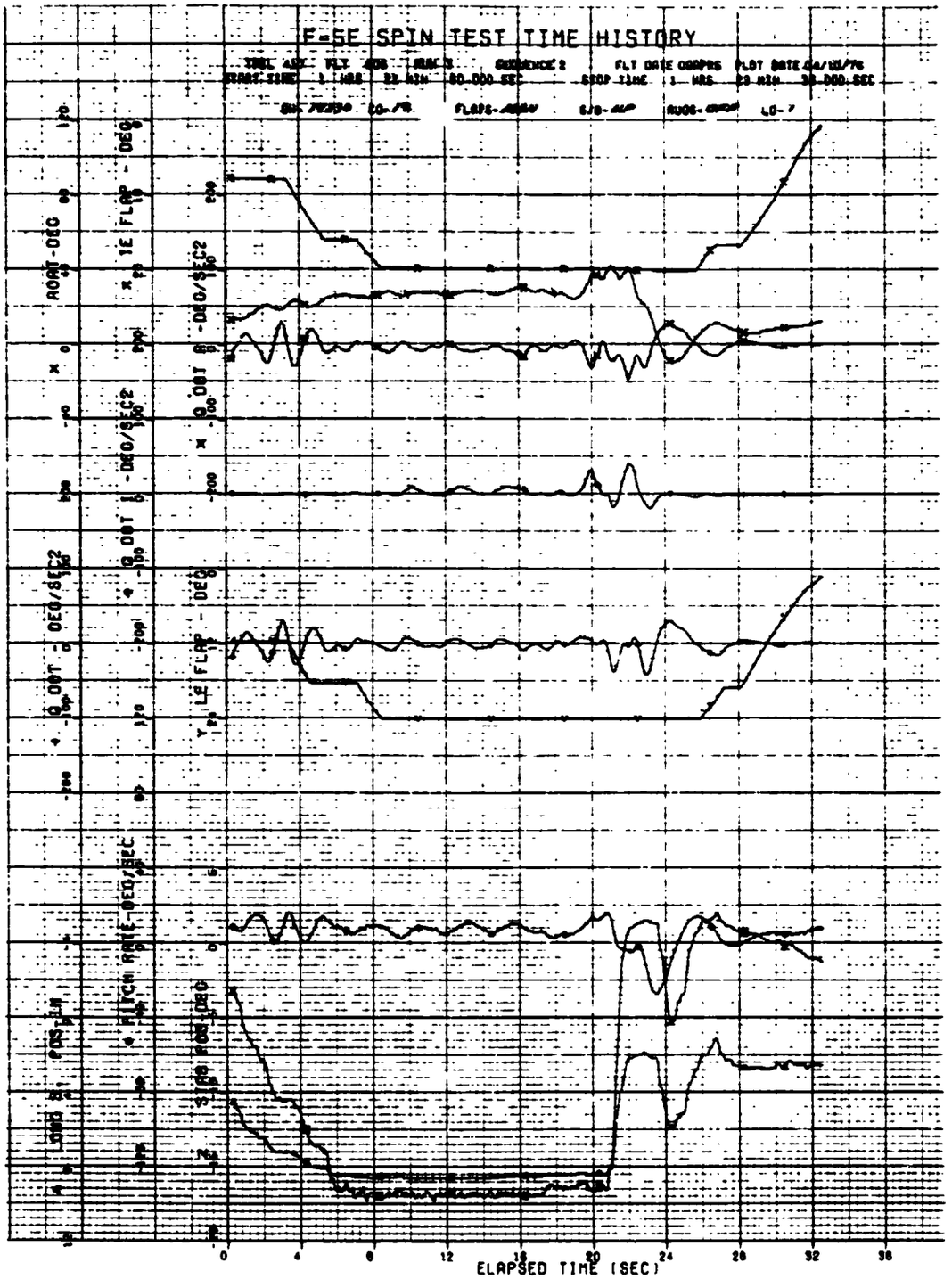

FIGURE 6. F-5E CLEAN CONFIGURATION. 1-g STALL, AFT STICK ALONE, FLAPS MANEUVER (Sheet 3 of 5)

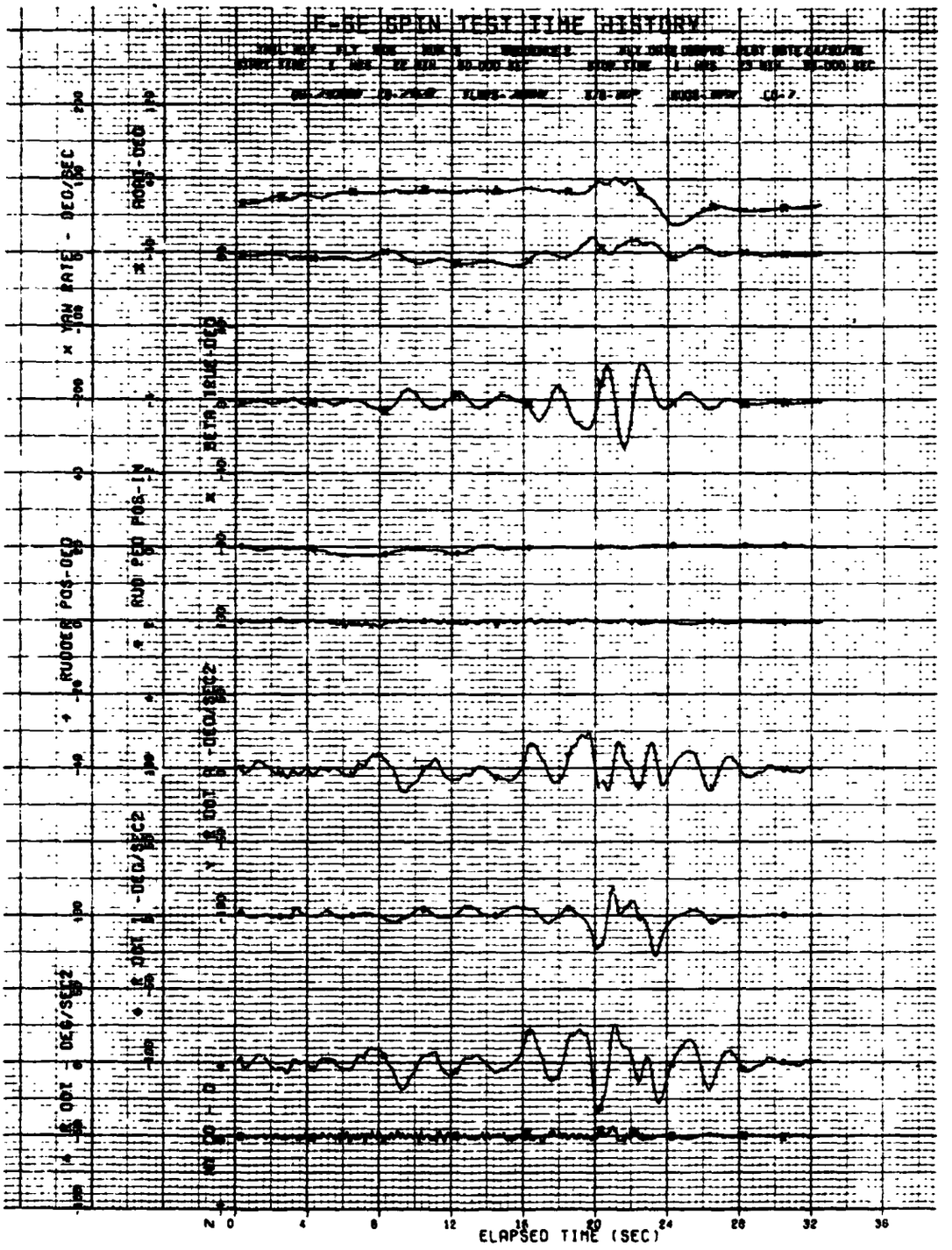

FIGURE 6. F-5E CLEAN CONFIGURATION.1-g STALL, AFT STICK ALONE, FLAPS MANEUVER (Sheet 4 of 5)

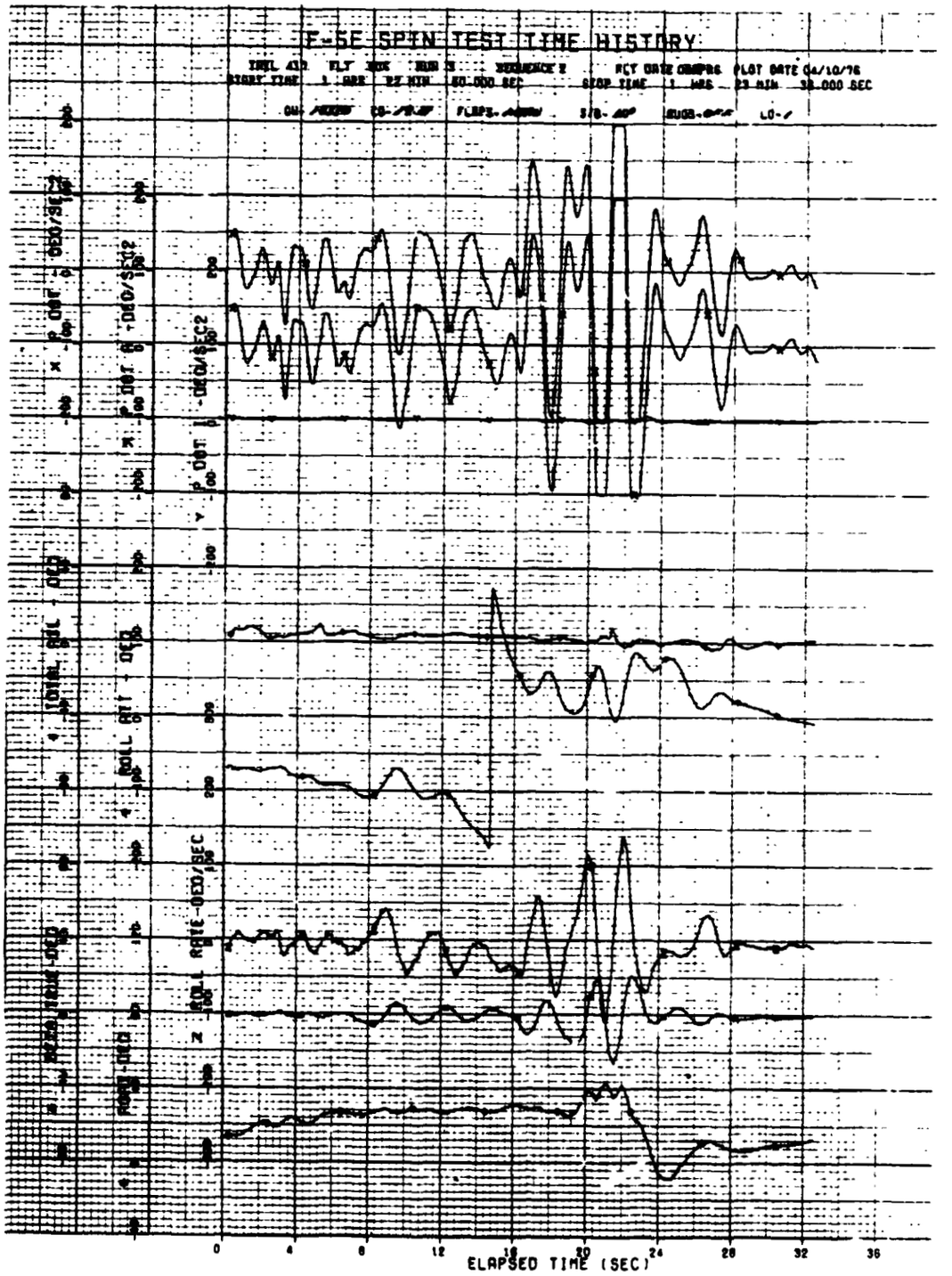

FIGURE 6. F-5E CLEAN CONFIGURATION. 1-g STALL, AFT STICK ALONE, FLAPS MANEUVER (Sheet 5 of 5)

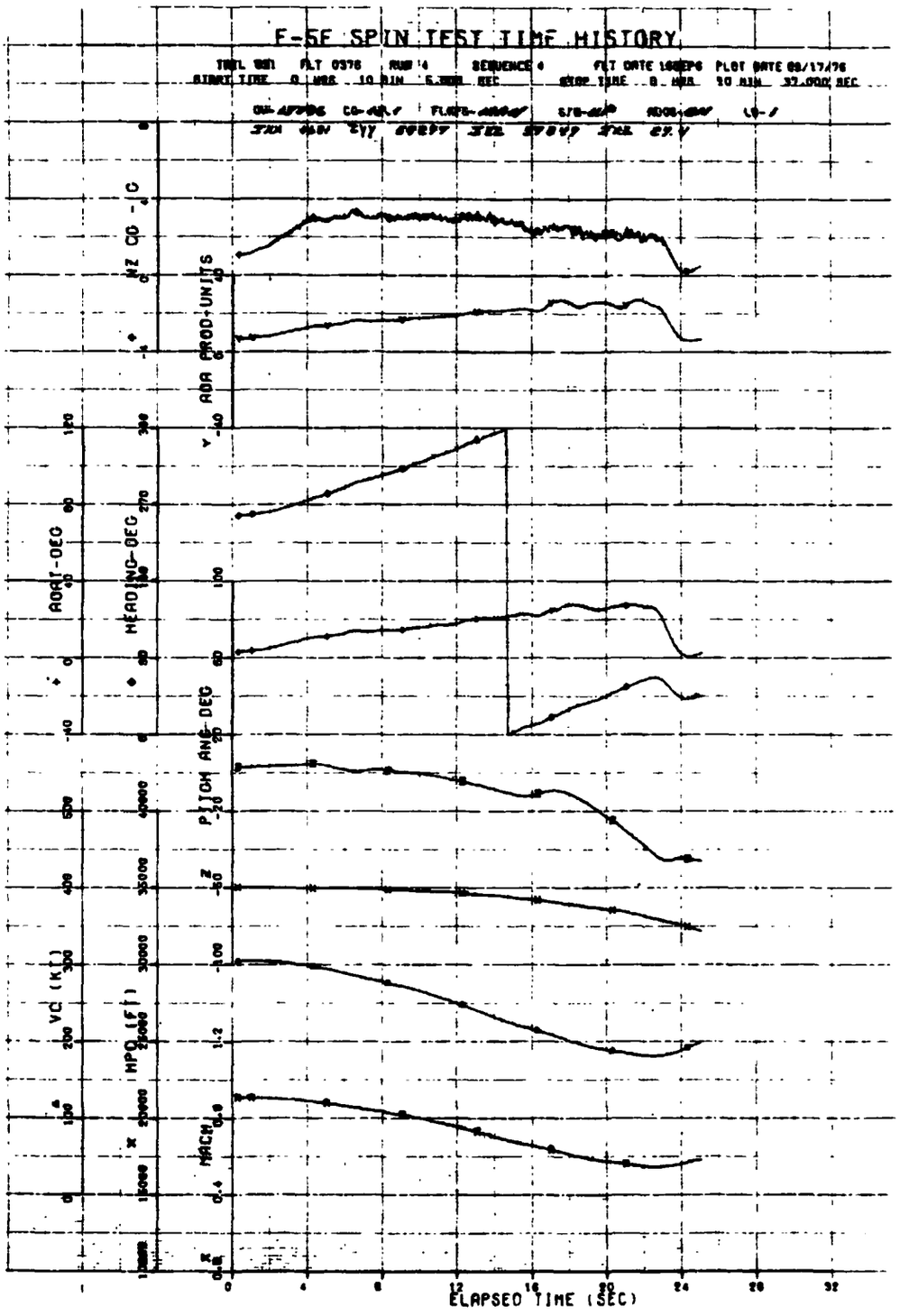

FIGURE 7. F-5F CLEAN CONFIGURATION, 1-g STALL, AFT STICK ALONE, FLAPS MANEUVER (Sheet 1 of 4)

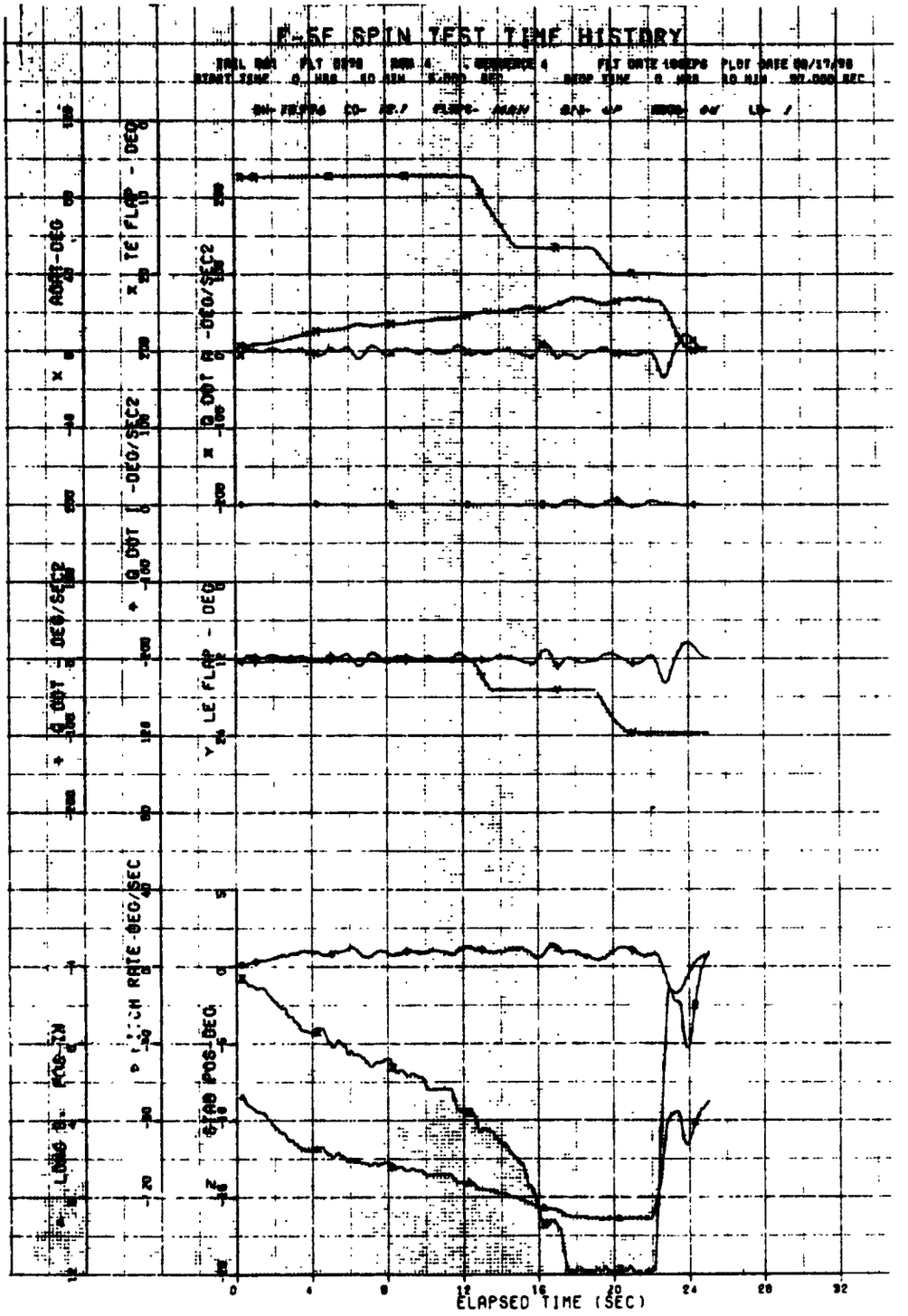

FIGURE 7. F-5F CLEAN CONFIGURATION. 1-g STALL, AFT STICK ALONE, FLAPS MANEUVER (Sheet 2 of 4)

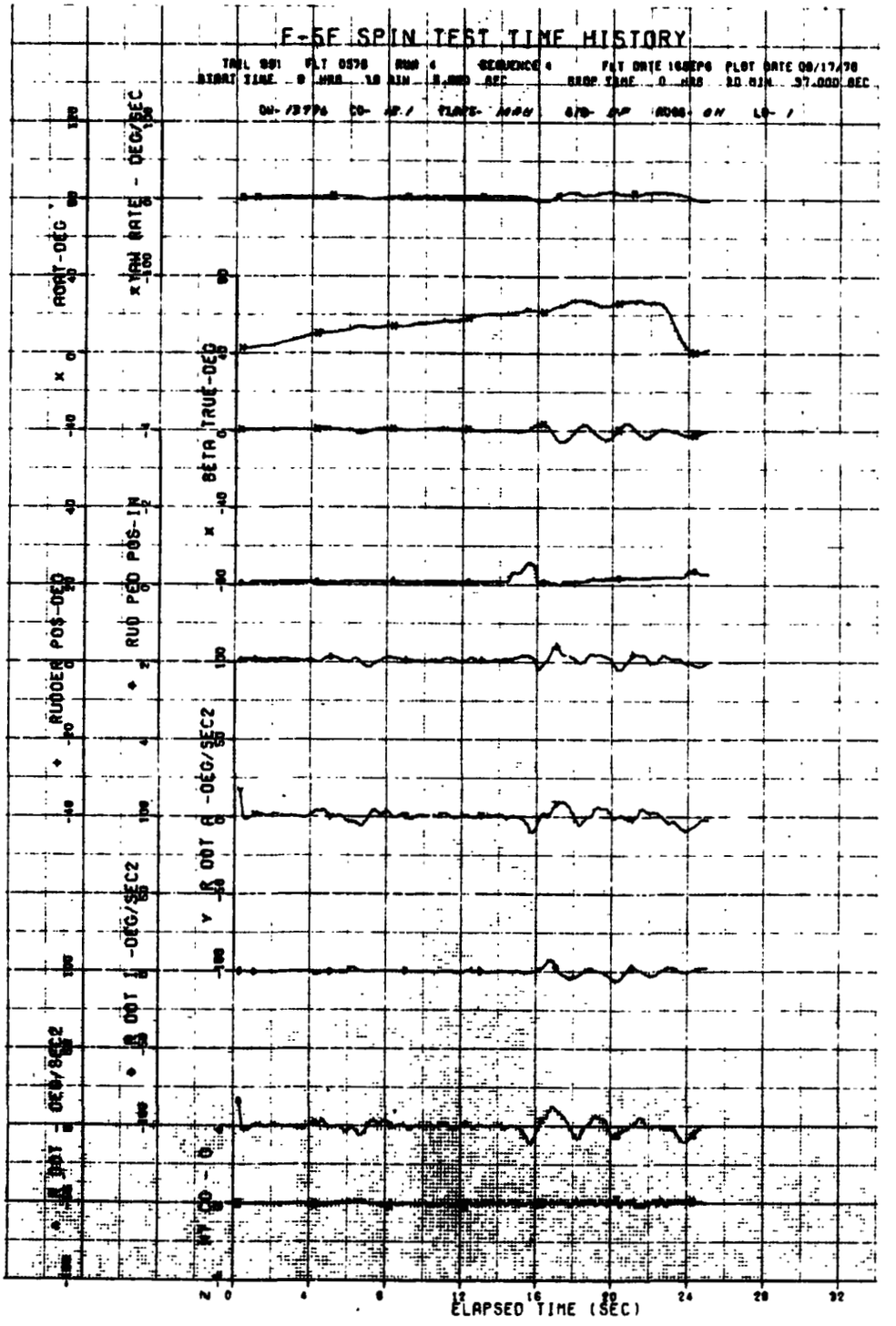

FIGURE 7. F-5F CLEAN CONFIGURATION. 1-g STALL, AFT STICK ALONE, FLAPS MANEUVER (Sheet 3 of 4)

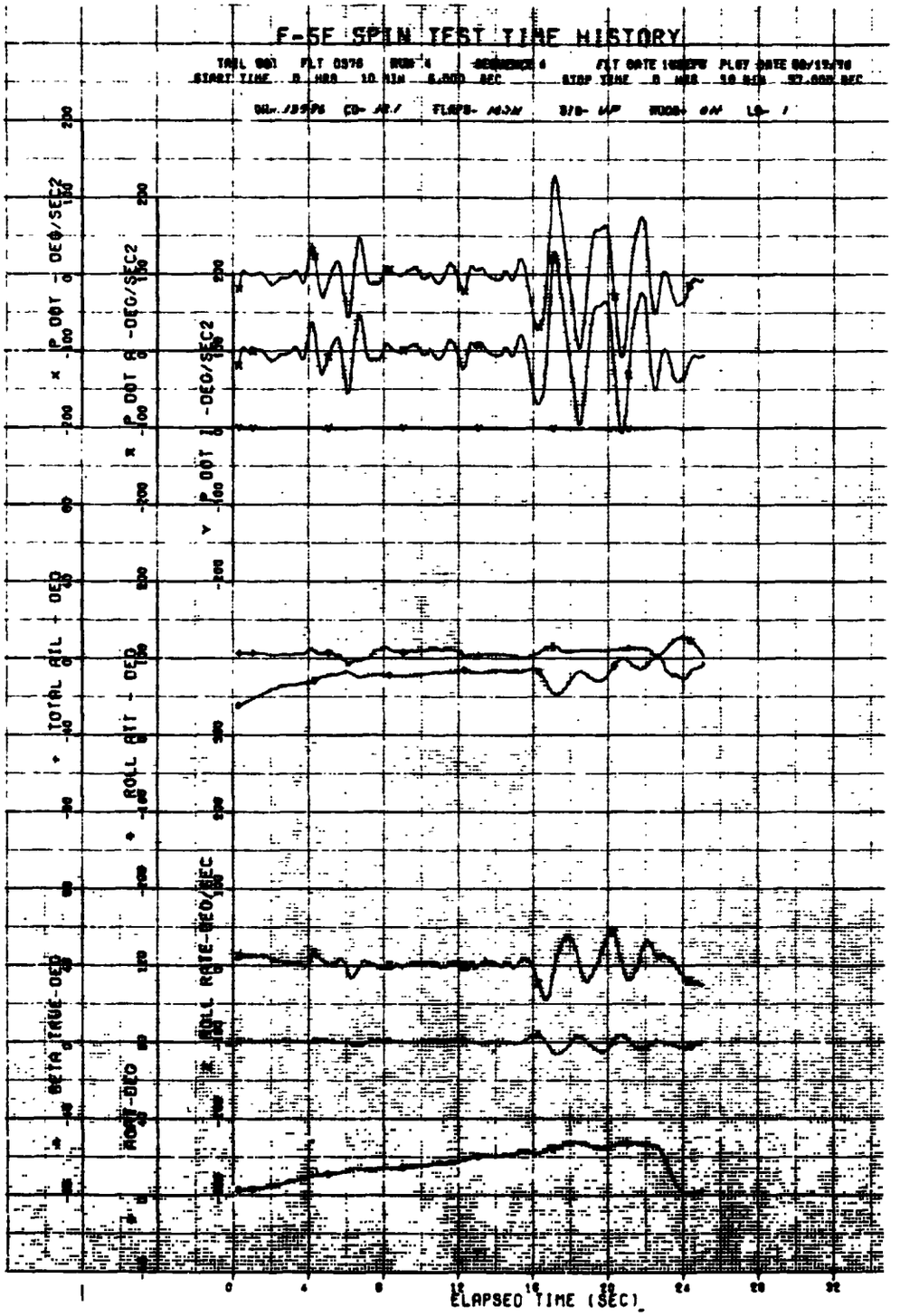

FIGURE 7. F-5F CLEAN CONFIGURATION. 1-g STALL, AFT STICK ALONE, FLAPS MANEUVER (Sheet 4 of 4)

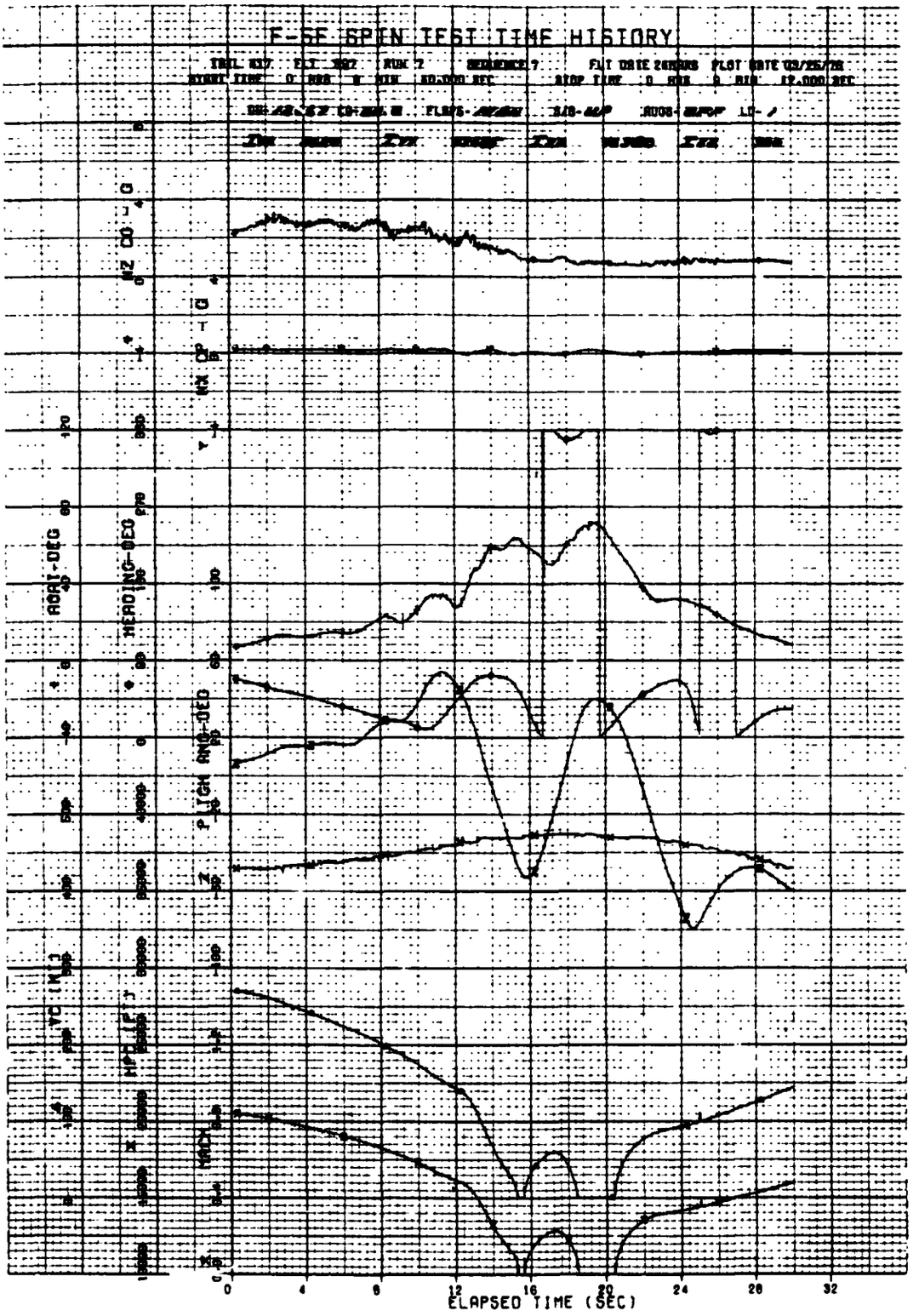

FIGURE 8. F-5E POST-STALL GYRATION WITH CLEAN CONFIGURATION (Sheet 1 of 5)

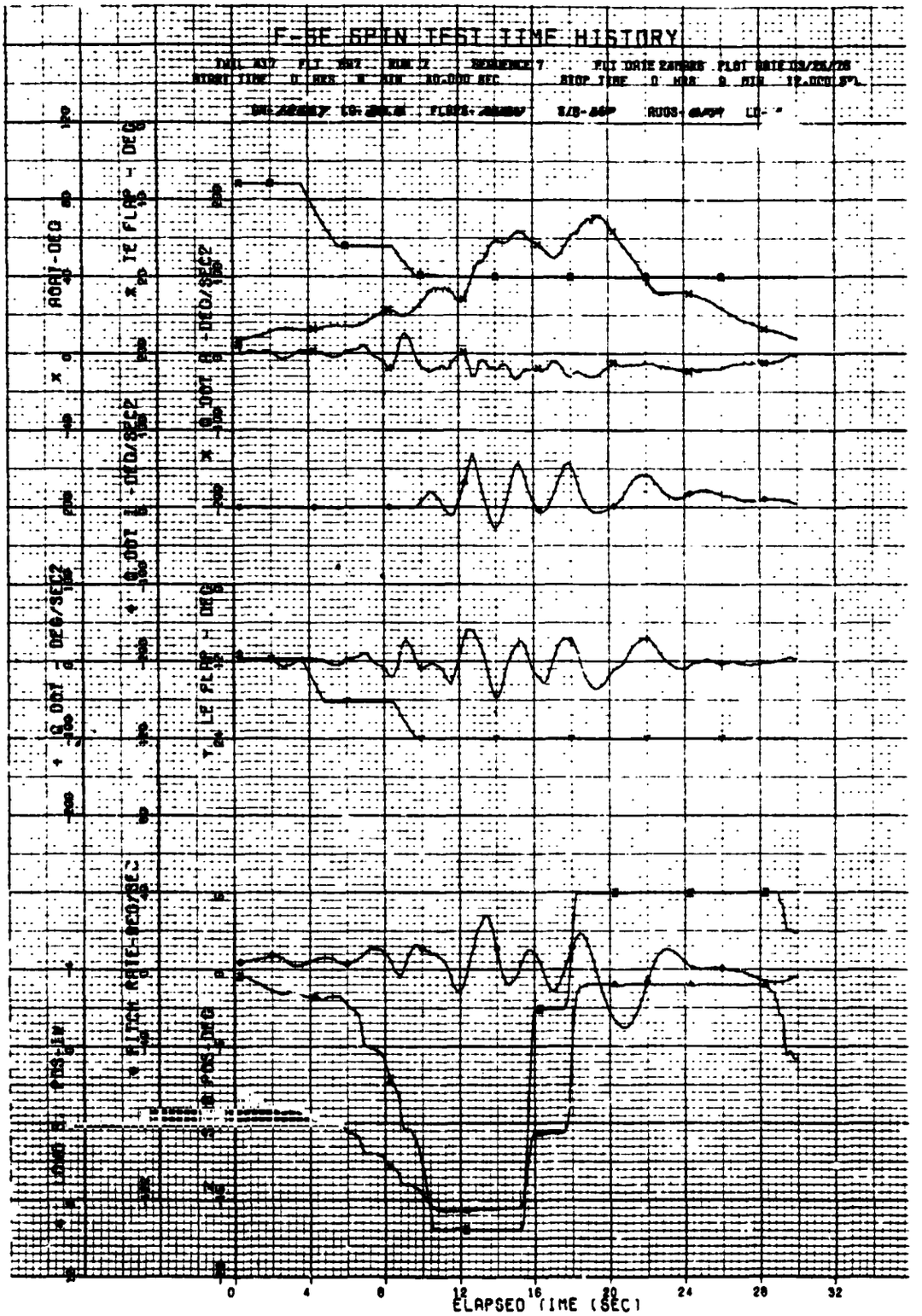

FIGURE 8. F-5E POST-STALL GYRATION WITH CLEAN CONFIGURATION (Sheet 2 of 5)

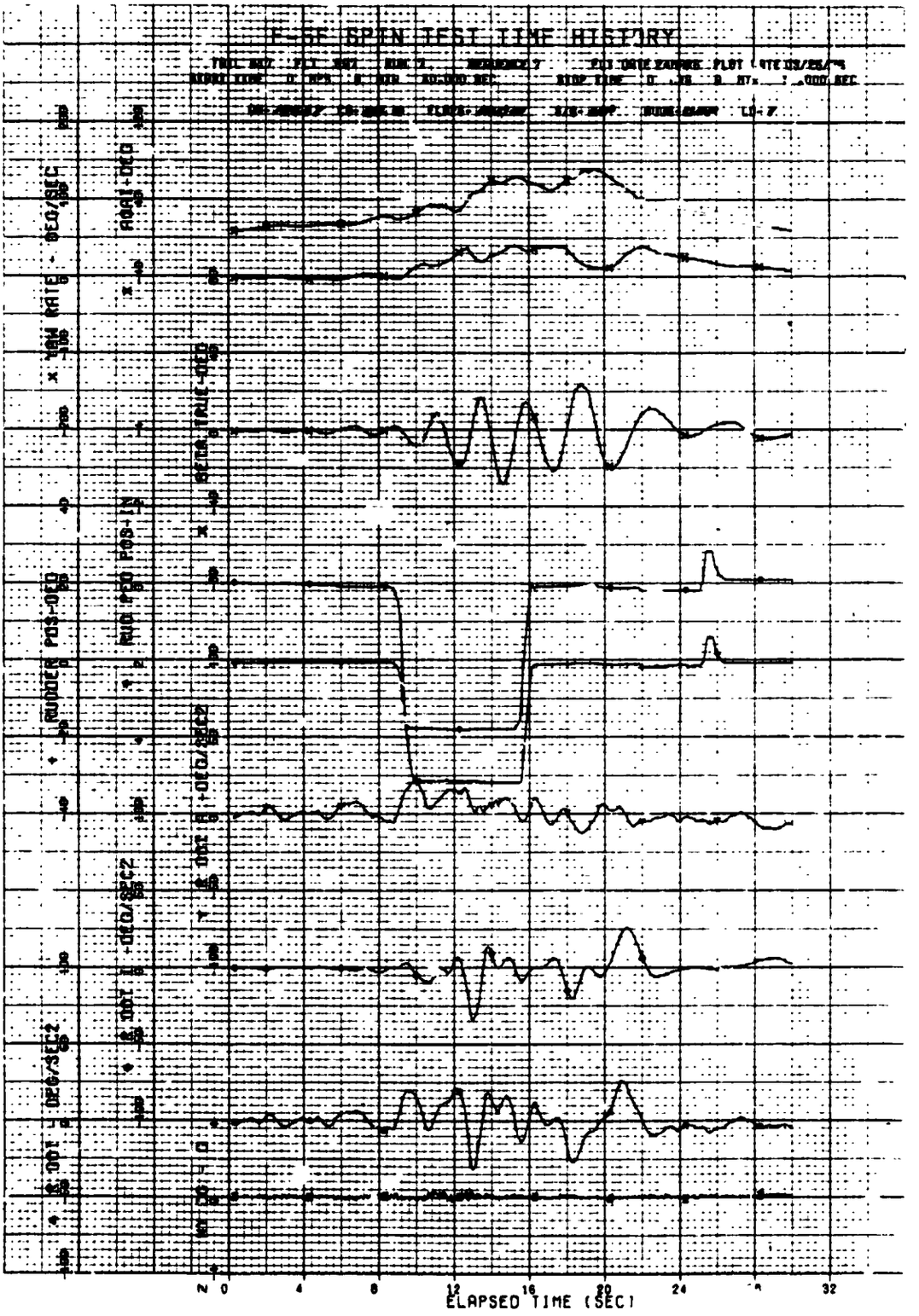

FIGURE 8. F-5E POST-STALL GYRATION WITH CLEAN CONFIGURATION (Sheet 3 of 5)

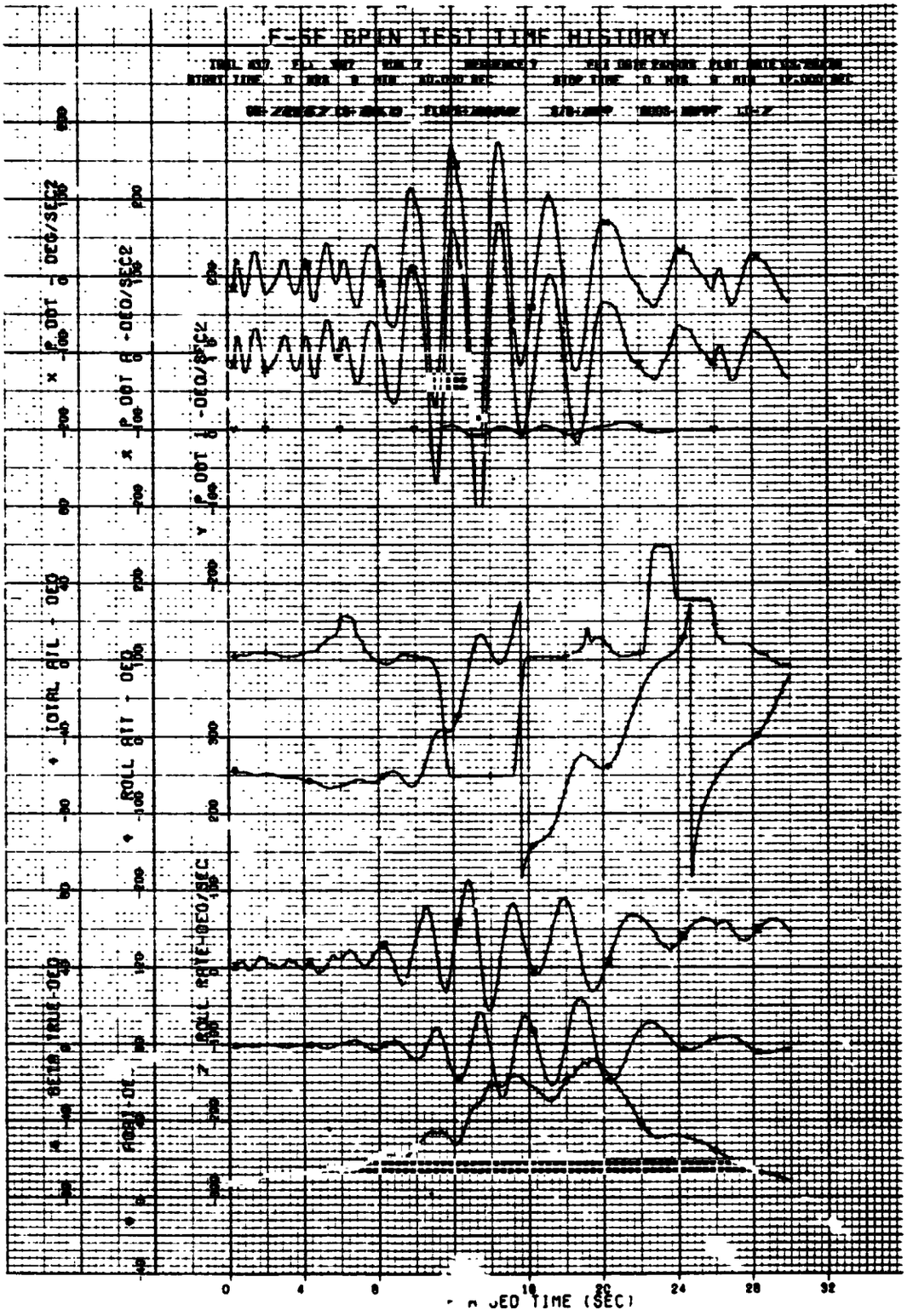

FIGURE 8. F-5E POST-STALL GYRATION WITH CLEAN CONFIGURATION (Sheet 4 of 5)

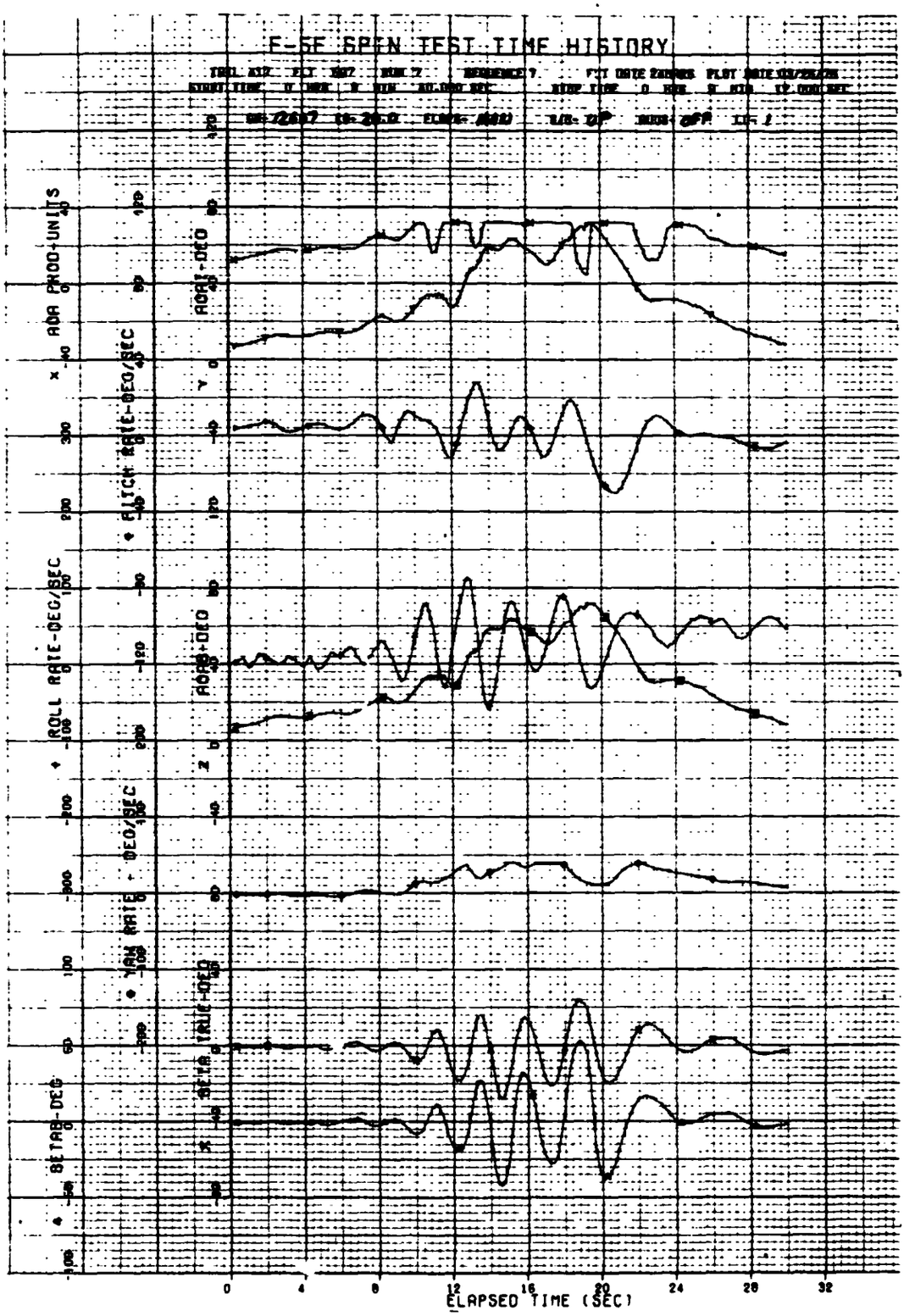

FIGURE 8. F-5F POST-STALL GYRATION WITH CLEAN CONFIGURATION (Sheet 5 of 5)

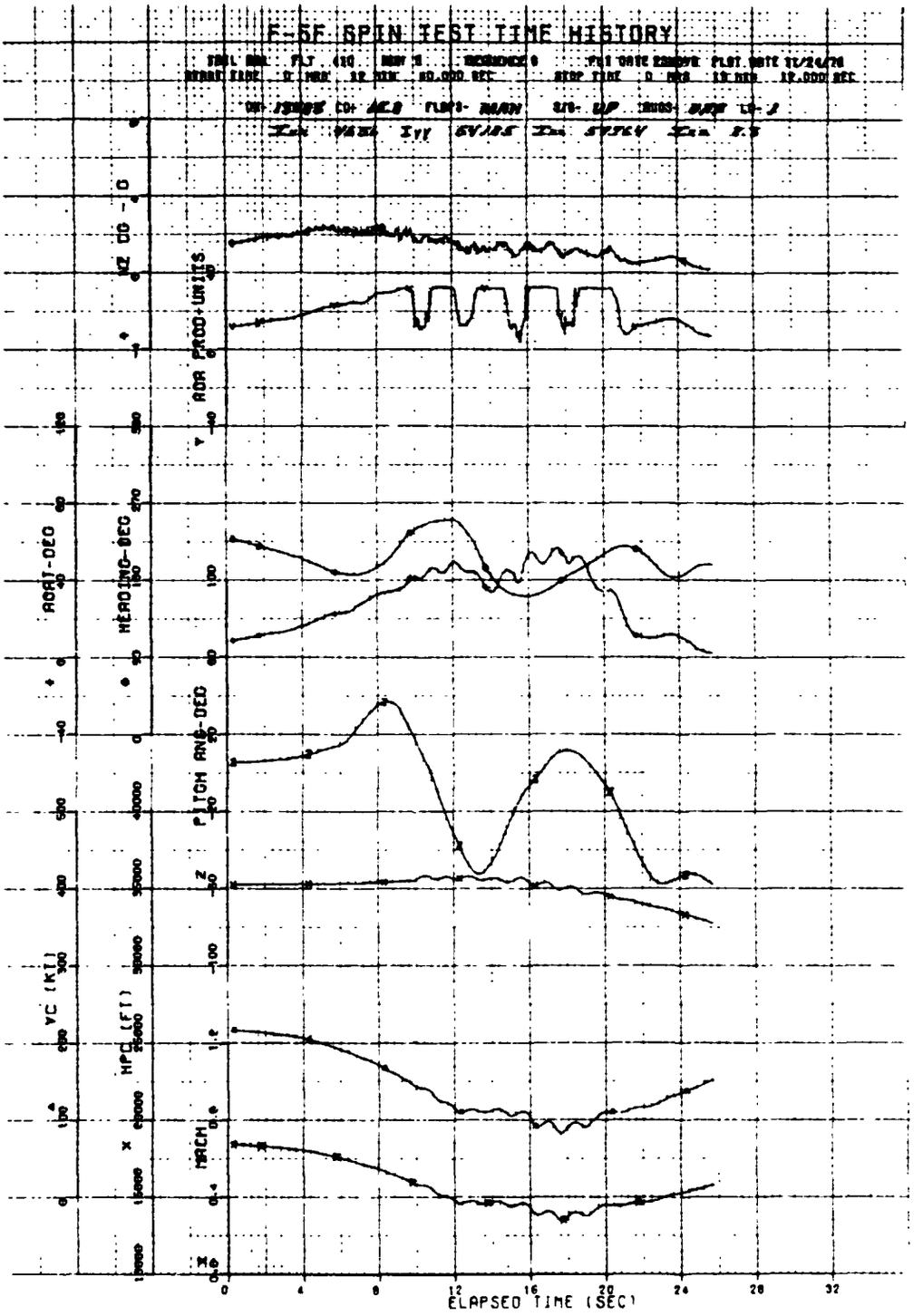

FIGURE 9. F-5F ERECT POST-STALL GYRATION WITH CLEAN CONFIGURATION (Sheet 1 of 4)

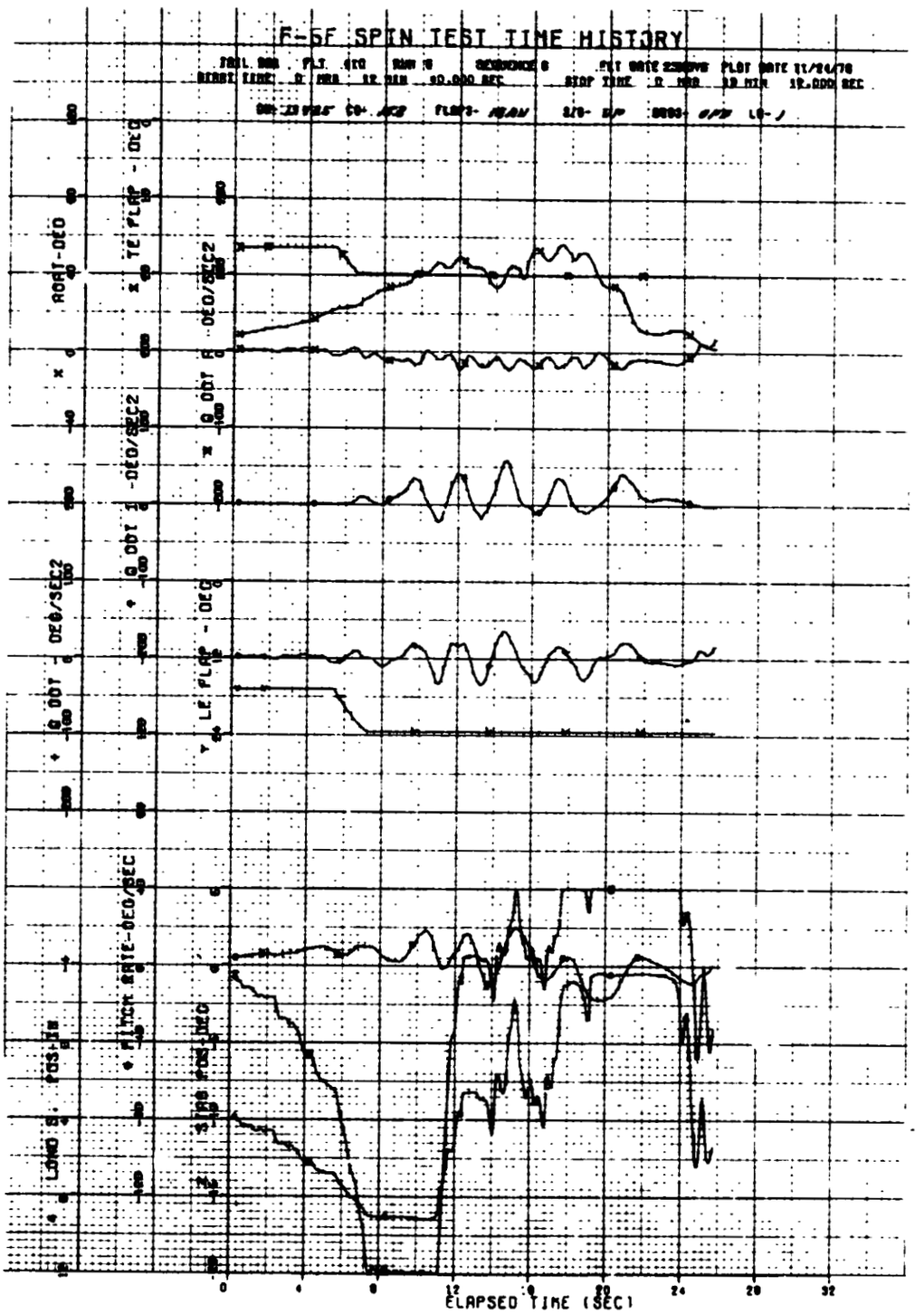

FIGURE 9. F-5F ERECT POST-STALL GYRATION WITH CLEAN CONFIGURATION (Shee_ 2 of 4)

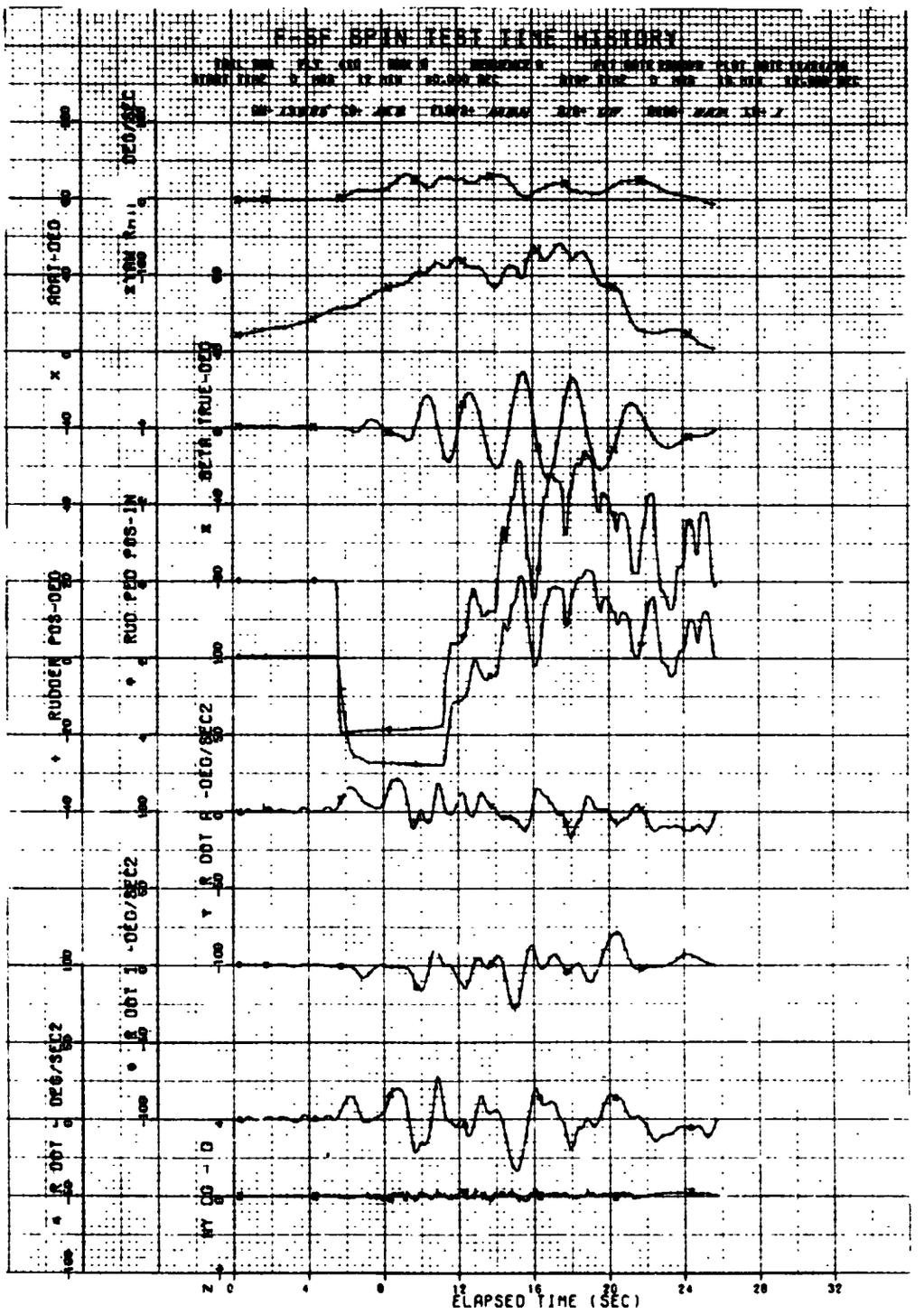

FIGURE 9. F-5F ERECT POST-STALL GYRATION WITH CLEAN CONFIGURATION (Sheet 3 of 4)

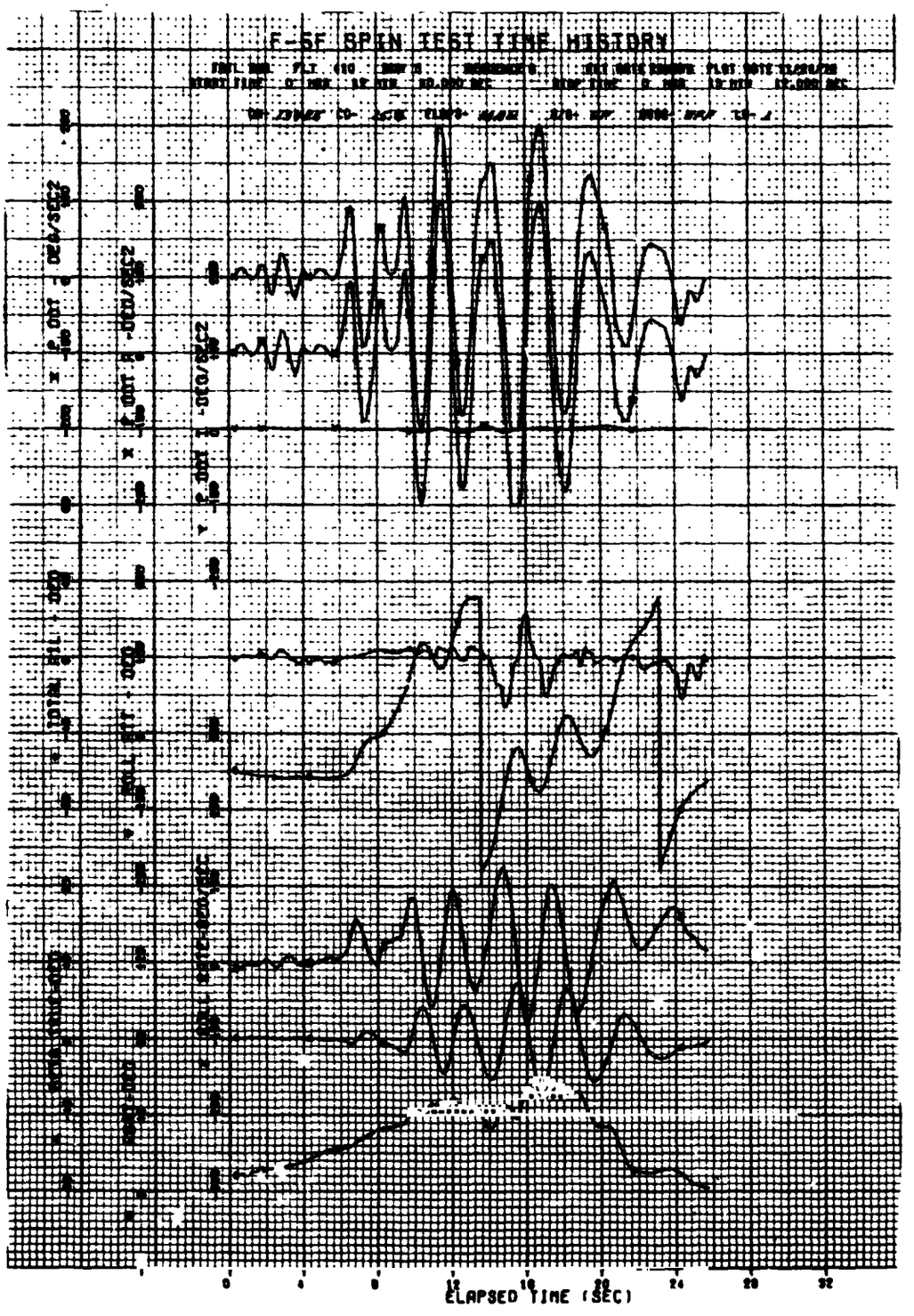

FIGURE 9. F-5F ERECT POST-STALL GYRATION WITH CLEAN CONFIGURATION (Sheet 4 of 4)

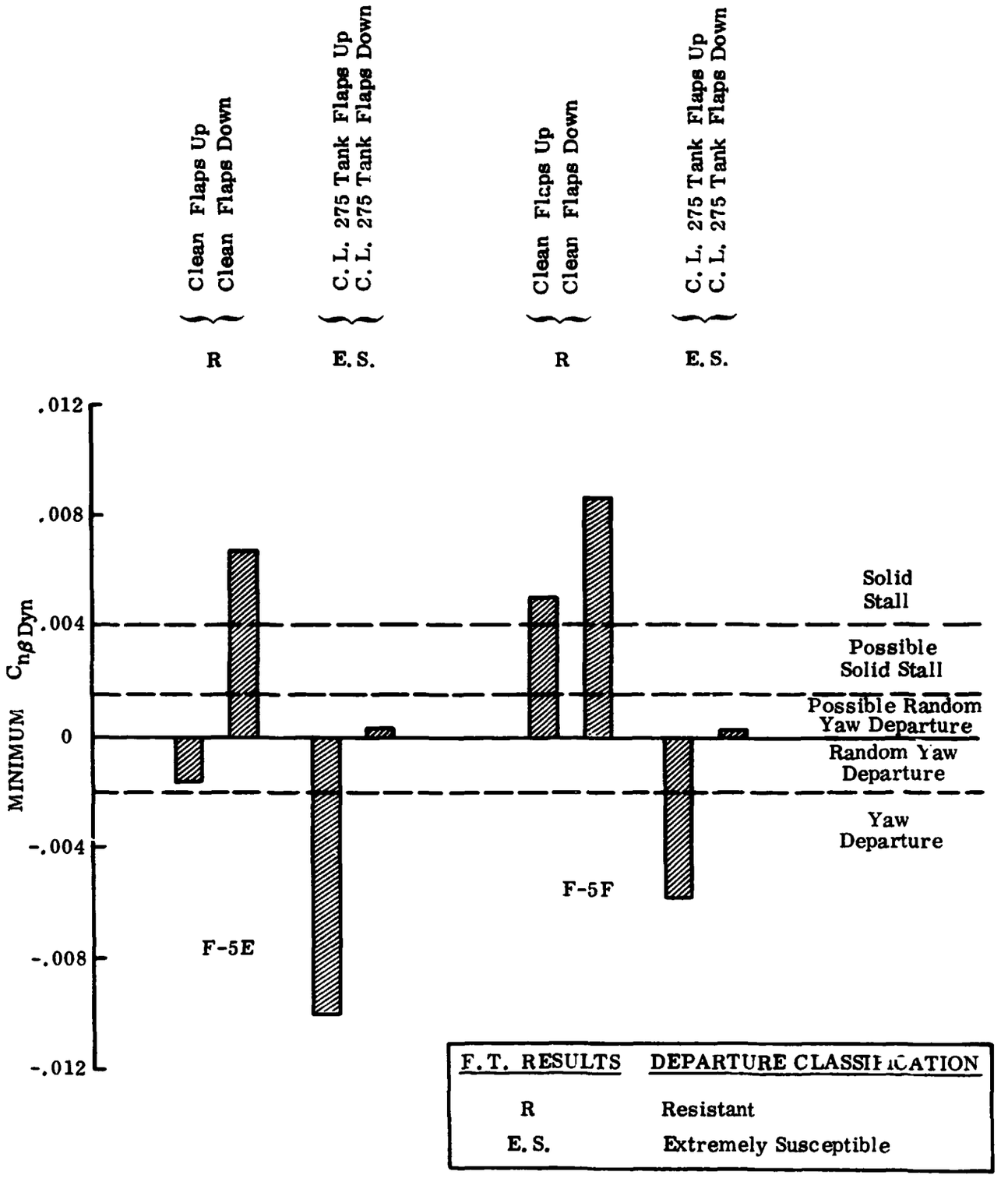

FIGURE 10. F-5E/F MINIMUM $C_{n_{\beta Dynamic}}$ FOR FLIGHT TESTED CONFIGURATIONS

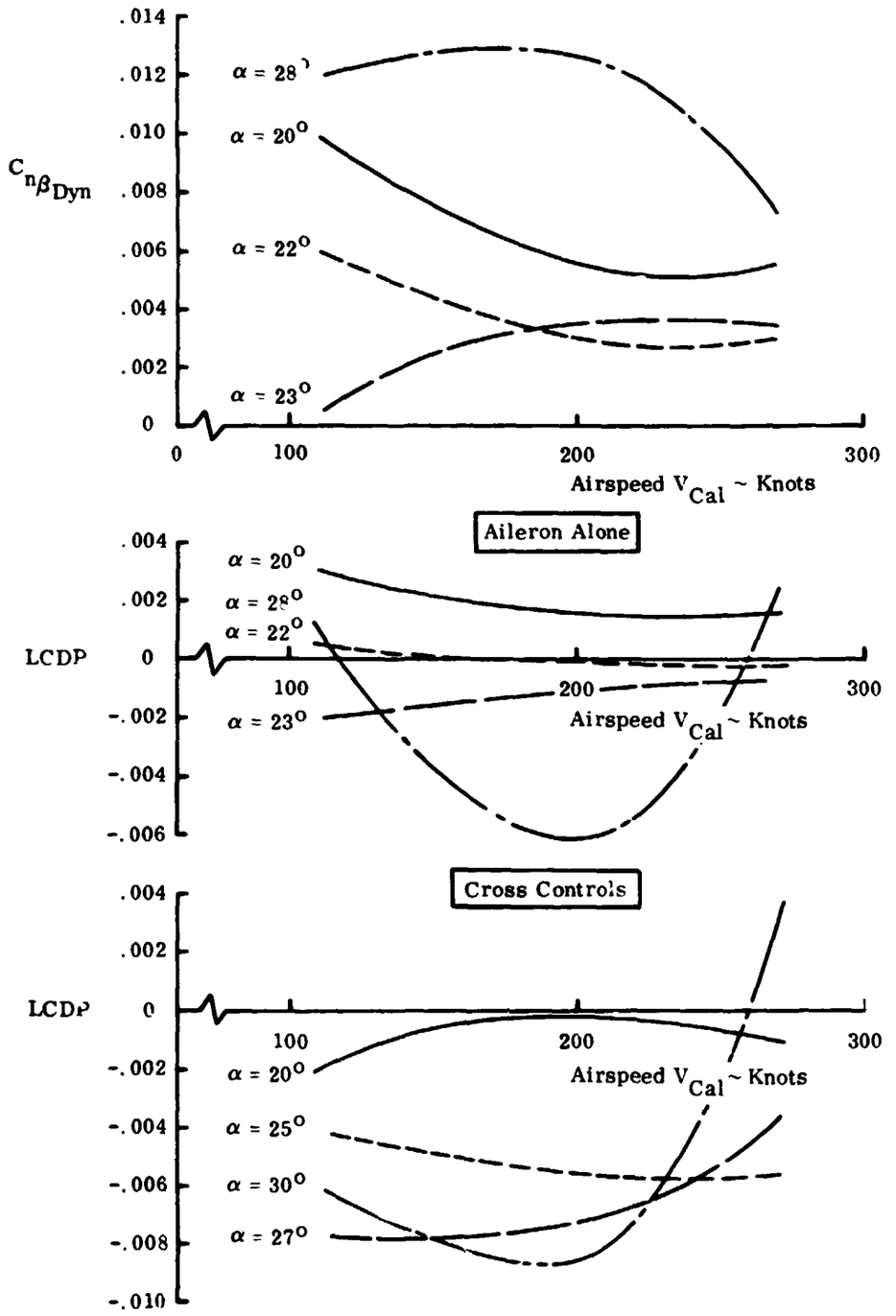

FIGURE 11. F-5E MISSILE CONFIGURATION.$C_{n_{\beta_{Dynamic}}}$ AND LCDP VERSUS V_{Cal} AT 10,600 m

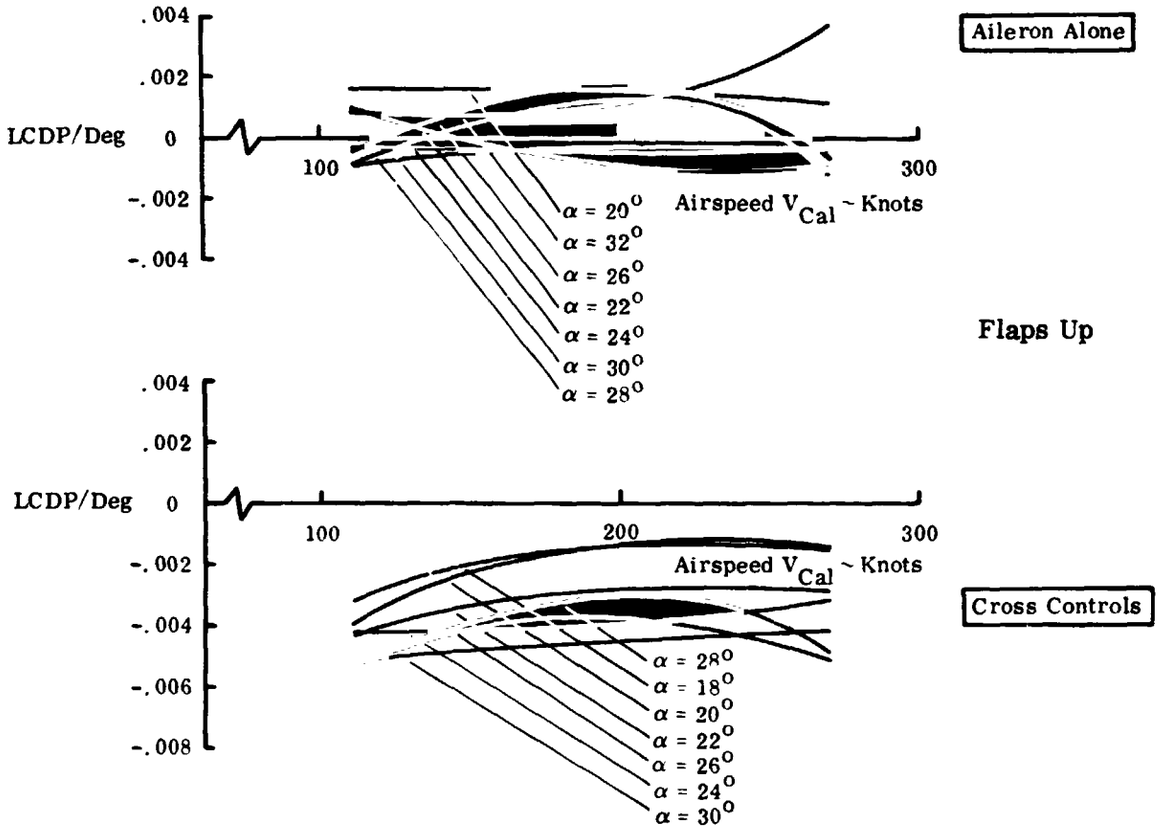

FIGURE 12. F-5F MISSILE CONFIGURATION. LCDP VERSUS V_{Cal} AT 10,600 m

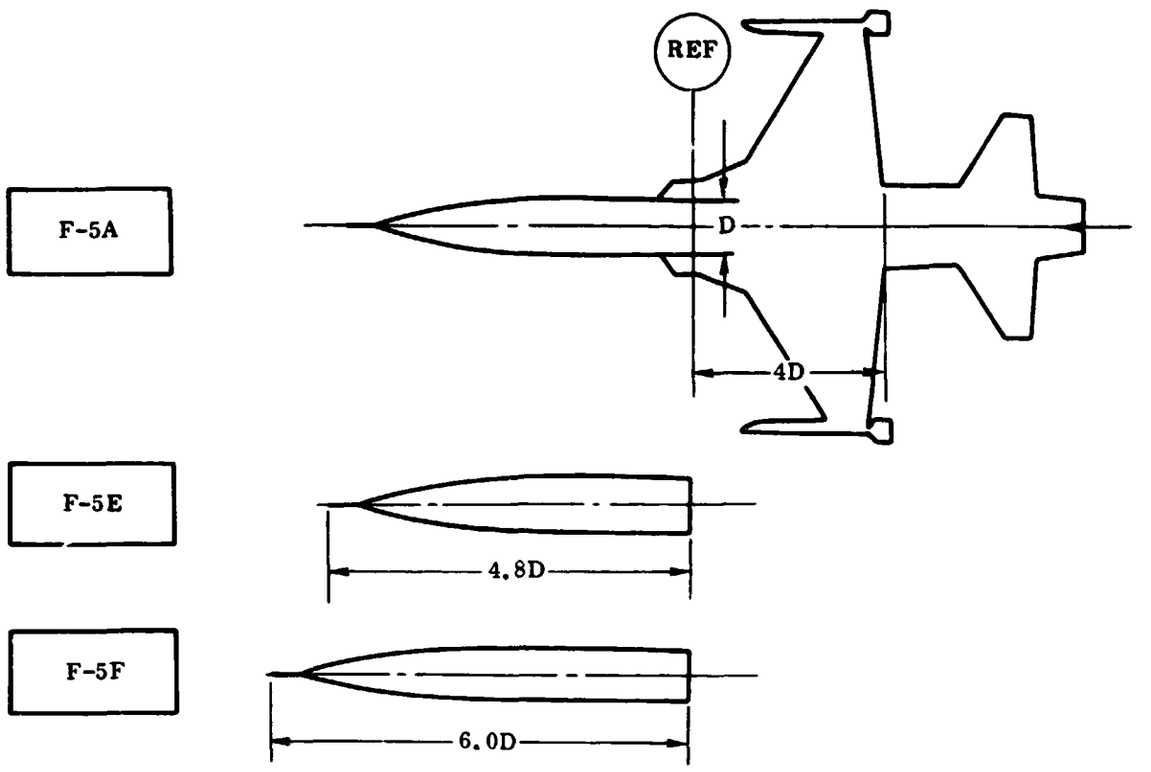

FIGURE 13. F-5E/F FOREBODY FINENESS RATIO COMPARISON

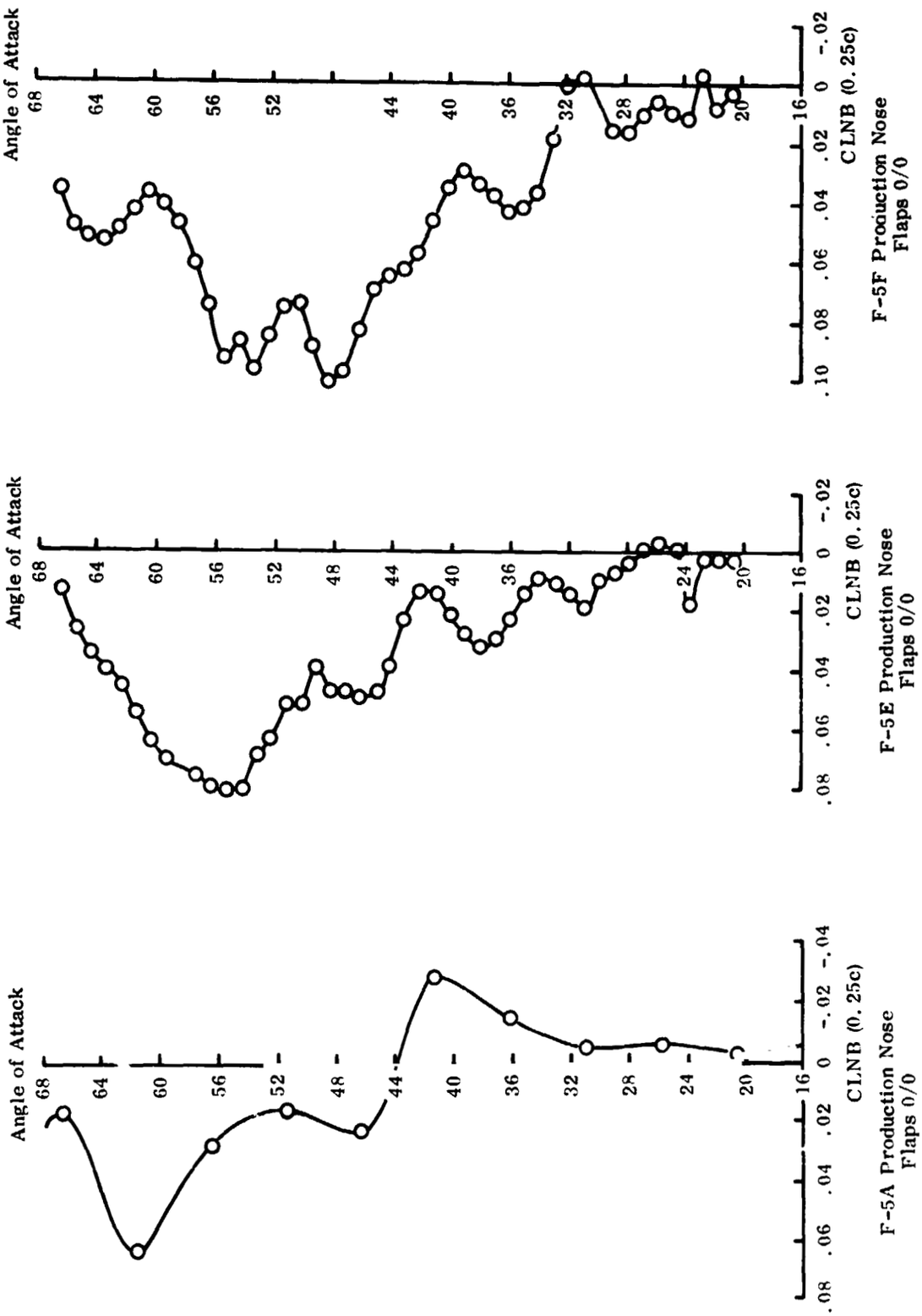

FIGURE 14. F-5A AND F-5E/F COMPARISON OF AERO ASYMMETRIES

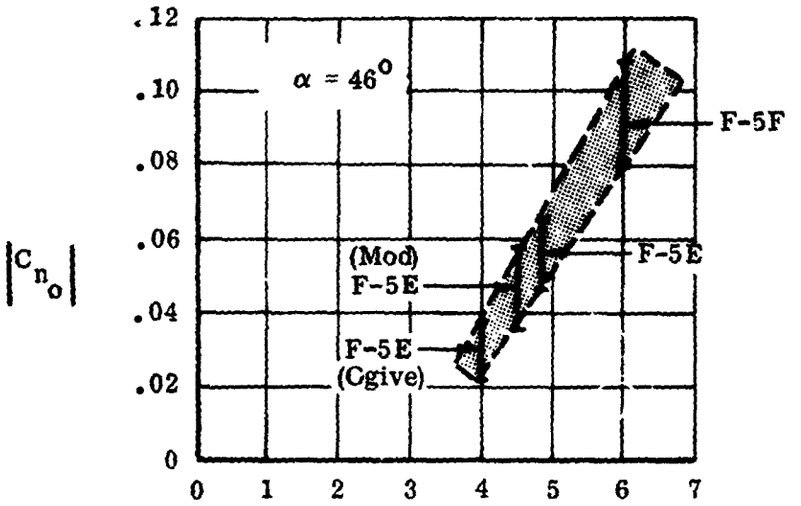

FIGURE 15. EFFECT OF FINENESS RATIO ON $|C_{n_o}|$

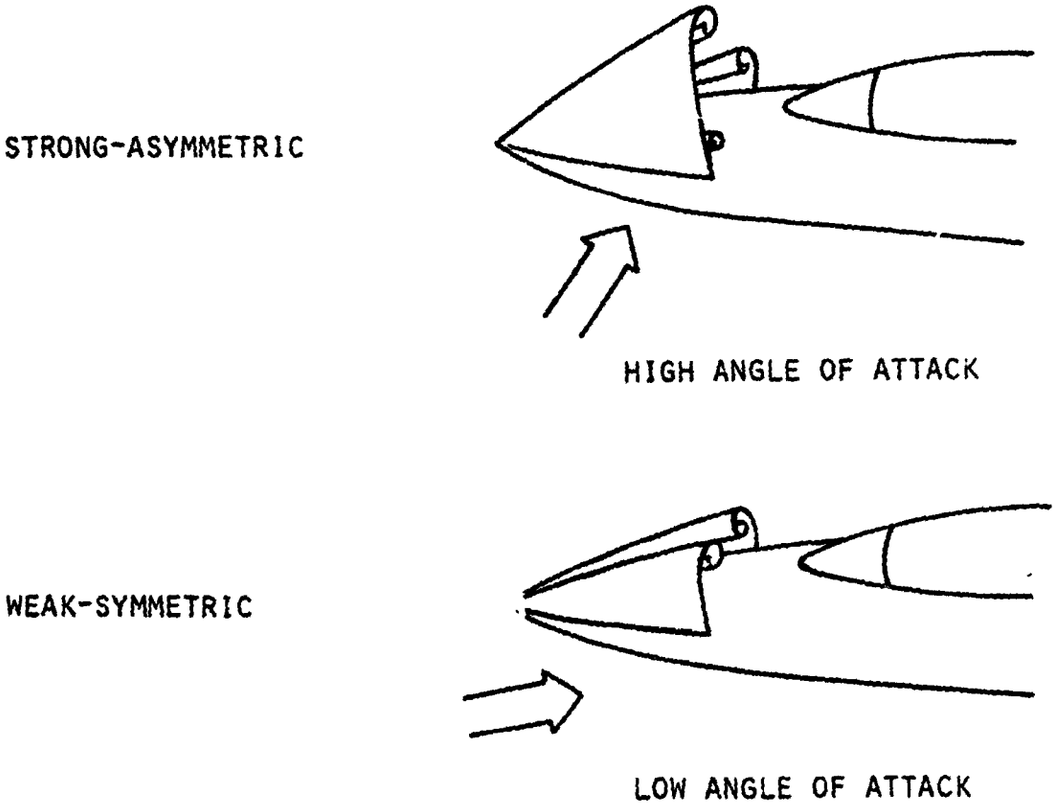

FIGURE 16. F-5F FOREBODY VORTEX PATTERNS

FIGURE 17. F-5F CLEAN CONFIGURATION. WATER TUNNEL VORTEX VISUALIZATION

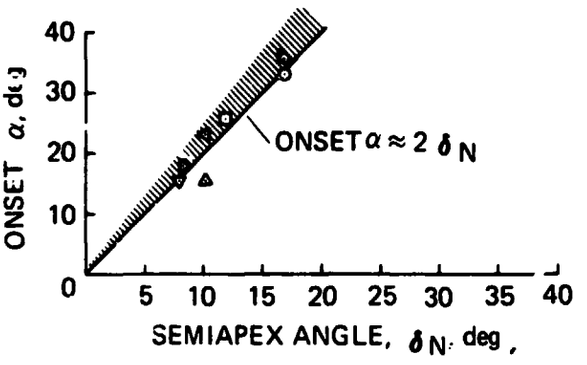

(a) POINTED CIRCULAR FOREBODIES

CIRCULAR CROSS SECTION			
PLANFORM SHAPE	ℓ/d	δ_N deg	REFERENCE
○ TAN. OGIVE	3.5	16.3	KEENER & CHAPMAN
□ TAN. OGIVE	5.0	11.4	" "
◇ TAN. OGIVE	3.5	16.3	COE et al.
▷ PARABOLOID	3.5	16.3	KEENER & CHAPMAN
◁ CONE	2.84	10.0	" "
▷ CONE	3.5	8.13	COE et al.
△ CONE	2.84	10.0	ORLIK-RUCKEMANN
▽ CONE	3.68	7.75	" "
	M < 0.6	$\beta = 0$	

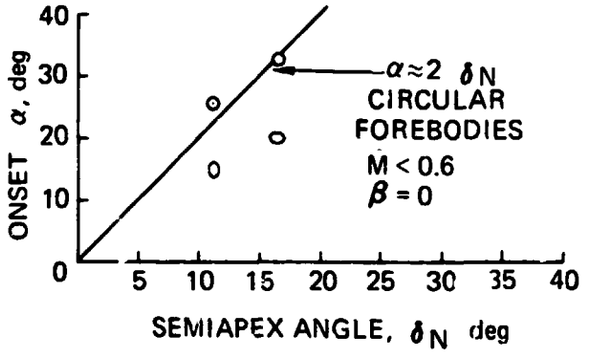

(b) POINTED ELLIPTIC FOREBODIES

○ 0 ELLIPTIC TANGENT OGIVES

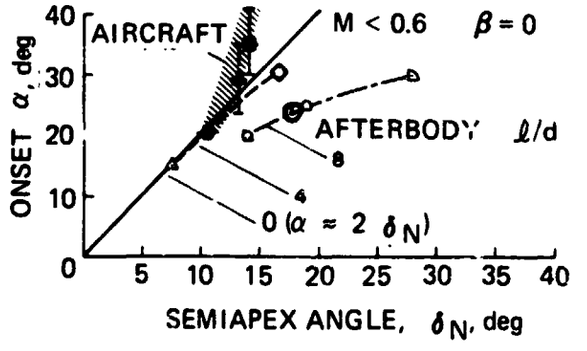

(c) EFFECT OF AFTERBODY AND WINGS

	FOREBODY	AFTERBODY	
	δ_N deg	ℓ/d	ℓ/d	REFERENCES
○	16.3	3.5	3.5	KEENER & CHAPMAN
◇	16.3	3.5	3.5	COE ET AL
△	15.0	6.5	4.0	LETKO
▷	28.1	2.0	8.0	PICK
□	18.9	3.0	8.0	PICK
○	14.2	4.0	8.0	PICK
▷	14.2	4.0	6.0	KROUSE
◆	17.4*	5.5	–	F-104
●	14.2*	4.0	–	F-11
▲	13.0*	4.4	–	F-5
NO ONSET	29.1*	2.0	–	F-4
	(*MEAN)			

FIGURE 18. ANGLE OF ATTACK FOR ONSET OF SIDE FORCE FOR POINTED FOREBODIES (FROM REF 9)

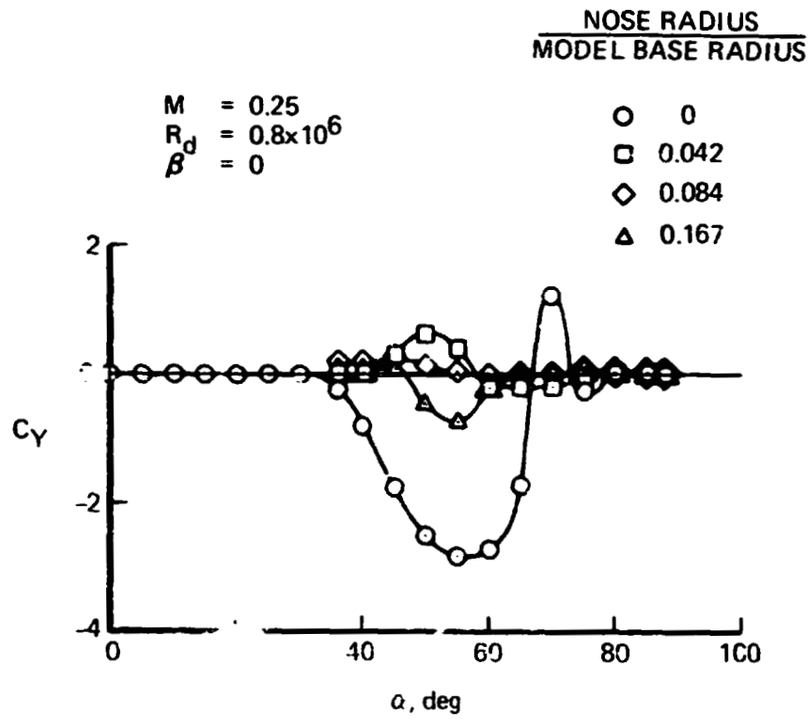

FIGURE 19. EFFECT OF NOSE BLUNTNESS ON SIDE FORCE FOR ℓ/d = 3.5 POINTED TANGENT OGIVE (FROM REF. 9)

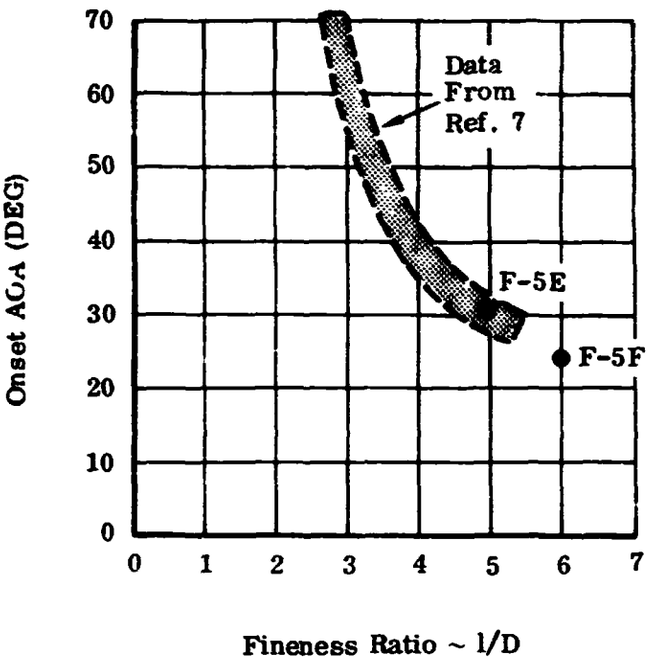

FIGURE 20. EFFECT OF FINENESS RATIO ON ONSET ANGLE OF ATTACK

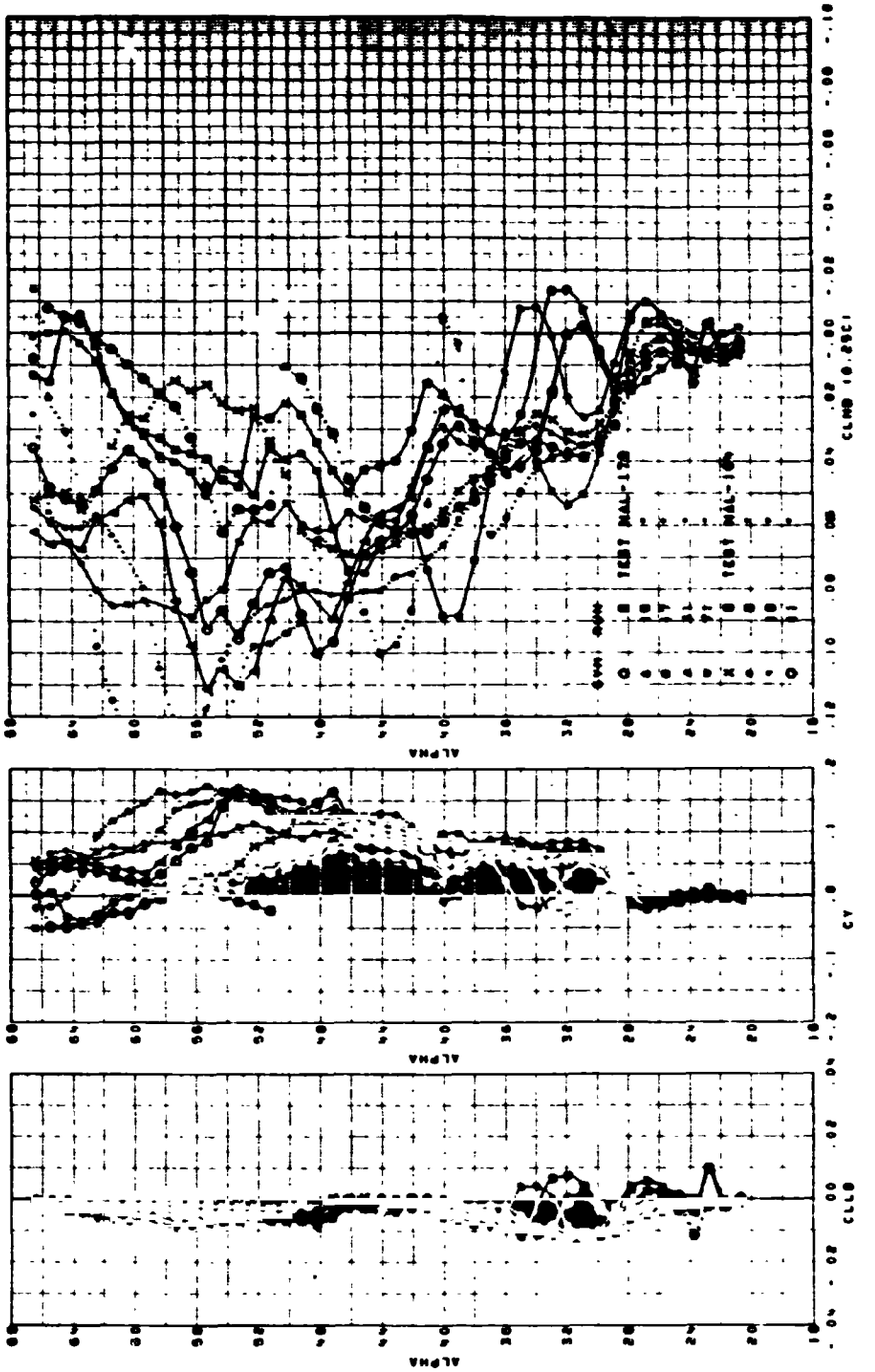

FIGURE 21. F-5F CLEAN CONFIGURATION. ZERO SIDESLIP ASYMMETRIC WIND TUNNEL DATA

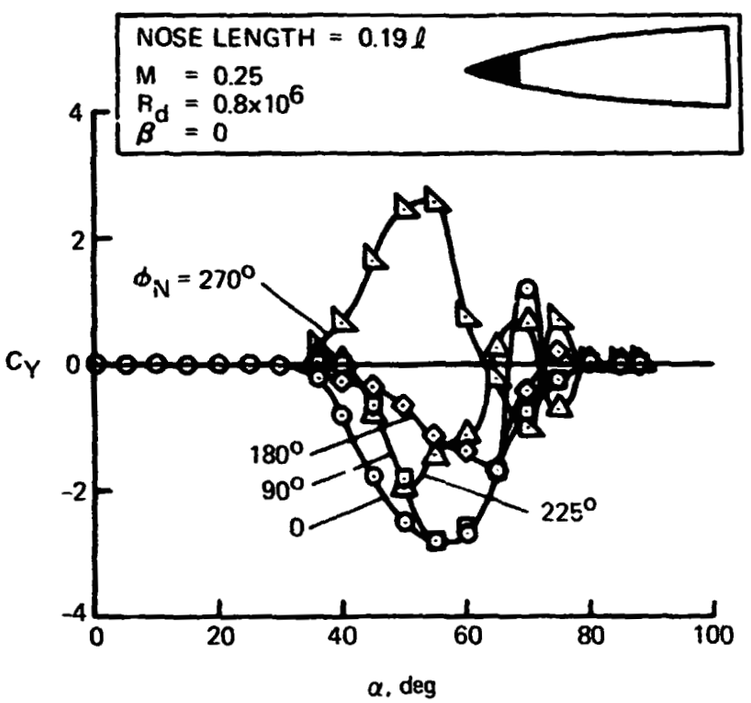

FIGURE 22. EFFECT OF ROLL-ANGLE POSITION OF REMOVABLE-NOSE-TIP SECTION ON SIDE FORCE FOR ℓ/d = 3.5 POINTED TANGENT OGIVE (FROM REF 9)

Full Scale Dimensions

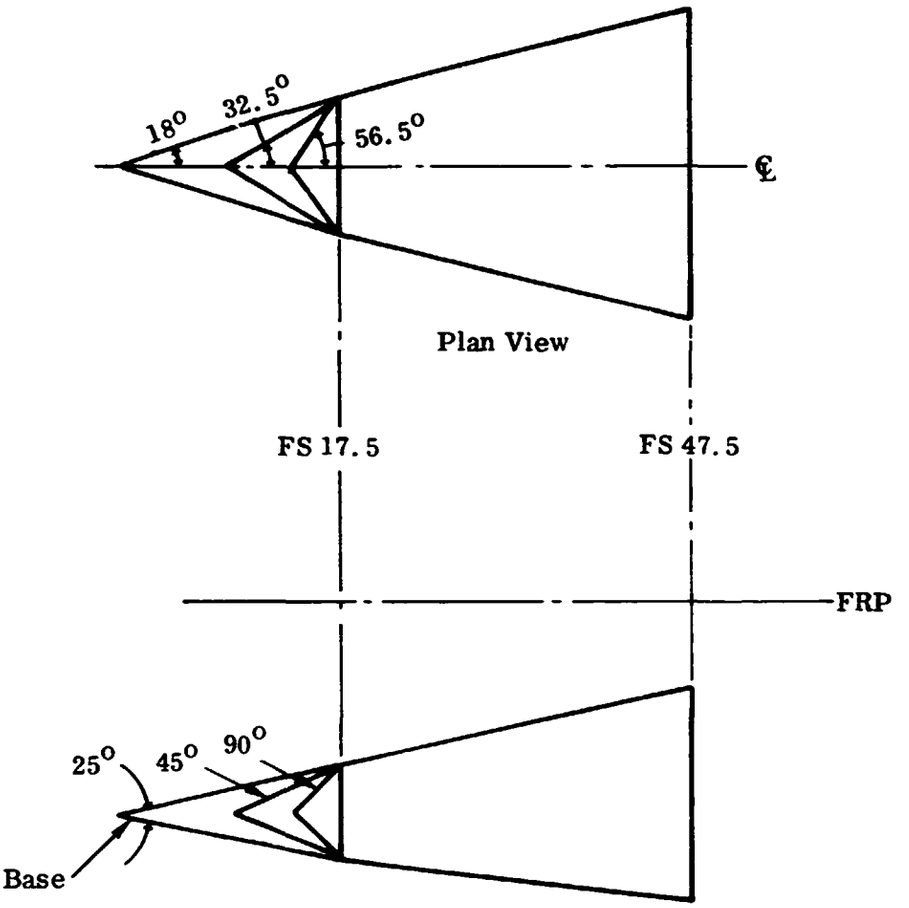

FIGURE 23. F-5F NOSE SEMI-APEX ANGLE GEOMETRIES

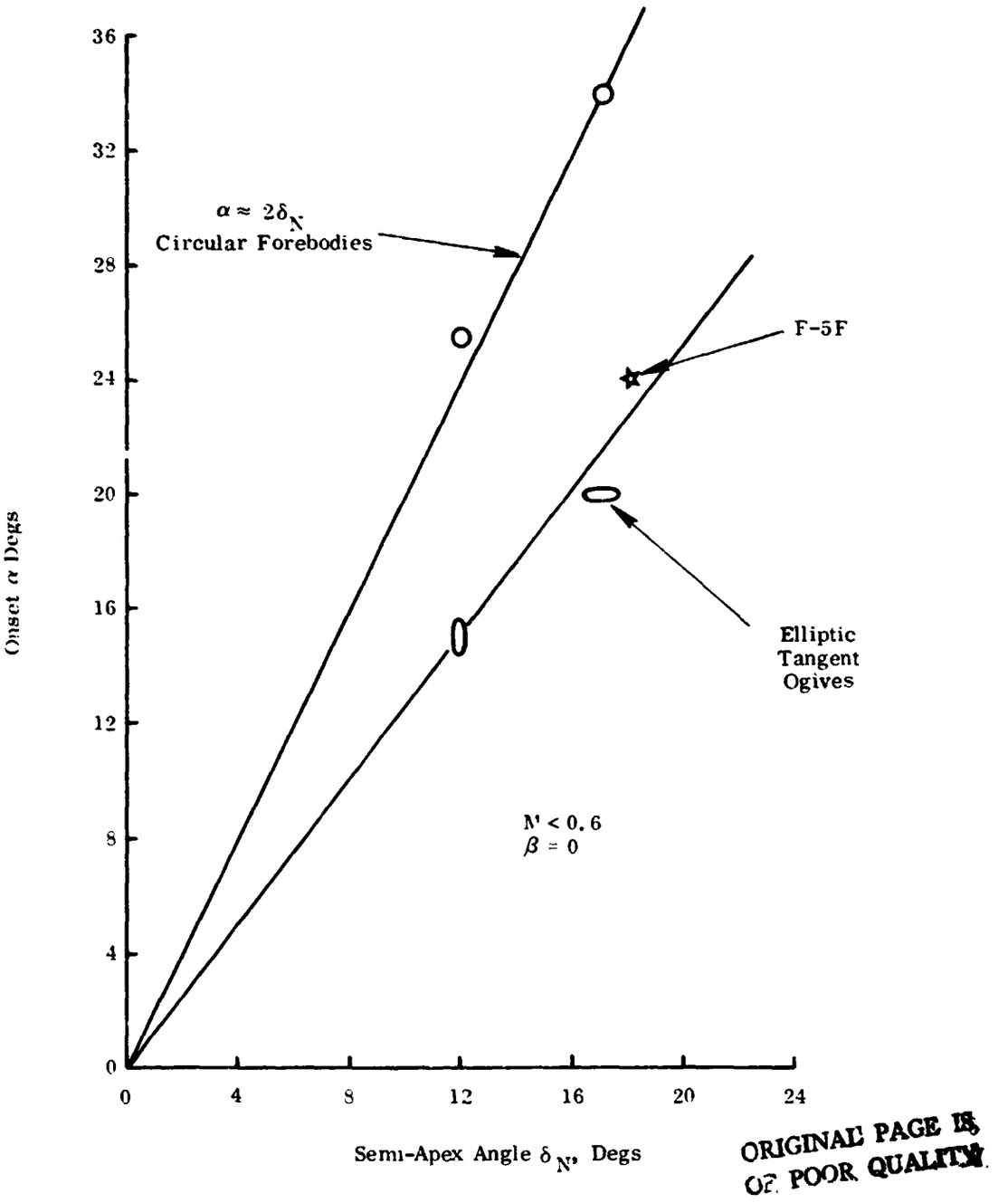

FIGURE 24. CORRELATION OF ONSET ANGLE WITH SEMI-APEX ANGLE

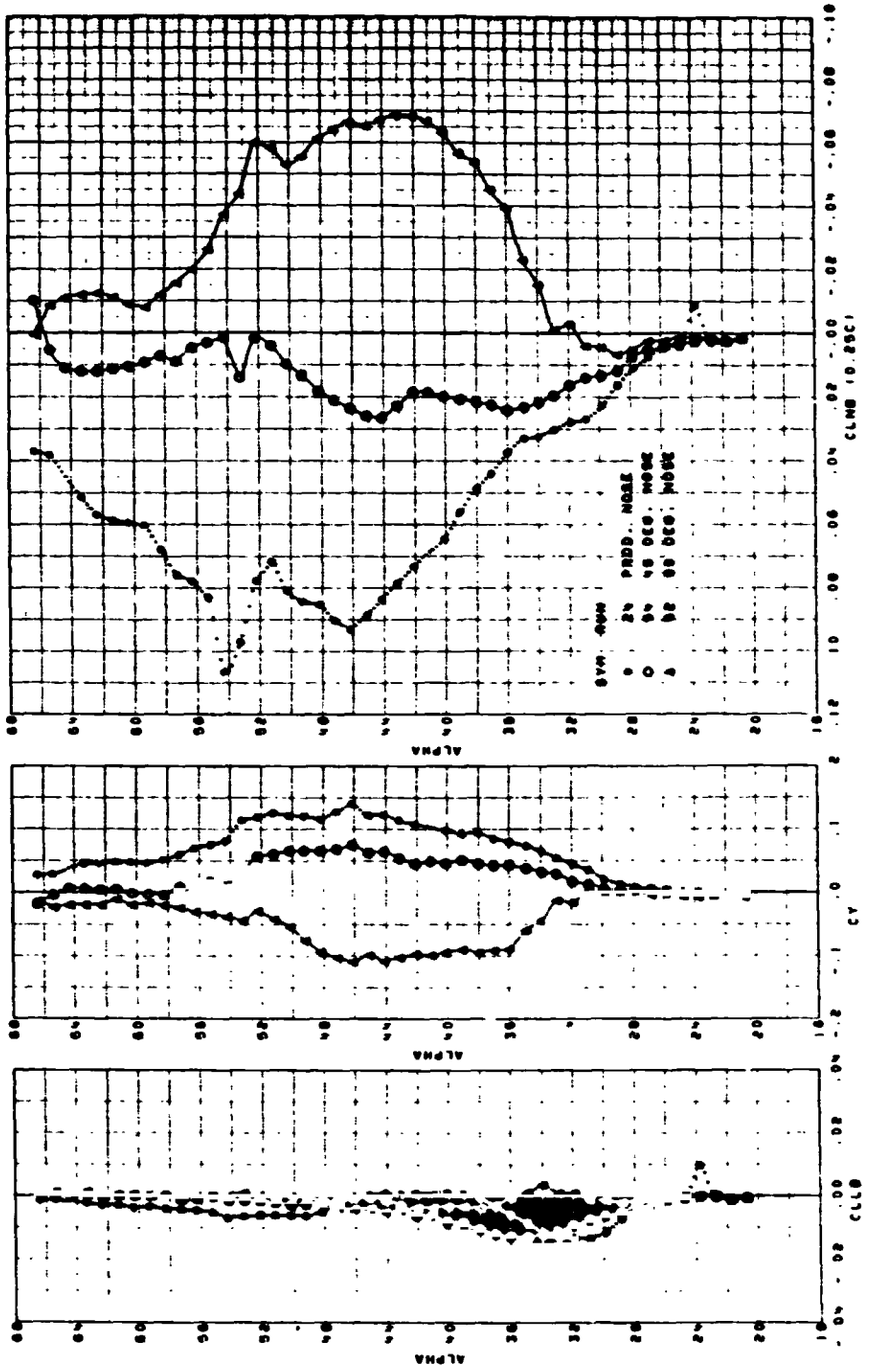

FIGURE 25. F-5F CLEAN CONFIGURATION. EFFECT OF NOSE ANGLE AT ZERO SIDESLIP, LAT/DIR DATA

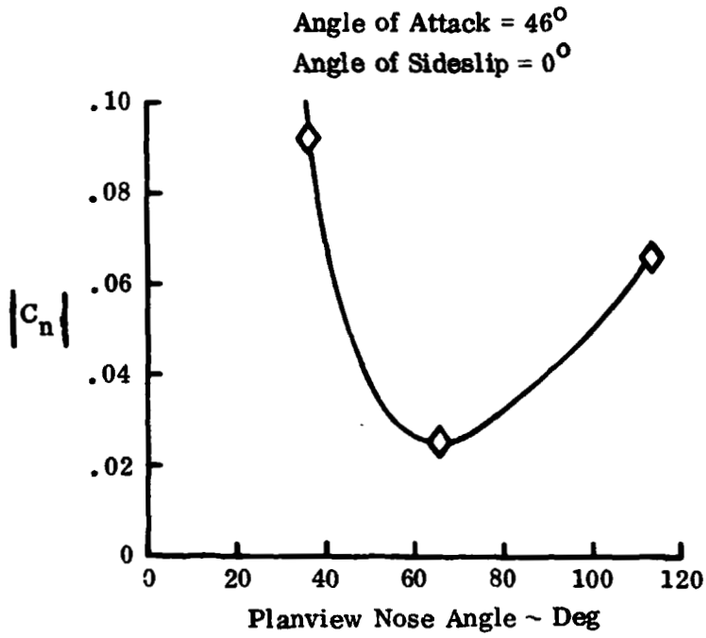

FIGURE 26. F-5F CLEAN CONFIGURATION. EFFECT OF PLANVIEW NOSE ANGLE ON $|C_n|$

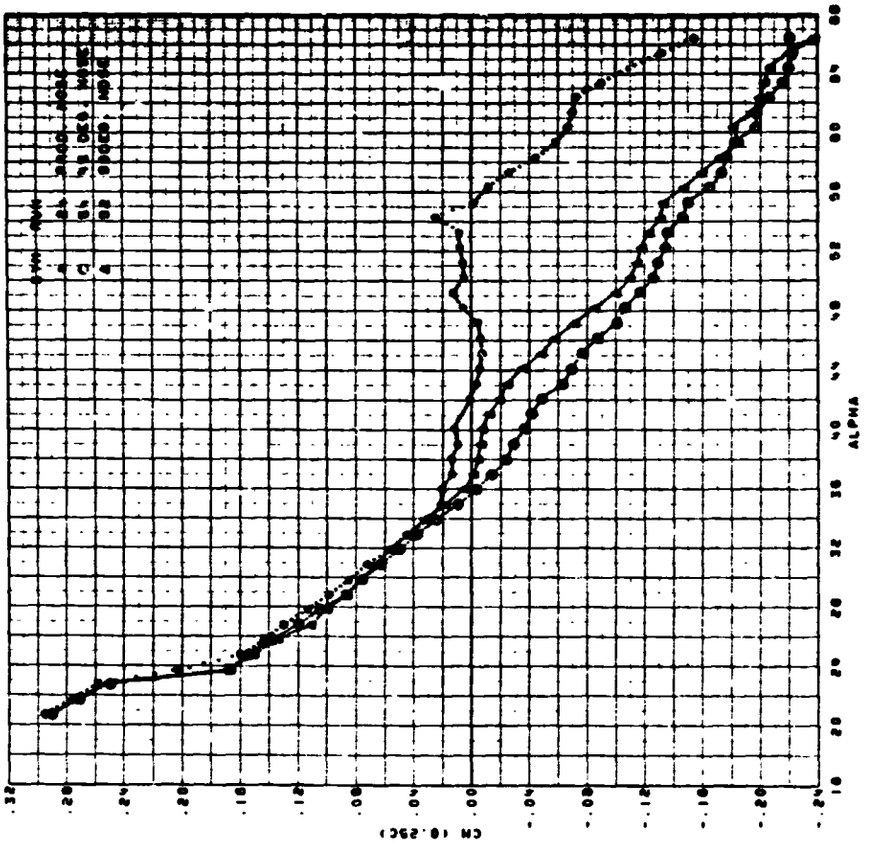

FIGURE 27. F-5F CLEAN CONFIGURATION. EFFECT OF NOSE ANGLE AT ZERO SIDESLIP, PITCHING MOMENT DATA

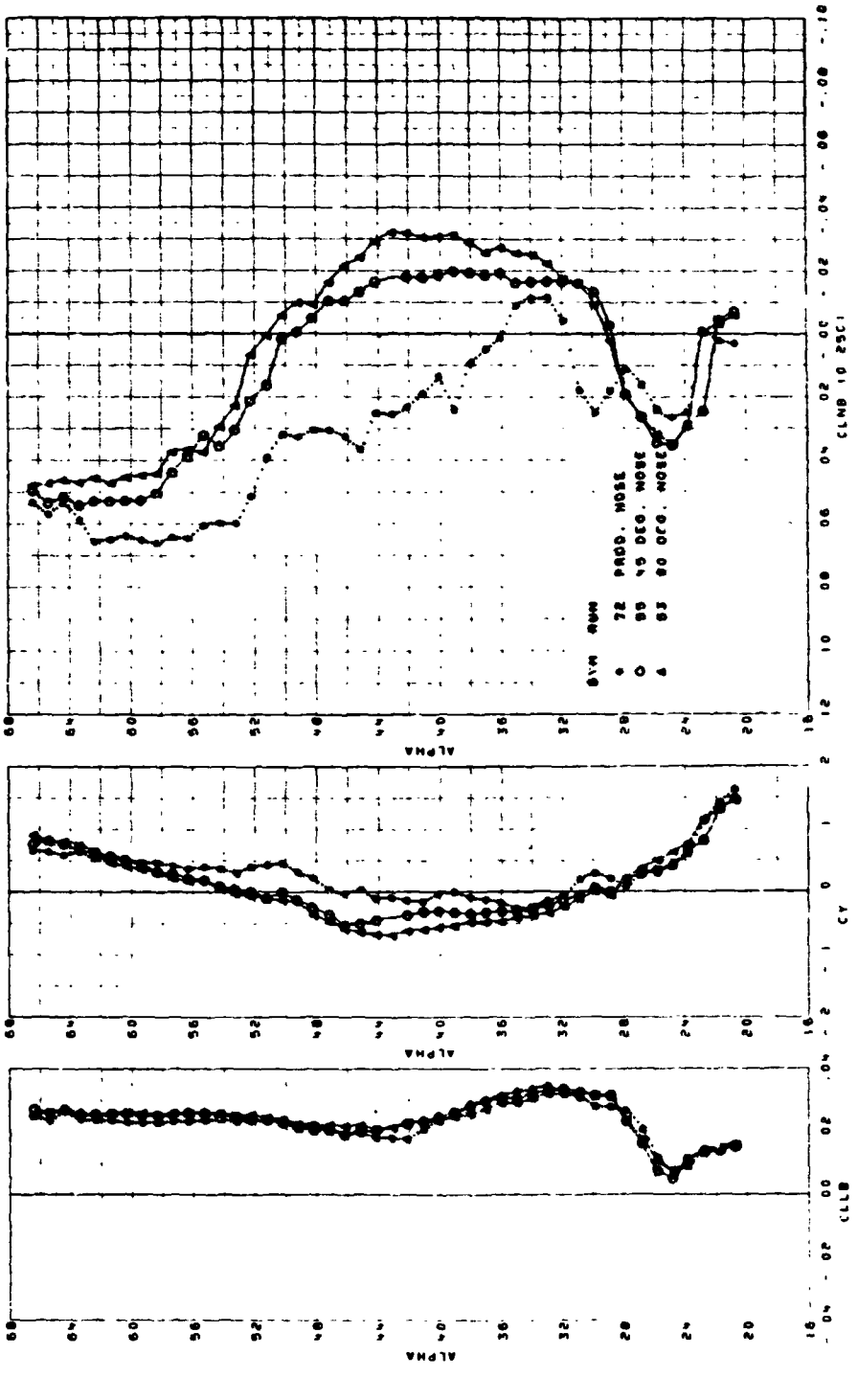

FIGURE 28. F-5F CLEAN CONFIGURATION. EFFECT OF NOSE ANGLE AT -10° SIDESLIP, LAT/DIR DATA.

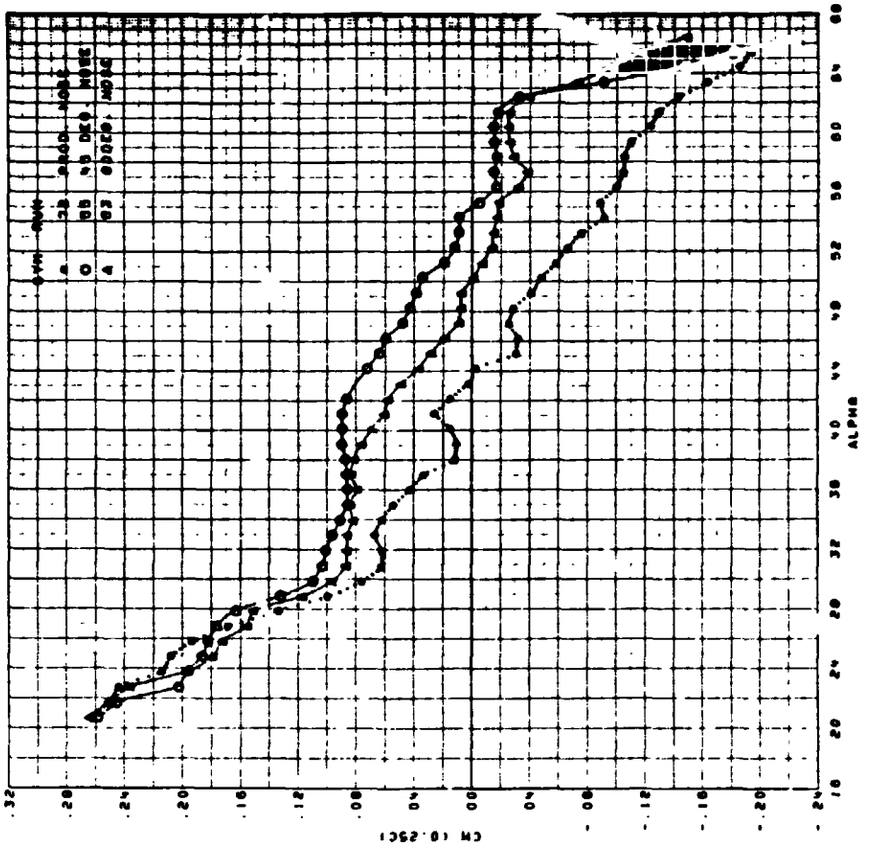

FIGURE 29. F-5F CLEAN CONFIGURATION. EFFECT OF NOSE ANGLE AT -10° SIDESLIP, PITCHING MOMENT DATA

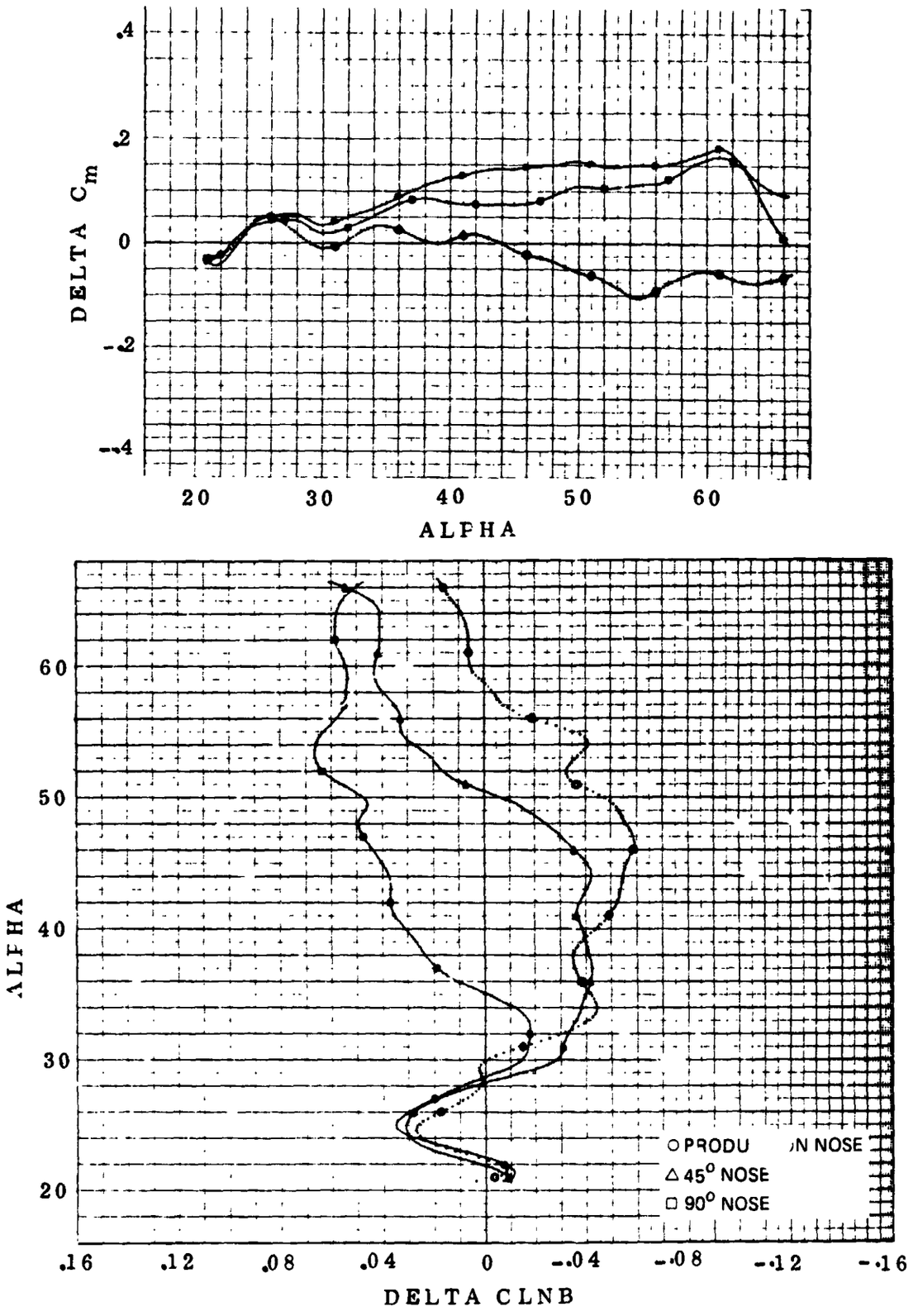

FIGURE 30. F-5F CLEAN CONFIGURATION. EFFECT OF NOSE ANGLE ON INCREMENTAL C_n AND C_m DUE TO -10° SIDESLIP

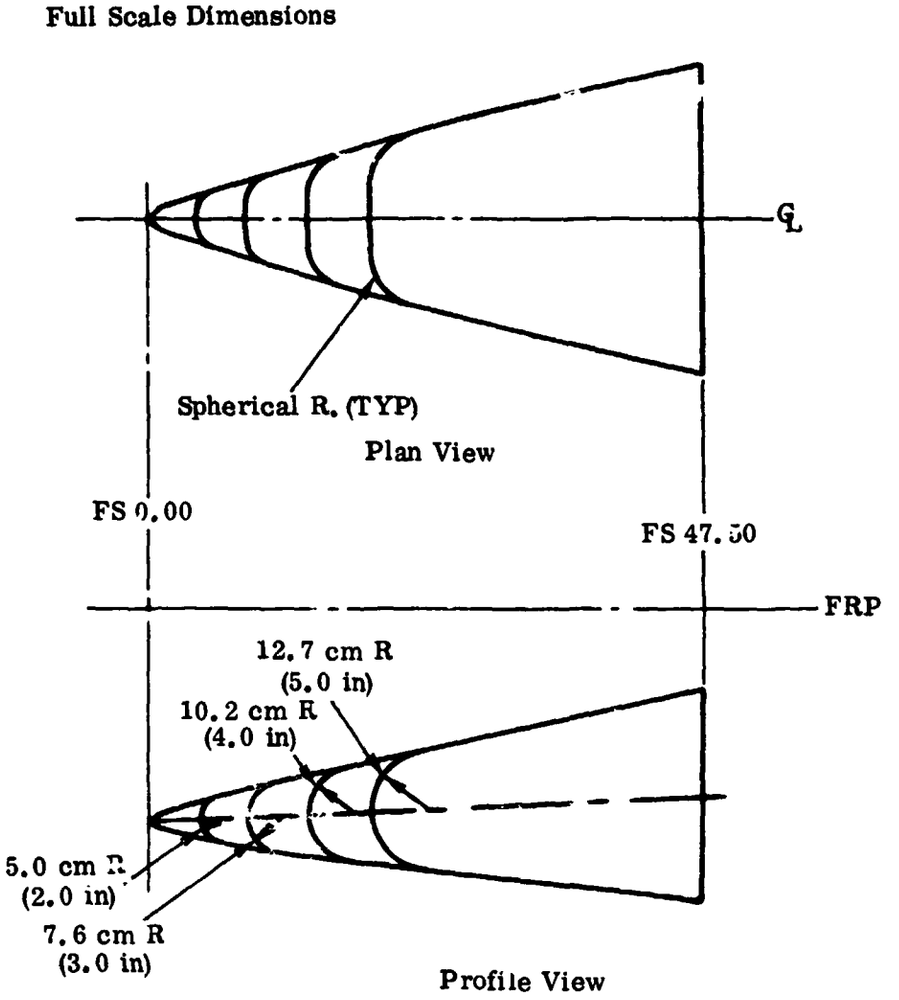

FIGURE 31. F-5F NOSE RADIUS GEOMETRIES

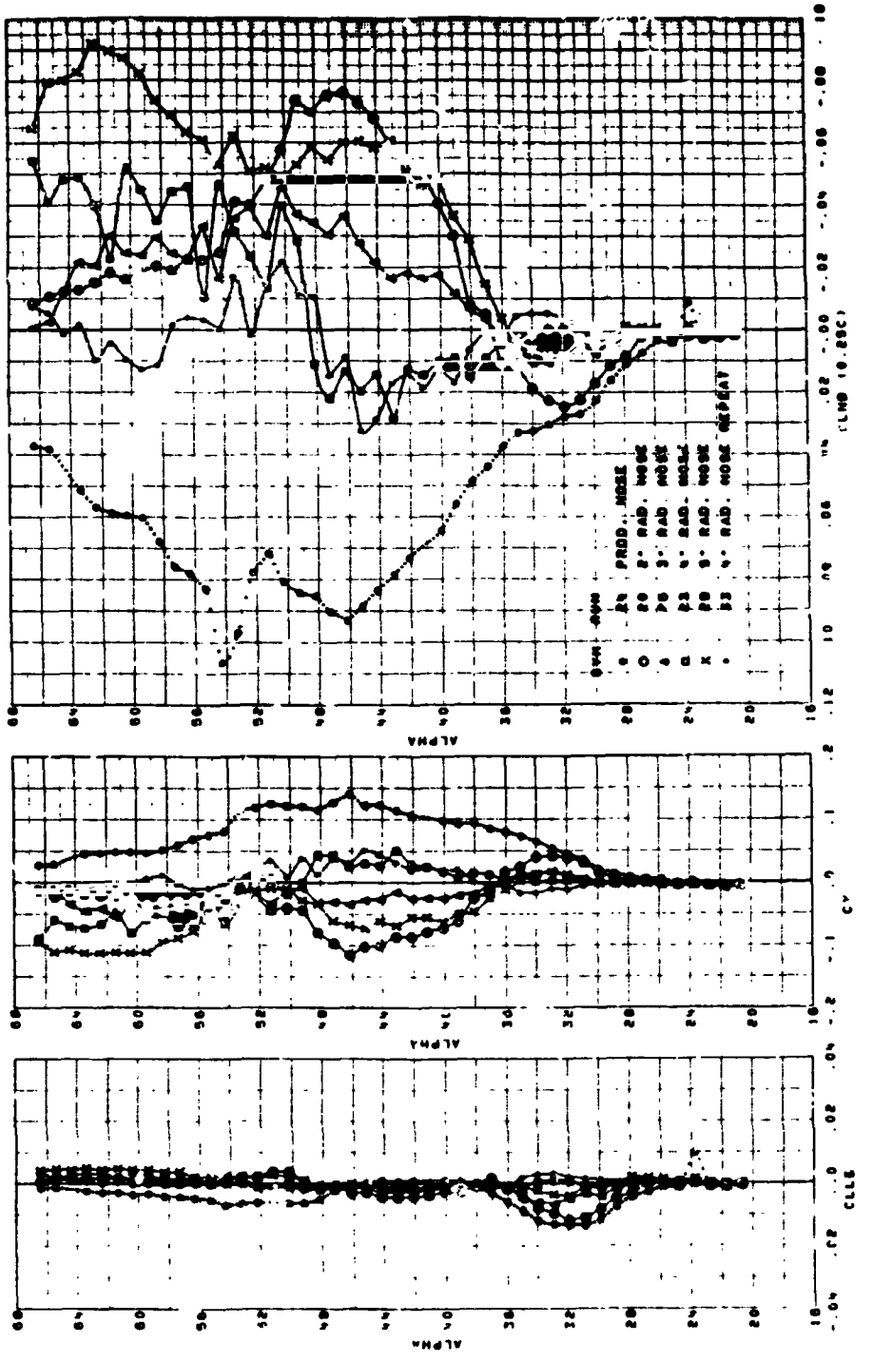

FIGURE 32. F-5F CLEAN CONFIGURATION. EFFECT OF NOSE RADIUS AT ZERO SIDESLIP, LAT. DIR DATA

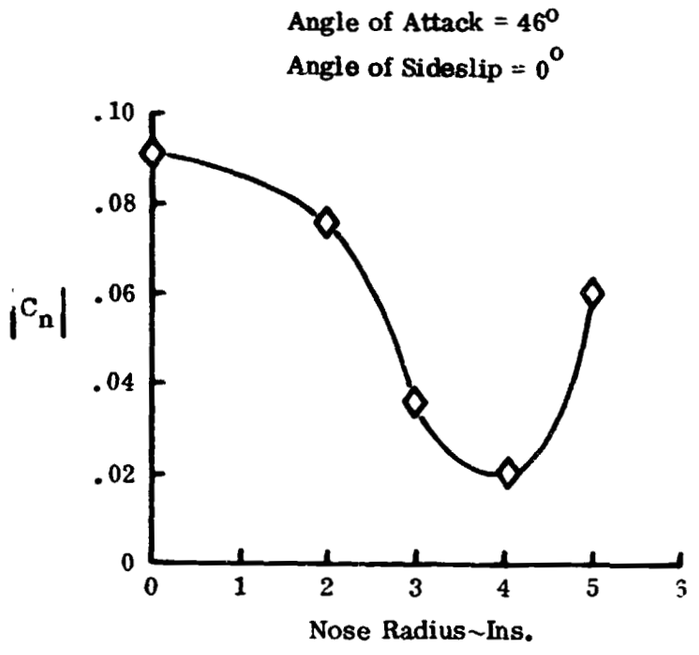

FIGURE 33. F-5F CLEAN CONFIGURATION. EFFECT OF NOSE RADIUS ON $|C_n|$

C-2

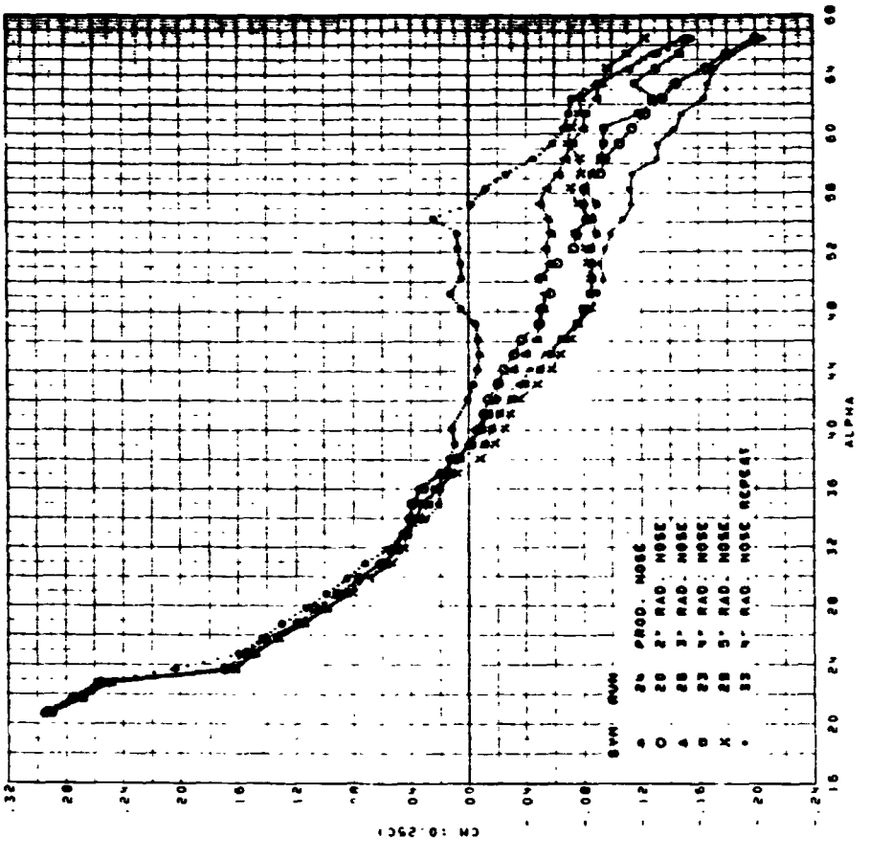

FIGURE 34. F-5F CLEAN CONFIGURATION. EFFECT OF NOSE RADIUS AT ZERO SIDESLIP, PITCHING MOMENT DATA

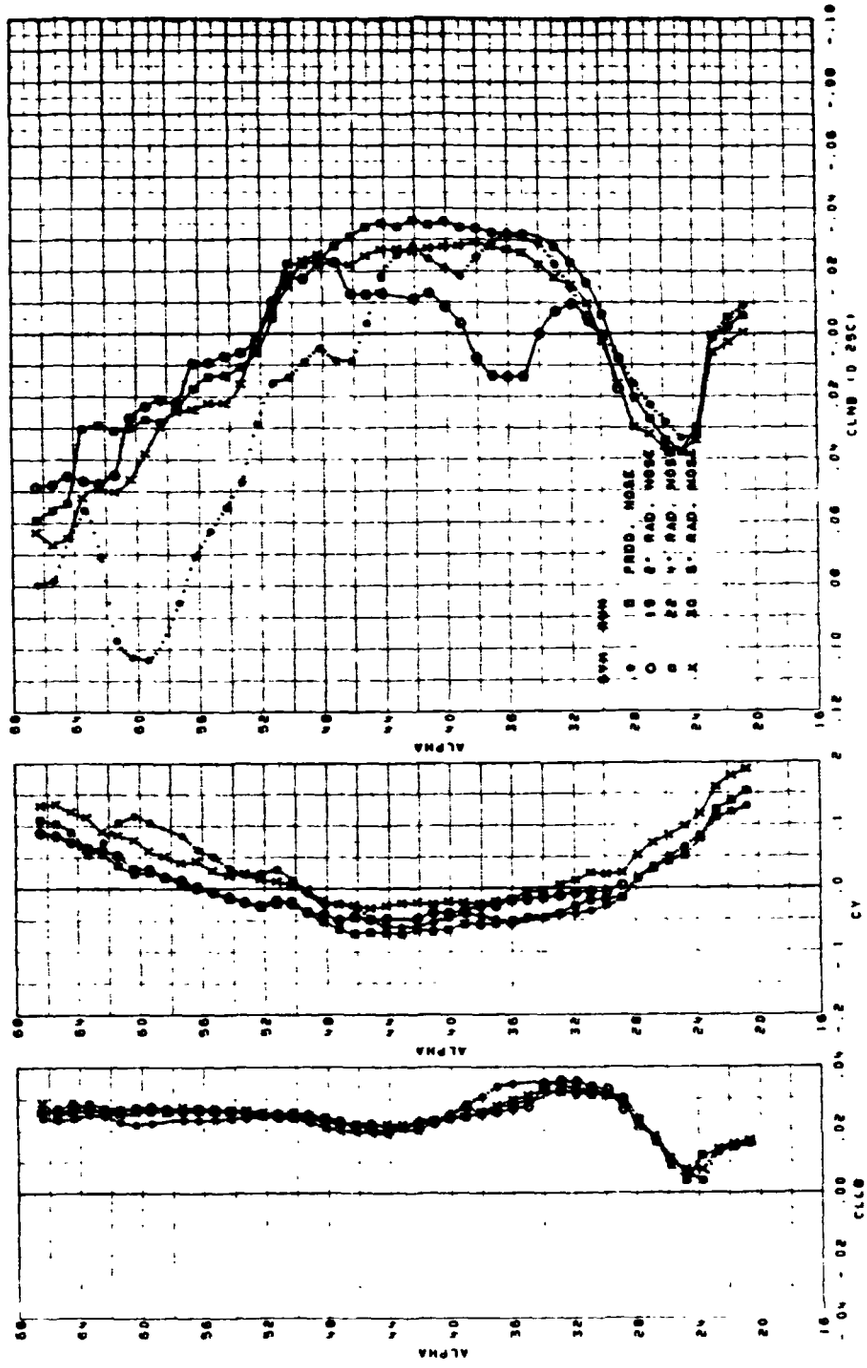

FIGURE 35. F-5F CLEAN CONFIGURATION. EFFECT OF NOSE RADIUS AT -10° SIDESLIP, LAT/DIR DATA

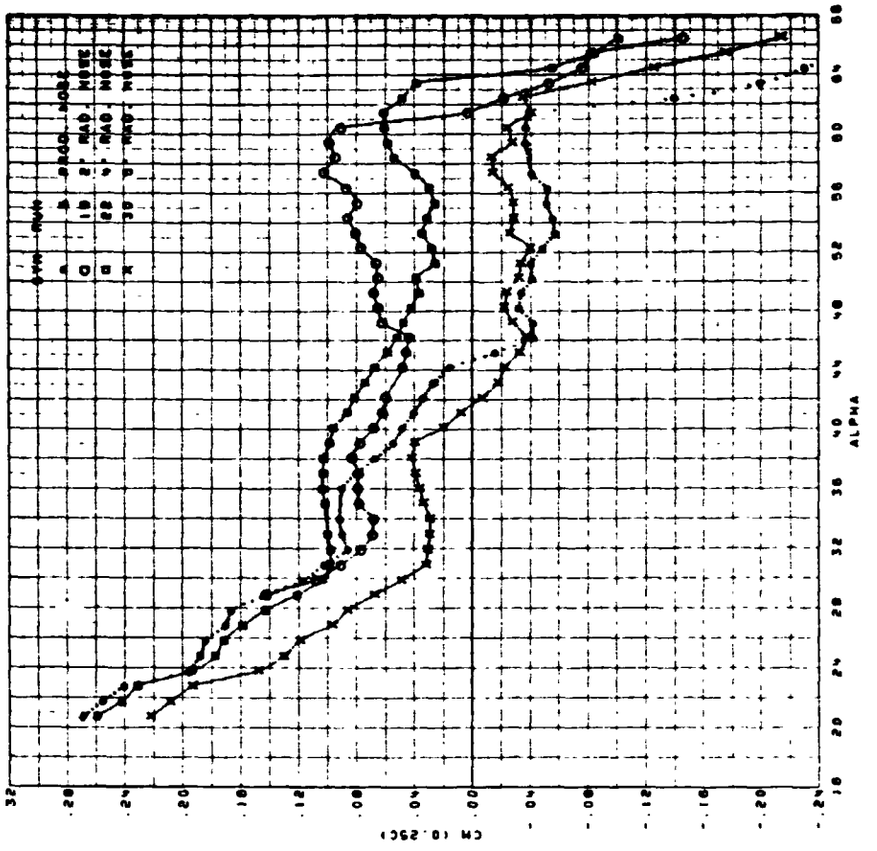

FIGURE 36. F-5F CLEAN CONFIGURATION. EFFECT OF NOSE RADIUS AT -10° SIDESLIP, PITCHING MOMENT DATA

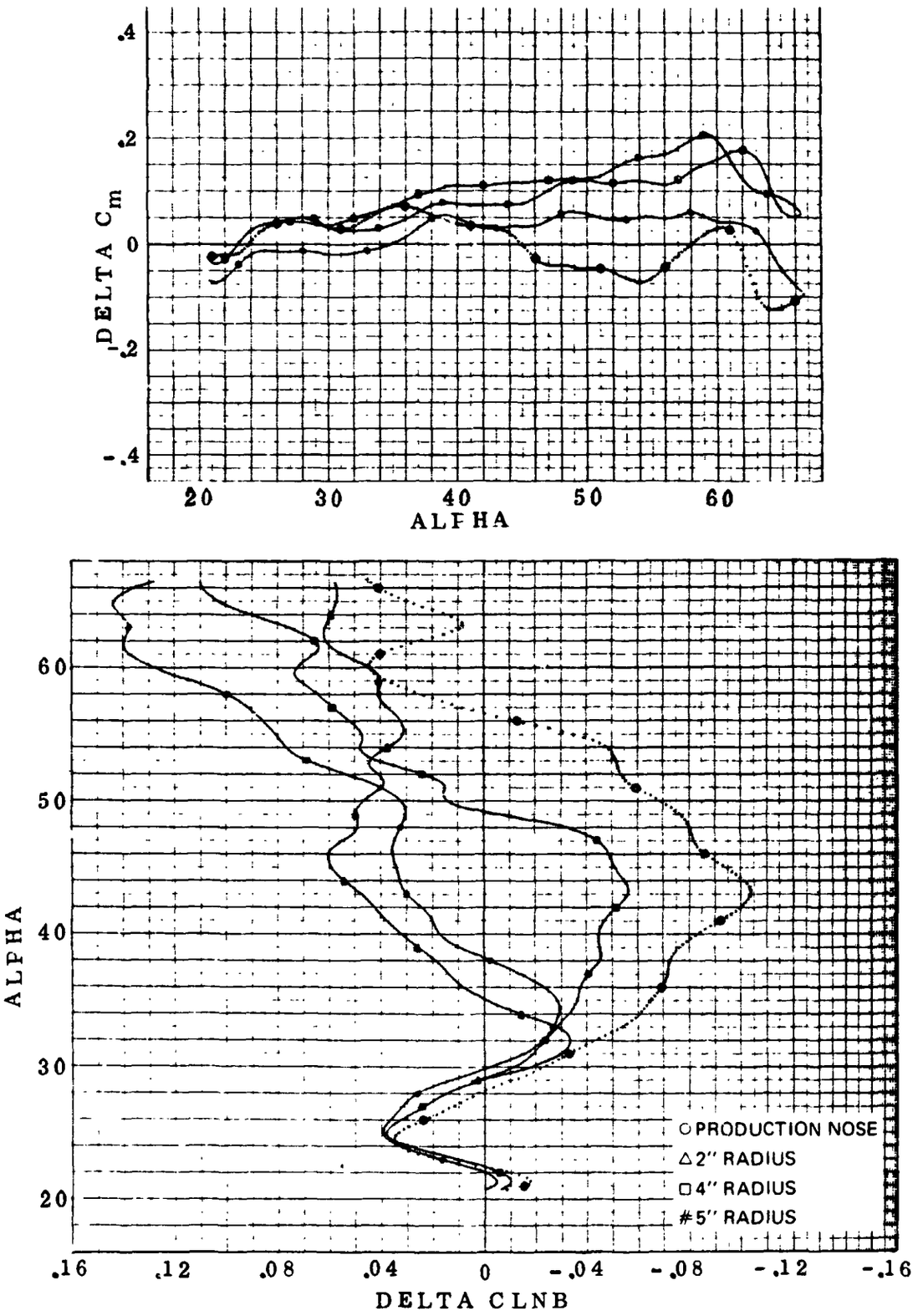

FIGURE 37. F-5F CLEAN CONFIGURATION. EFFECT OF NOSE RADIUS ON INCREMENTAL C_n AND C_m DUE TO -10° SIDESLIP

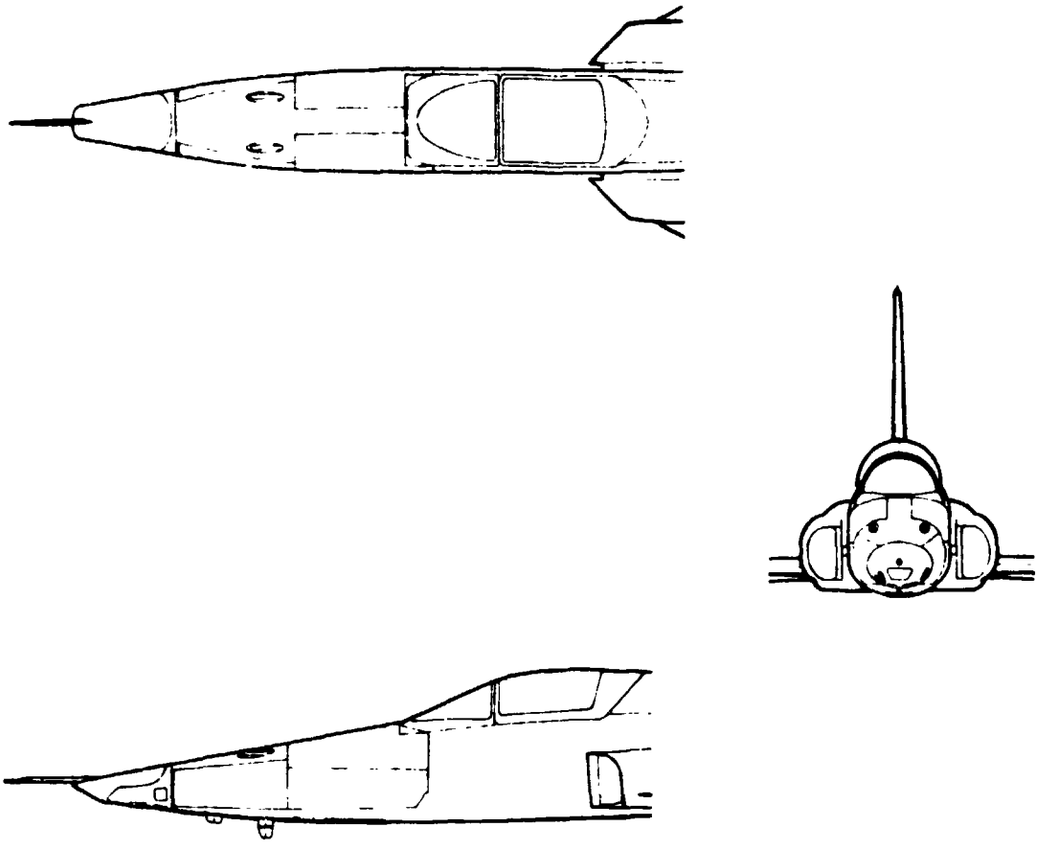

FIGURE 38. F-5E RECONNAISSANCE NOSE CONFIGURATION (RECCE)

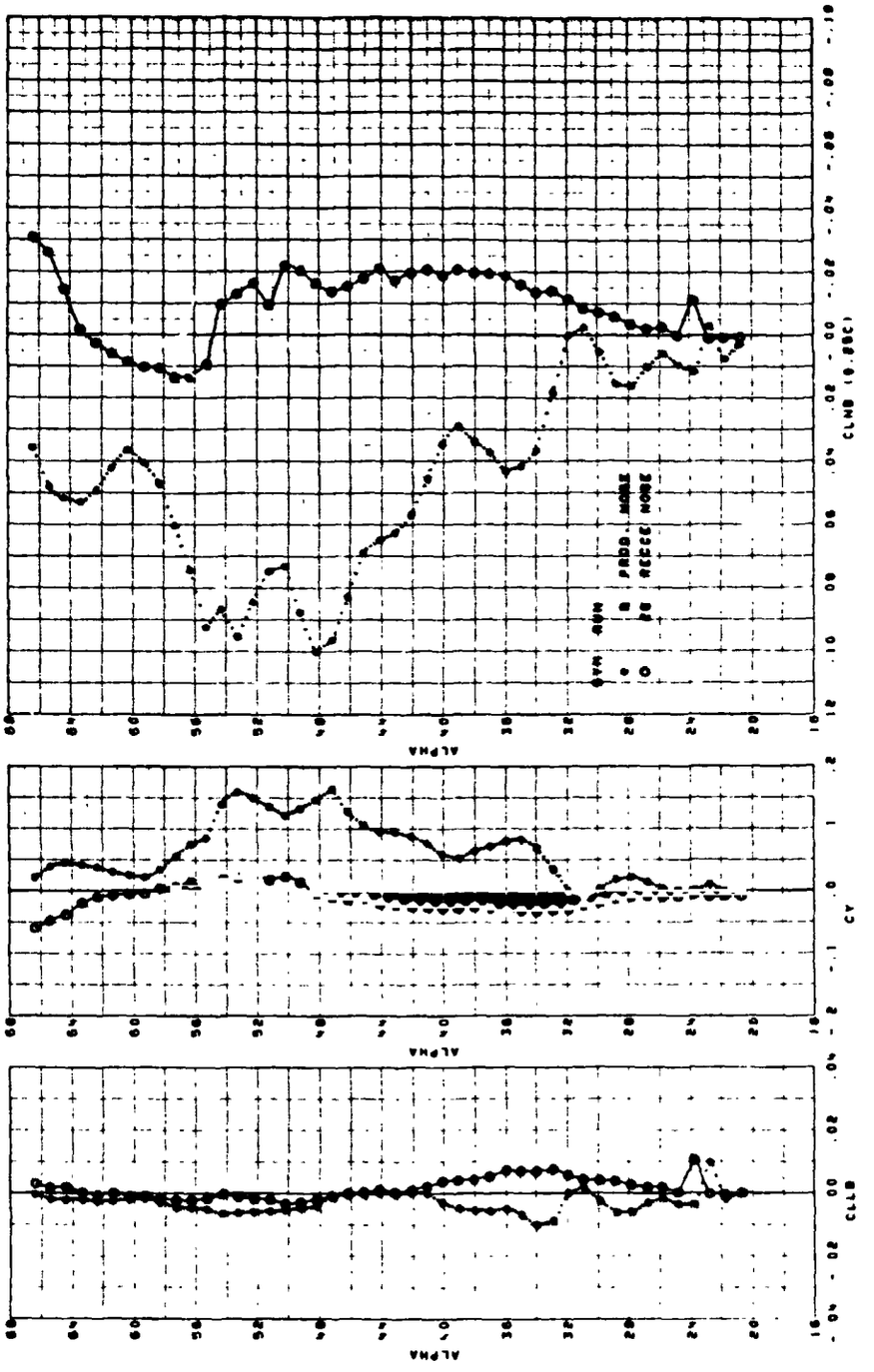

FIGURE 39. F-5F CLEAN CONFIGURATION. COMPARISON OF PRODUCTION AND RECCE NOSE AT ZERO SIDESLIP, LAT/DIR DATA

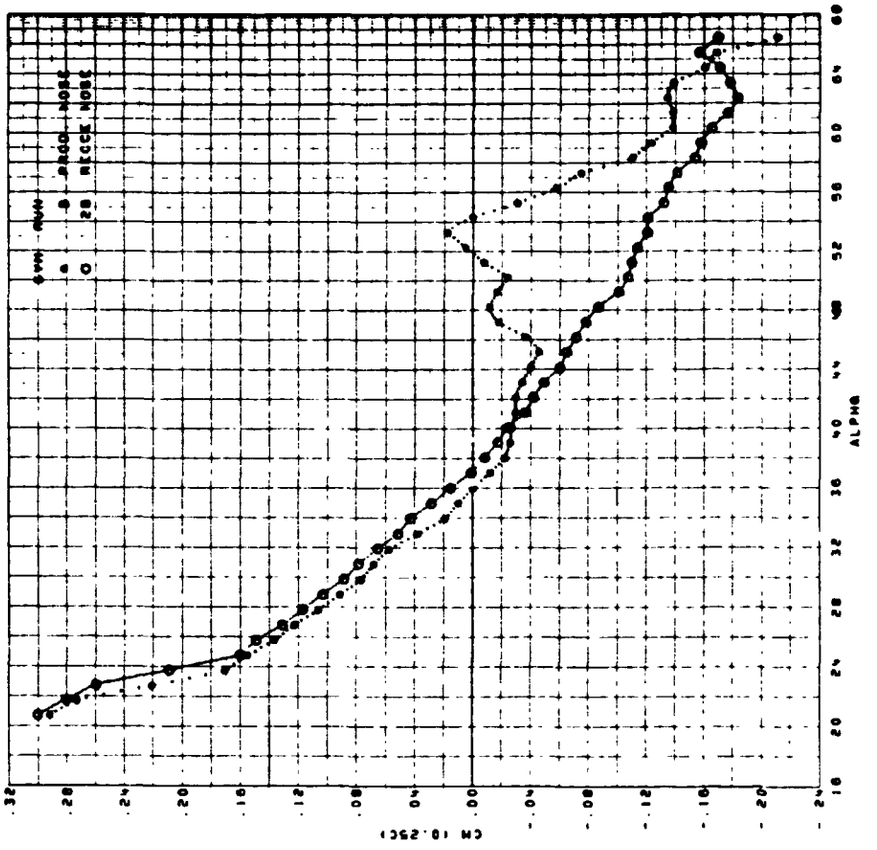

FIGURE 40. F-5F CLEAN CONFIGURATION. COMPARISON OF PRODUCTION AND RECCE NOSE AT ZERO SIDESLIP, PITCHING MOMENT DATA

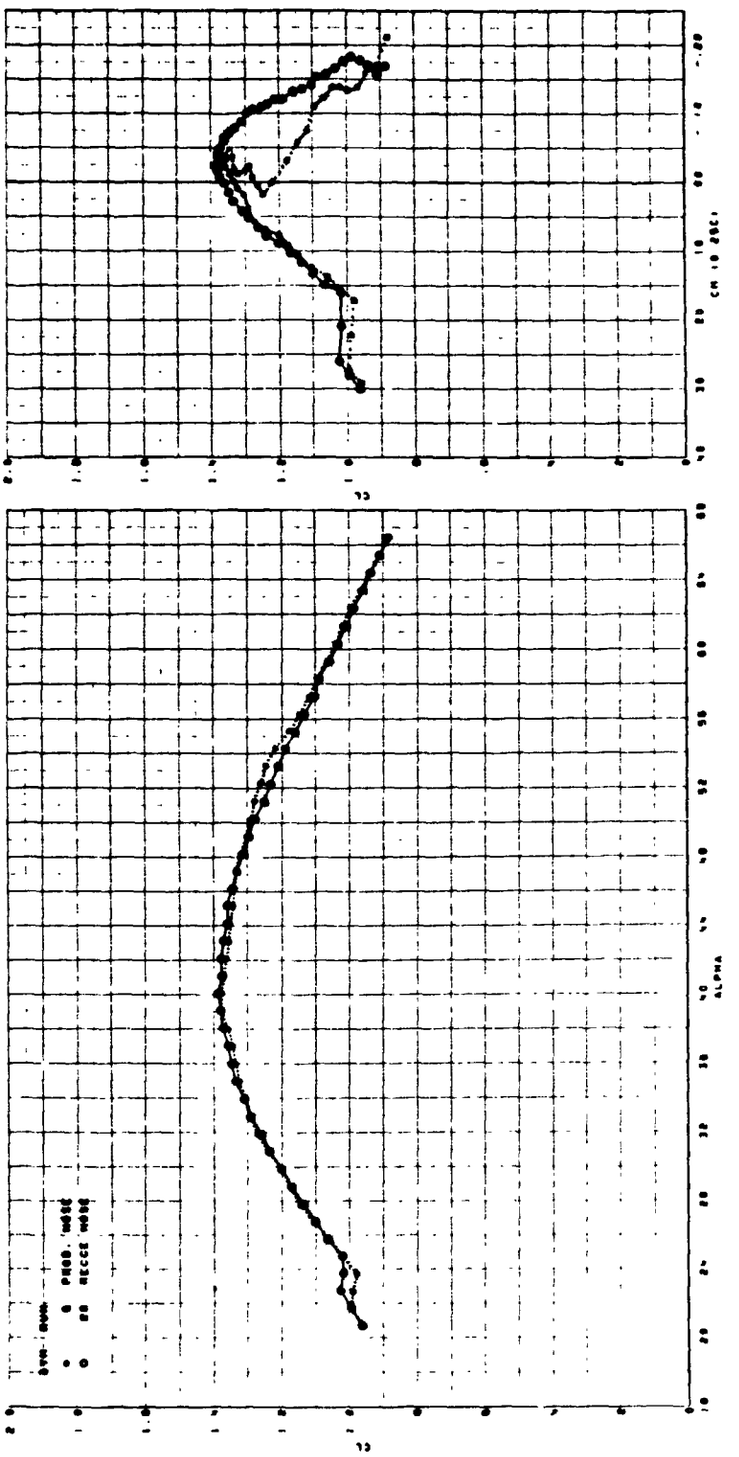

FIGURE 41. F-5F CLEAN CONFIGURATION. COMPARISON OF PRODUCTION AND RECCE NOSE AT ZERO SIDESLIP, LIFT AND PITCH DATA

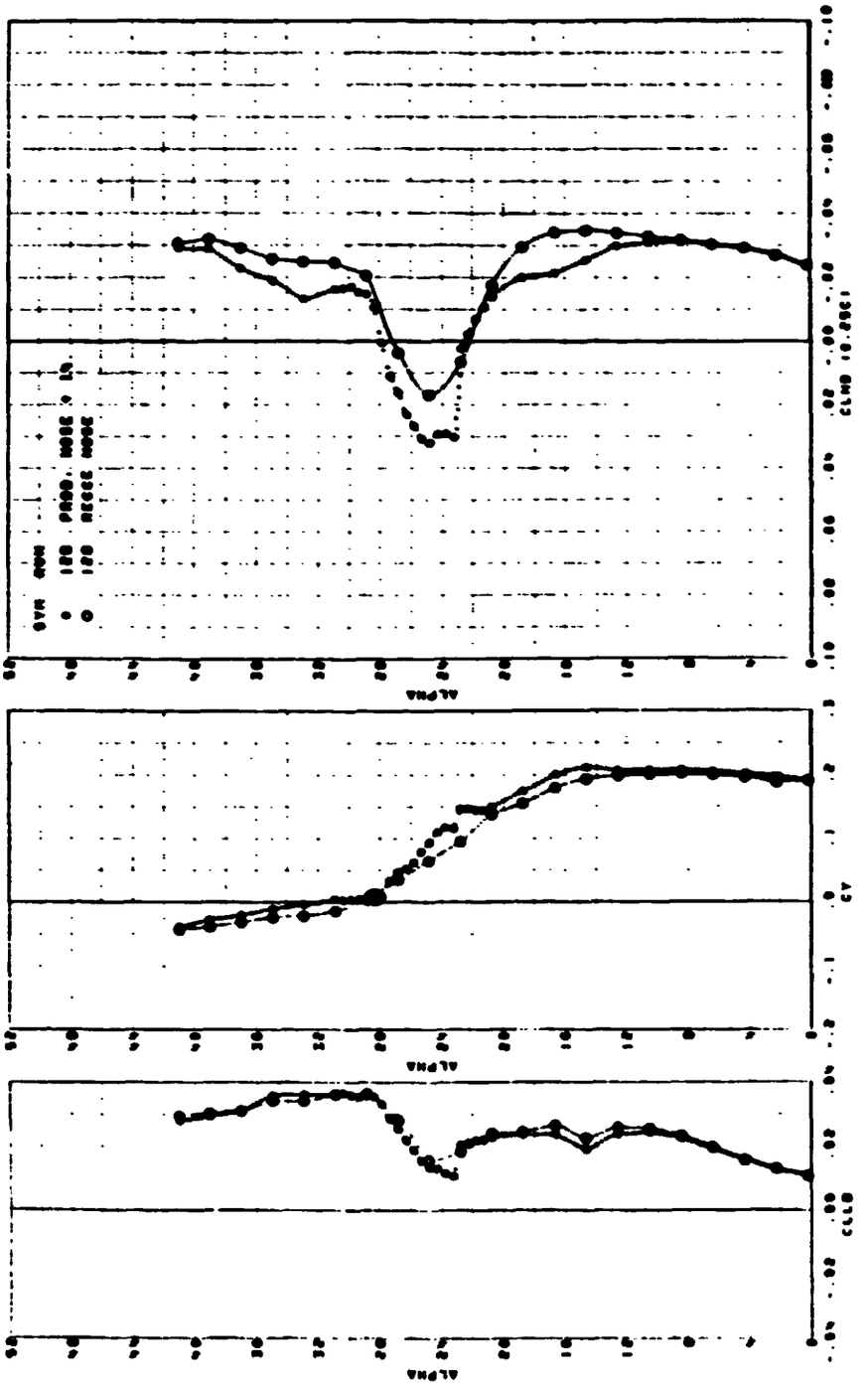

FIGURE 42. F-5F CLEAN CONFIGURATION. COMPARISON OF PRODUCTION AND RECCE NOSE AT -10° SIDESLIP, LAT/DIR DATA

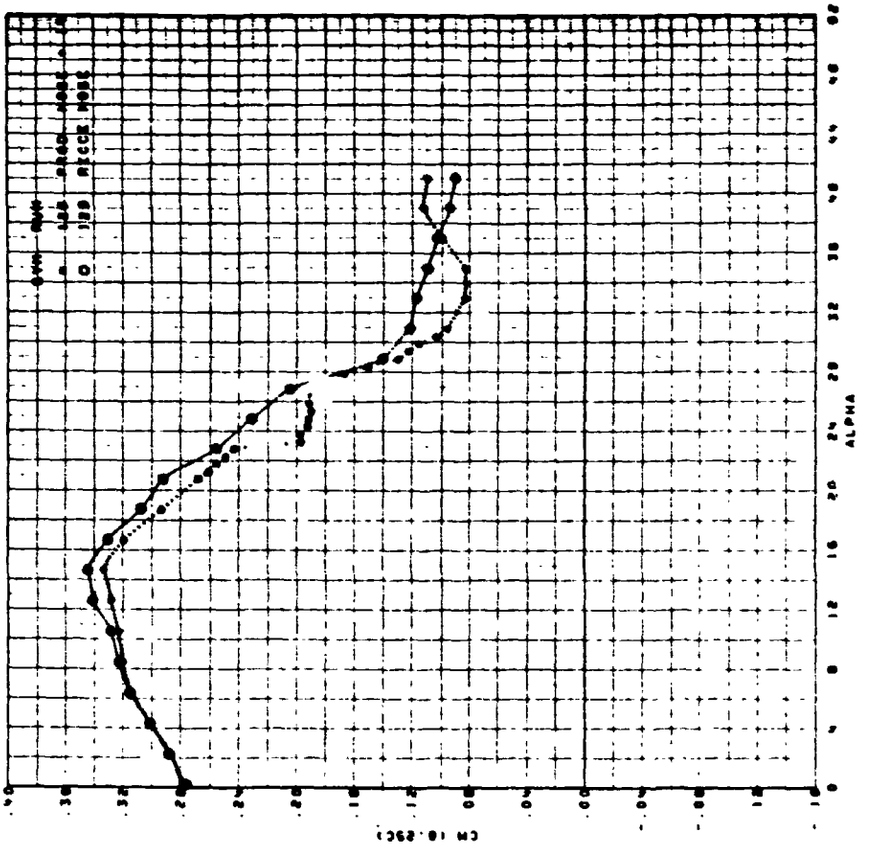

FIGURE 43. F-5F CLEAN CONFIGURATION. COMPARISON OF PRODUCTION AND RECCE NOSE AT -10° SIDESLIP, PITCHING MOMENT DATA

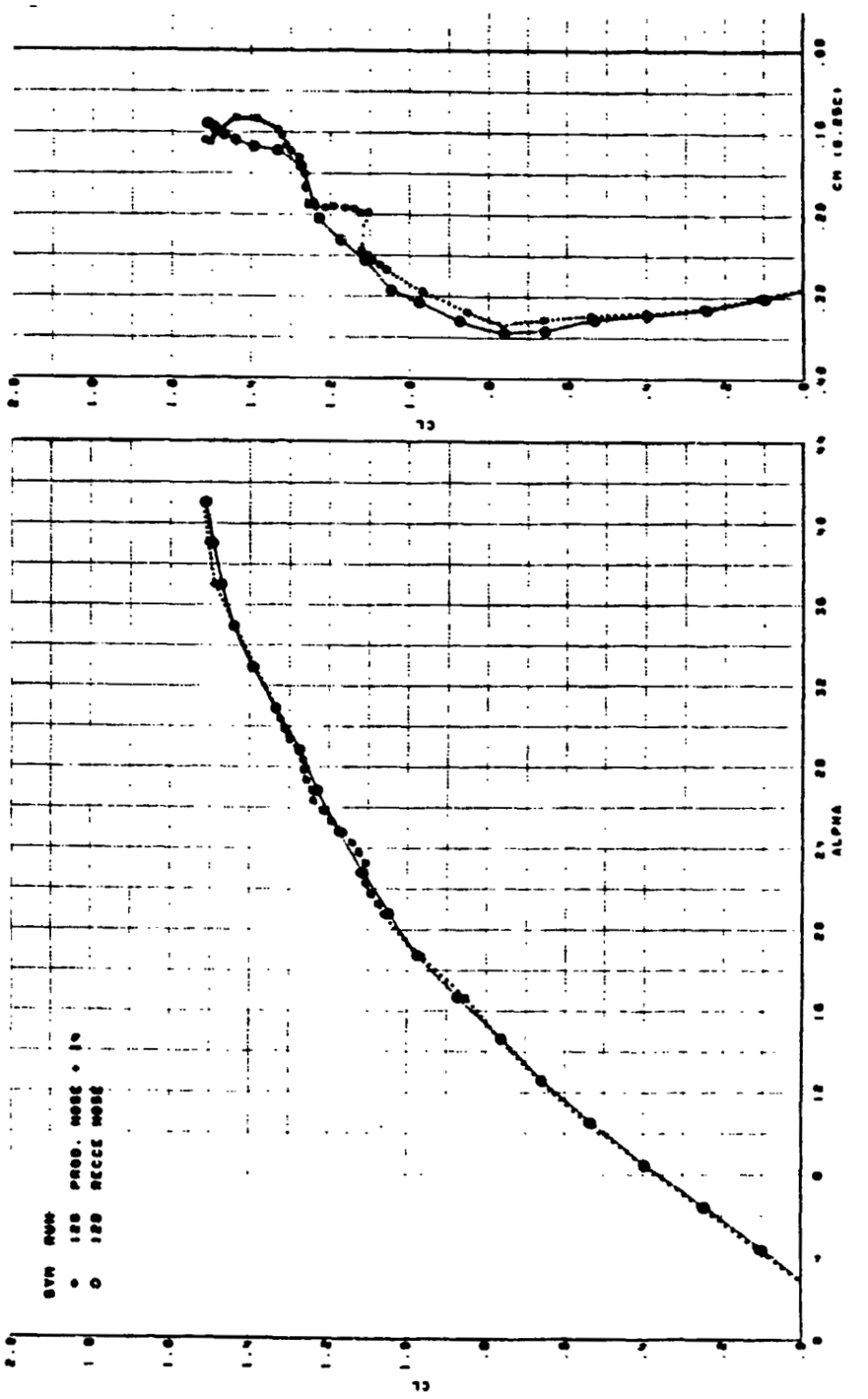

FIGURE 44. F-5F CLEAN CONFIGURATION. COMPARISON OF PRODUCTION AND RECCE NOSE AT -10° SIDESLIP, LIFT AND PITCH DATA

Full Scale Dimensions

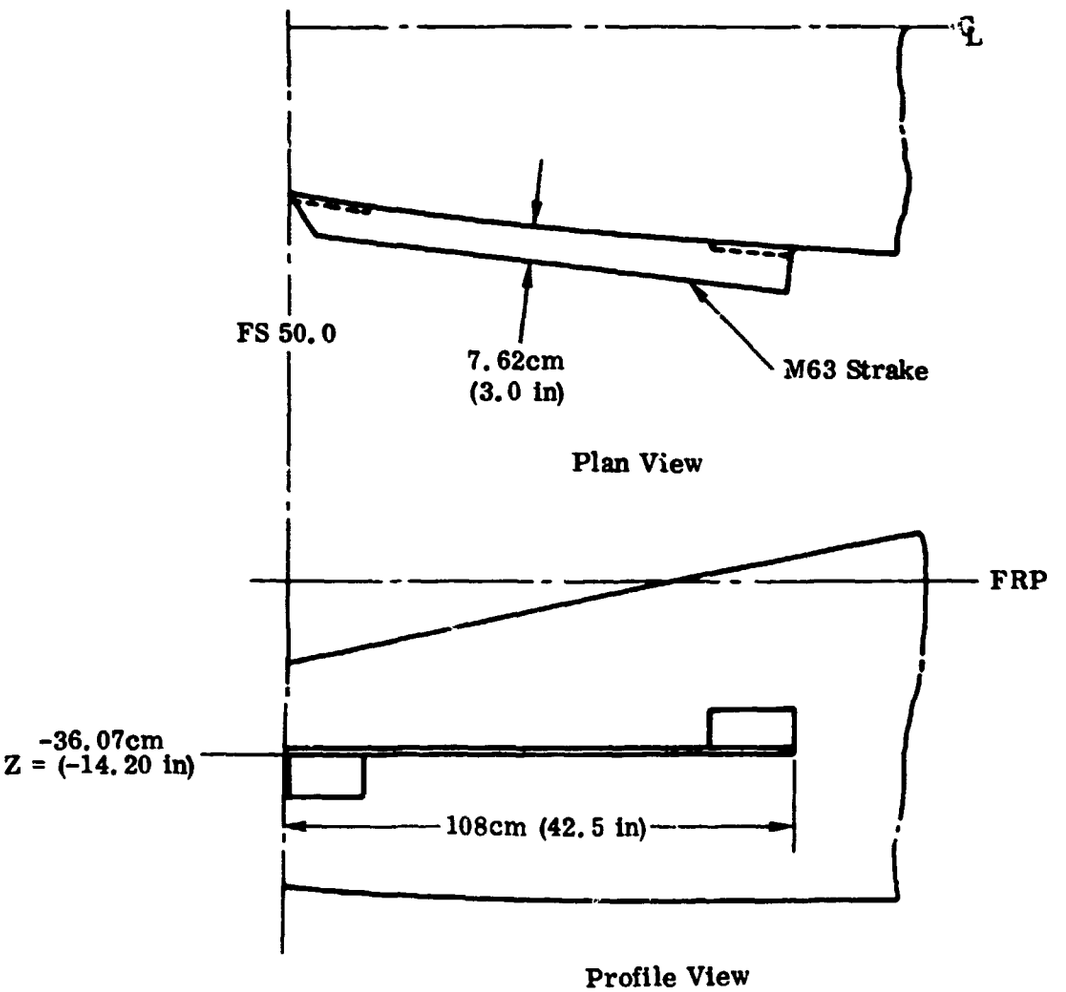

FIGURE 45. F-5F STRAKE M63 GEOMETRY

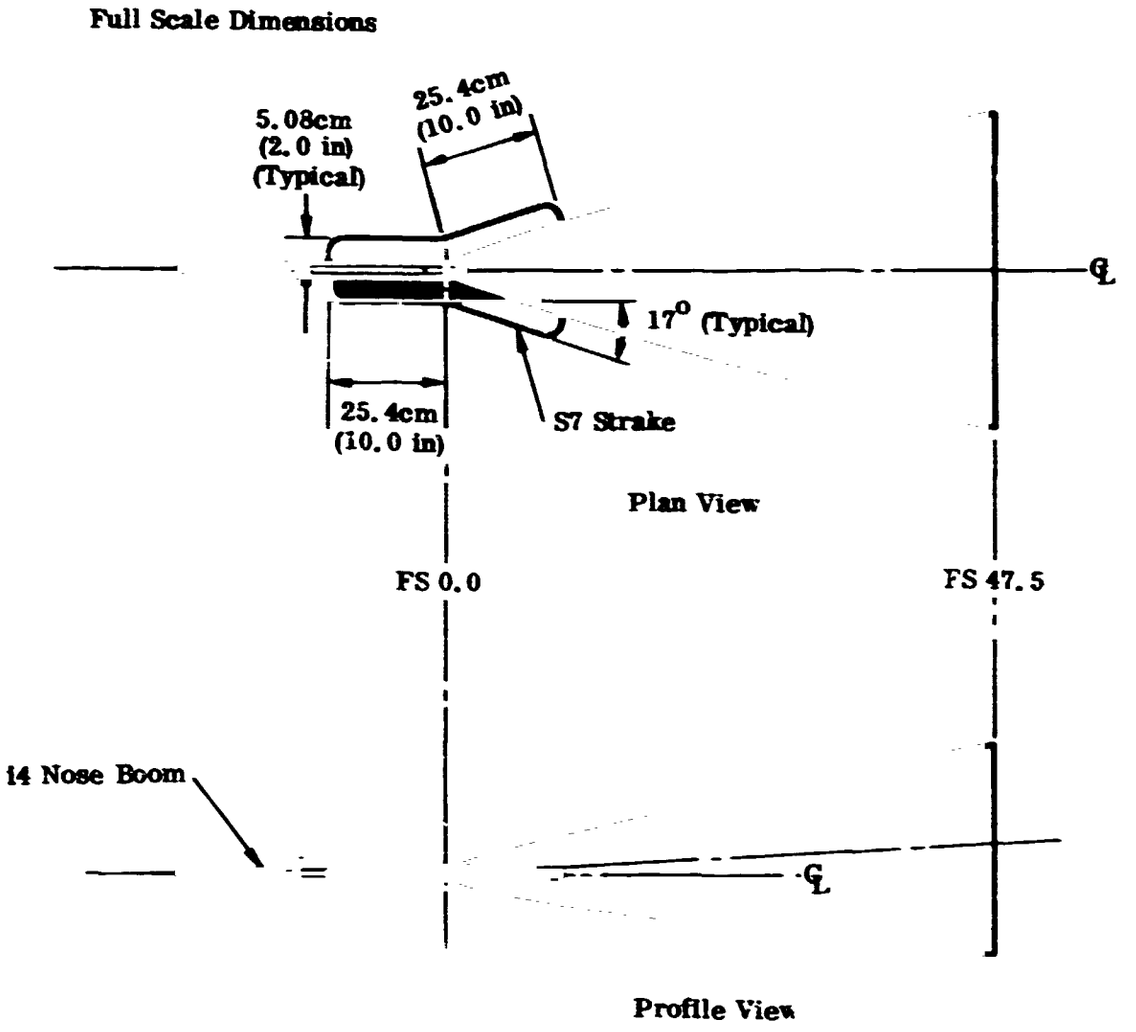

FIGURE 46. F-5F STRAKE S7 GEOMETRY

Full Scale Dimensions

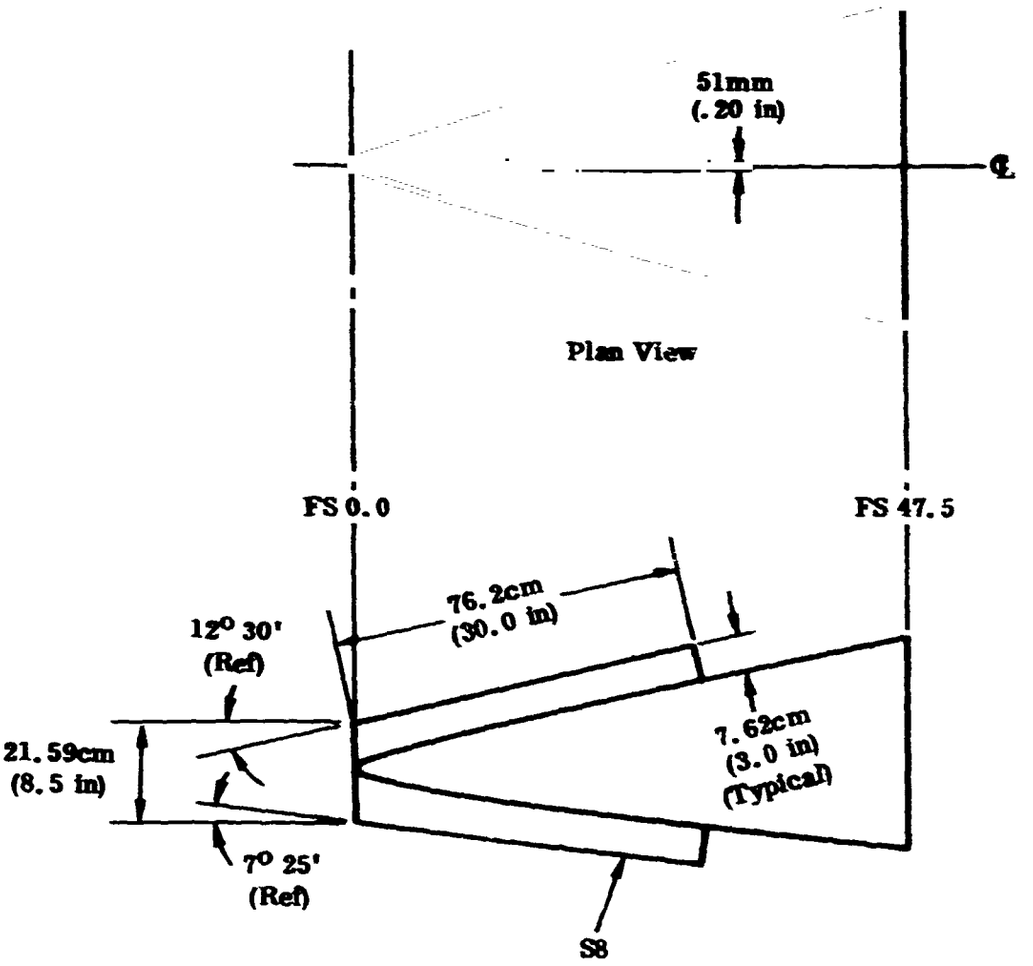

FIGURE 47. F-5F STRAKE S8 GEOMETRY

Full Scale Dimensions

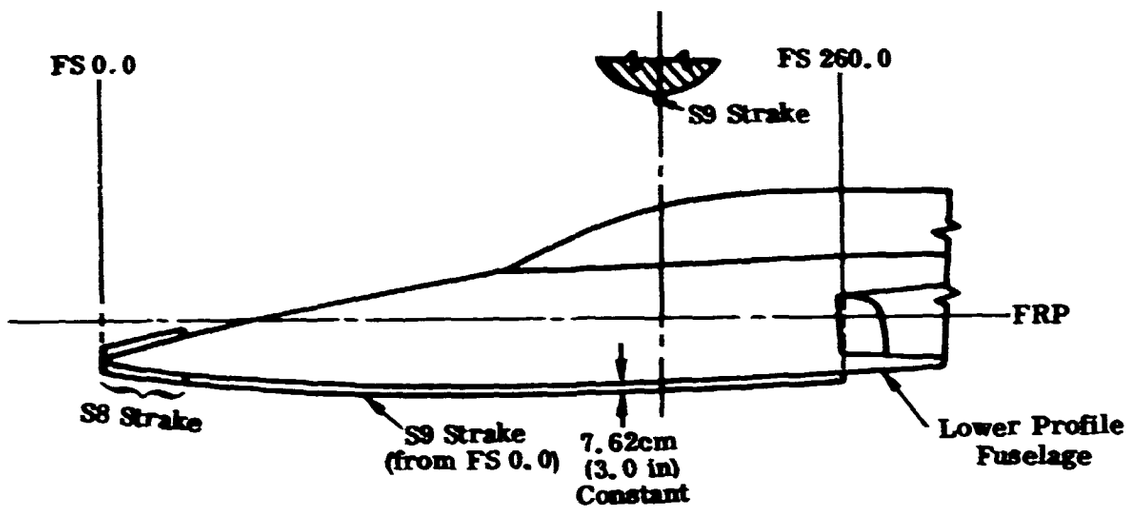

FIGURE 48. F-5F STRAKE S8 AND S9 GEOMETRY

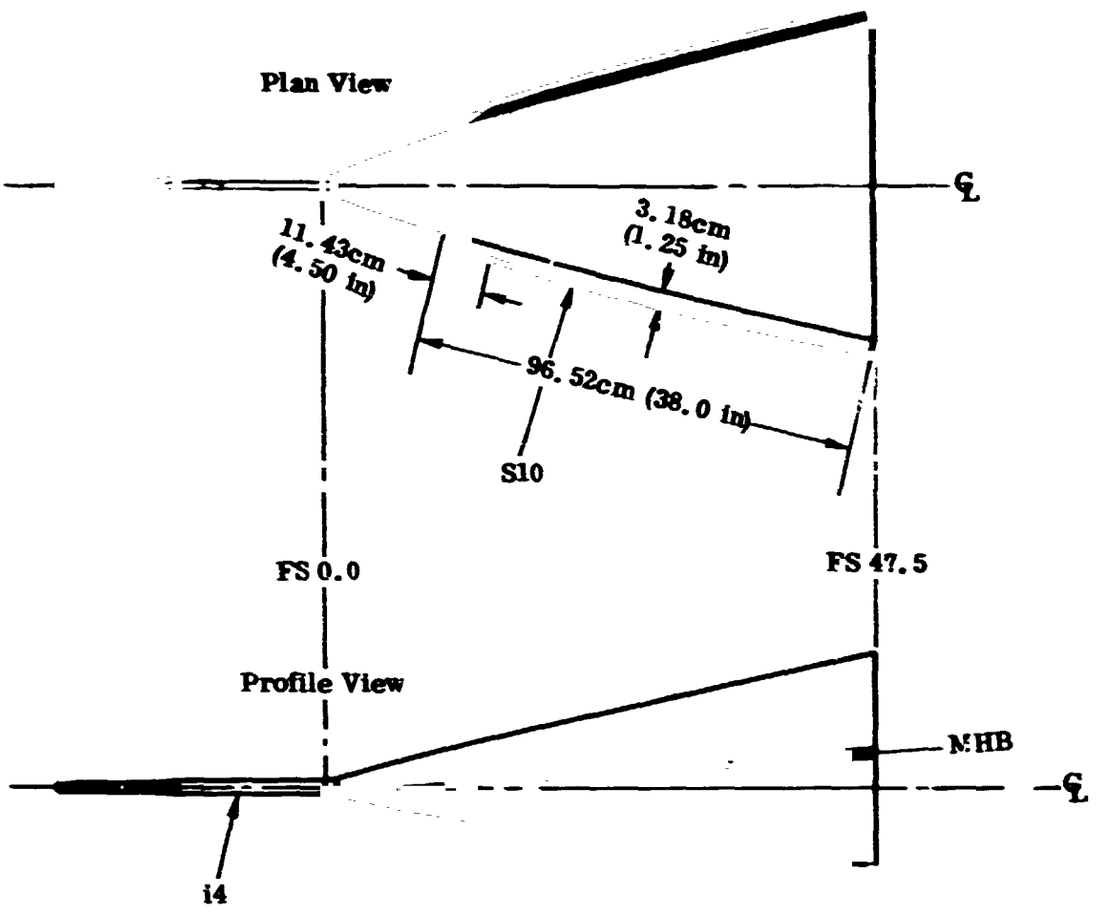

FIGURE 49. F-5F STRAKE S10 GEOMETRY

FIGURE 50. F-5F STRAKE S11 GEOMETRY

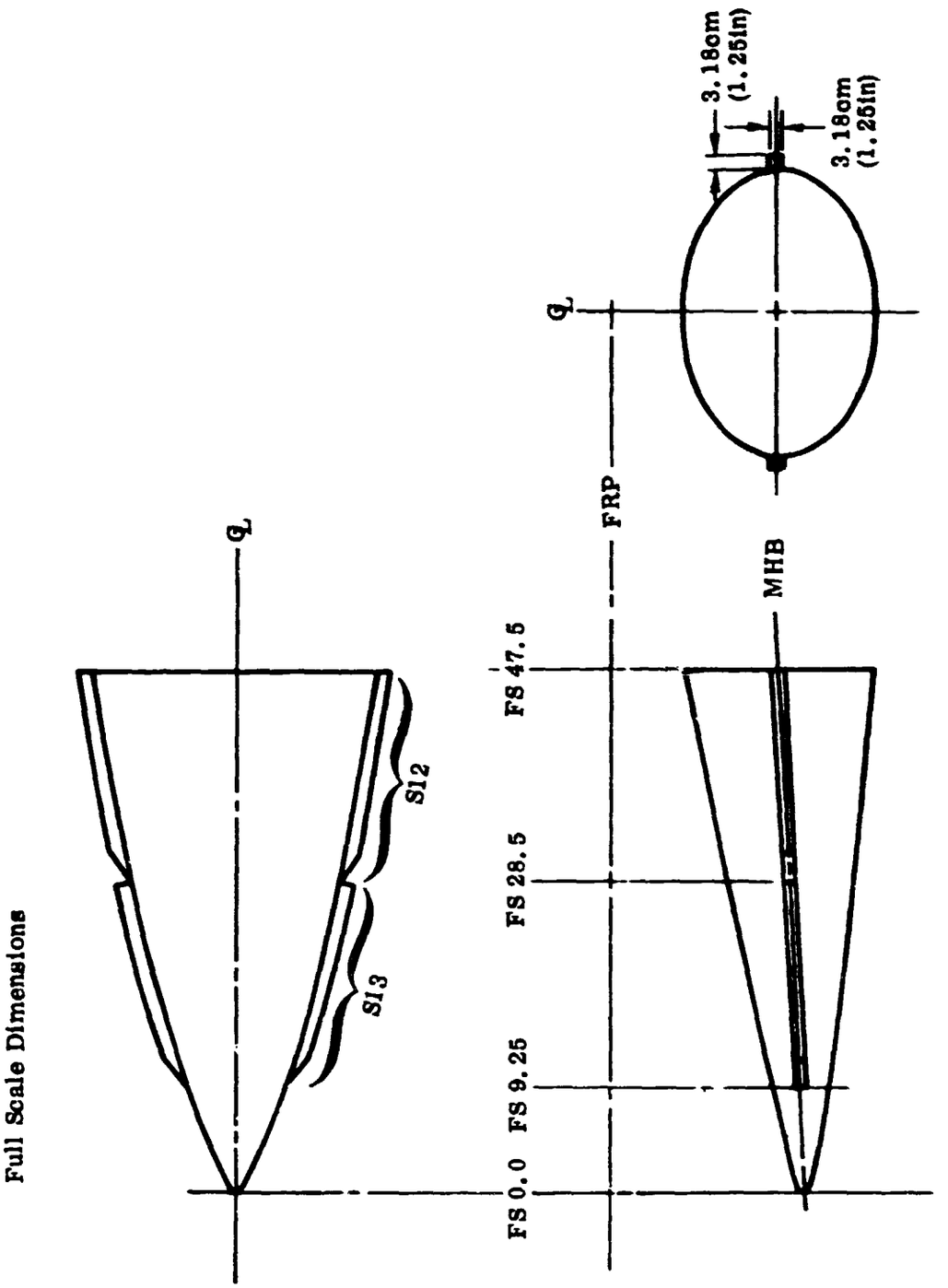

FIGURE 51. F-5F STRAKE S12 AND S13 GEOMETRY

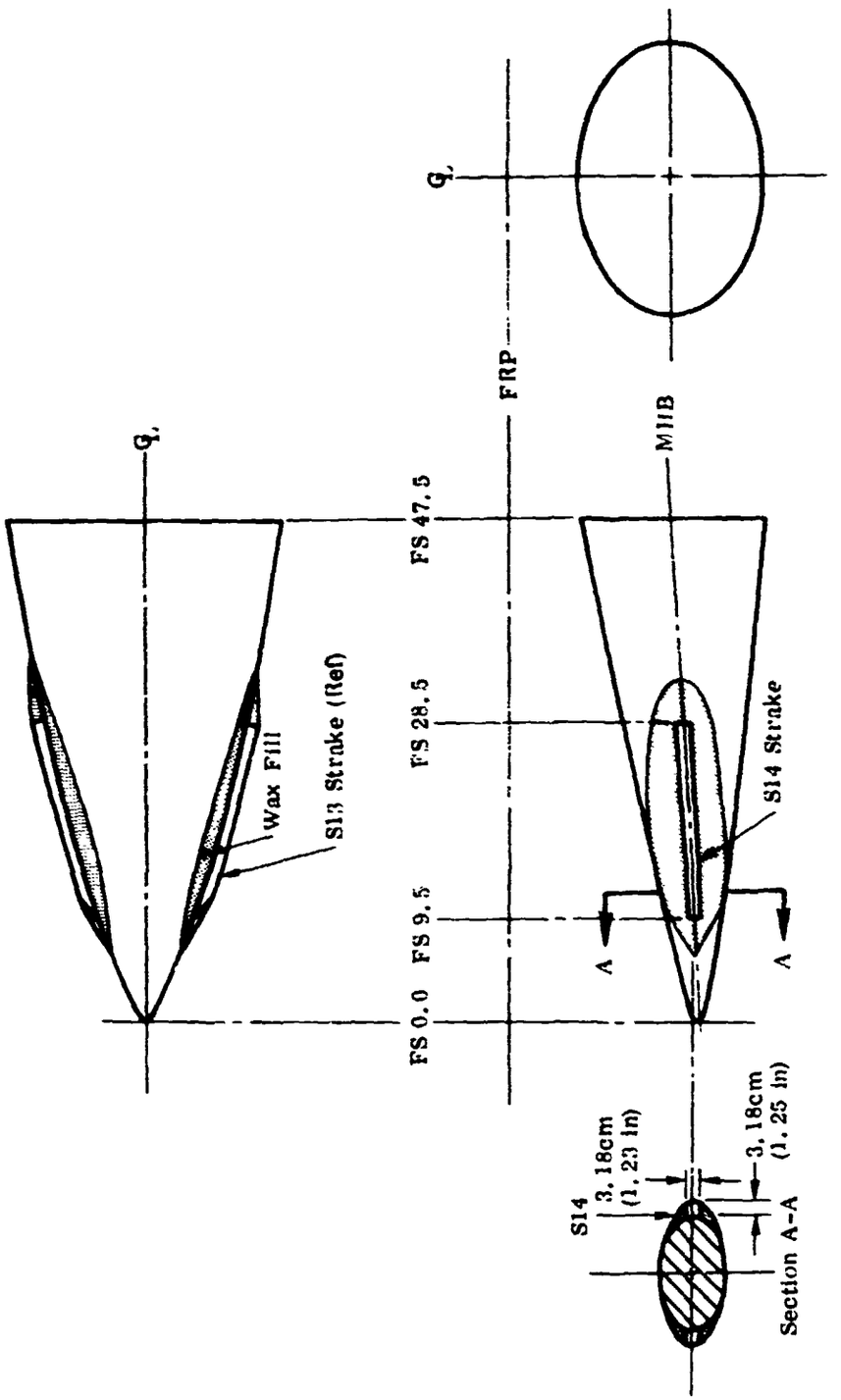

FIGURE 52. F-5F STRAKE S14 GEOMETRY

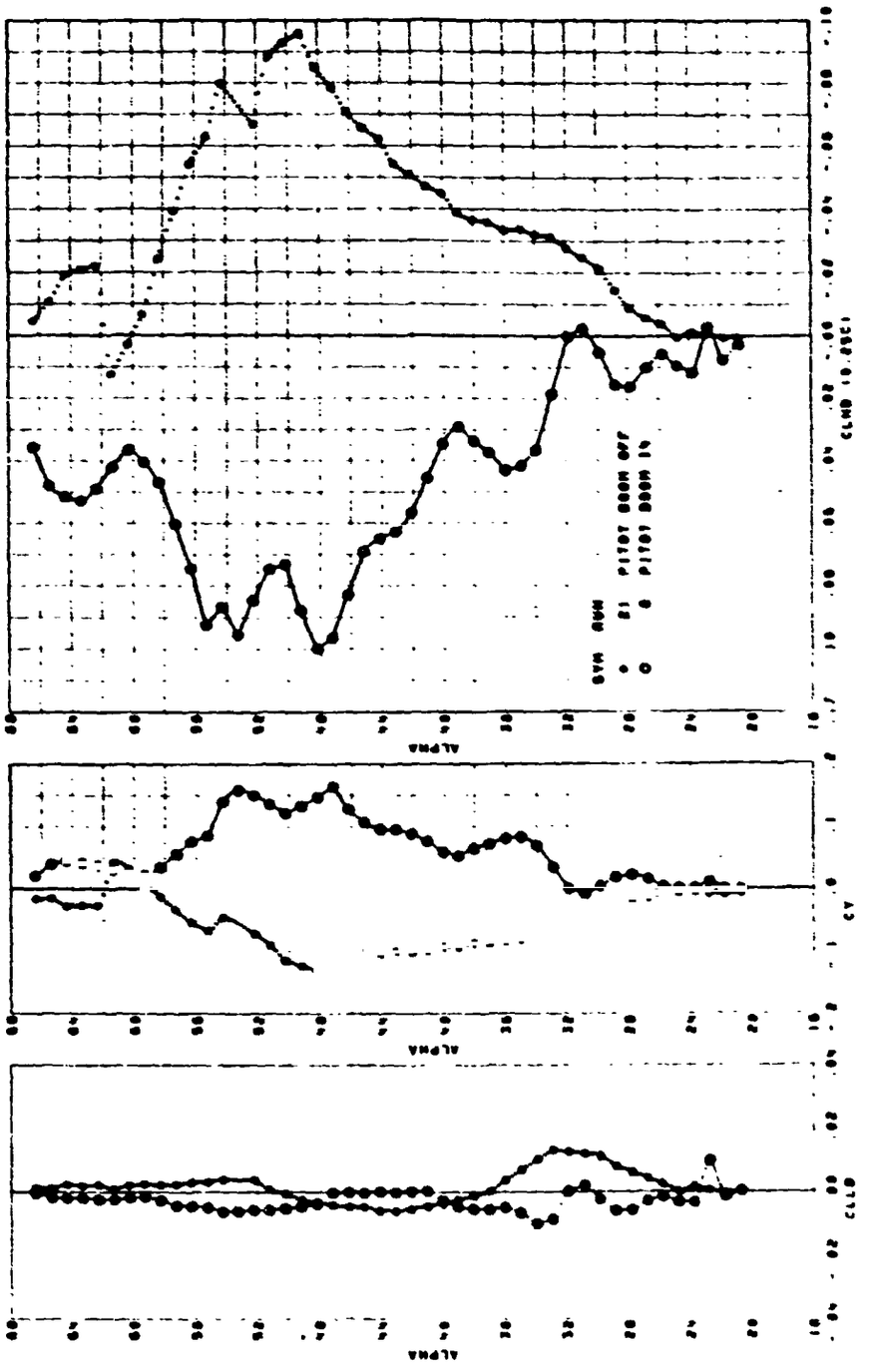

FIGURE 53. F-5F CLEAN CONFIGURATION. EFFECT OF PITOT BOOM i4 AT ZERO SIDESLIP, LAT/DIR DATA

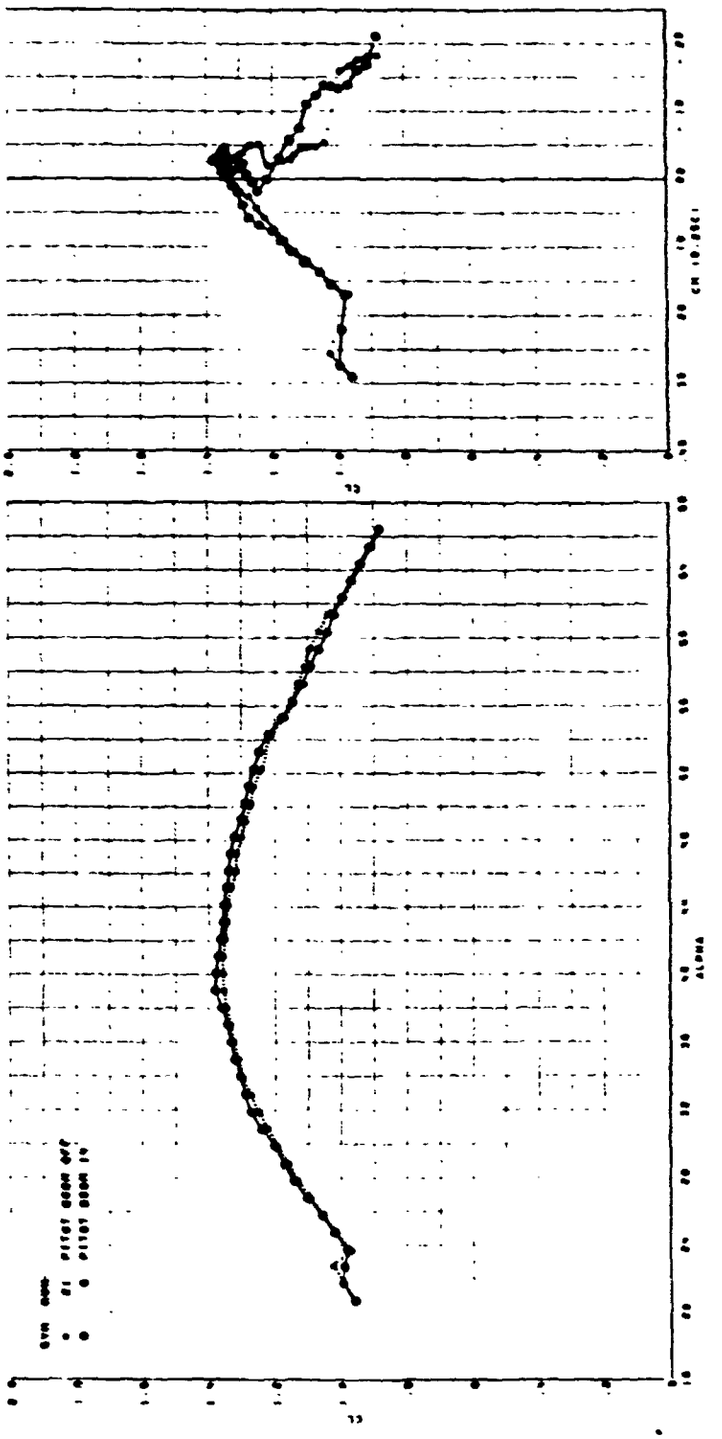

FIGURE 54. F-5F CLEAN CONFIGURATION. EFFECT OF PITOT BOOM i4 AT ZERO SIDESLIP, LIFT AND PITCH DATA

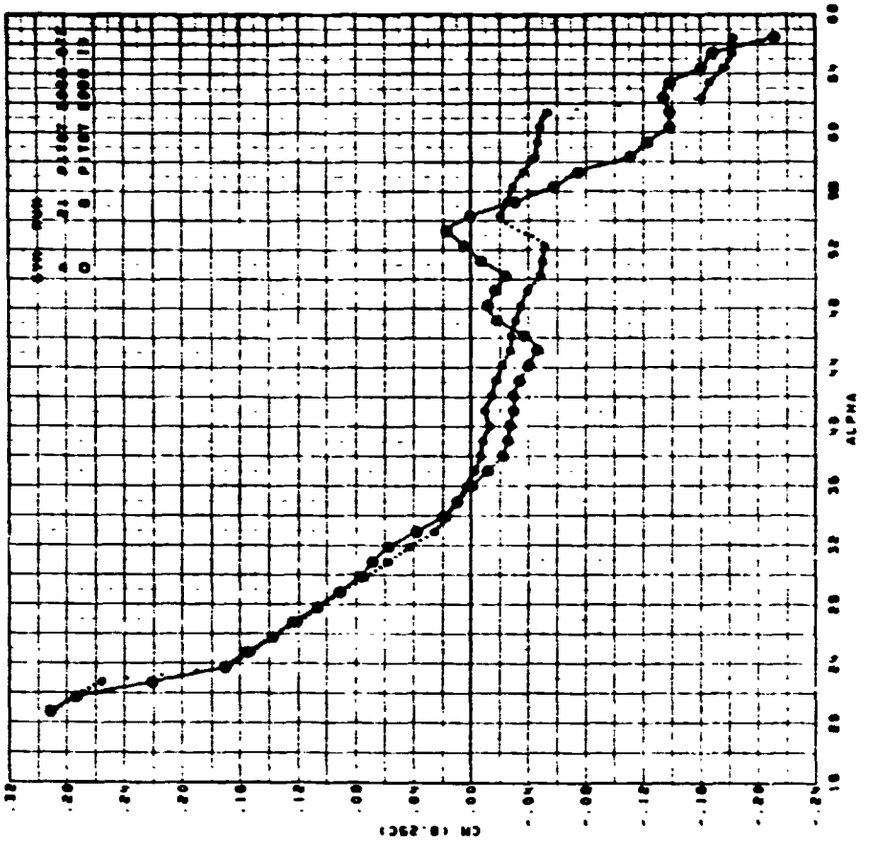

FIGURE 55. F-5F CLEAN CONFIGURATION. EFFECT OF PITOT BOOM i4 AT ZERO SIDESLIP, PITCHING MOMENT DATA

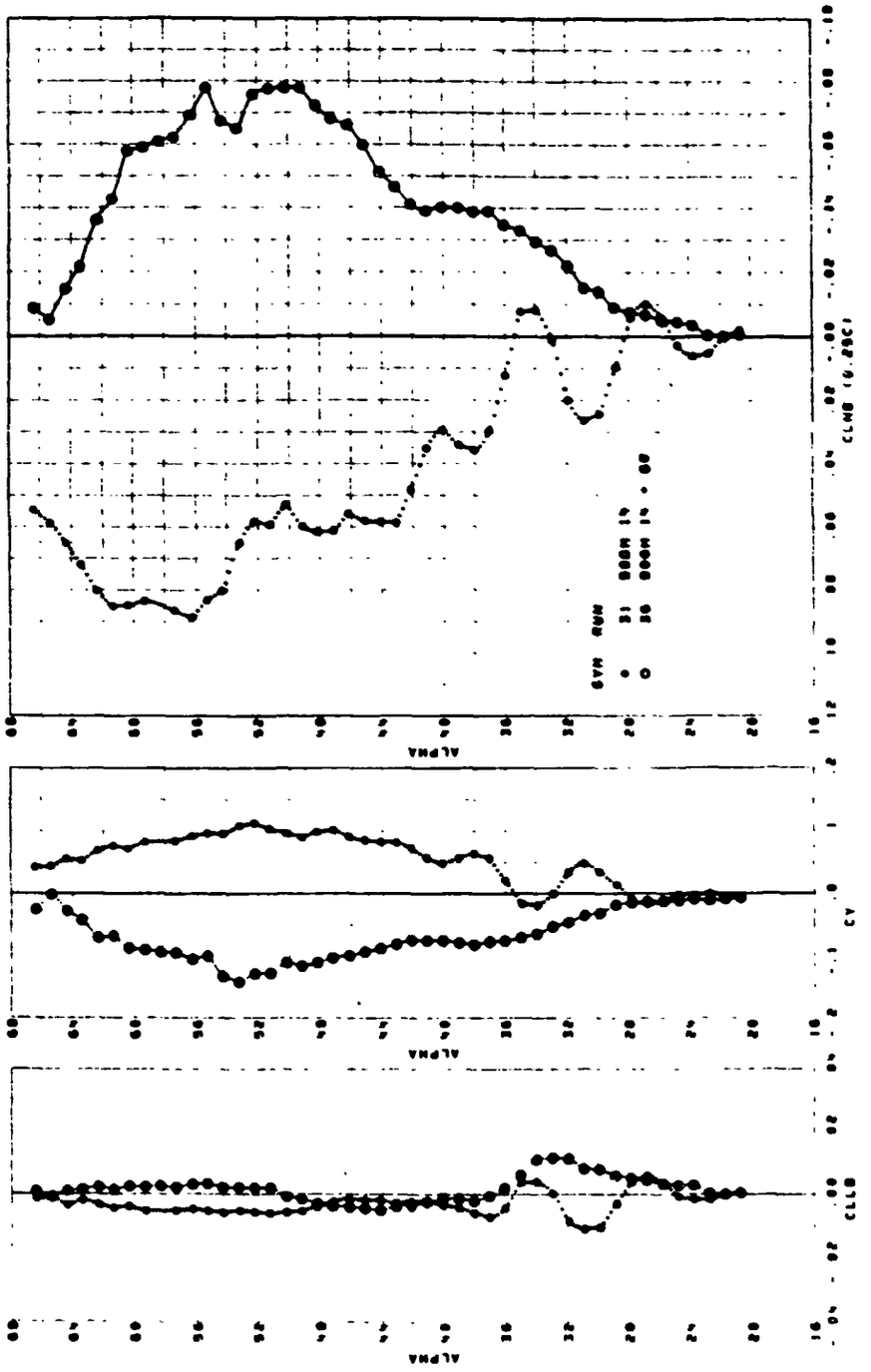

FIGURE 56. F-5F CLEAN CONFIGURATION. EFFECT OF STRAKE S7 AT ZERO SIDESLIP, LAT/DIR DATA

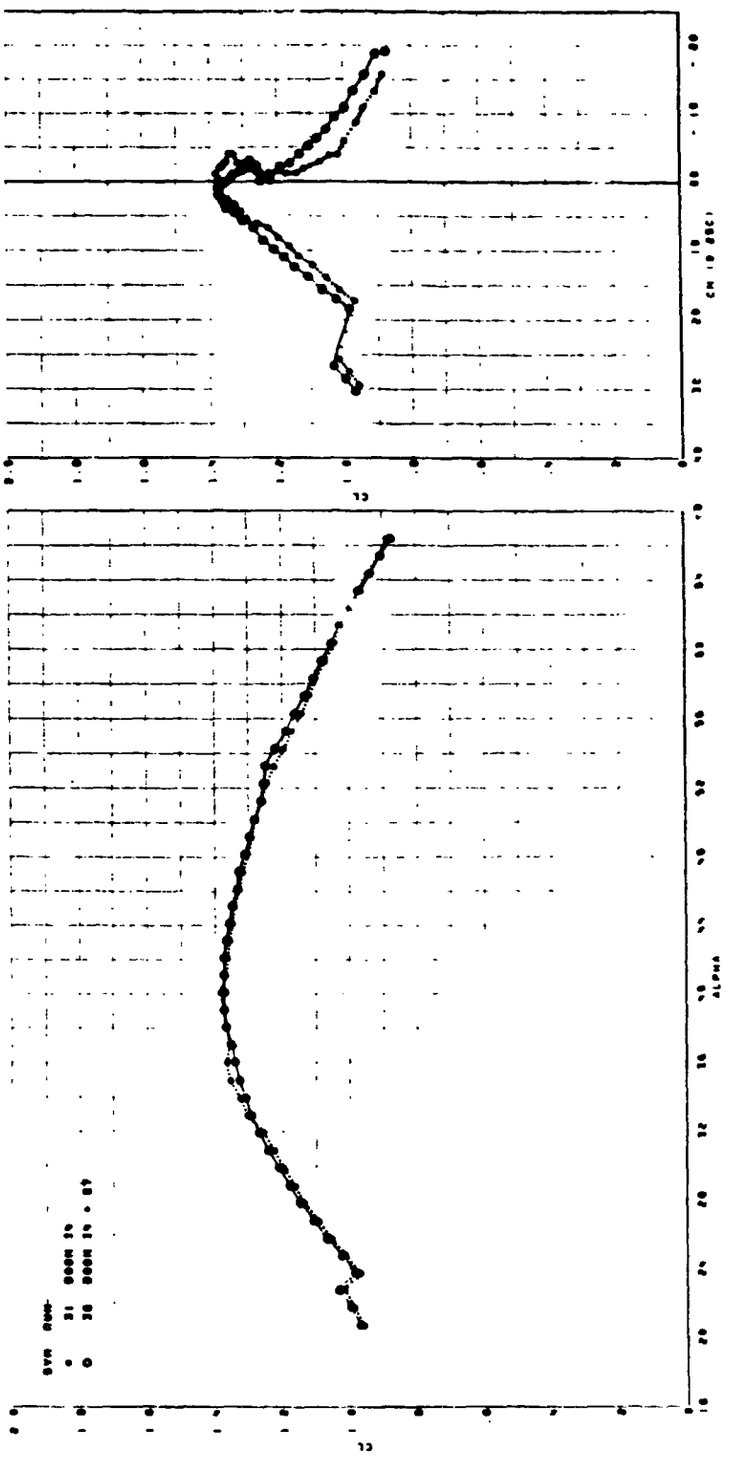

FIGURE 57. F-5F CLEAN CONFIGURATION. EFFECT OF STRAKE S7 AT ZERO SIDESLIP, LIFT AND PITCH DATA

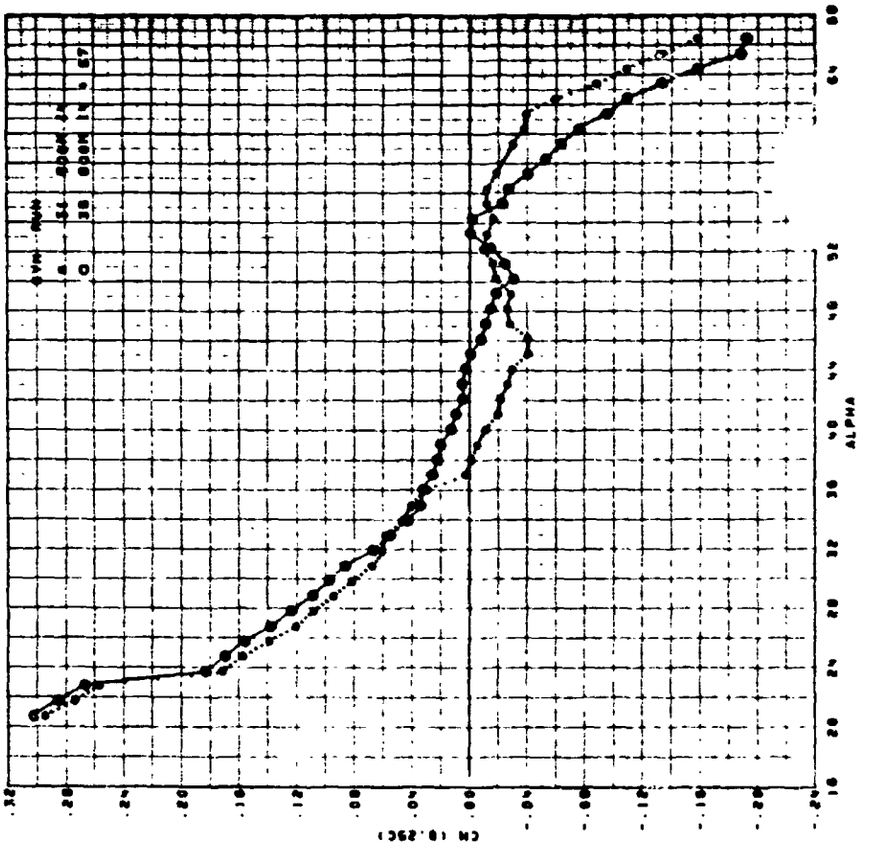

FIGURE 58. F-5F CLEAN CONFIGURATION EFFECT OF STRAKE S7 AT ZERO SIDESLIP, PITCHING MOMENT DATA

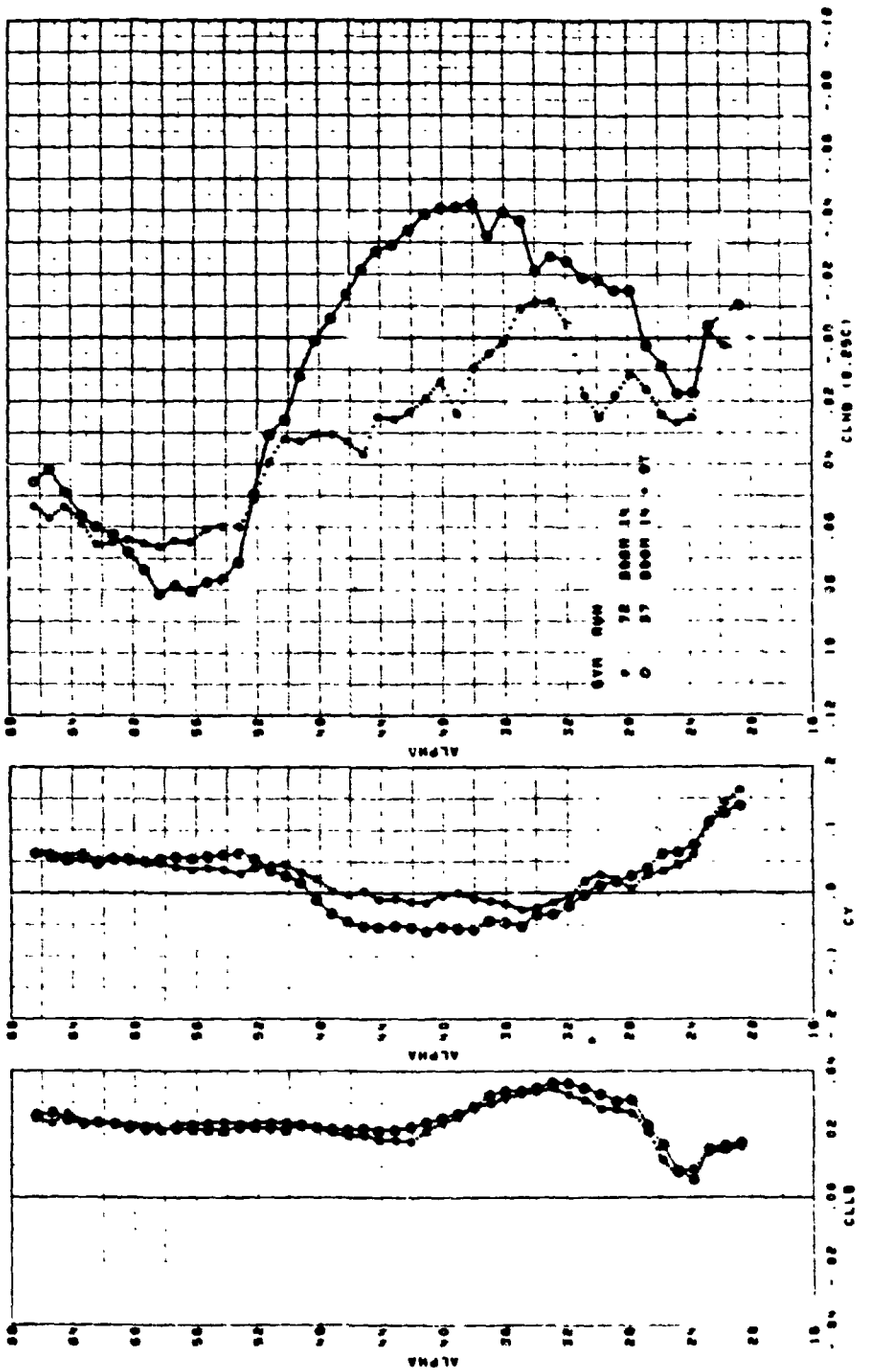

FIGURE 59. F-5F CLEAN CONFIGURATION. EFFECT OF STRAKE S7 AT -10^{O} SIDESLIP, LAT/DIR DATA

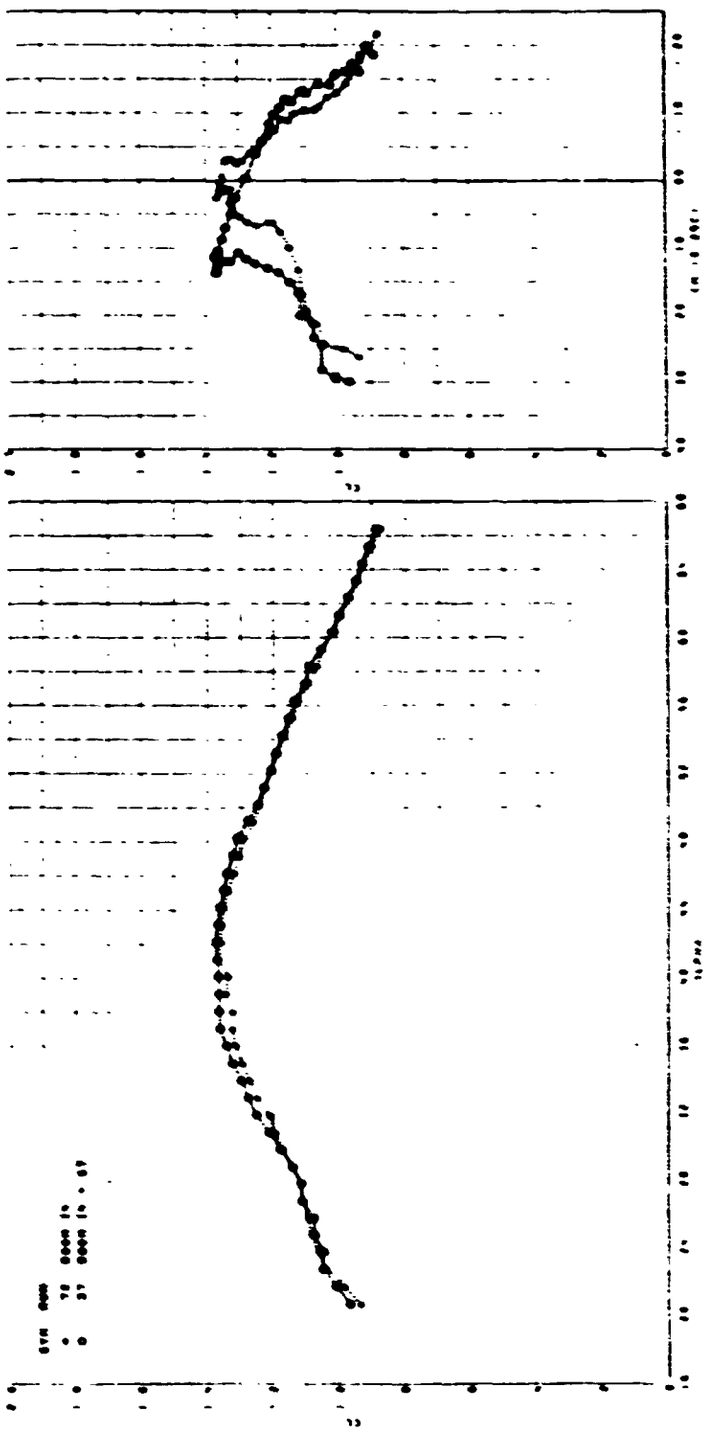

FIGURE 60. F-5F CLEAN CONFIGURATION. EFFECT OF STRAKE AT -10° SIDESLIP. LIFT AND PITCH DATA

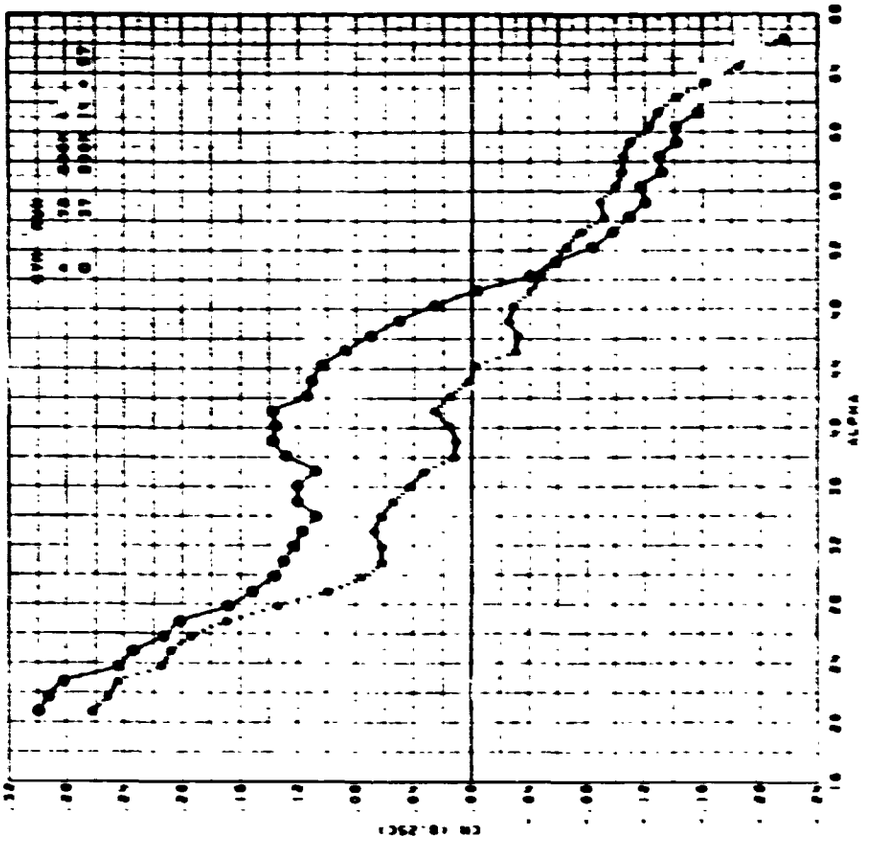

FIGURE 61. F-5F CLEAN CONFIGURATION. EFFECT OF STRAKE S7 AT -10° SIDESLIP, PITCHING MOMENT DATA

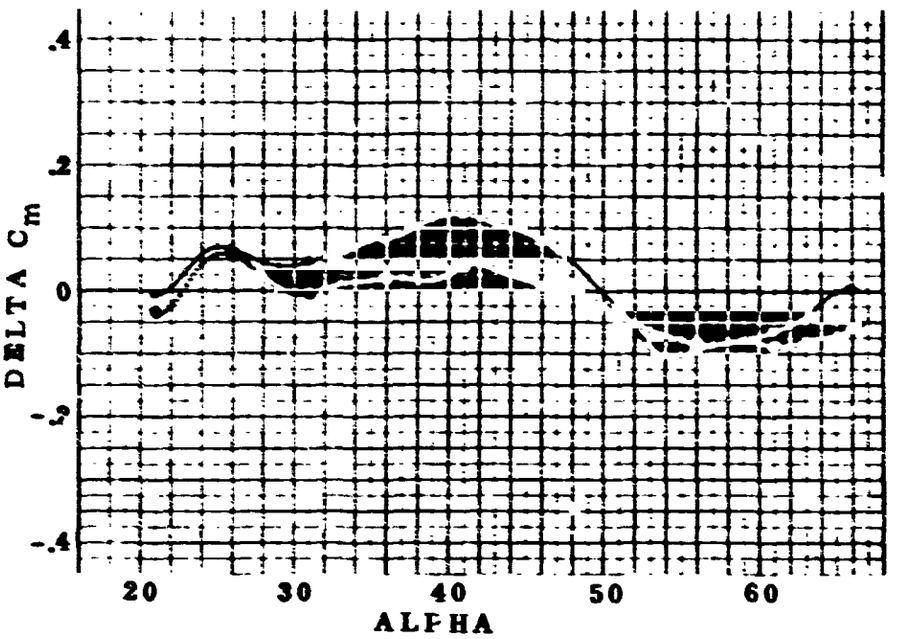

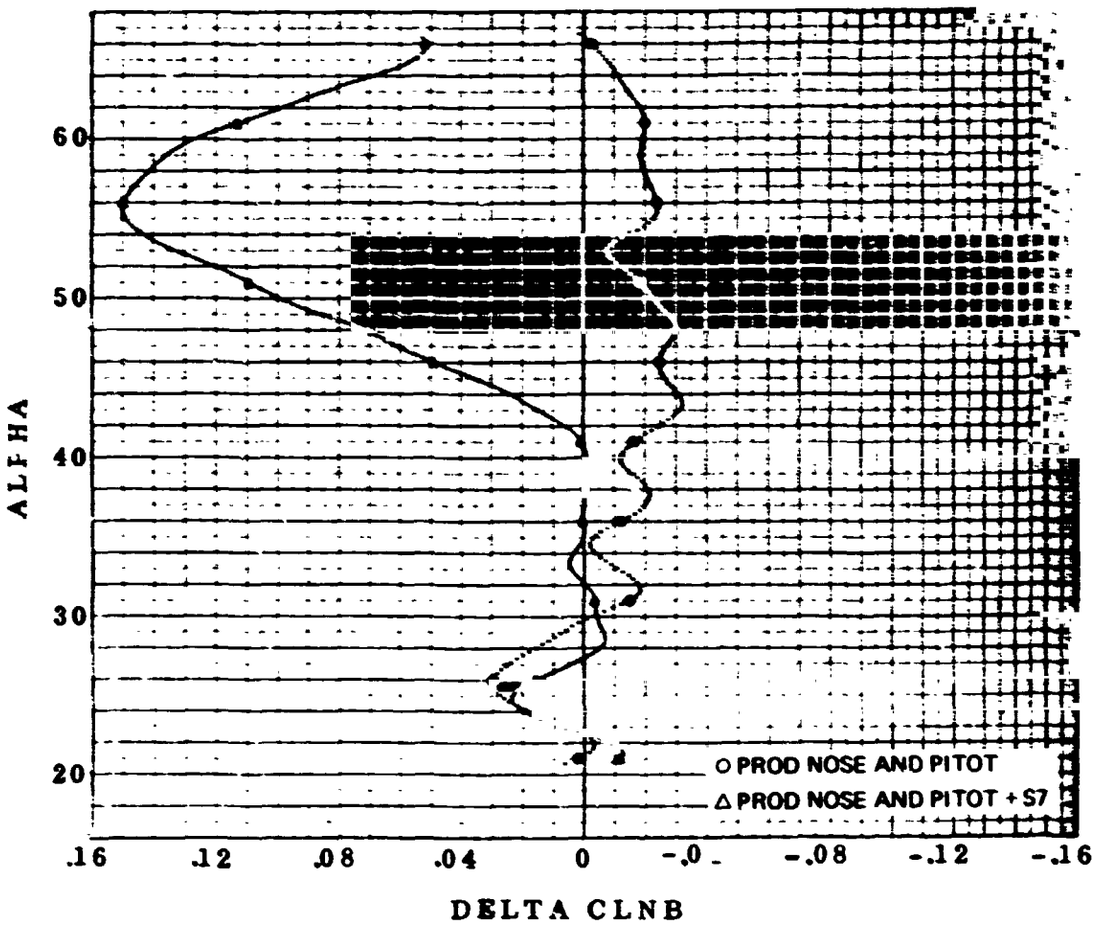

FIGURE 62. F-5F CLEAN CONFIGURATION. EFFECT OF STRAKE S7 ON INCREMENTAL C_n AND C_m DUE TO -10° SIDESLIP

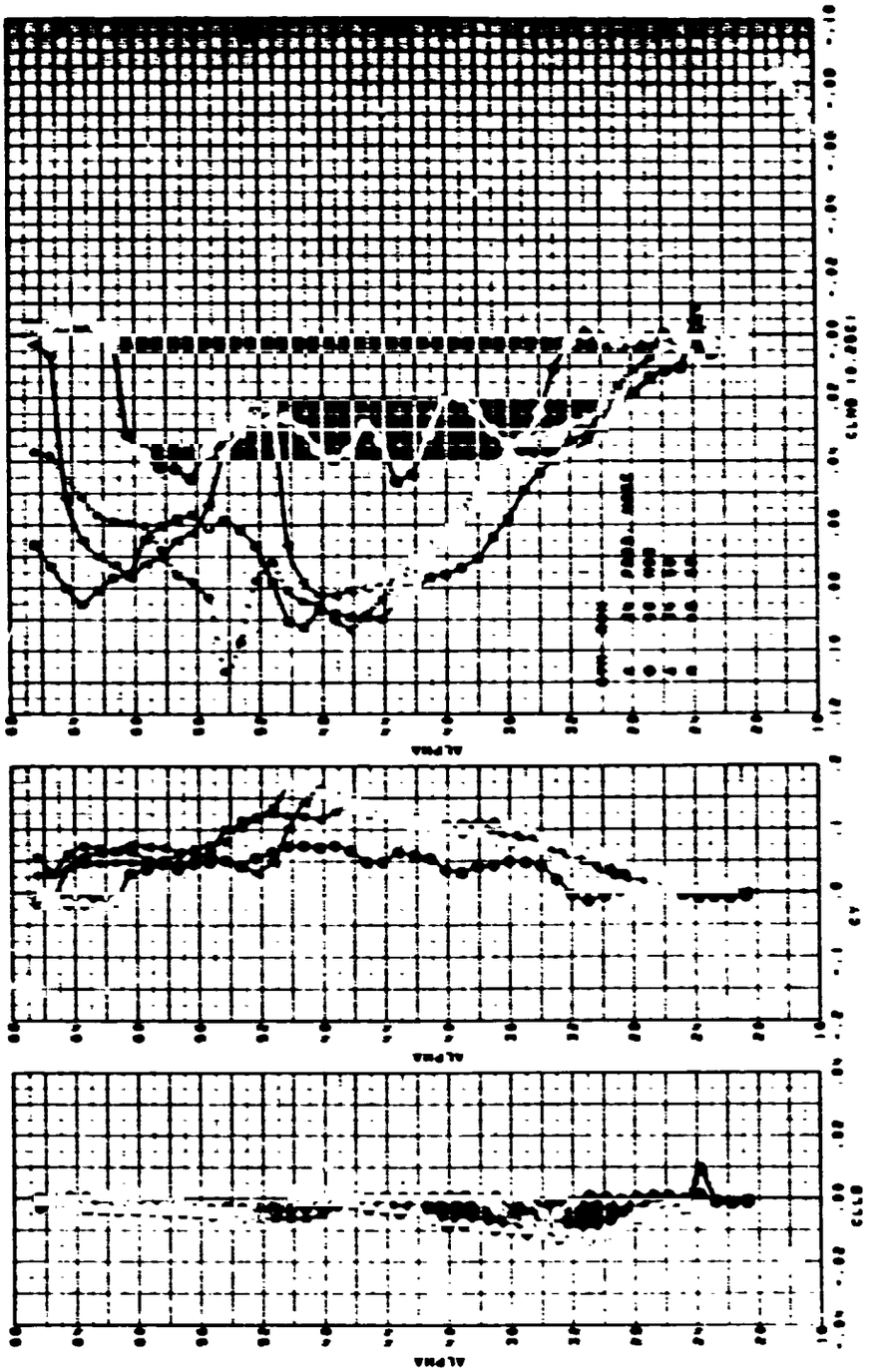

FIGURE 63. F-5F CLEAN CONFIGURATION. EFFECT OF STRAKES M63, S8 AND S9 AT ZERO SIDESLIP, LAT/DIR DATA

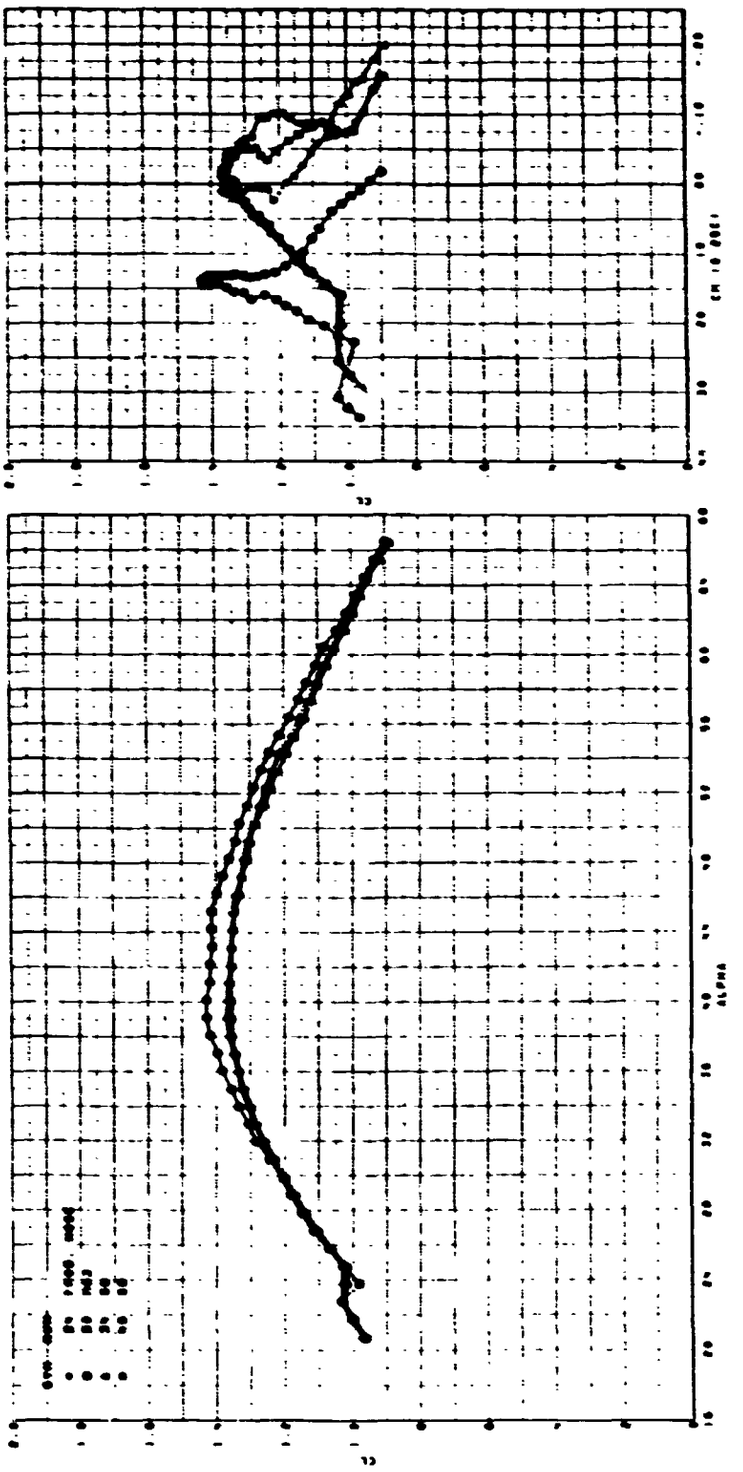

FIGURE 64. F-5F CLEAN CONFIGURATION. EFFECT OF STRAKES M03, S8 AND S9 AT ZERO SIDESLIP. LIFT AND PITCH DATA

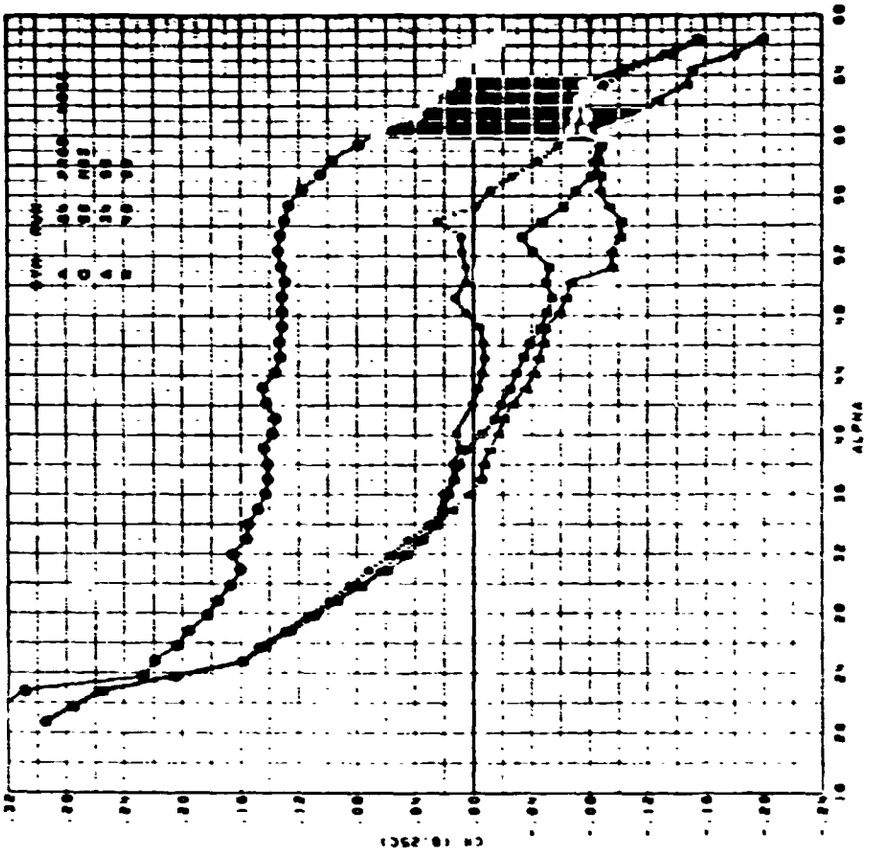

FIGURE 65. F-5F CLEAN CONFIGURATION. EFFECT OF STRAKES M63, S8 AND S9 AT ZERO SIDESLIP, PITCHING MOMENT DATA

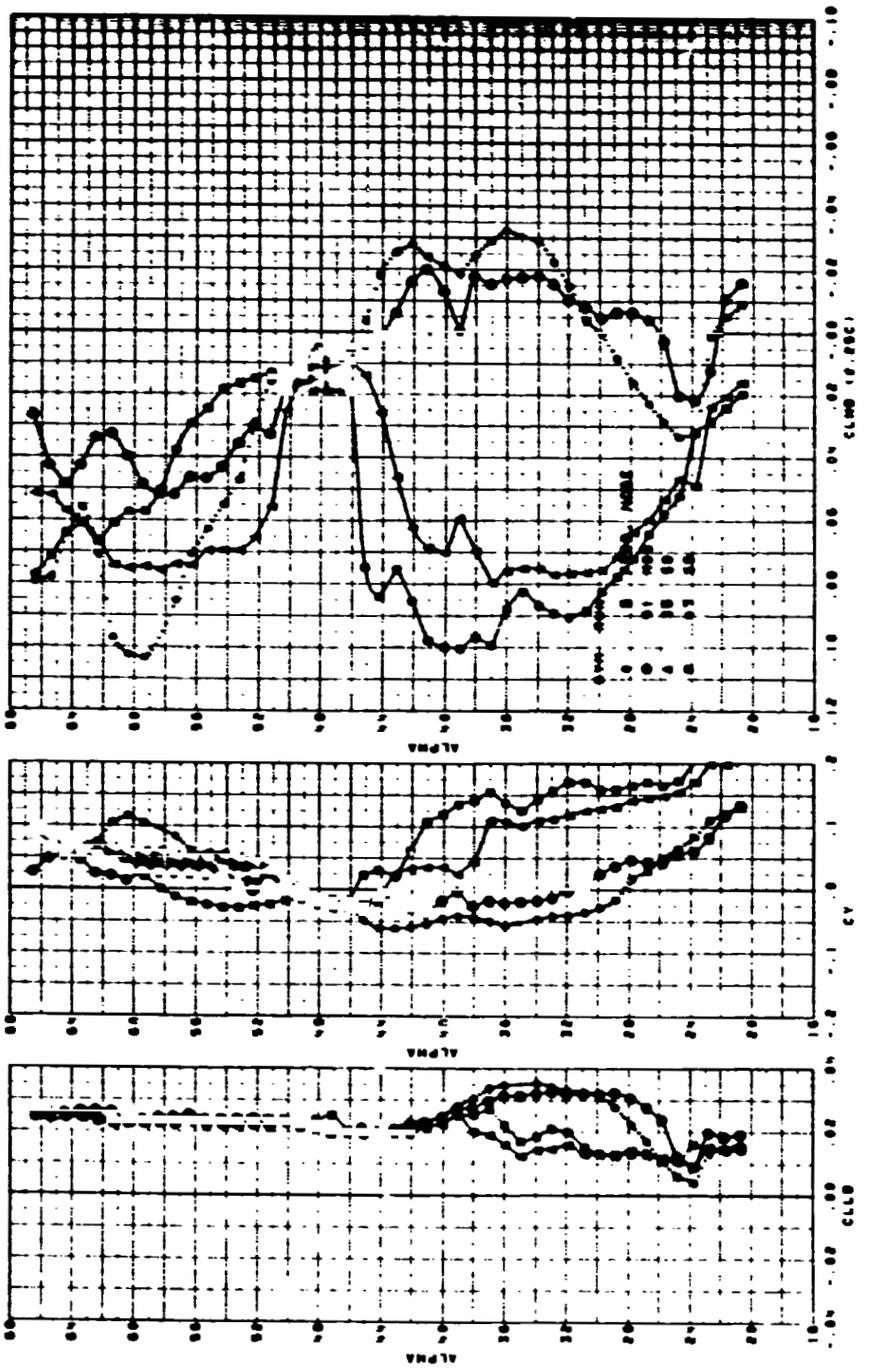

FIGURE 66. F-5F CLEAN CONFIGURATION. EFFECT OF STRAKES M63, S3 AND S9 AT -10° SIDESLIP, LAT/DIR DATA

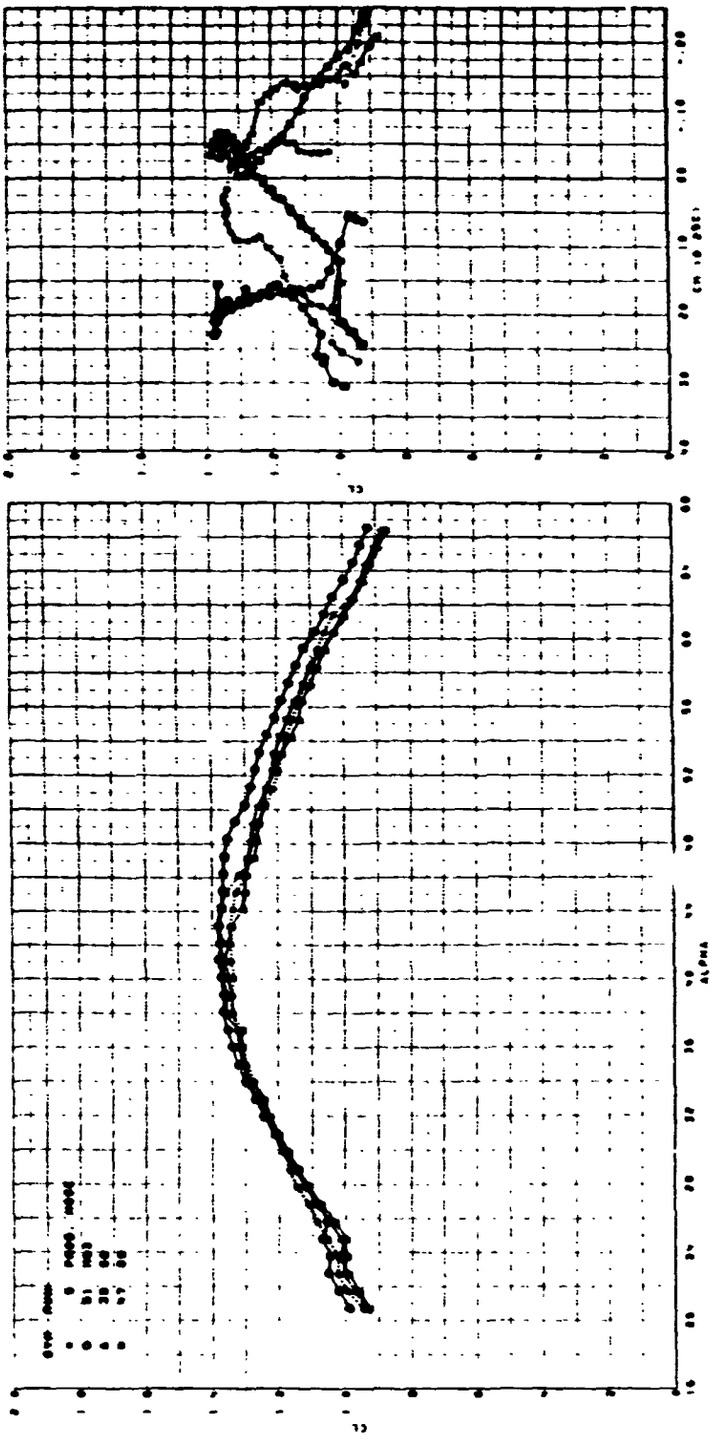

FIGURE 67. F-5F CLEAN CONFIGURATION. EFFECT OF STRAKES M63, S8 AND S9 AT -10^{o} SIDESLIP, LIFT AND PITCH DATA

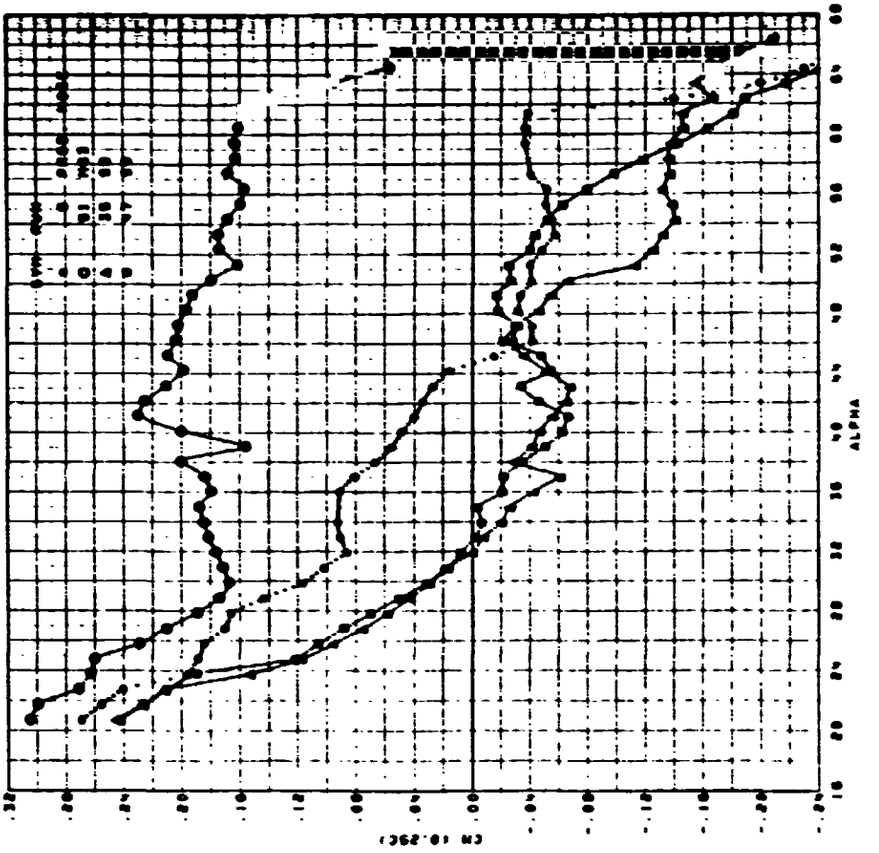

FIGURE 68. F-5F CLEAN CONFIGURATION. EFFECT OF STRAKES M63, S8 AND S9 AT -10^{O} SIDESLIP, PITCHING MOMENT DATA

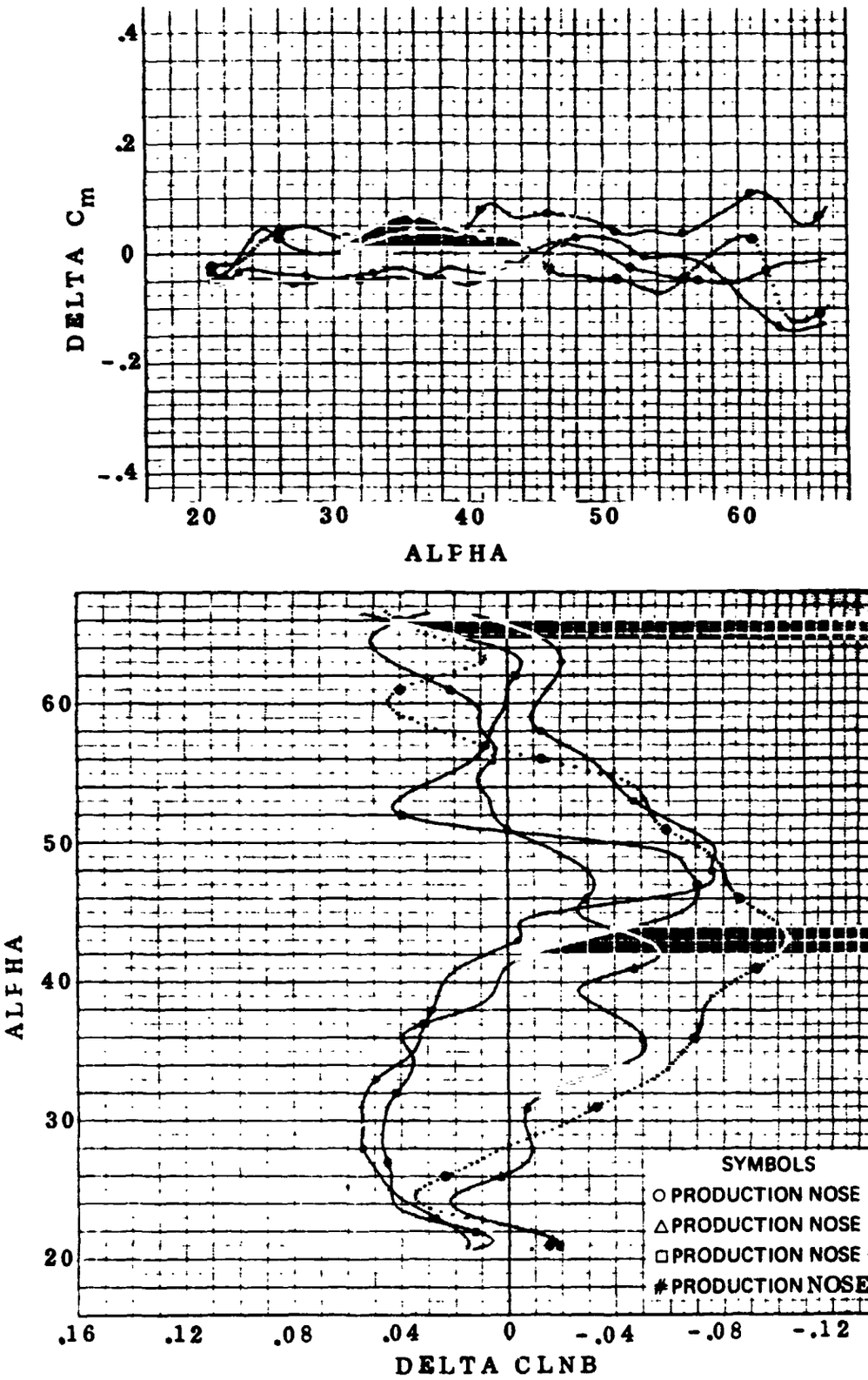

FIGURE 69. F-5F CLEAN CONFIGURATION. EFFECT OF STRAKES M63, S8 AND S9 ON INCREMENTAL C_n AND C_m DUE TO -10^o SIDESLIP

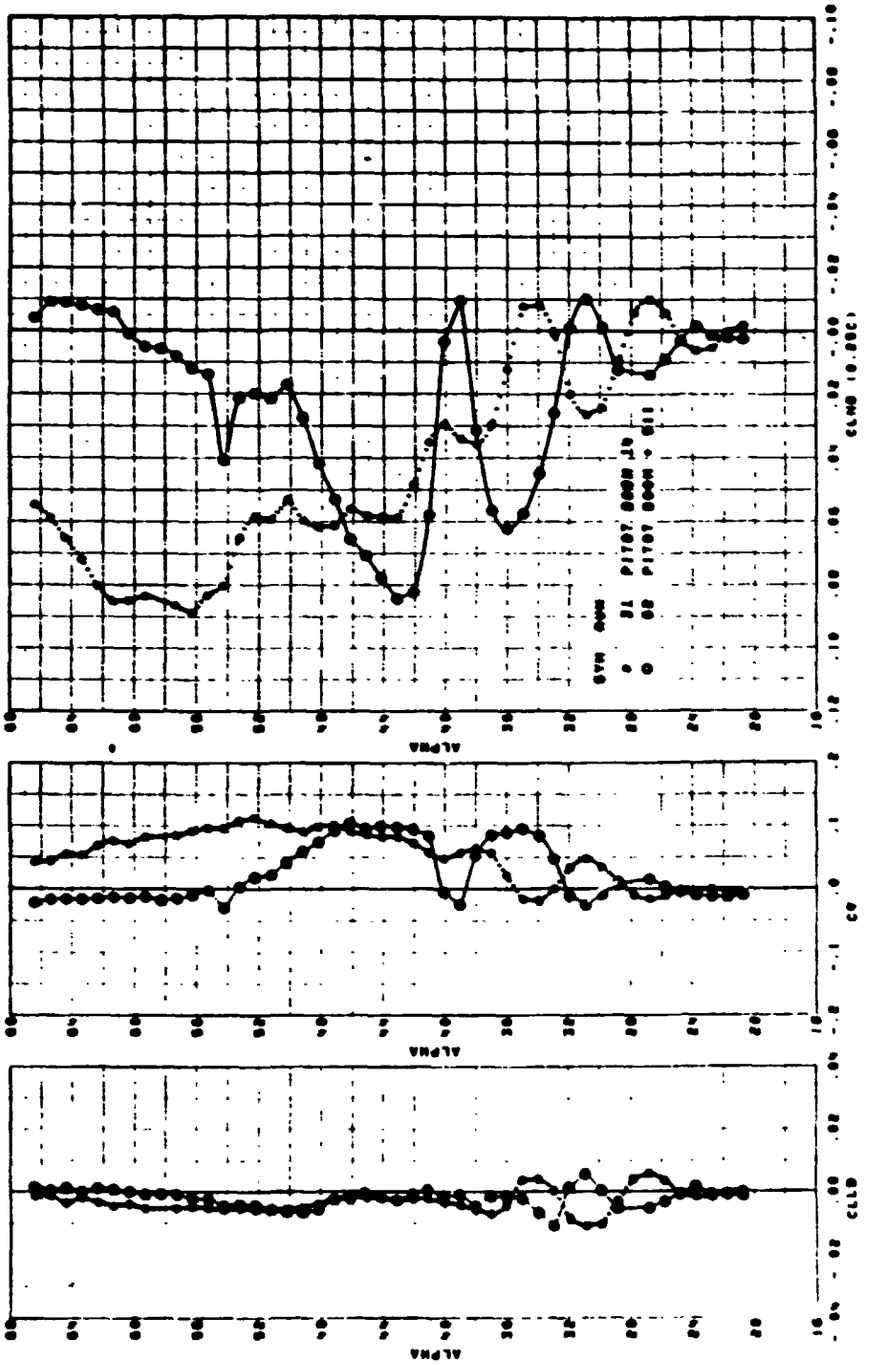

FIGURE 70. F-5F CLEAN CONFIGURATION. EFFECT OF STRAKE S11 AT ZERO SIDESLIP, LAT/DIR DATA

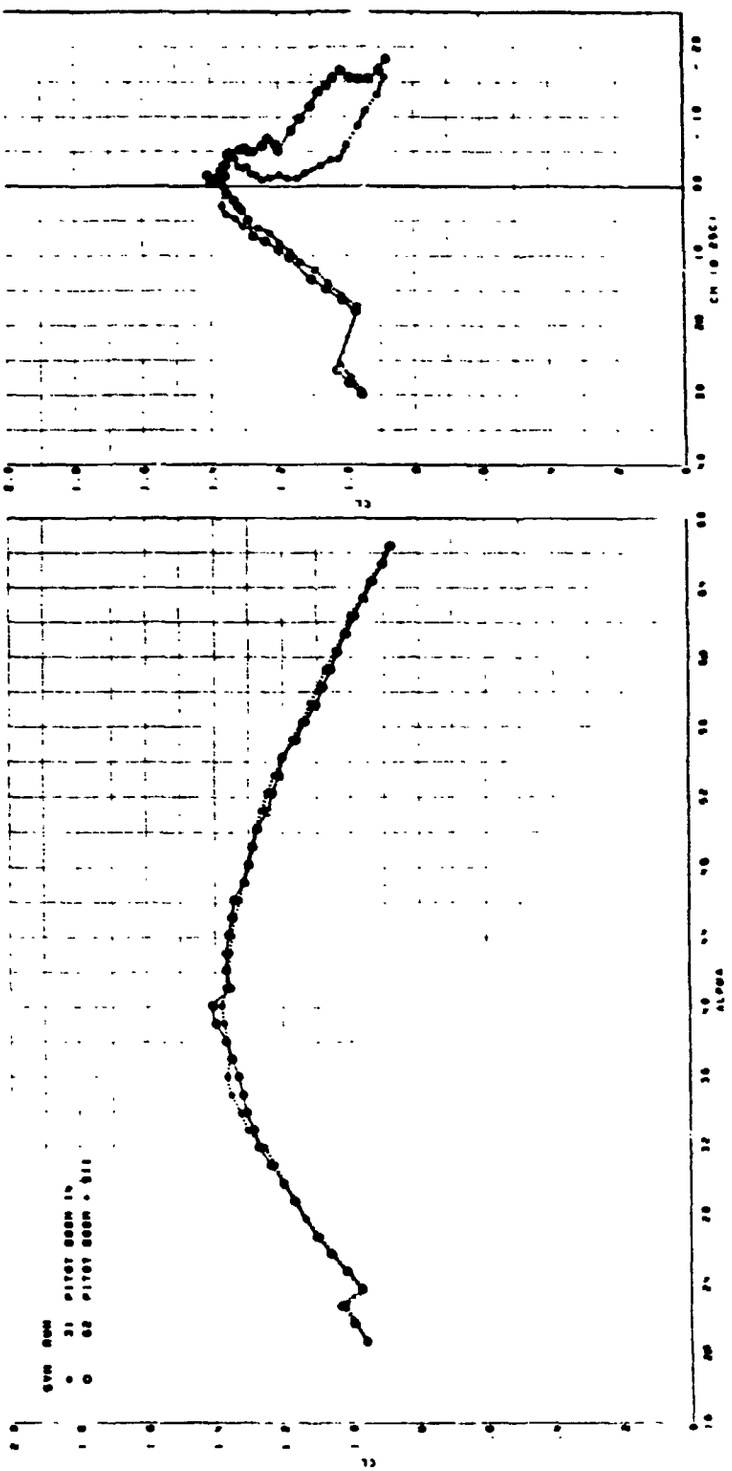

FIGURE 71. F-5F CLEAN CONFIGURATION. EFFECT OF STRAKE S11 AT ZERO SIDESLIP, LIFT AND PITCH DATA

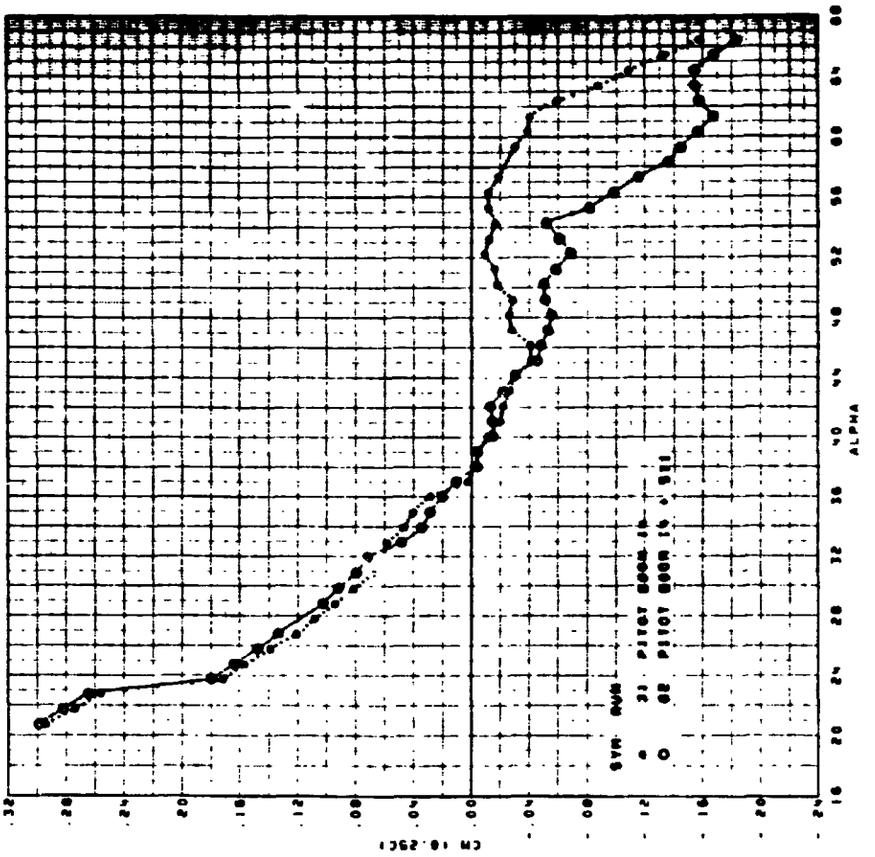

FIGURE 72. F-5F CLEAN CONFIGURATION. EFFECT OF STRAKE S11 AT ZERO SIDESLIP, PITCHING MOMENT DATA

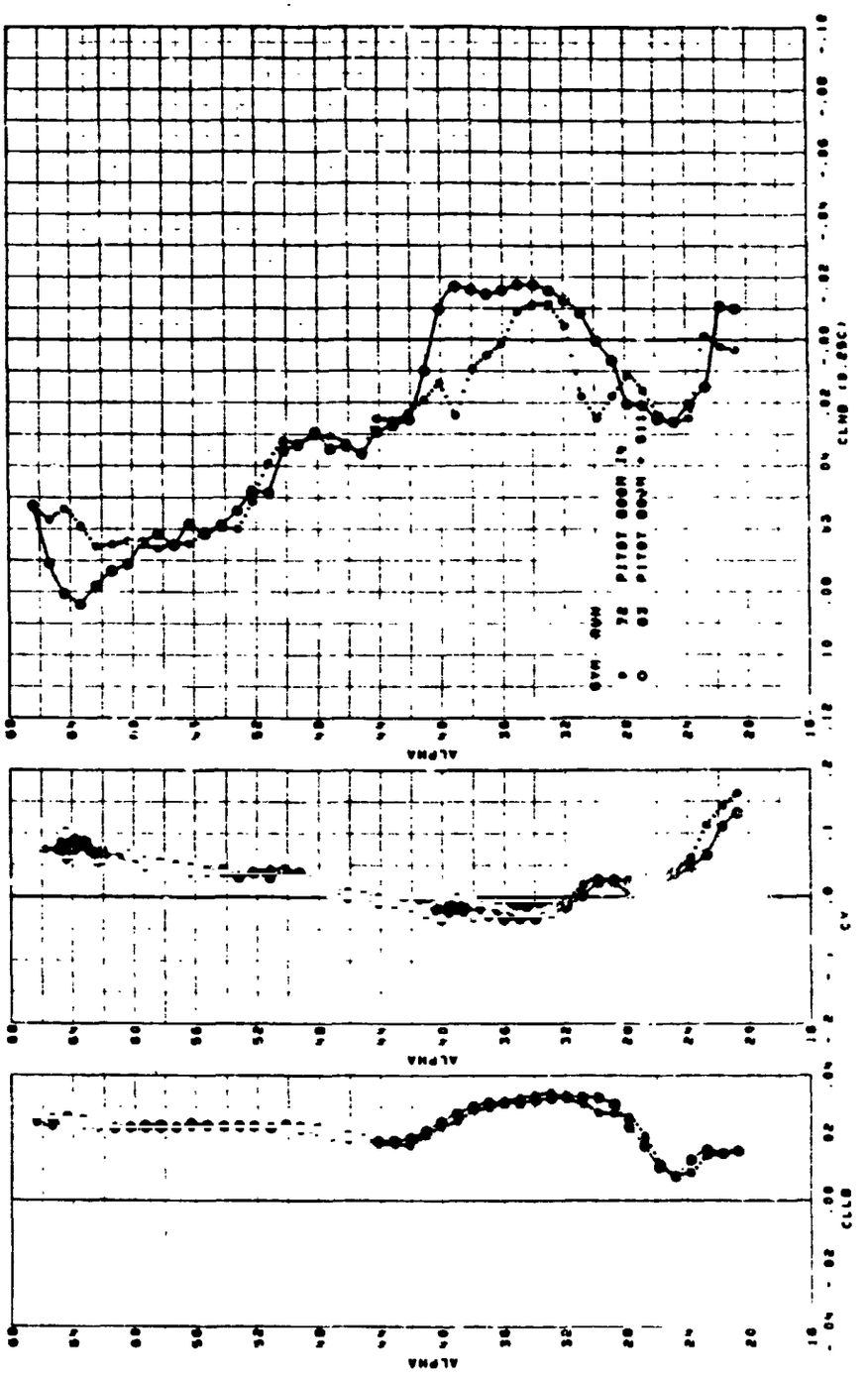

FIGURE 73. F-5F CLEAN CONFIGURATION. EFFECT OF STRAKE S11 AT -10° SIDESLIP, LAT/DIR DATA

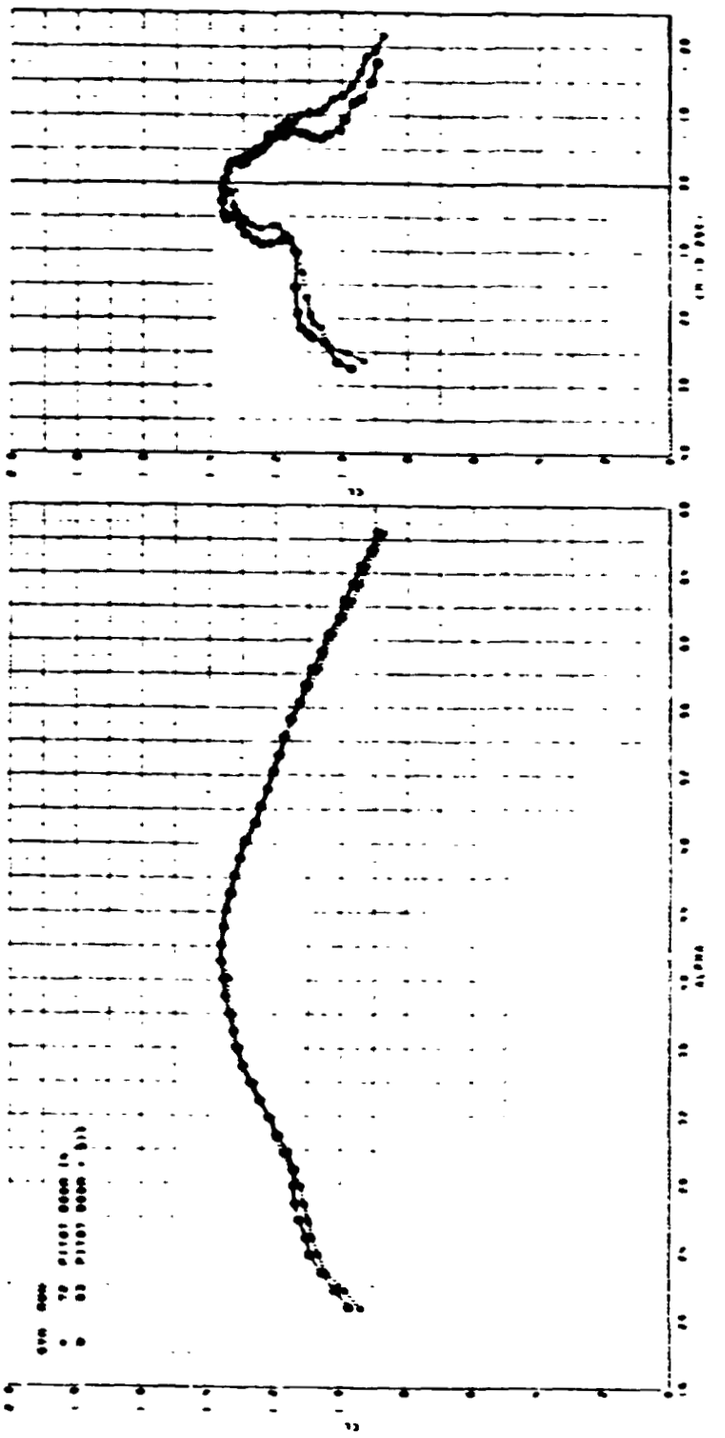

FIGURE 74. F-5F CLEAN CONFIGURATION. EFFECT OF STRAKE S11 AT -10° SIDESLIP, LIFT AND PITCH DATA

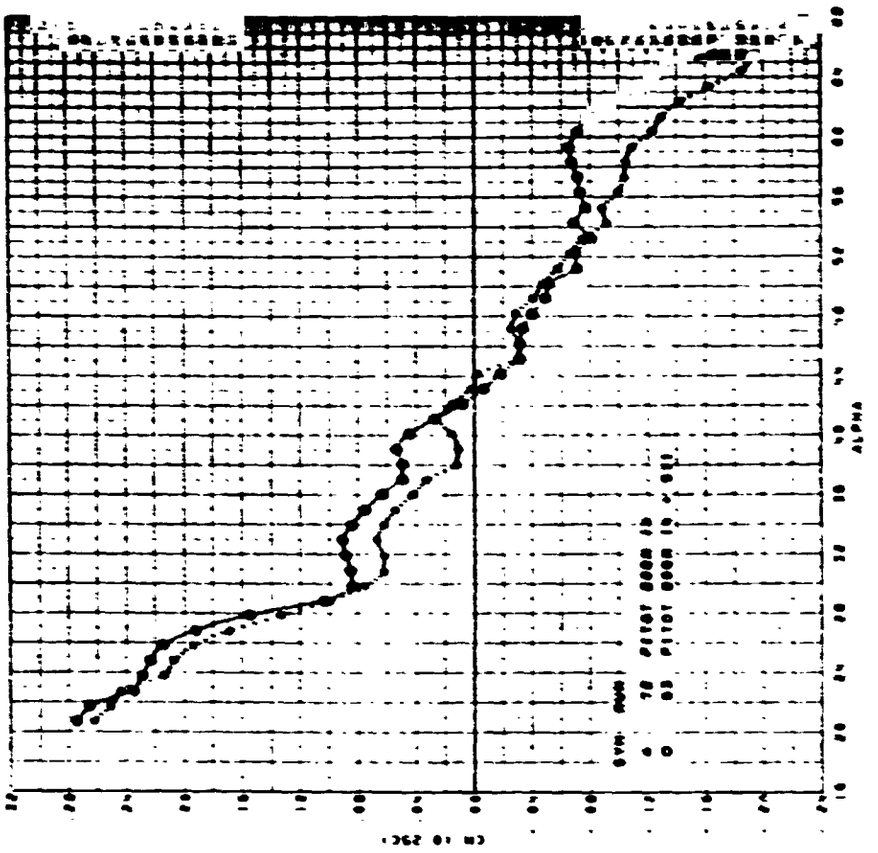

FIGURE 75. F-5F CLEAN CONFIGURATION. EFFECT OF STRAKE S11 AT -10° SIDESLIP, PITCHING MOMENT DATA

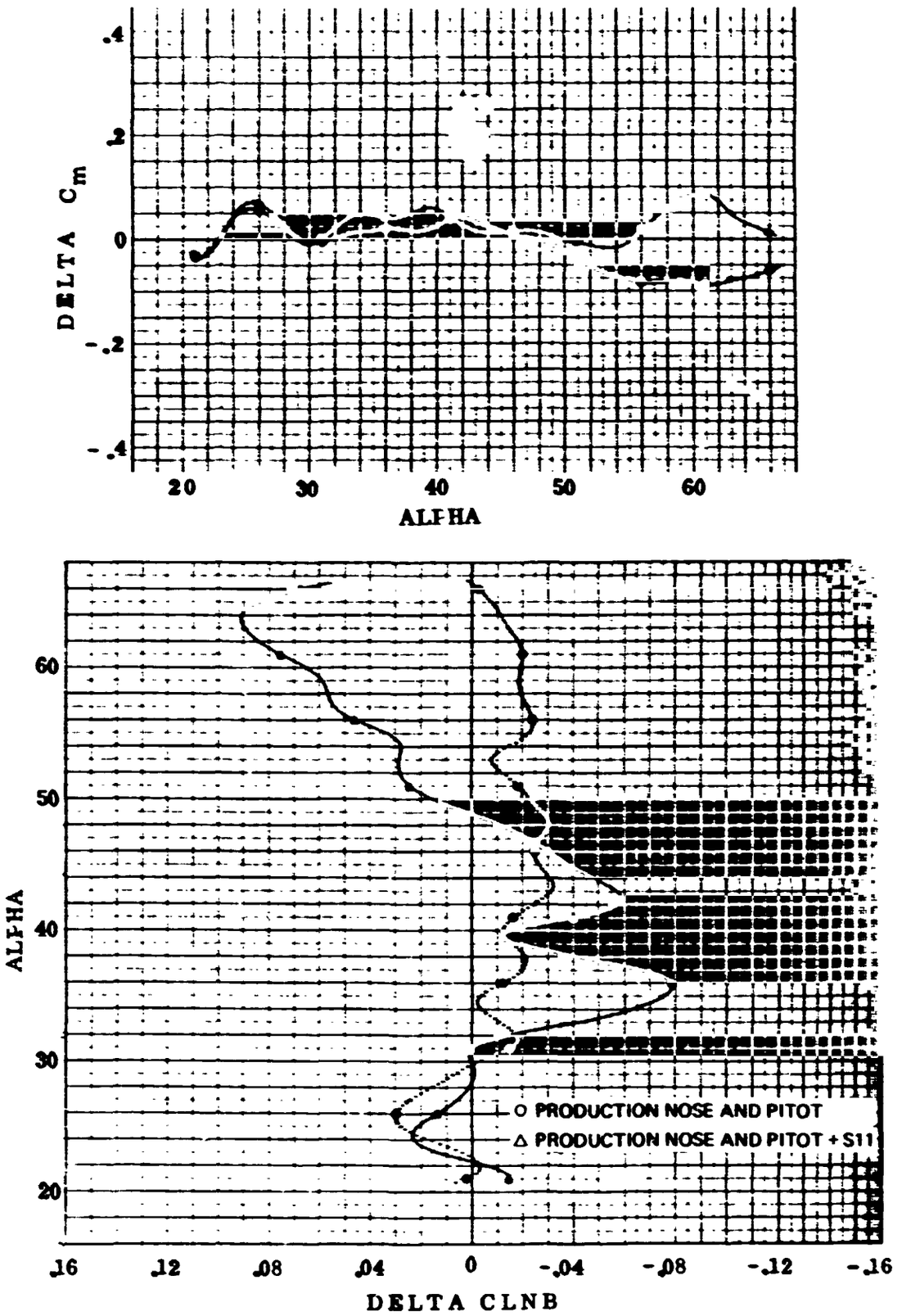

FIGURE 76. F-5F CLEAN CONFIGURATION. EFFECT OF STRAKE S11 ON INCREMENTAL C_n AND C_m DUE TO -10° SIDESLIP

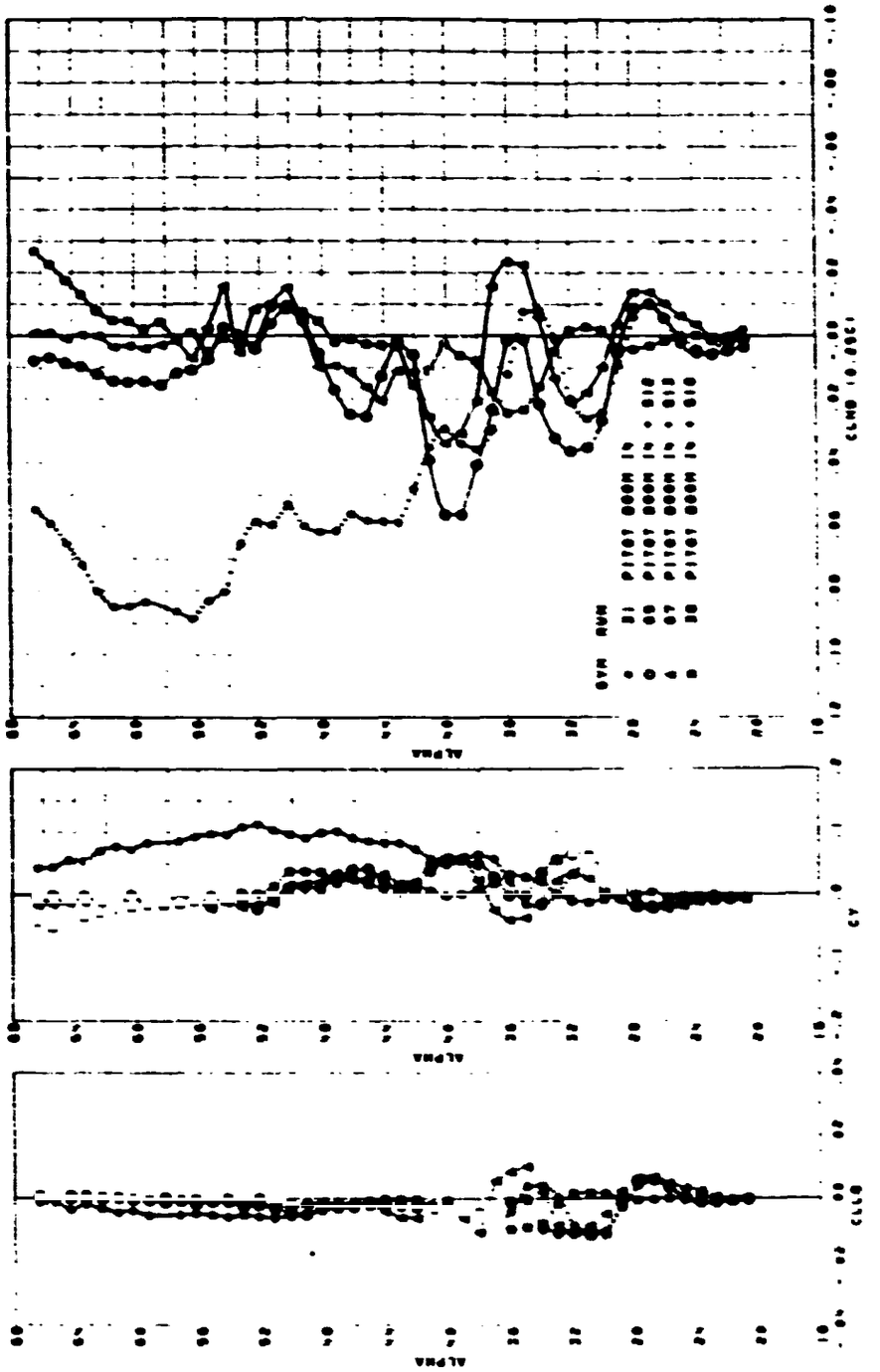

FIGURE 77. F-5F CLEAN CONFIGURATION. EFFECT OF STRAKES S10, S12 AND S13 AT ZERO SIDESLIP, LAT/DIR DATA

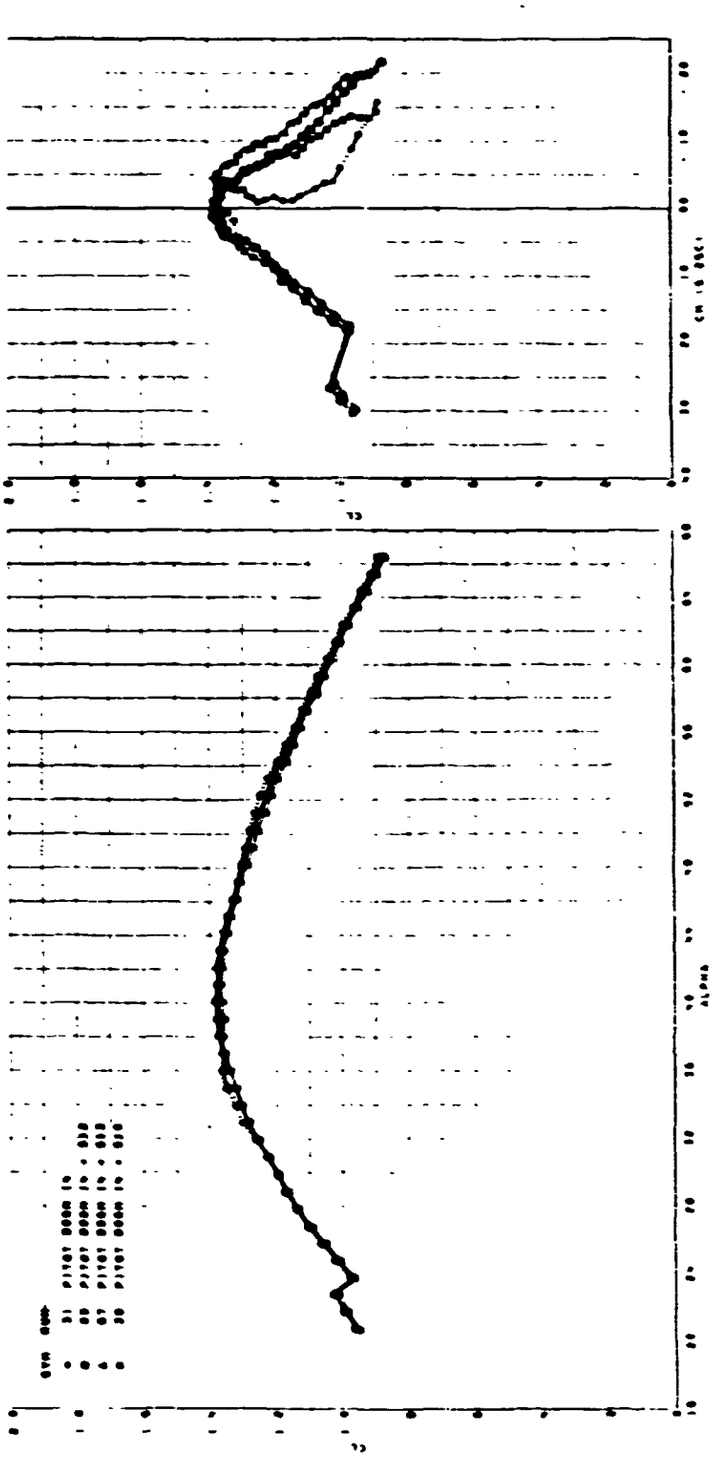

FIGURE 78. F-5F CLEAN CONFIGURATION. EFFECT OF STRAKES S10, S12 AND S13 AT ZERO SIDESLIP, LIFT AND PITCH DATA

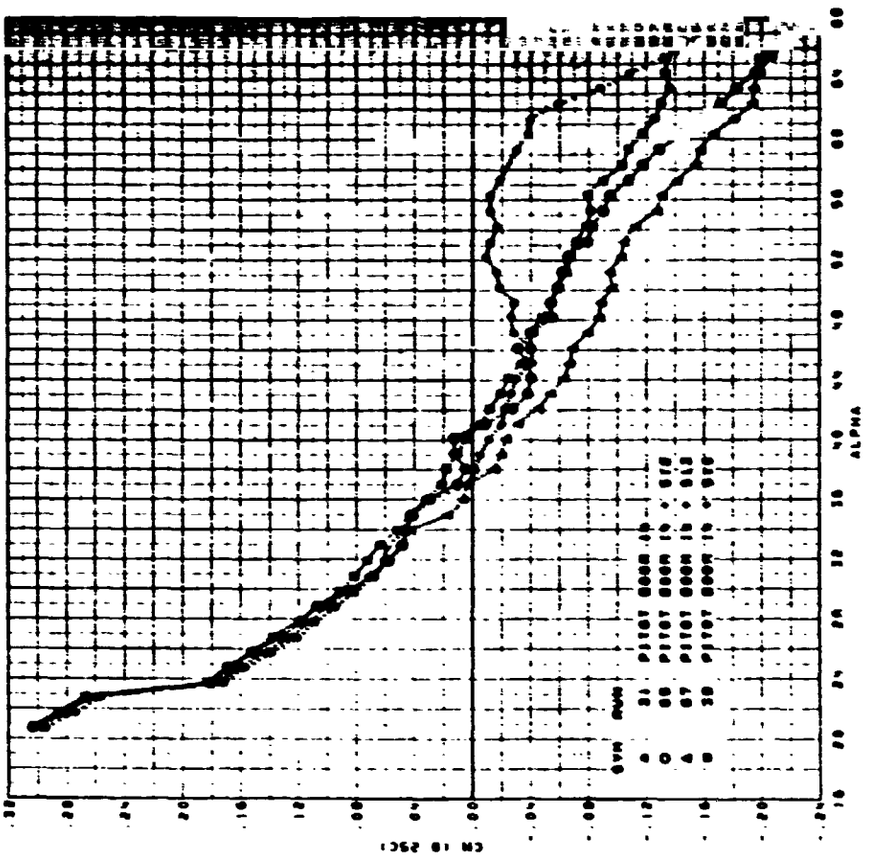

FIGURE 79. F-5F CLEAN CONFIGURATION. EFFECT OF STRAKES S10, S12 AND S13 AT ZERO SIDESLIP, PITCHING MOMENT DATA

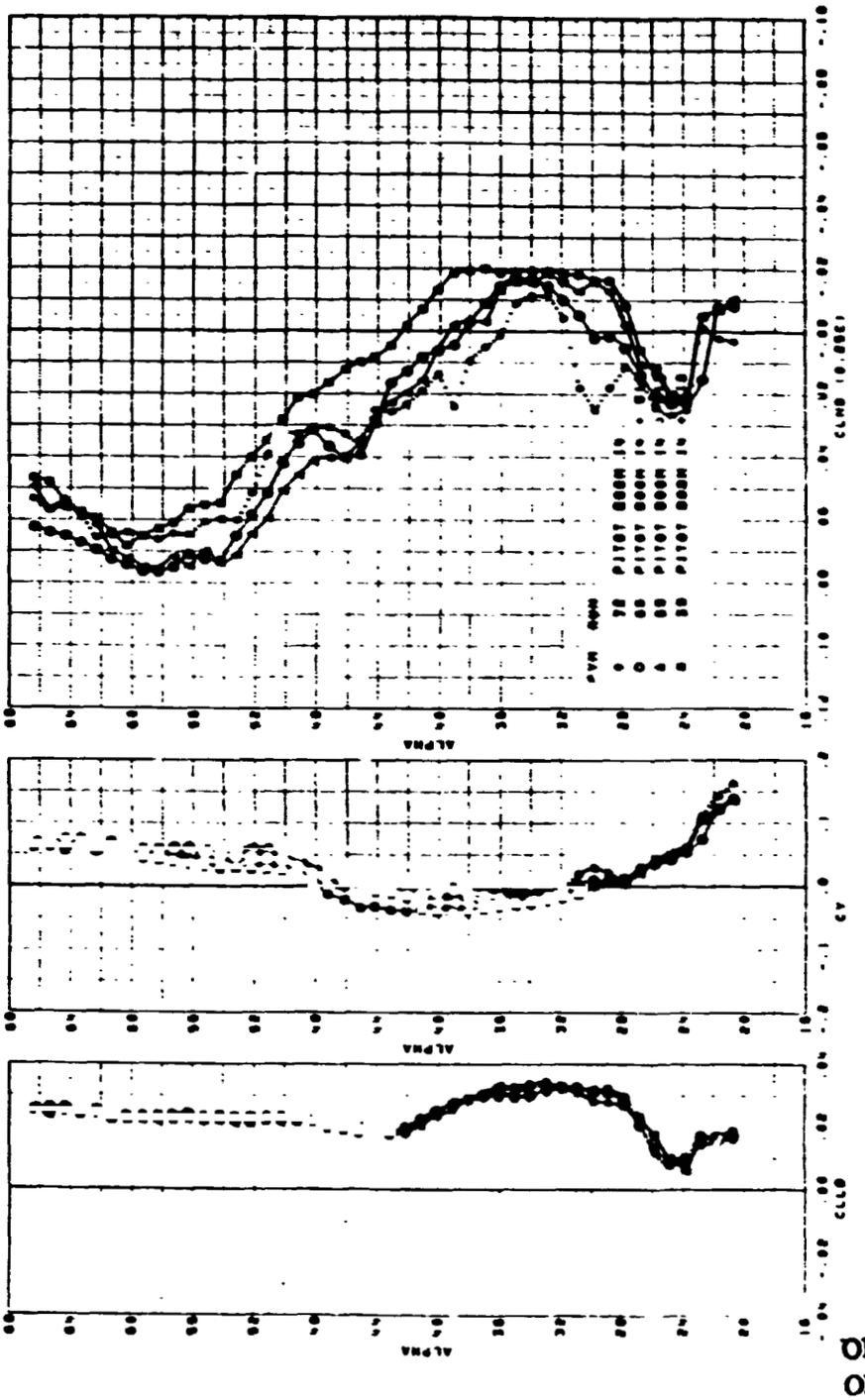

FIGURE 80. F-5F CLEAN CONFIGURATION. EFFECT OF STRAKES S10, S12 AND S13 AT -10° SIDESLIP, LAT/DIR DATA

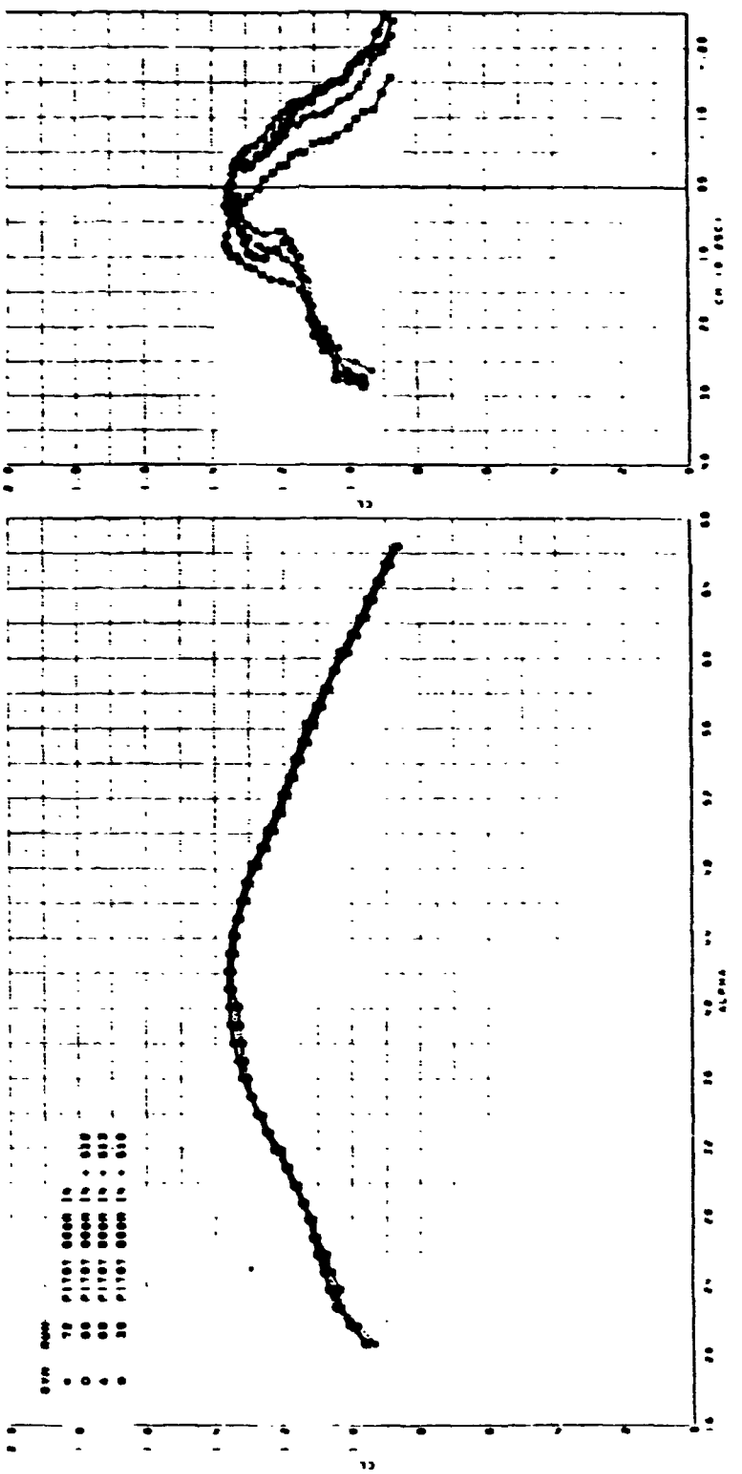

FIGURE 81. F-5F CLEAN CONFIGURATION. EFFECT OF STRAKES S10, S12 AND S13 AT -10° SIDESLIP, LIFT AND PITCH DATA

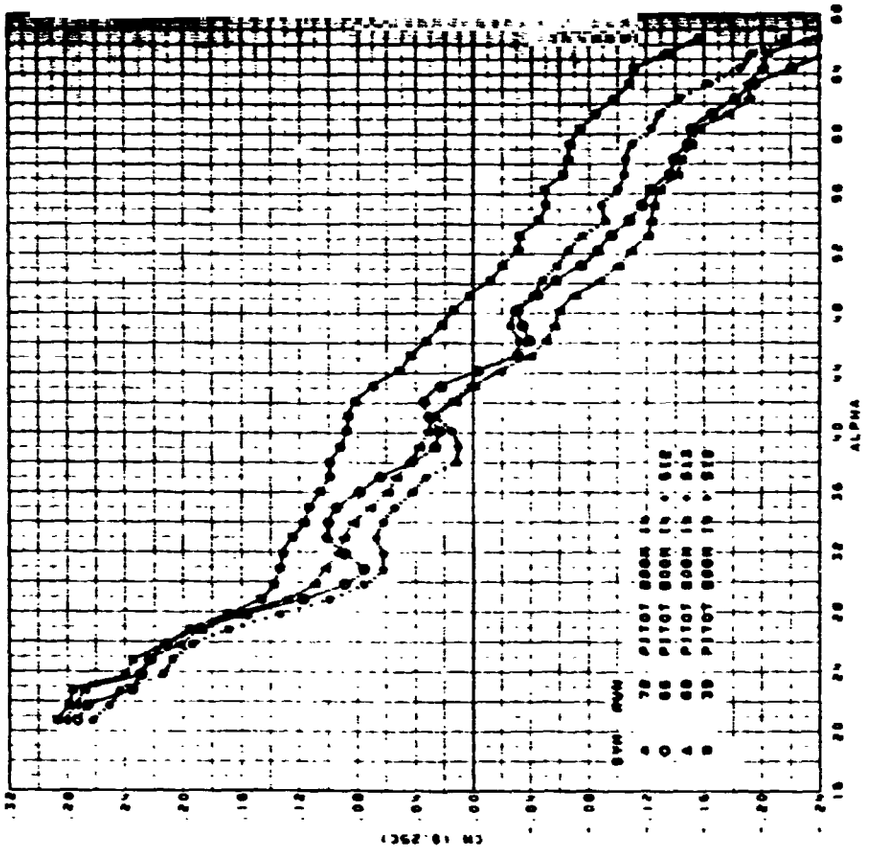

FIGURE 82. F-5F CLEAN CONFIGURATION. EFFECT OF STRAKES S10, S12 AND S13 AT -10° SIDESLIP, PITCHING MOMENT DATA

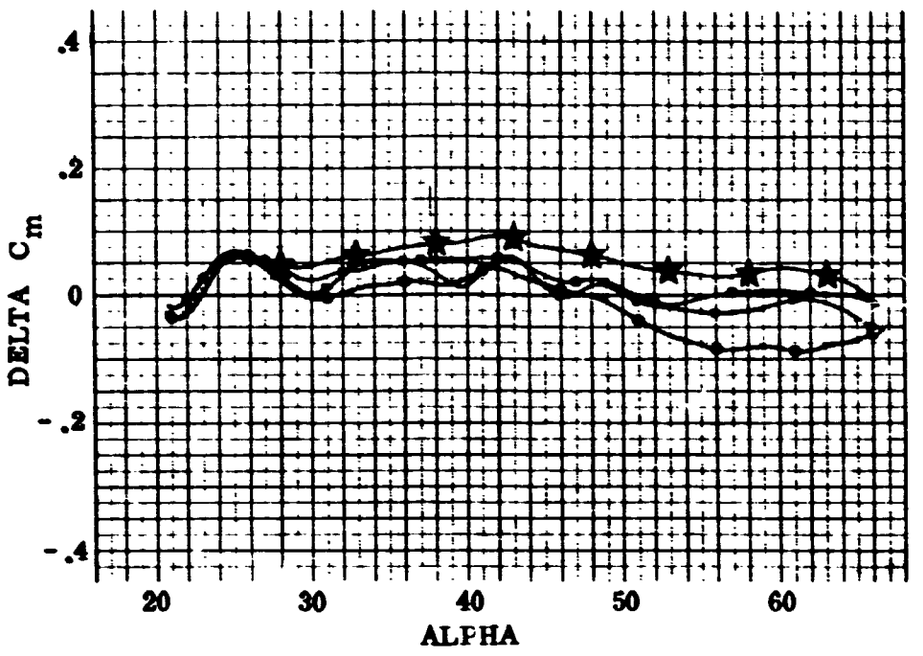

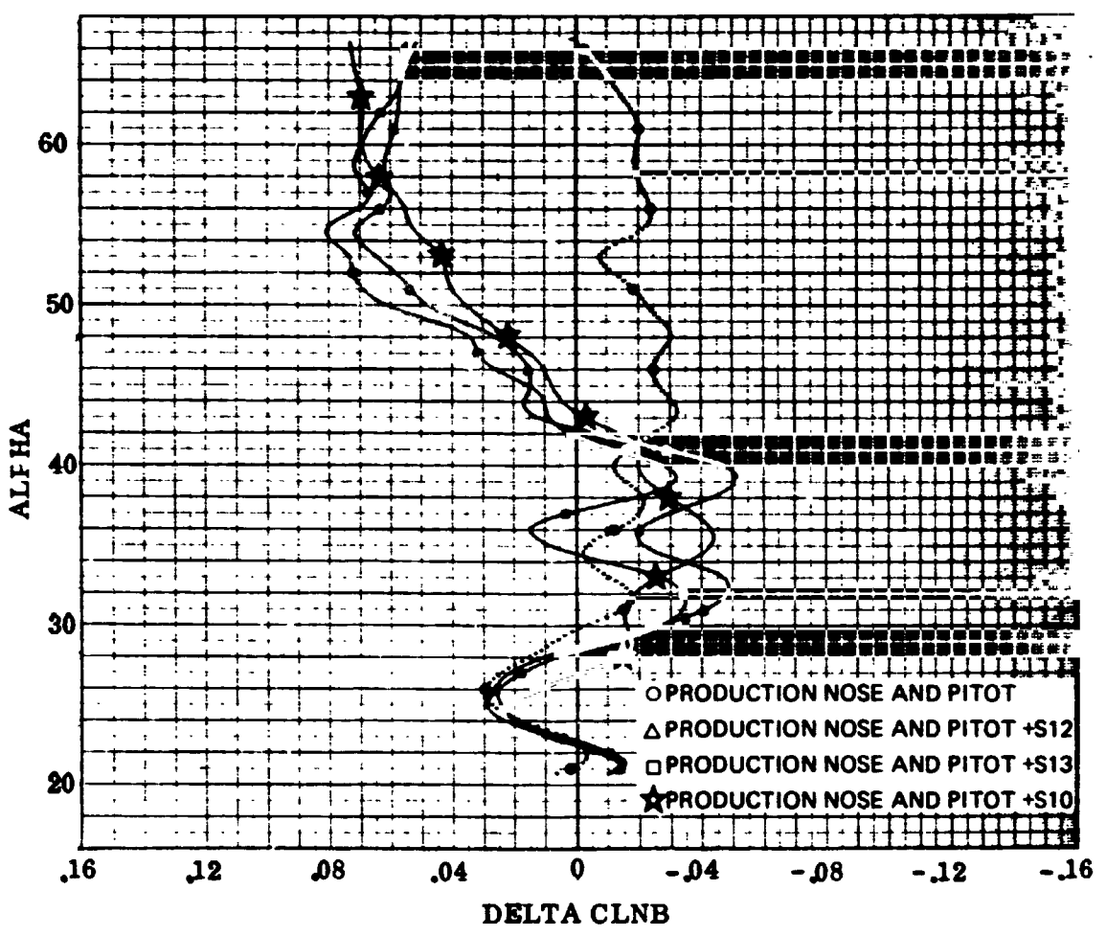

FIGURE 83. F-5F CLEAN CONFIGURATION. EFFECT OF STRAKES S10, S12 AND S13 ON INCREMENTAL C_n AND C_m DUE TO -10° SIDESLIP

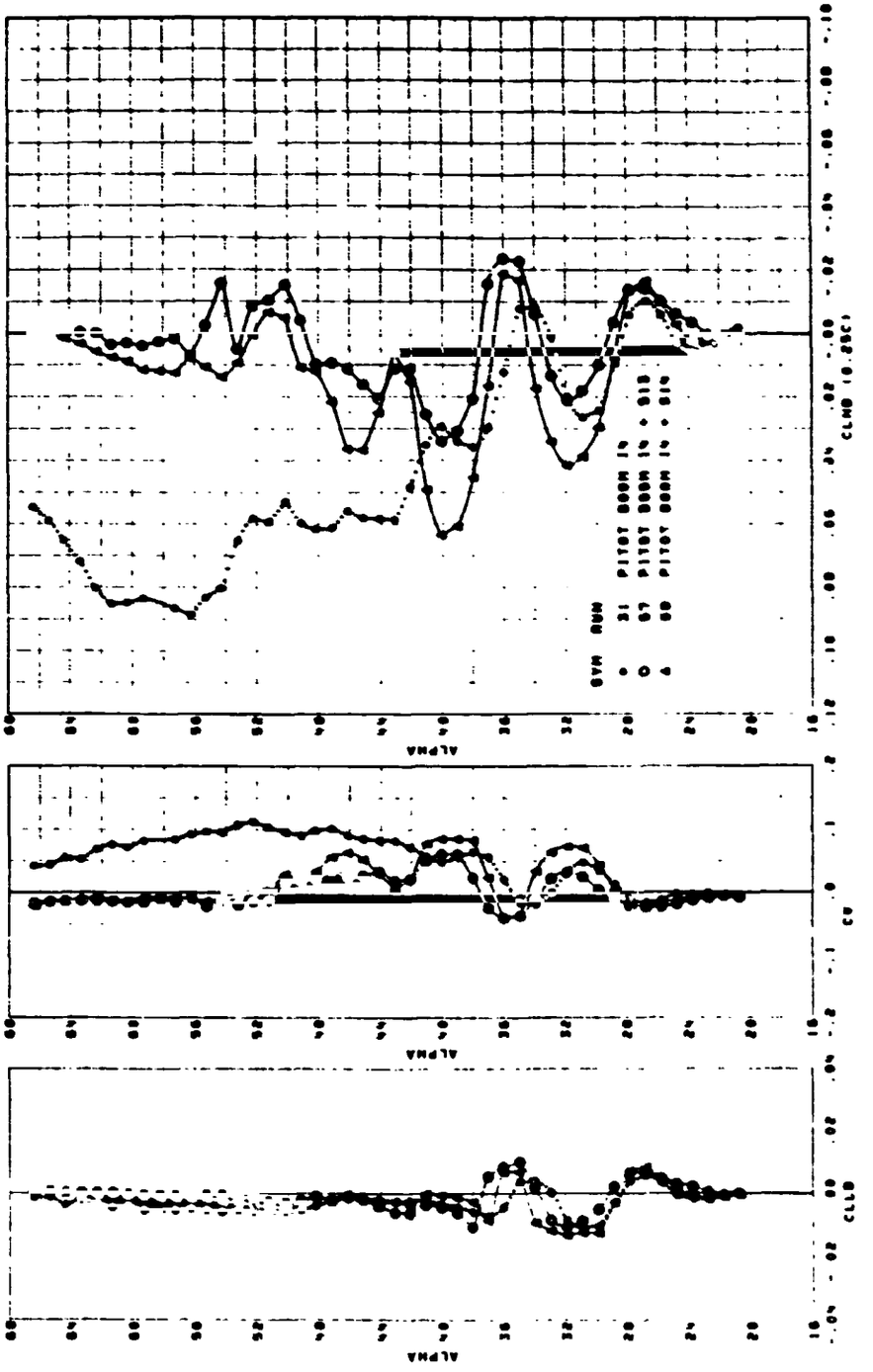

FIGURE 84. F-5F CLEAN CONFIGURATION. EFFECT OF STRAKES S13 AND S14 AT ZERO SIDESLIP, LAT/DIR DATA

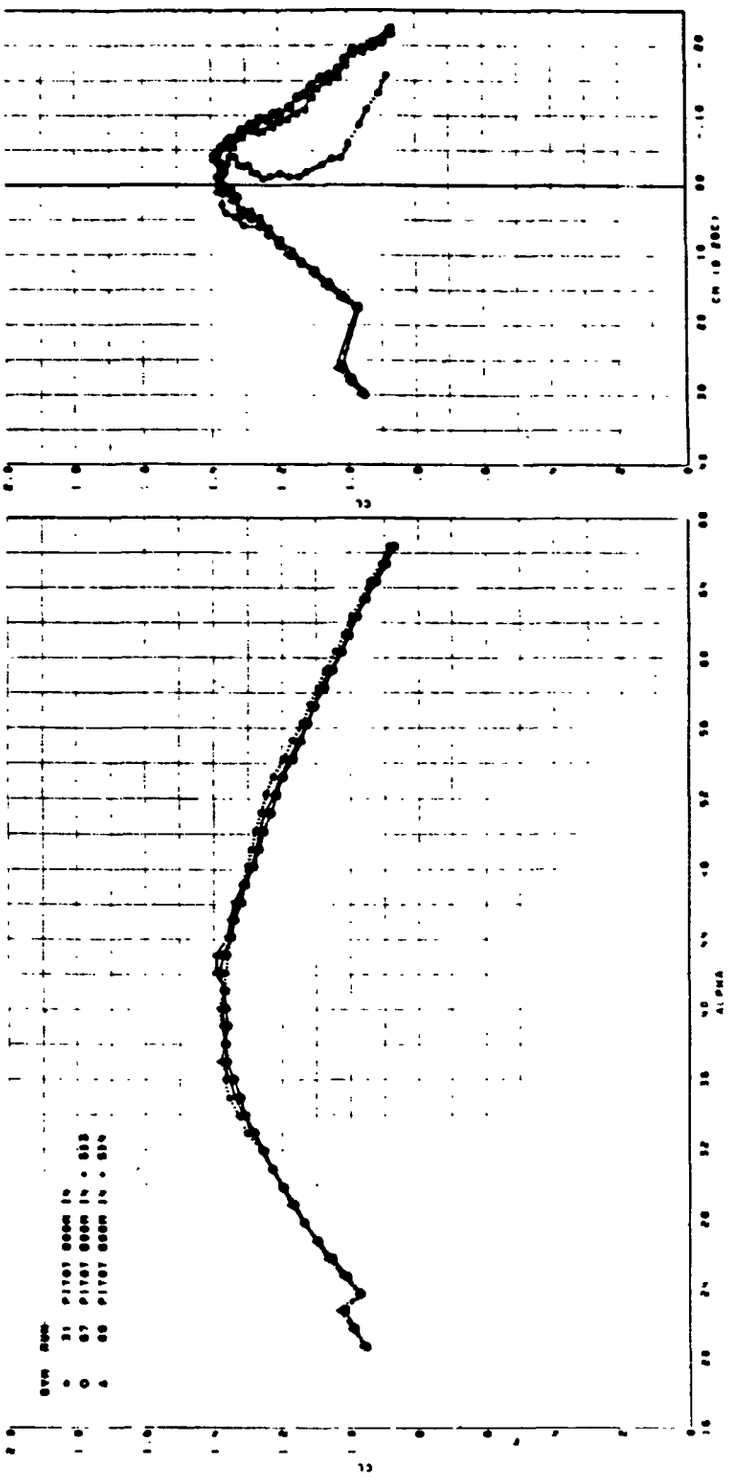

FIGURE 85. F-5F CLEAN CONFIGURATION. EFFECT OF STRAKES S13 AND S14 AT ZERO SIDESLIP, LIFT AND PITCH DATA

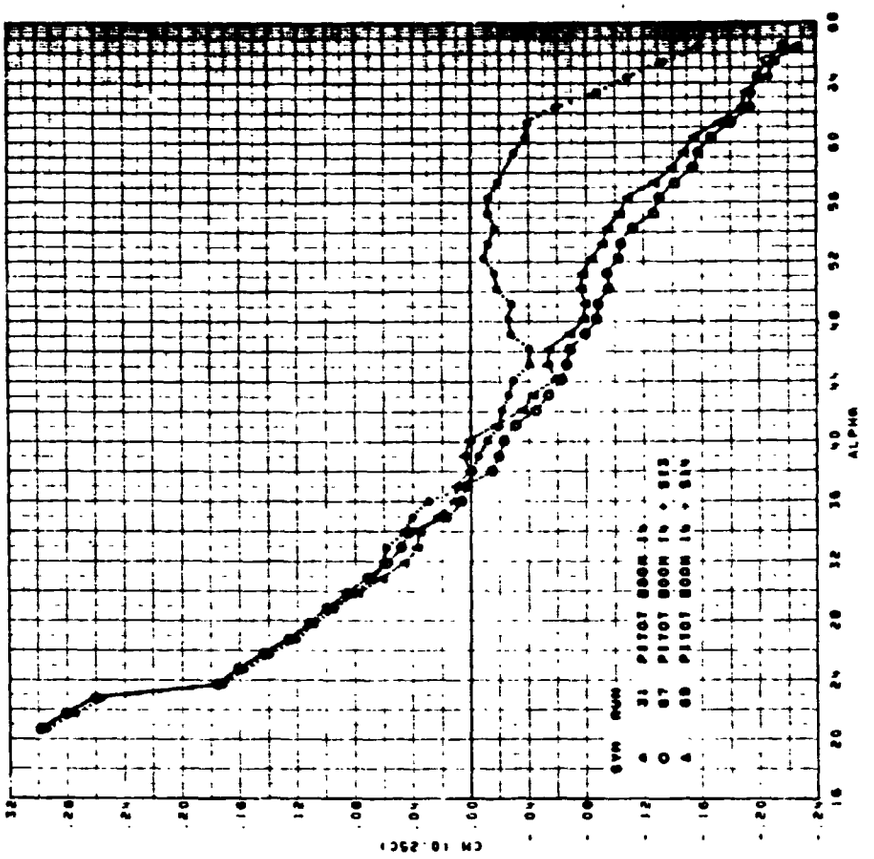

FIGURE 86. F-5F CLEAN CONFIGURATION. EFFECT OF STRAKES S13 AND S14 AT ZERO SIDESLIP, PITCHING MOMENT DATA

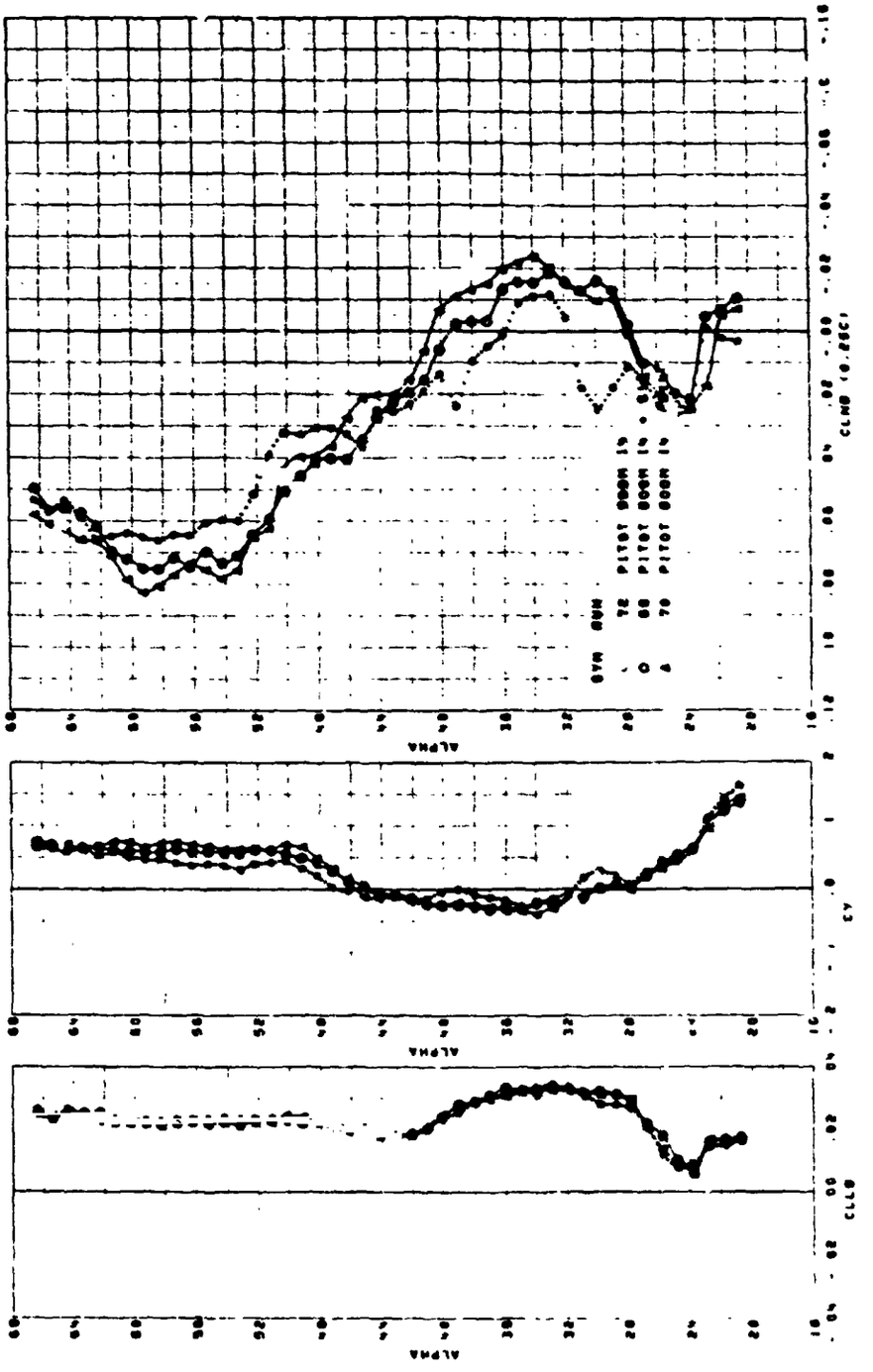

FIGURE 87. F-5F CLEAN CONFIGURATION. EFFECT OF STRAKES S13 AND S14 AT -10° SIDESLIP, LAT/DIR DATA

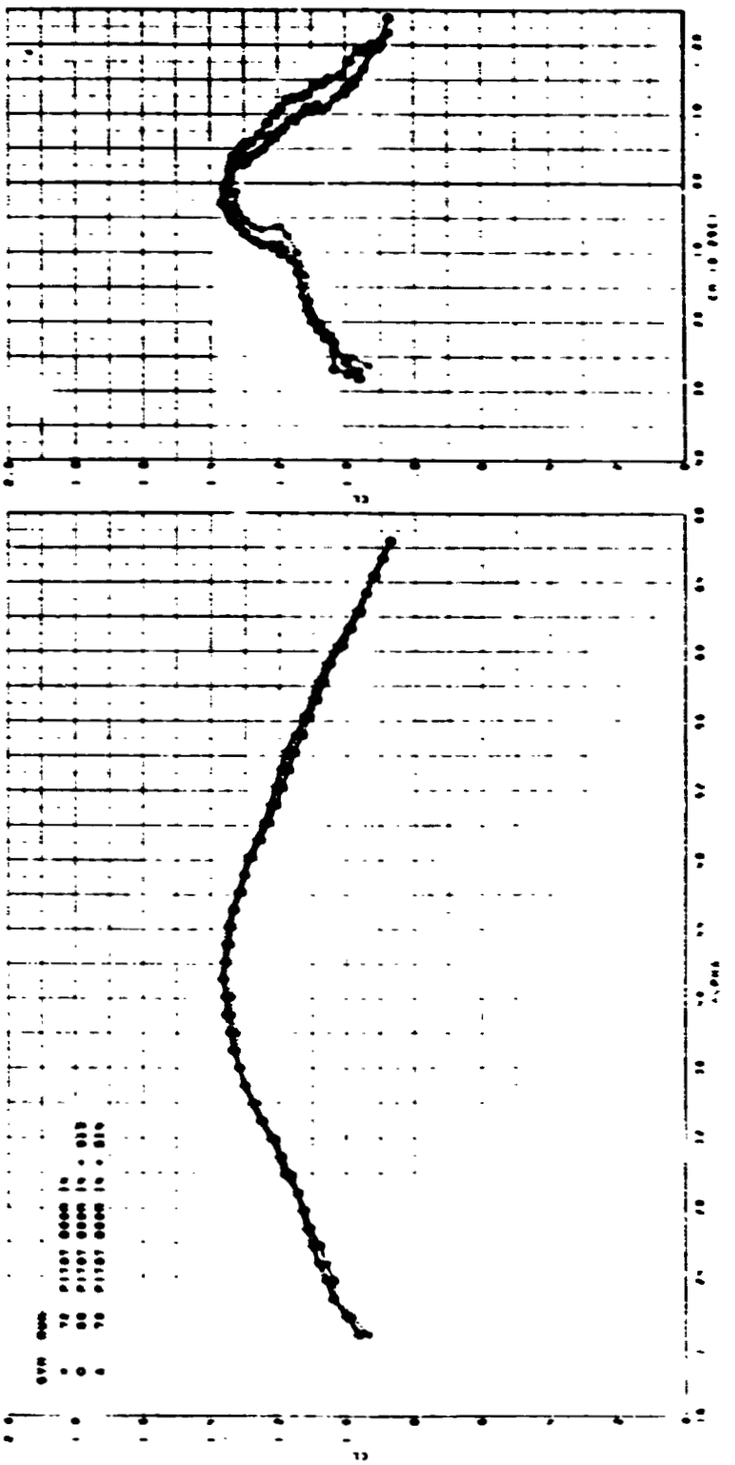

FIGURE 88. F-5F CLEAN CONFIGURATION. EFFECT OF STRAKES S13 AND S14 AT -10° SIDESLIP, LIFT AND PITCH DATA

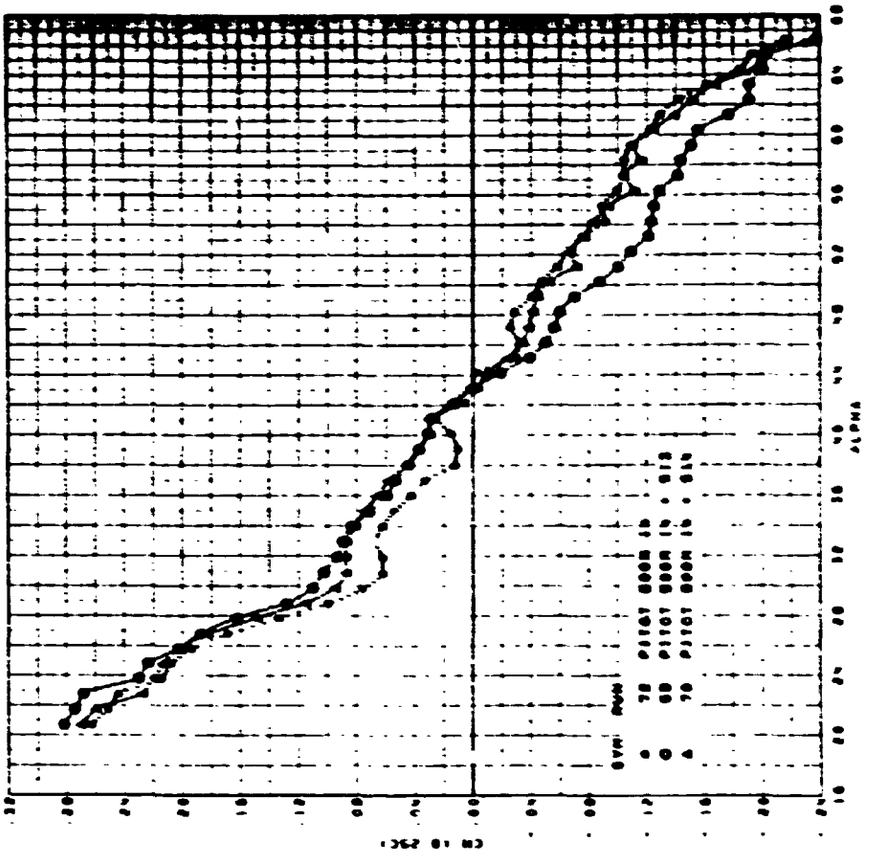

FIGURE 89. F-5F CLEAN CONFIGURATION. EFFECT OF STRAKES S13 AND S14 AT -10° SIDESLIP, PITCHING MOMENT DATA

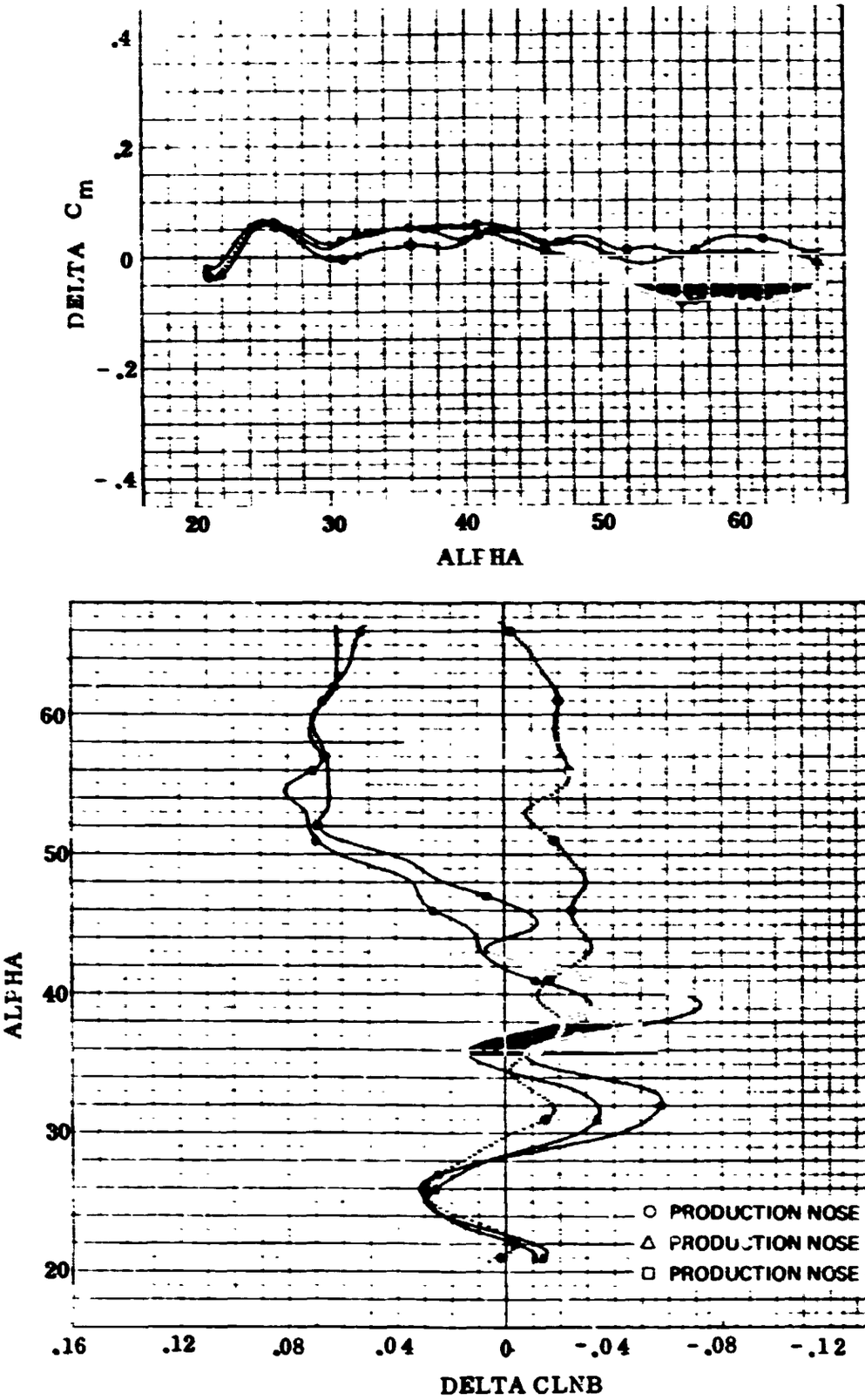

FIGURE 90. F-5F CLEAN CONFIGURATION. EFFECT OF STRAKES S13 AND S14 ON INCREMENTAL C_n AND C_m DUE TO -10° SIDESLIP

Full Scale Dimensions

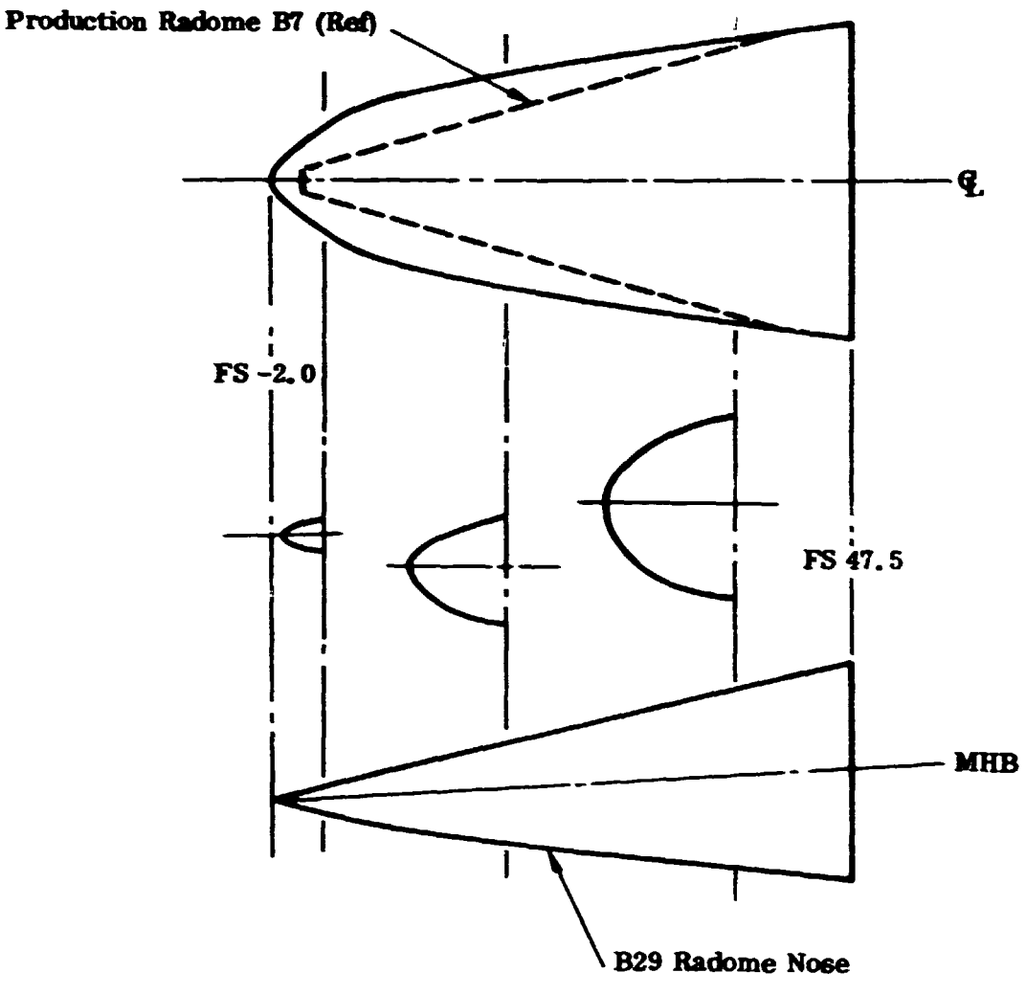

FIGURE 91. F-5F SHARK NOSE B29 GEOMETRY

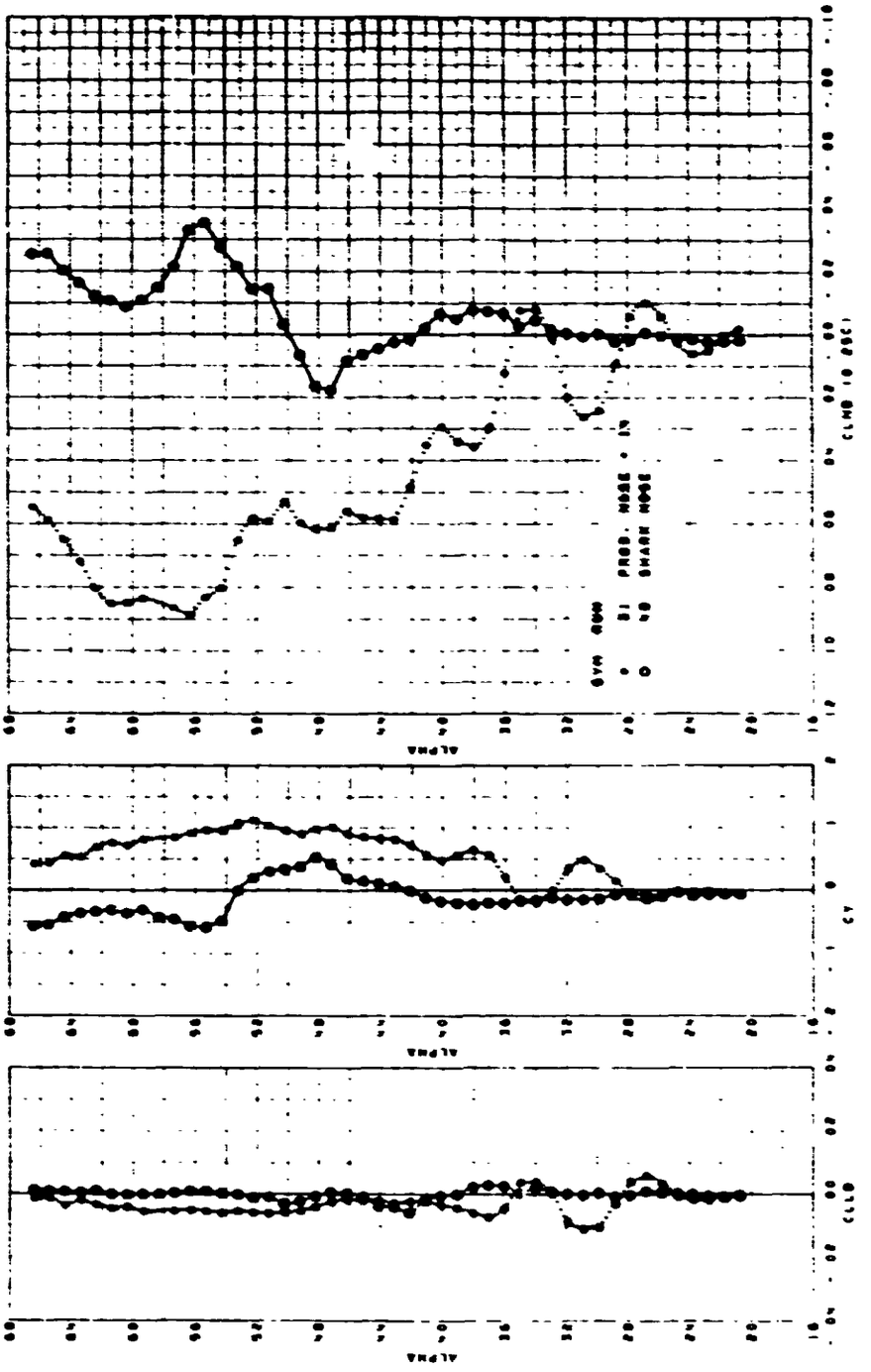

FIGURE 92. F-5F CLEAN CONFIGURATION. EFFECT OF SHARK NOSE B29 AT ZERO SIDESLIP, LAT/DIR DATA

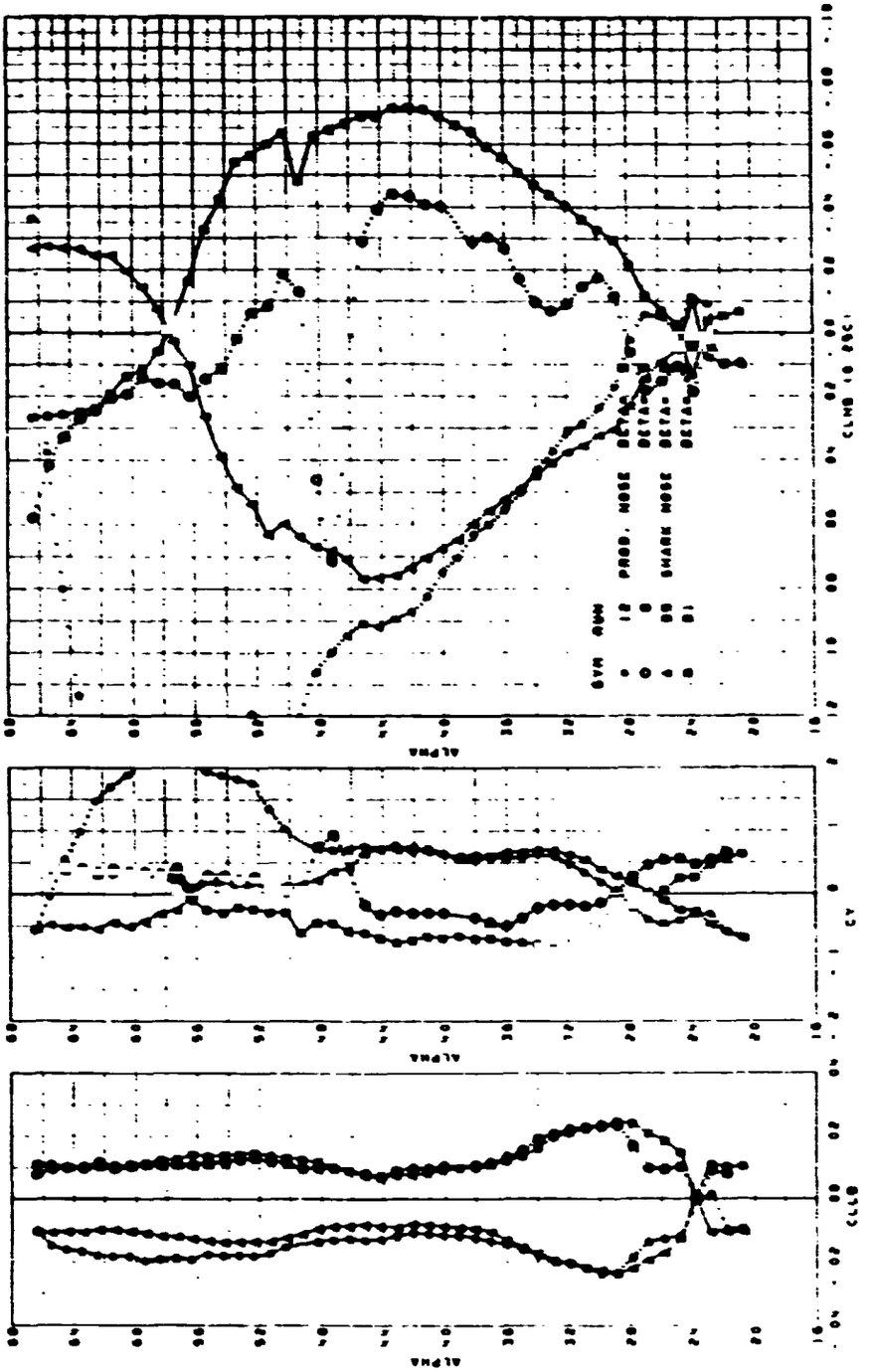

FIGURE 93. F-5F CLEAN CONFIGURATION. COMPARISON OF PRODUCTION AND SHARK NOSE B29 AT ±5° SIDESLIP, LAT/DIR DATA

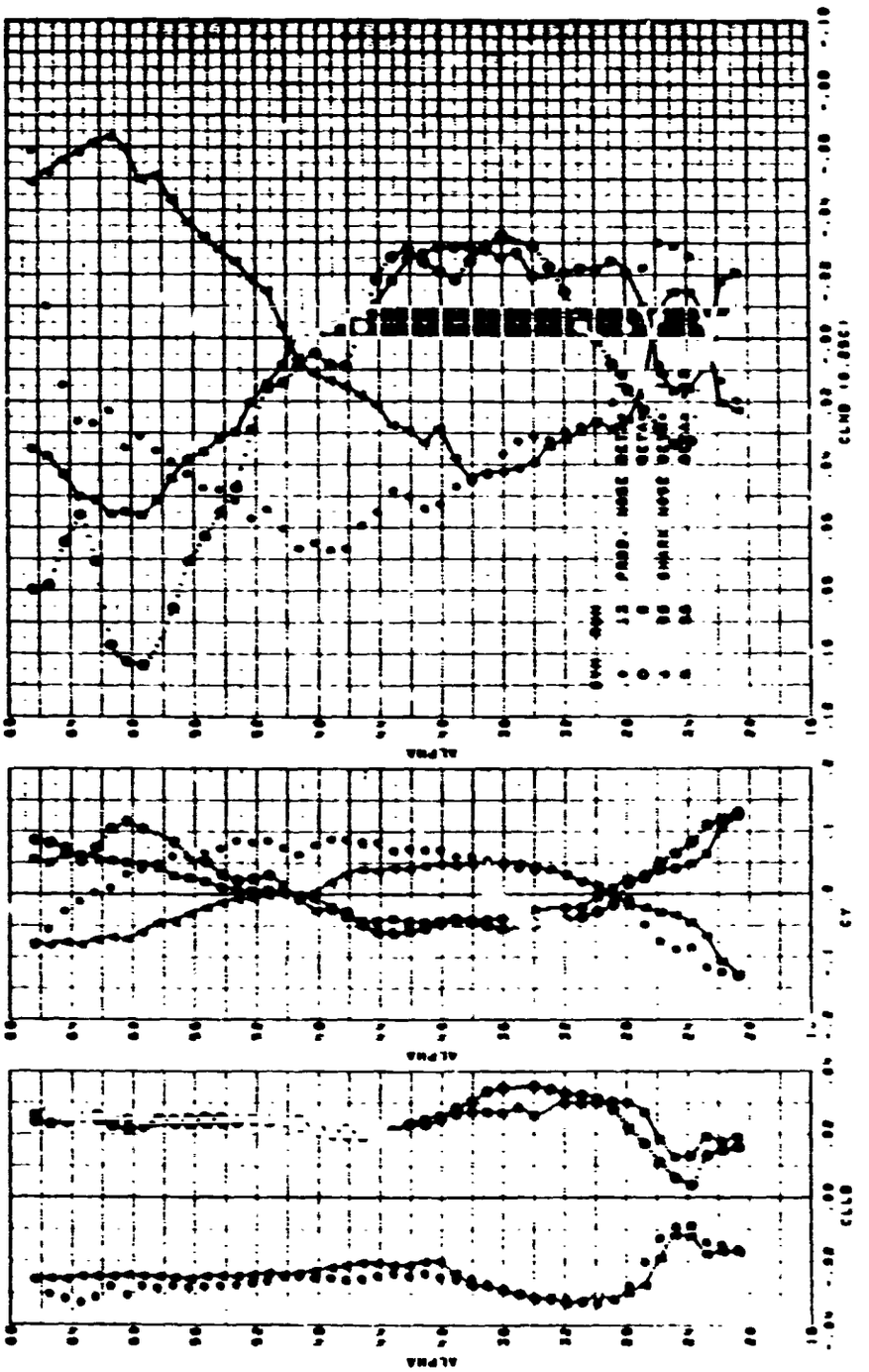

FIGURE 94. F-5F CLEAN CONFIGURATION. COMPARISON OF PRODUCTION AND SHARK NOSE B29 AT ±10° SIDESLIP, LAT/DIR DATA

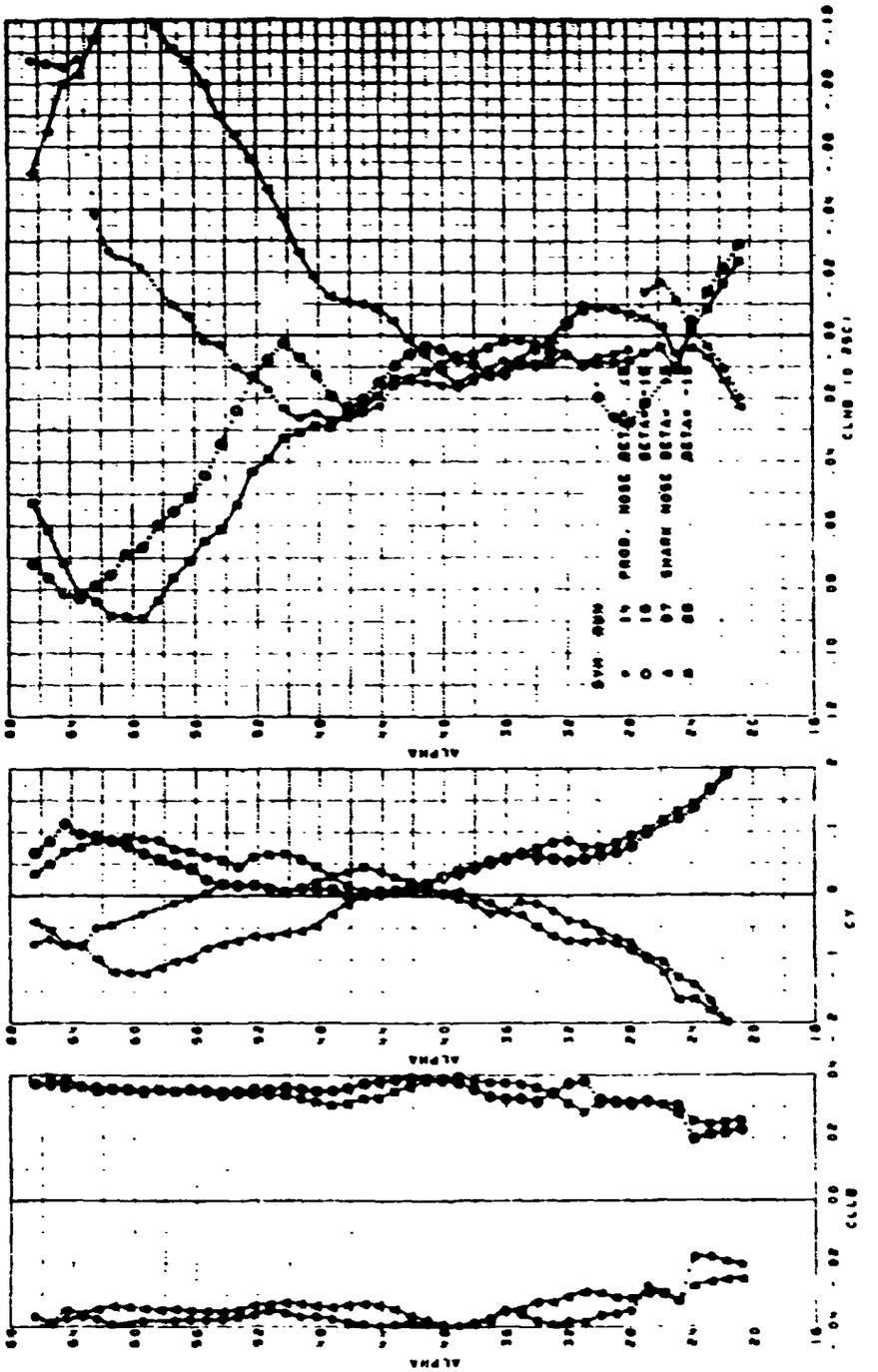

FIGURE 95. F-5F CLEAN CONFIGURATION. COMPARISON OF PRODUCTION AND SHARK NOSE B29 AT ±15° SIDESLIP, LAT/DIR DATA

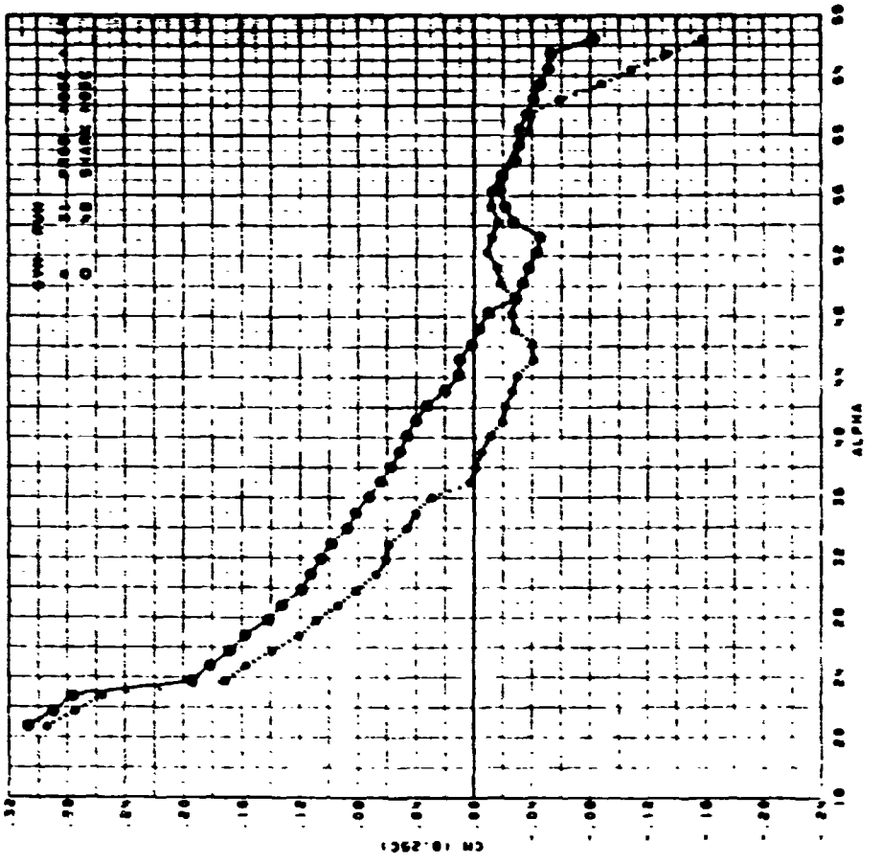

FIGURE 96. F-5F CLEAN CONFIGURATION. COMPARISON OF PRODUCTION AND SHARK NOSE B29 AT ZERO SIDESLIP, PITCHING MOMENT DATA

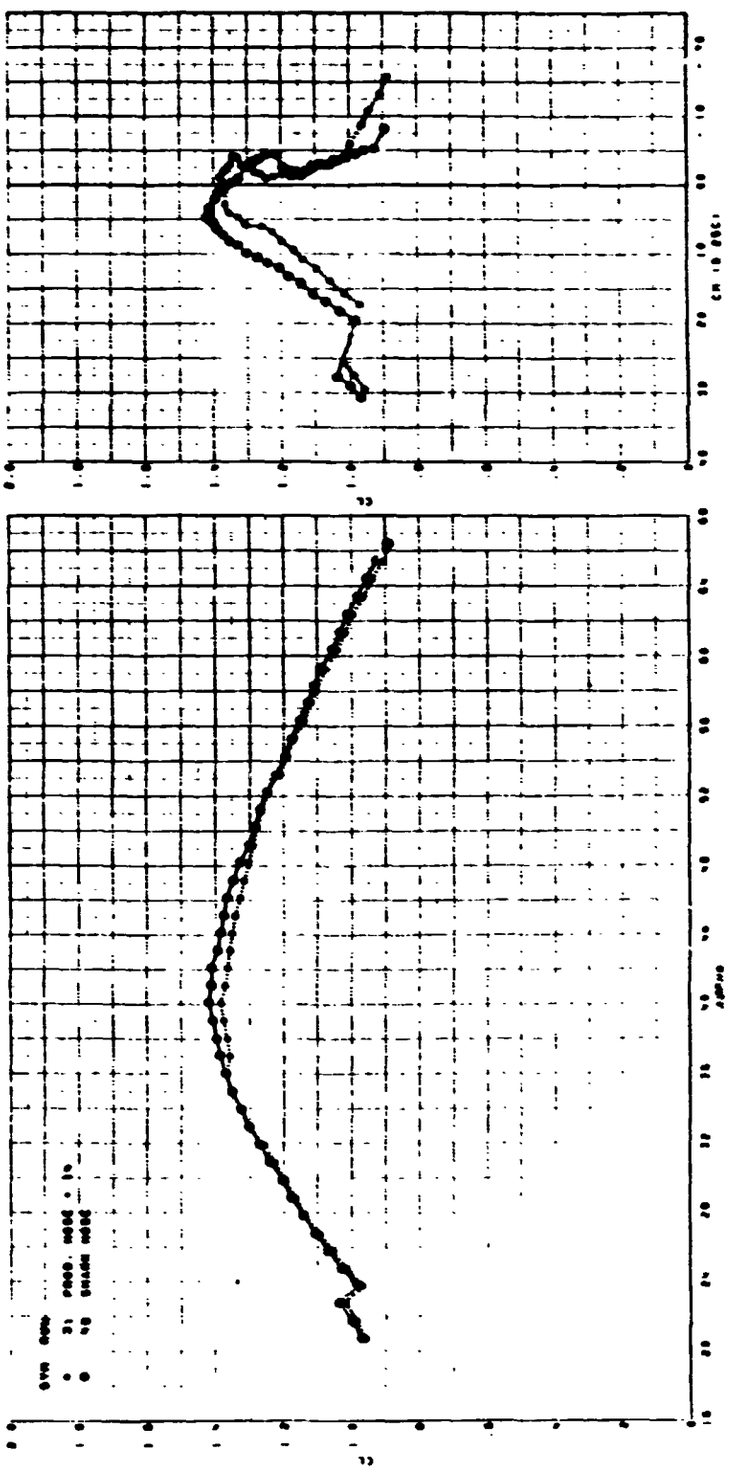

FIGURE 97. F-5F CLEAN CONFIGURATION. COMPARISON OF PRODUCTION AND SHARK NOSE B29 AT ZERO SIDESLIP, LIFT AND PITCH DATA

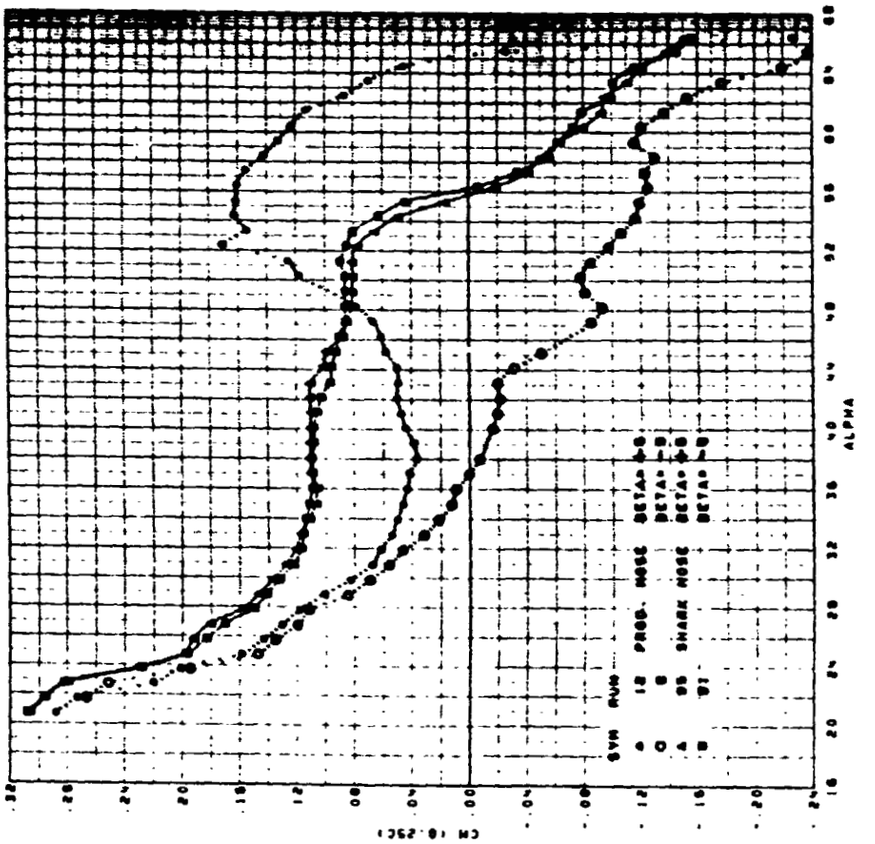

FIGURE 98. F-5F CLEAN CONFIGURATION. COMPARISON OF PRODUCTION AND SHARK NOSE B29 AT $\pm 5^{\circ}$ SIDESLIP, PITCHING MOMENT DATA

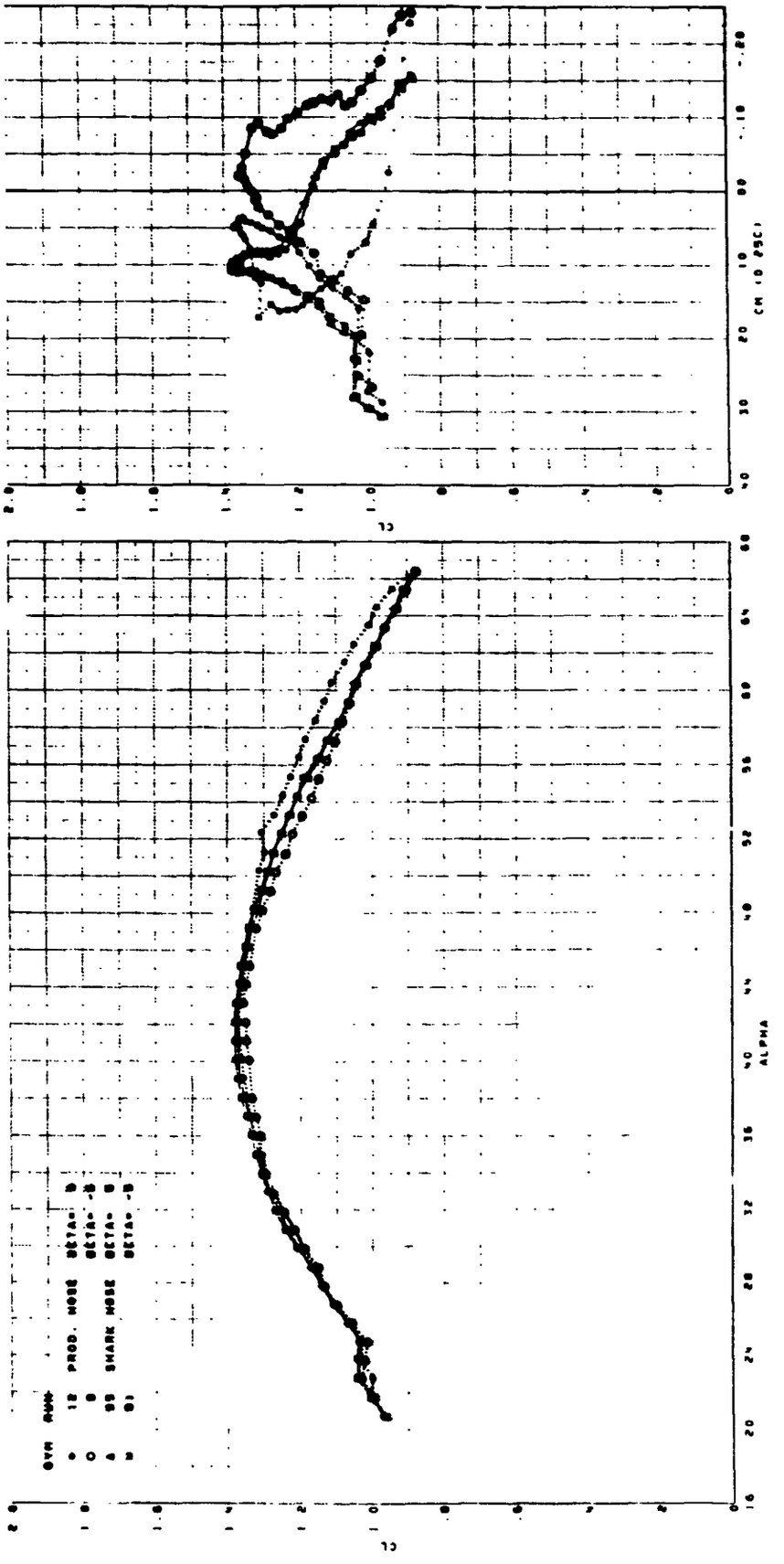

FIGURE 99. F-5F CLEAN CONFIGURATION. COMPARISON OF PRODUCTION AND SHARK NOSE B29 AT $\pm 5^{\circ}$ SIDESLIP, LIFT AND PITCH DATA

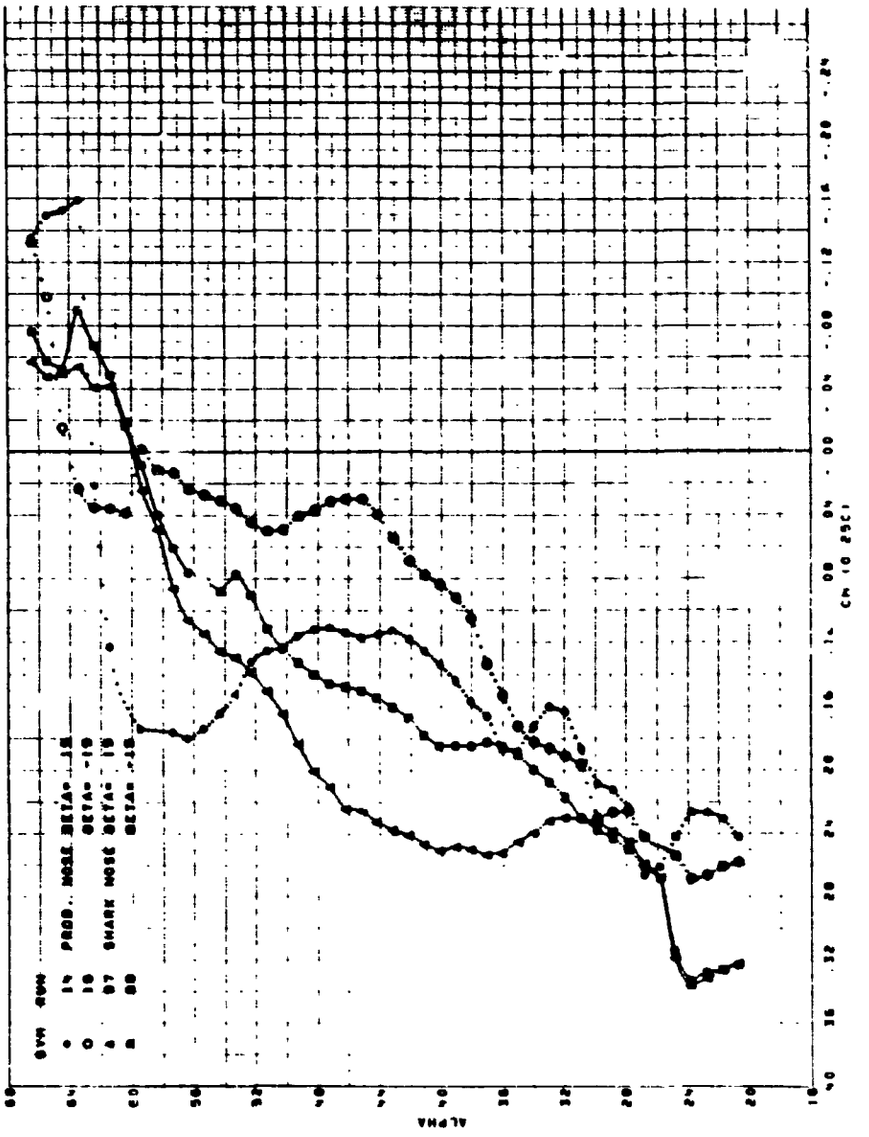

FIGURE 100. F-5F CLEAN CONFIGURATION. COMPARISON OF PRODUCTION AND SHARK NOSE B29 AT $\pm 15^{\circ}$ SIDESLIP, PITCHING MOMENT DATA

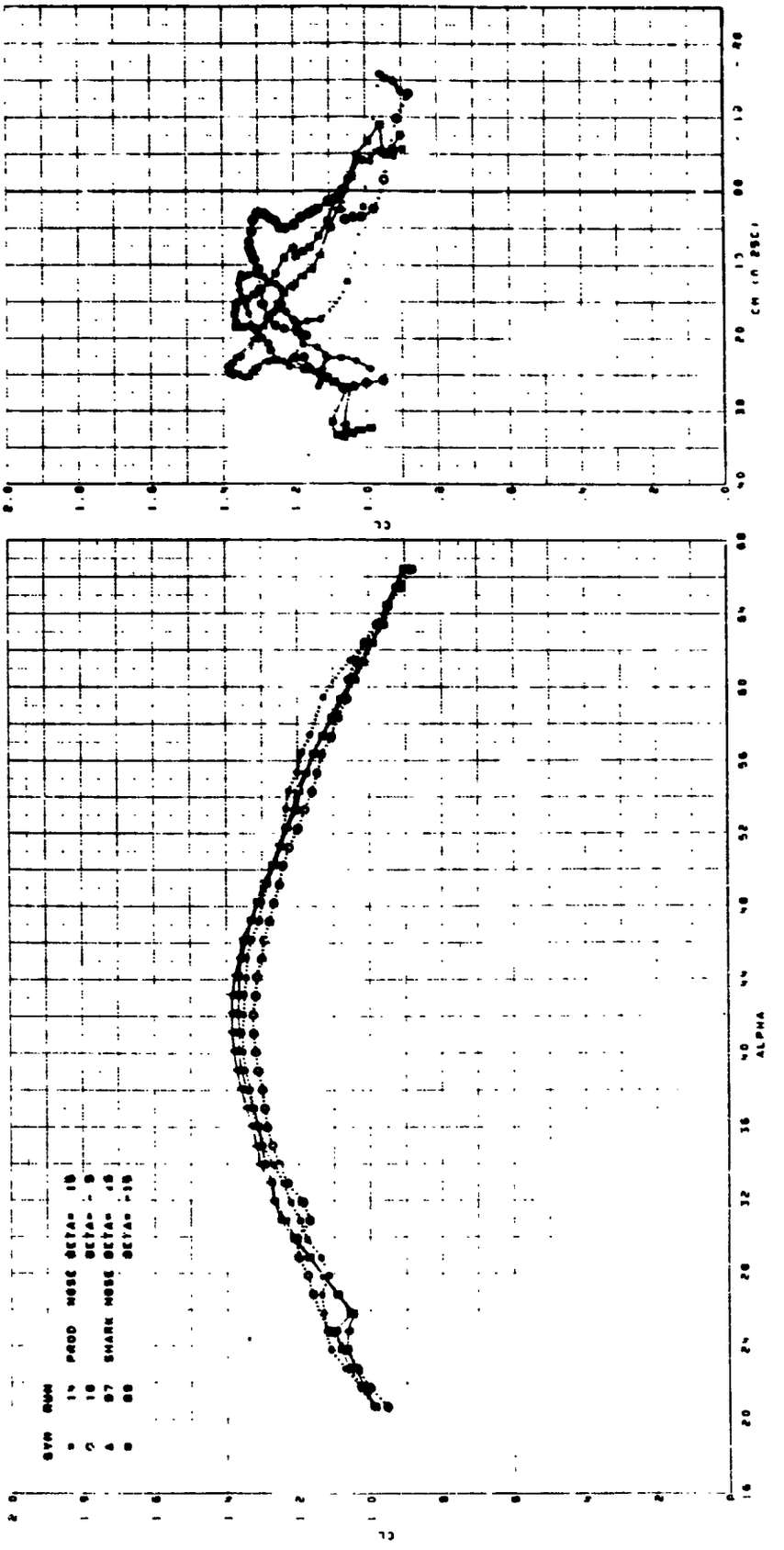

FIGURE 101. F-5F CLEAN CONFIGURATION. COMPARISON OF PRODUCTION AND SHARK NOSE B20 AT ±15° SIDESLIP, LIFT AND PITCH DATA

Full Scale Dimensions

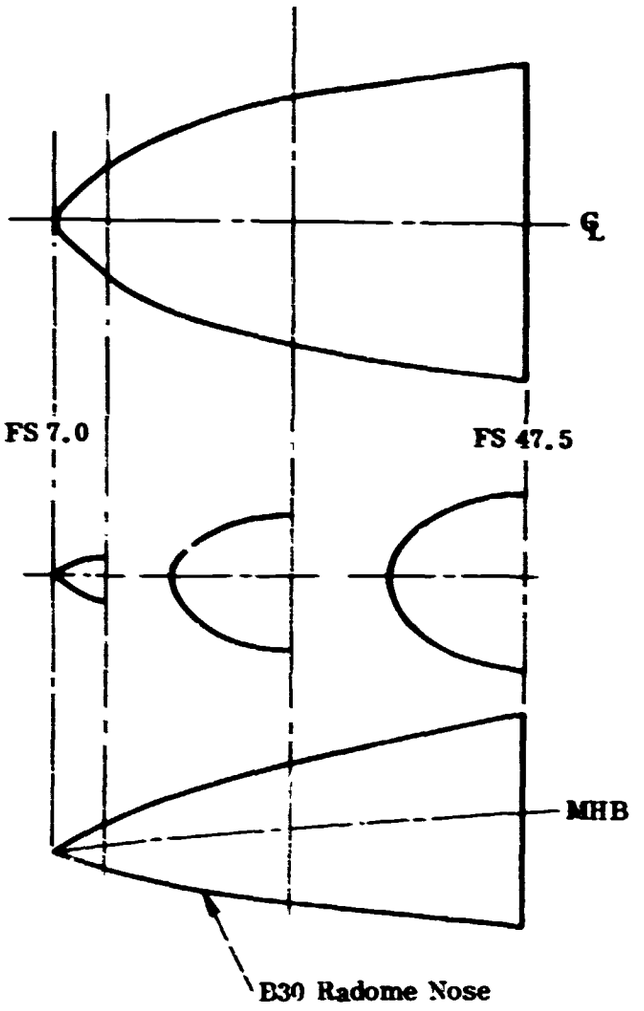

FIGURE 102. F-5F SHARK NOSE B30 GEOMETRY

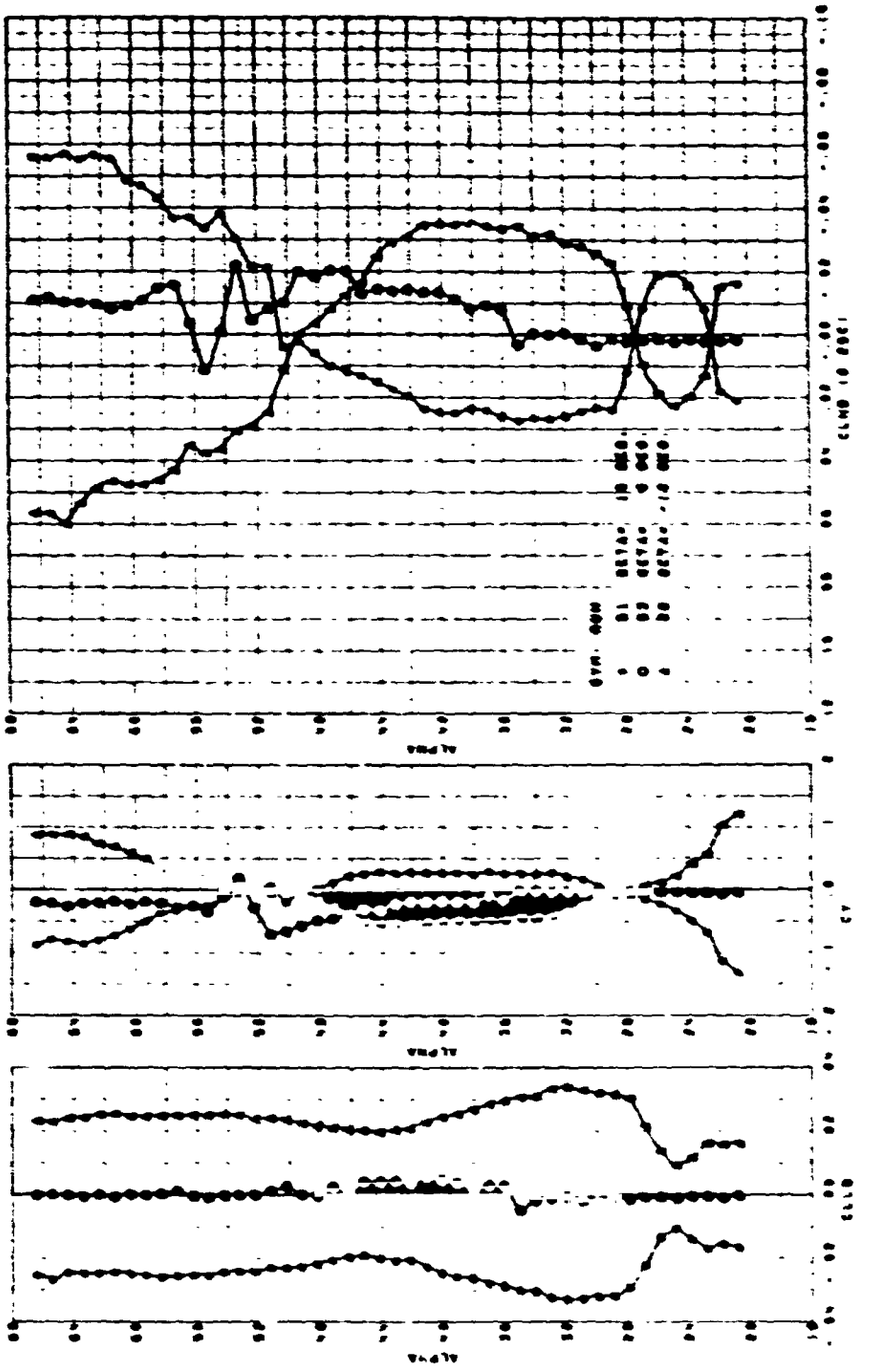

FIGURE 103. F-5F CLEAN CONFIGURATION. EFFECT OF SHARK NOSE B30 AT ±10° SIDESLIP, LAT/DIR DATA

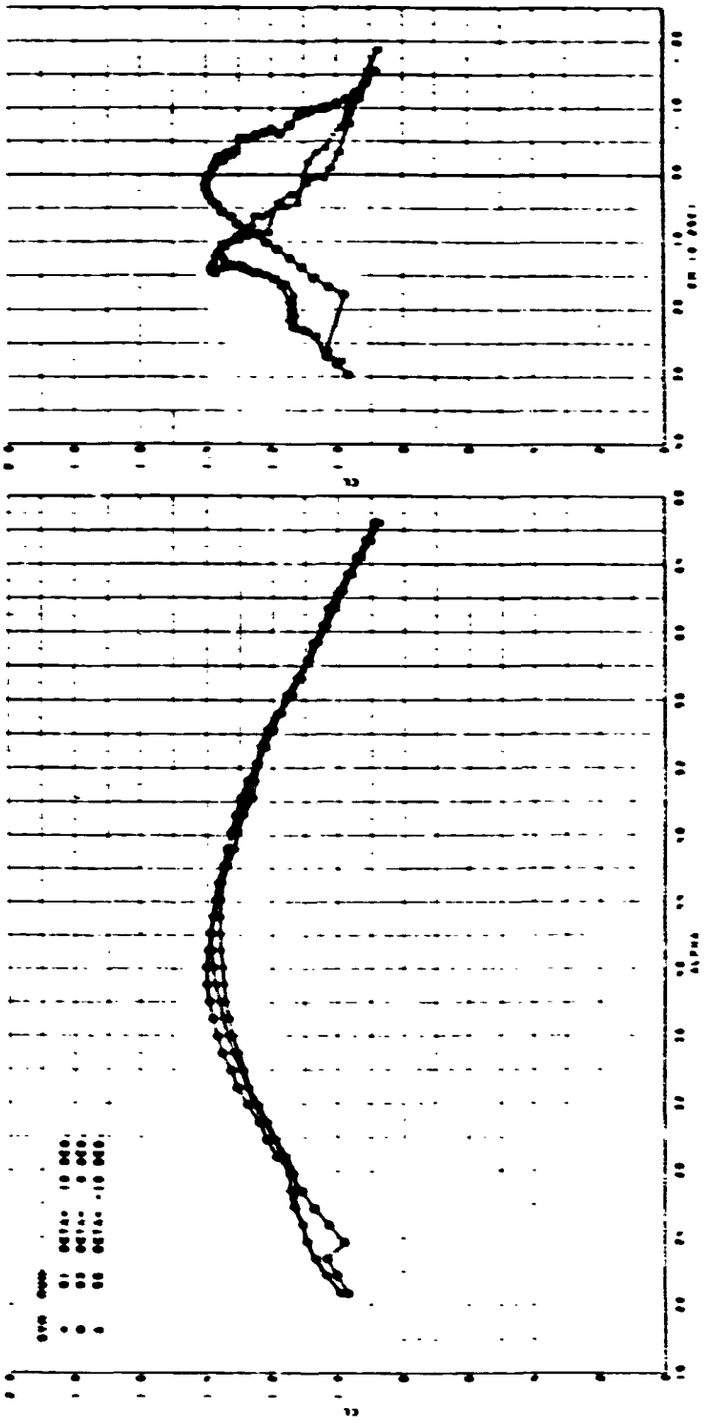

FIGURE 104. F-5F CLEAN CONFIGURATION. EFFECT OF SHARK NOSE B30 AT ±10° SIDESLIP, LIFT AND PITCH DATA

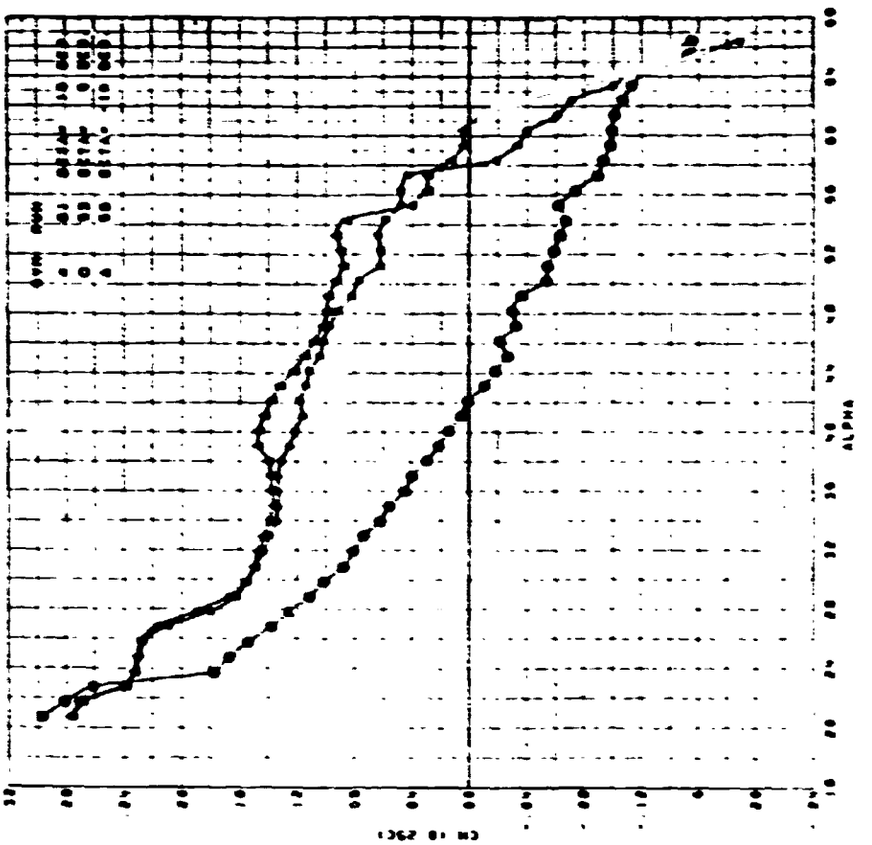

FIGURE 105. F-5F CLEAN CONFIGURATION. EFFECT OF SHARK NOSE B30 AT ±10° SIDESLIP, PITCHING MOMENT DATA

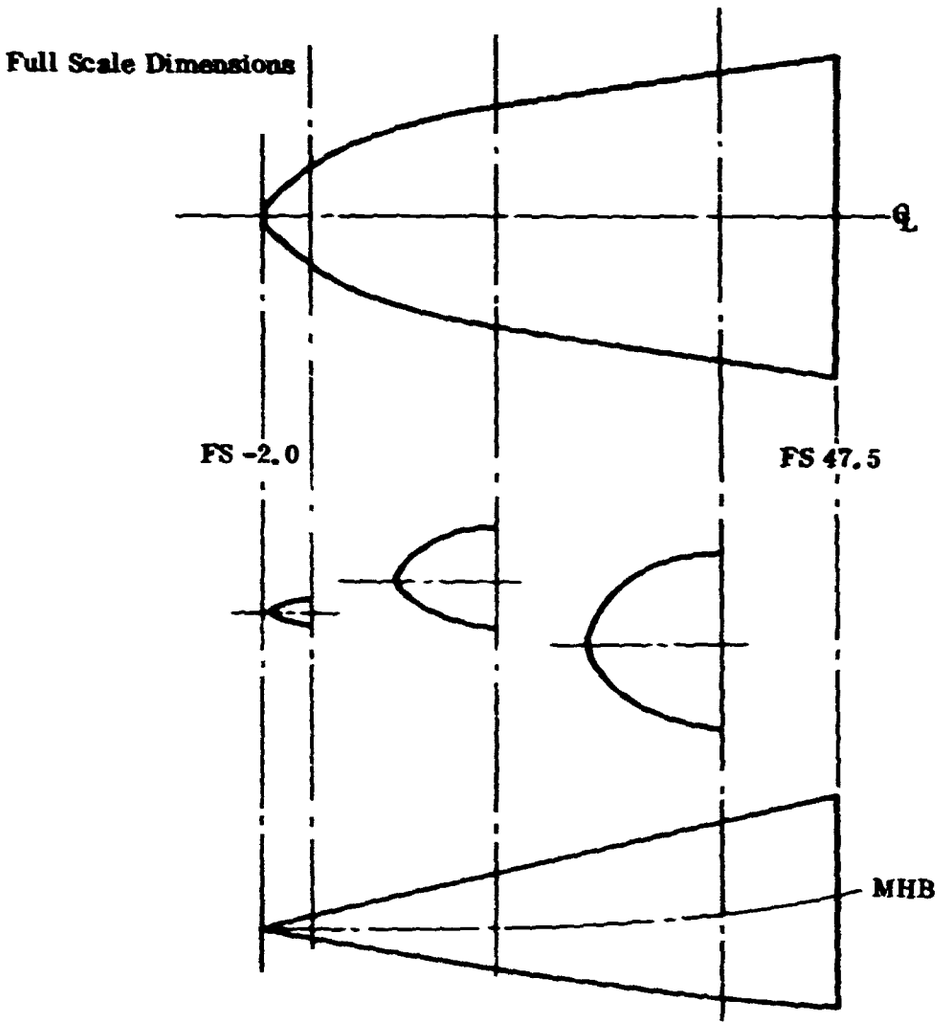

B31 Radome Nose

FIGURE 106. F-5F SHARK NOSE B31 GEOMETRY

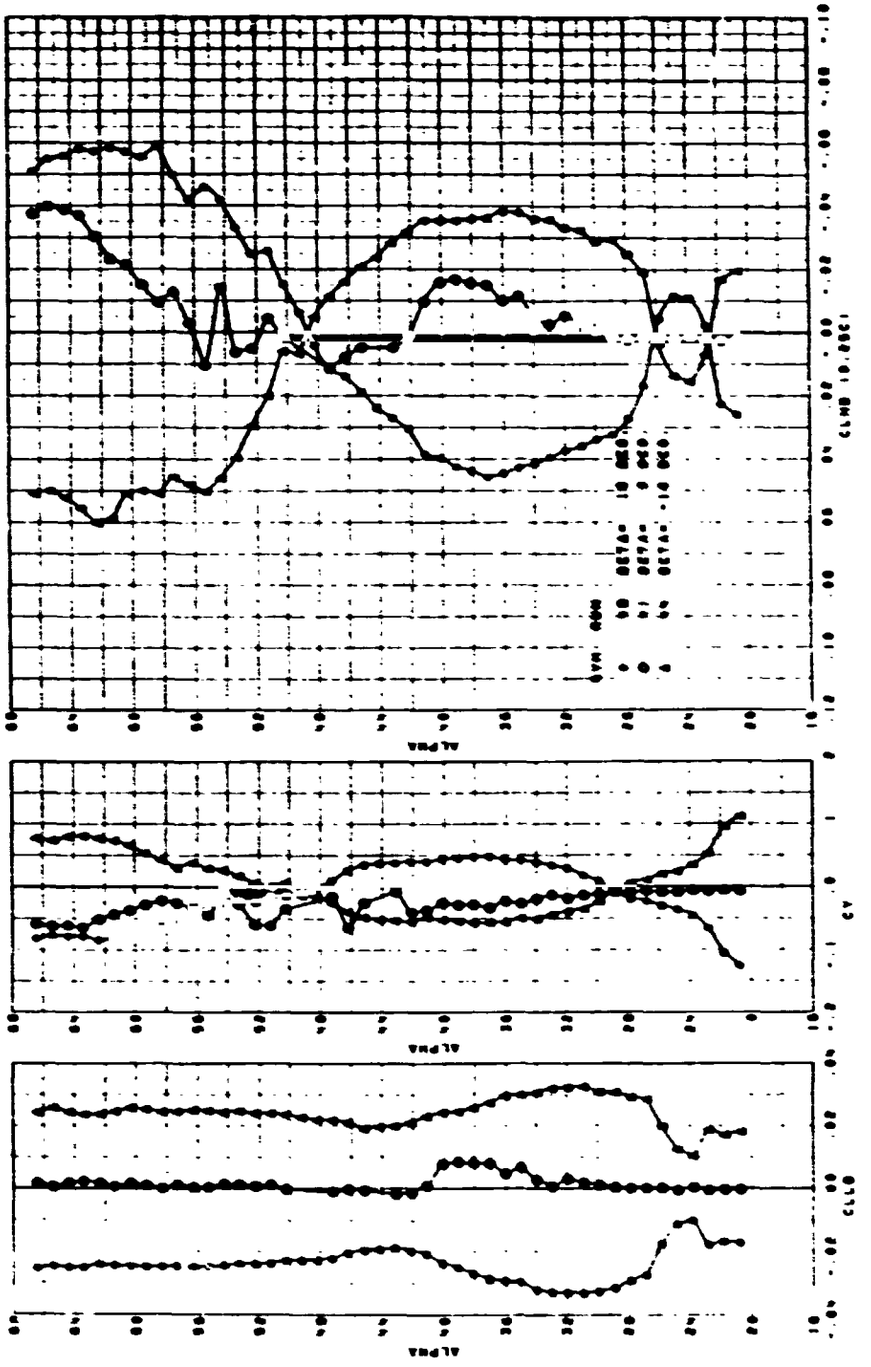

FIGURE 107. F-5F CLEAN CONFIGURATION. EFFECT OF SHARK NOSE B31 AT ±10° SIDESLIP, LAT/DIR DATA

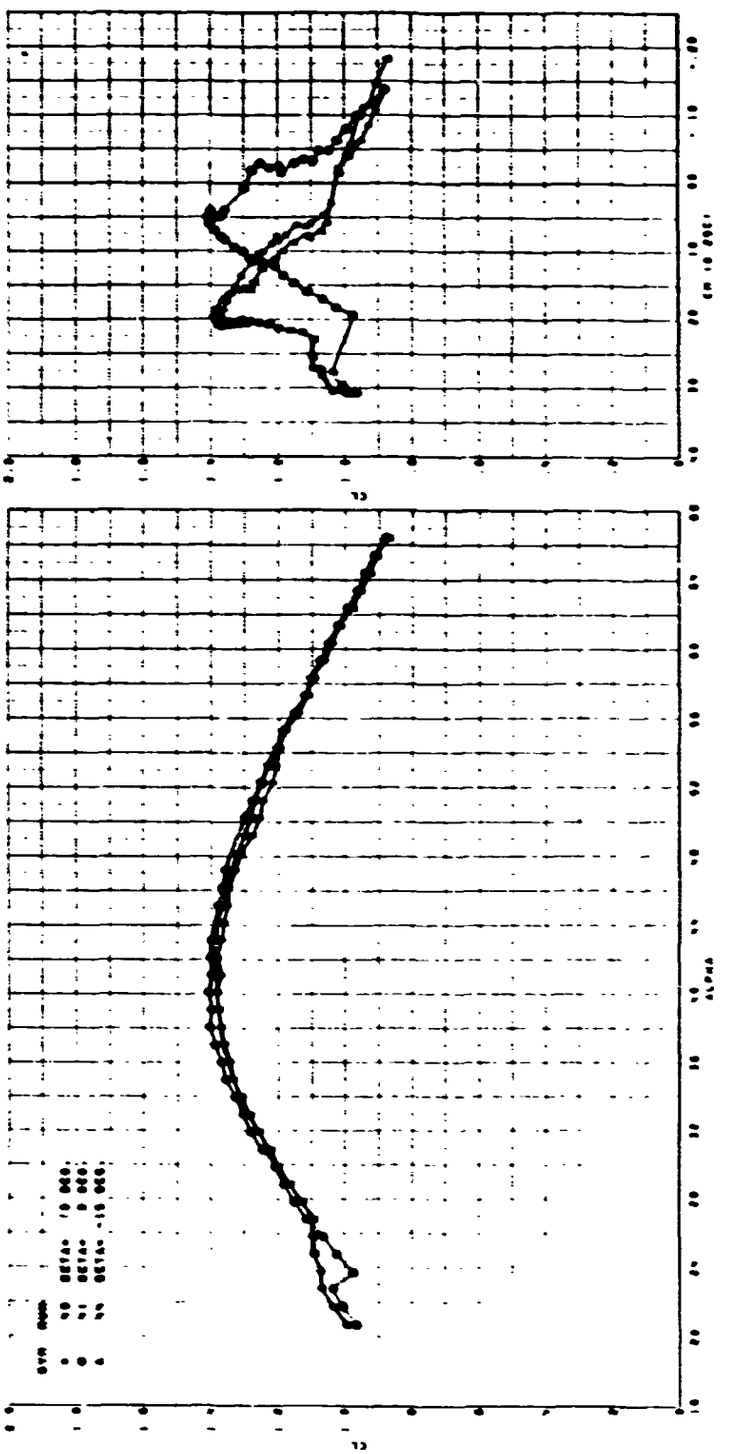

FIGURE 108. F-5F CLEAN CONFIGURATION. EFFECT OF SHARK NOSE B31 AT ±10° SIDESLIP, LIFT AND PITCH DATA

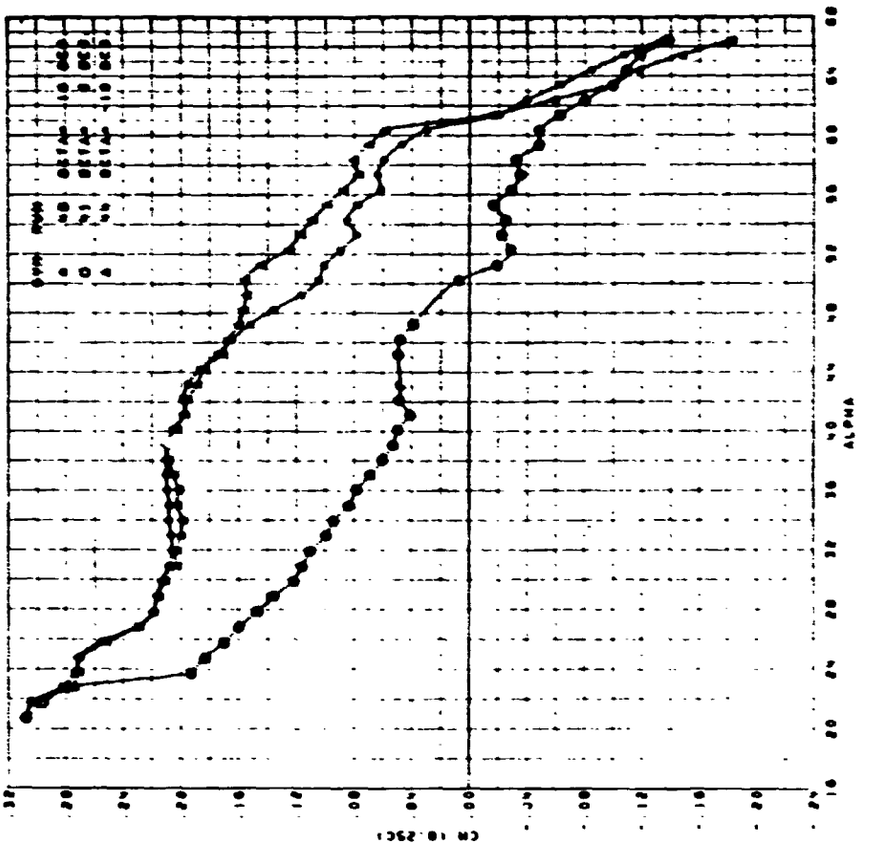

FIGURE 109. F-5F CLEAN CONFIGURATION. EFFECT OF SHARK NOSE B31 AT $\pm 10^{O}$ SIDESLIP, PITCHING MOMENT DATA

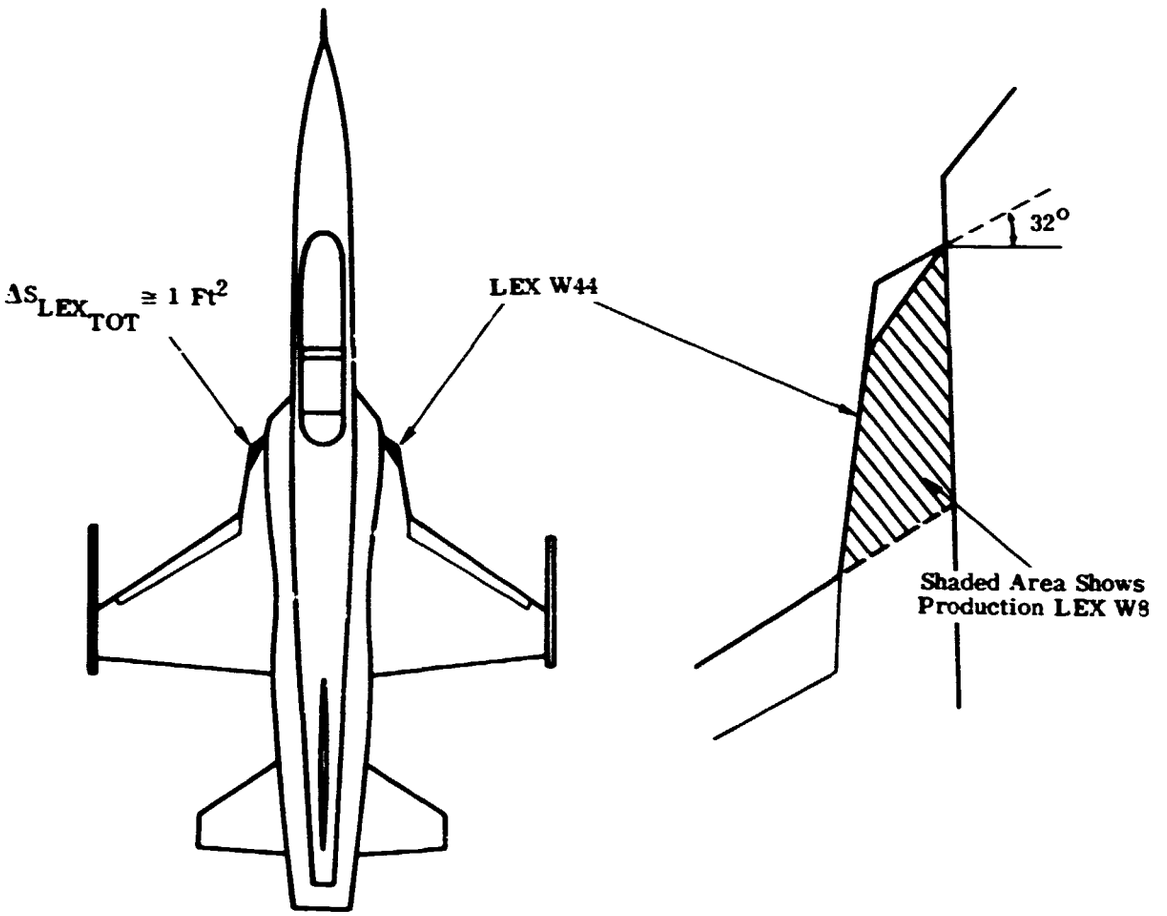

FIGURE 110. F-5F CLEAN CONFIGURATION. W44 LEX GEOMETRY

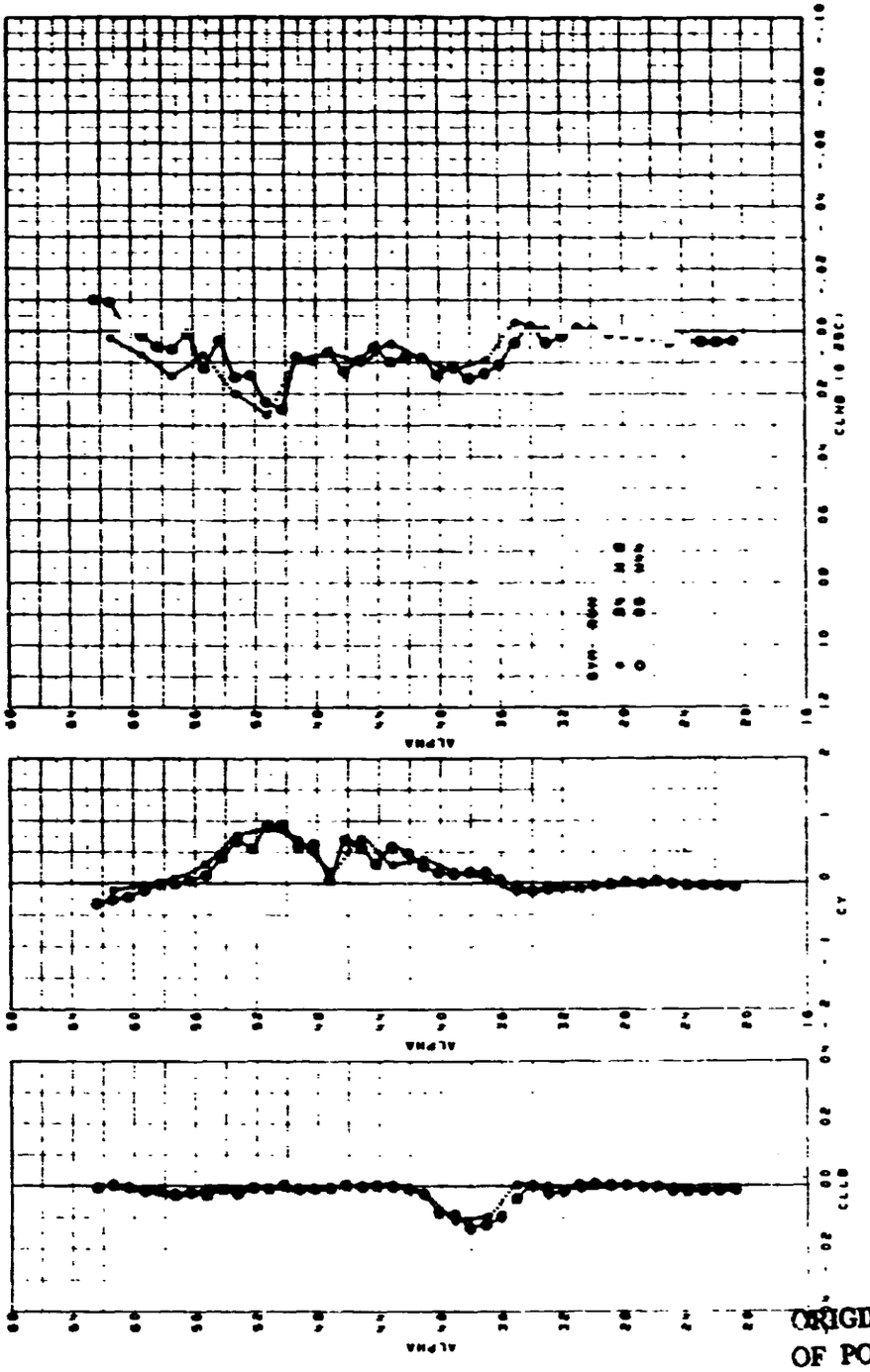

FIGURE 111. F-5F CLEAN CONFIGURATION. EFFECT OF SHARK NOSE AND W44 LEX AT ZERO SIDESLIP, LAT/DIR DATA

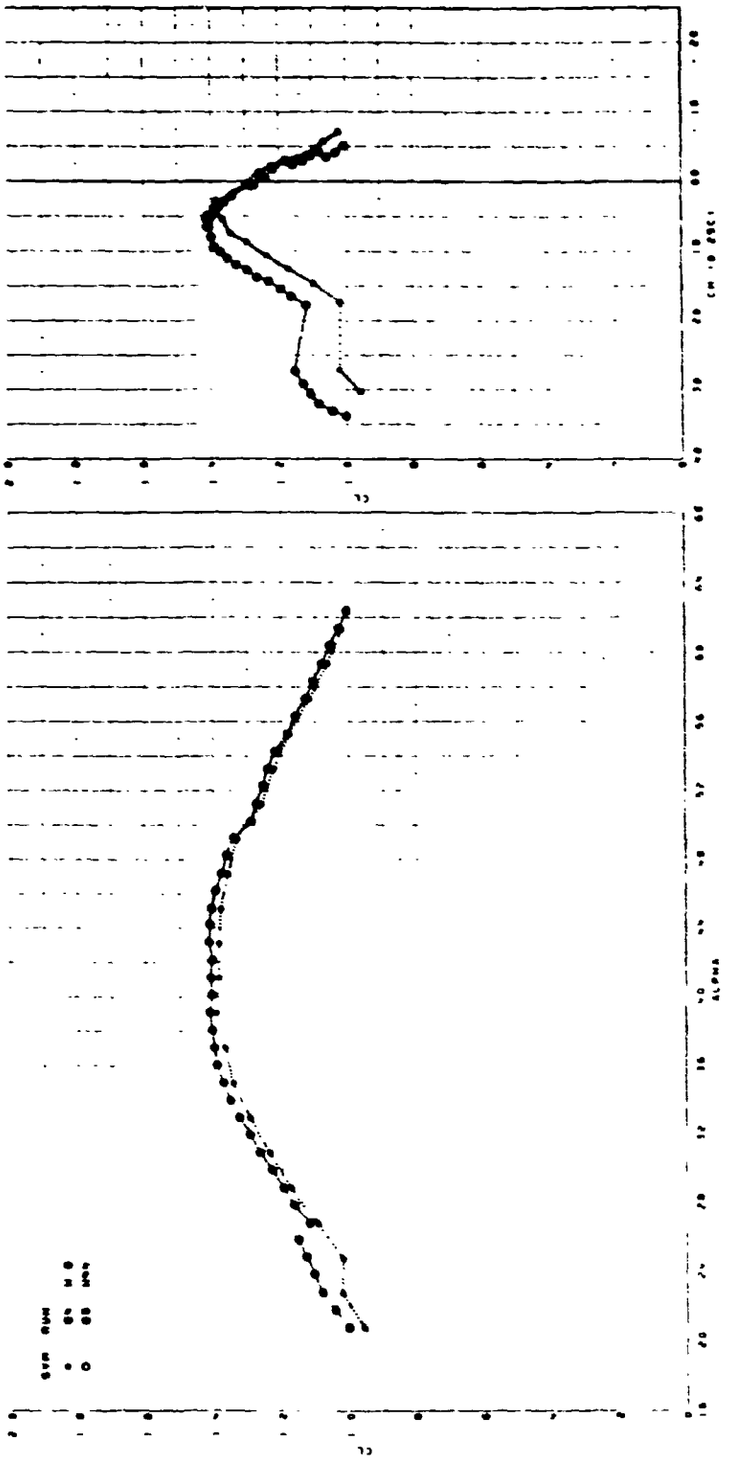

FIGURE 112. F-5F CLEAN CONFIGURATION. EFFECT OF SHARK NOSE AND W44 LEX AT ZERO SIDESLIP, LIFT AND PITCH DATA

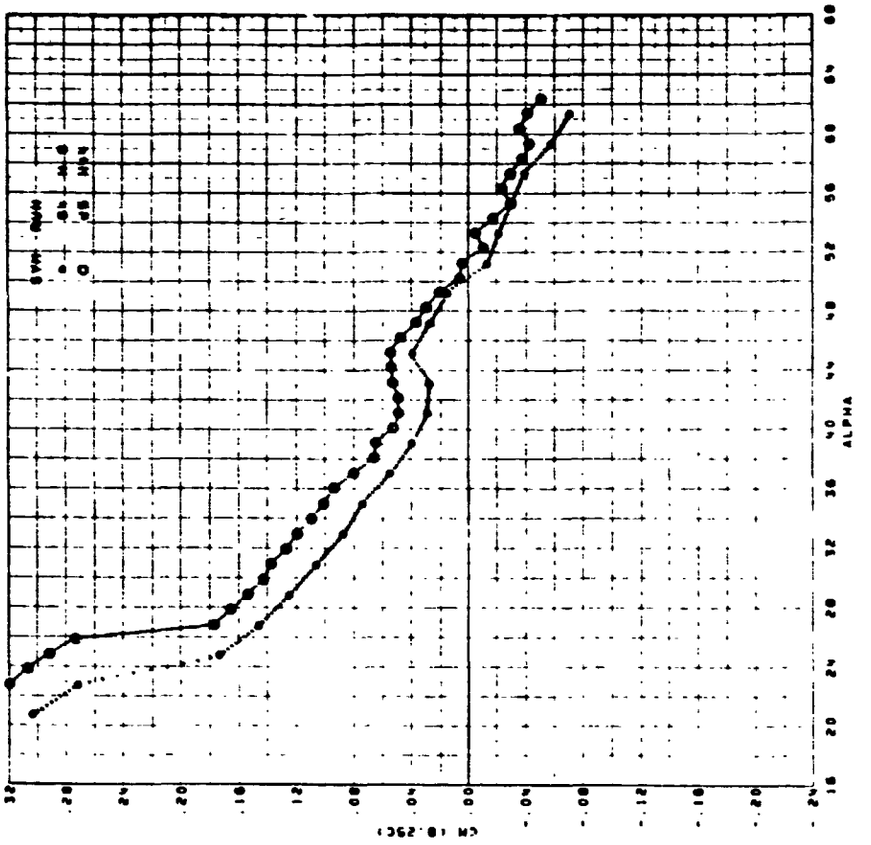

FIGURE 113. F-5F CLEAN CONFIGURATION. EFFECT OF SHARK NOSE & W44 LEX AT ZERO SIDESLIP, PITCHING MOMENT DATA

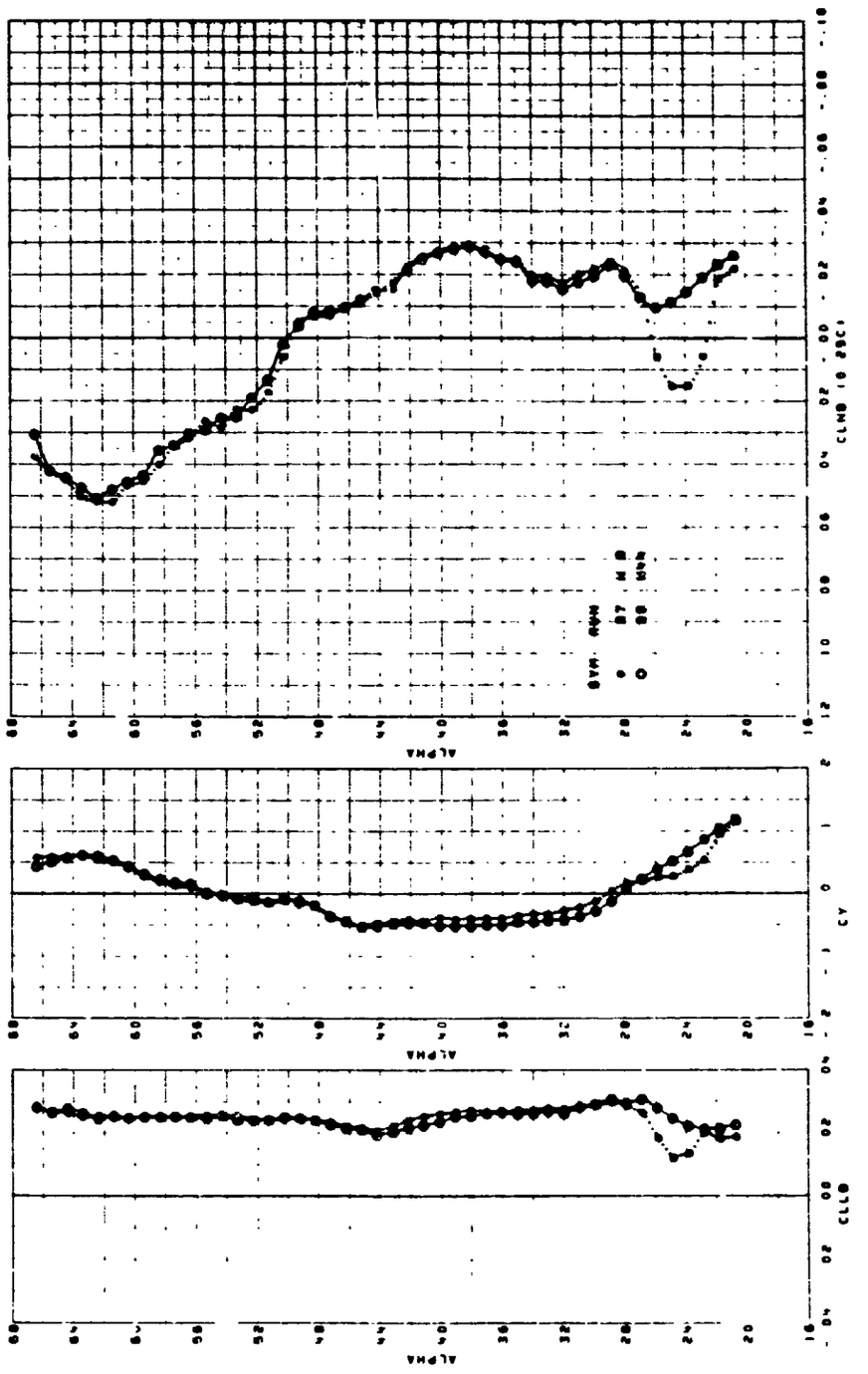

FIGURE 11⁄. F-5F CLEAN CONFIGURATION. EFFECT OF SHARK NOSE AND W4: LEX AT -10° SIDESLIP, LAT/DIR DATA

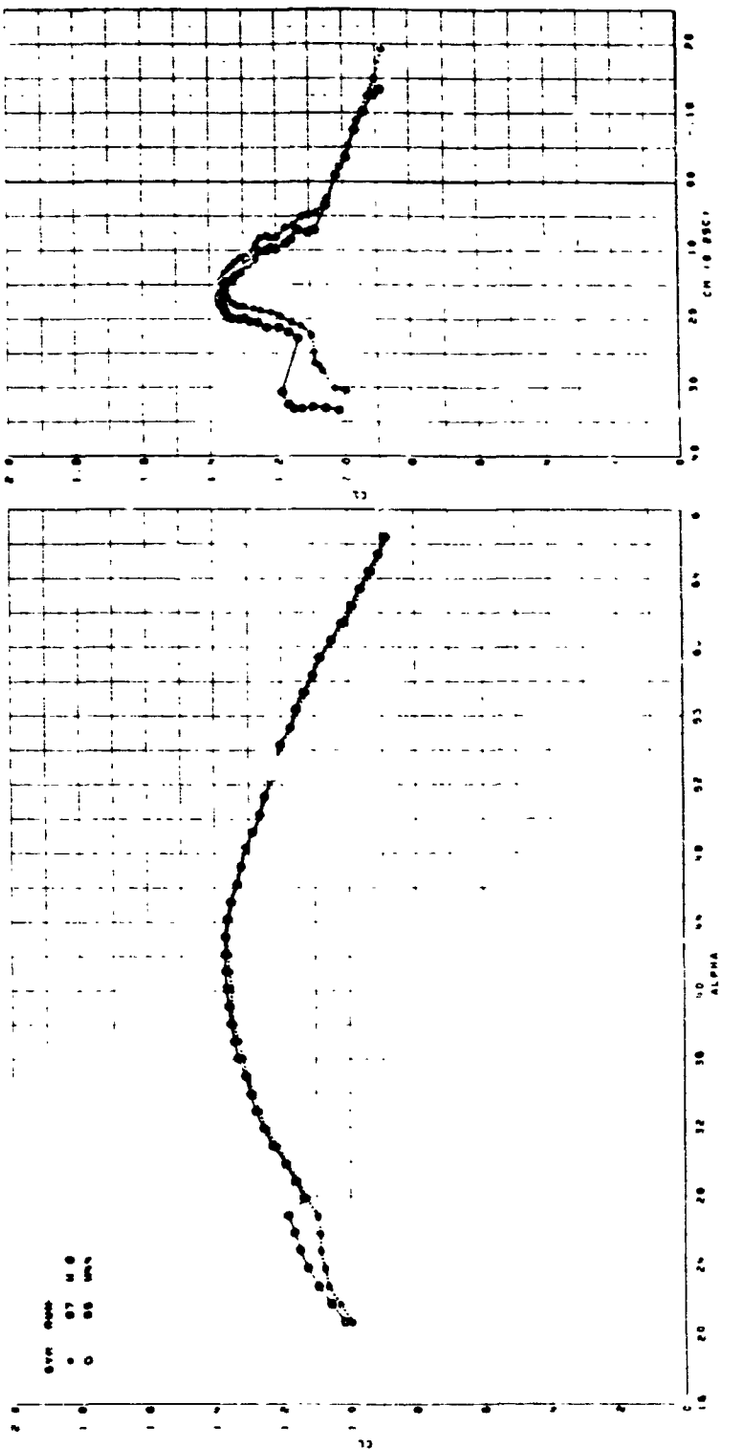

FIGURE 115. F-5F CLEAN CONFIGURATION. EFFECT OF CHINE NOSE AND W44 LEX AT -10° SIDESLIP, LIFT AND PITCH DATA

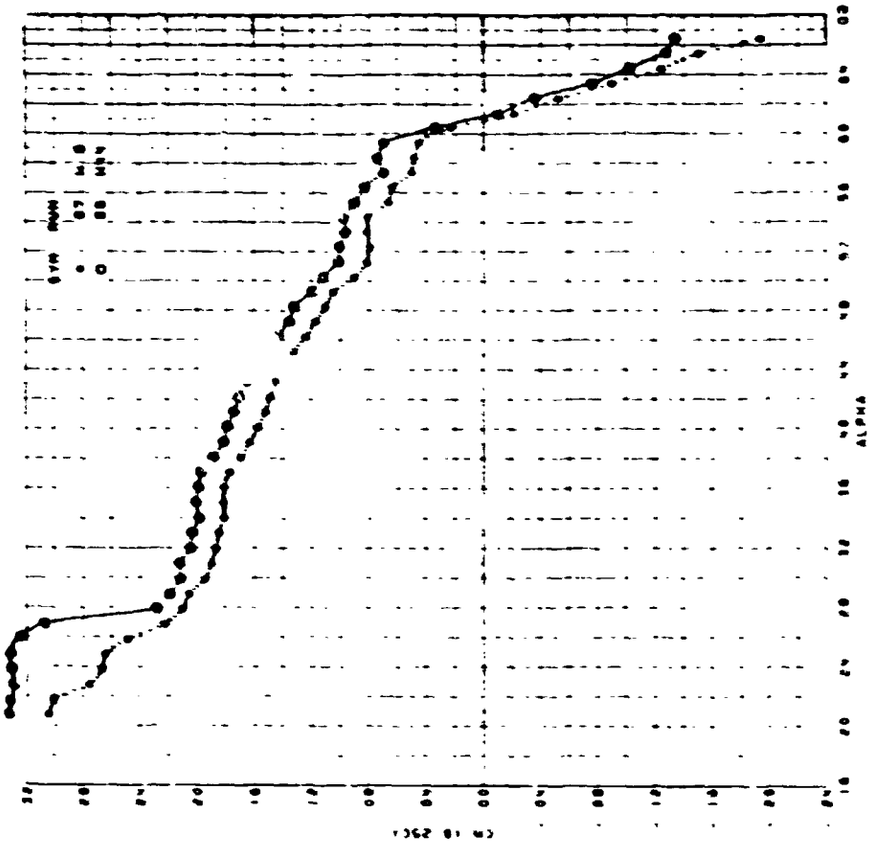

FIGURE 116. F-5F CLEAN CONFIGURATION. EFFECT OF SHARK NOSE AND W44 LEX AT -10° SIDESLIP, PITCHING MOMENT DATA

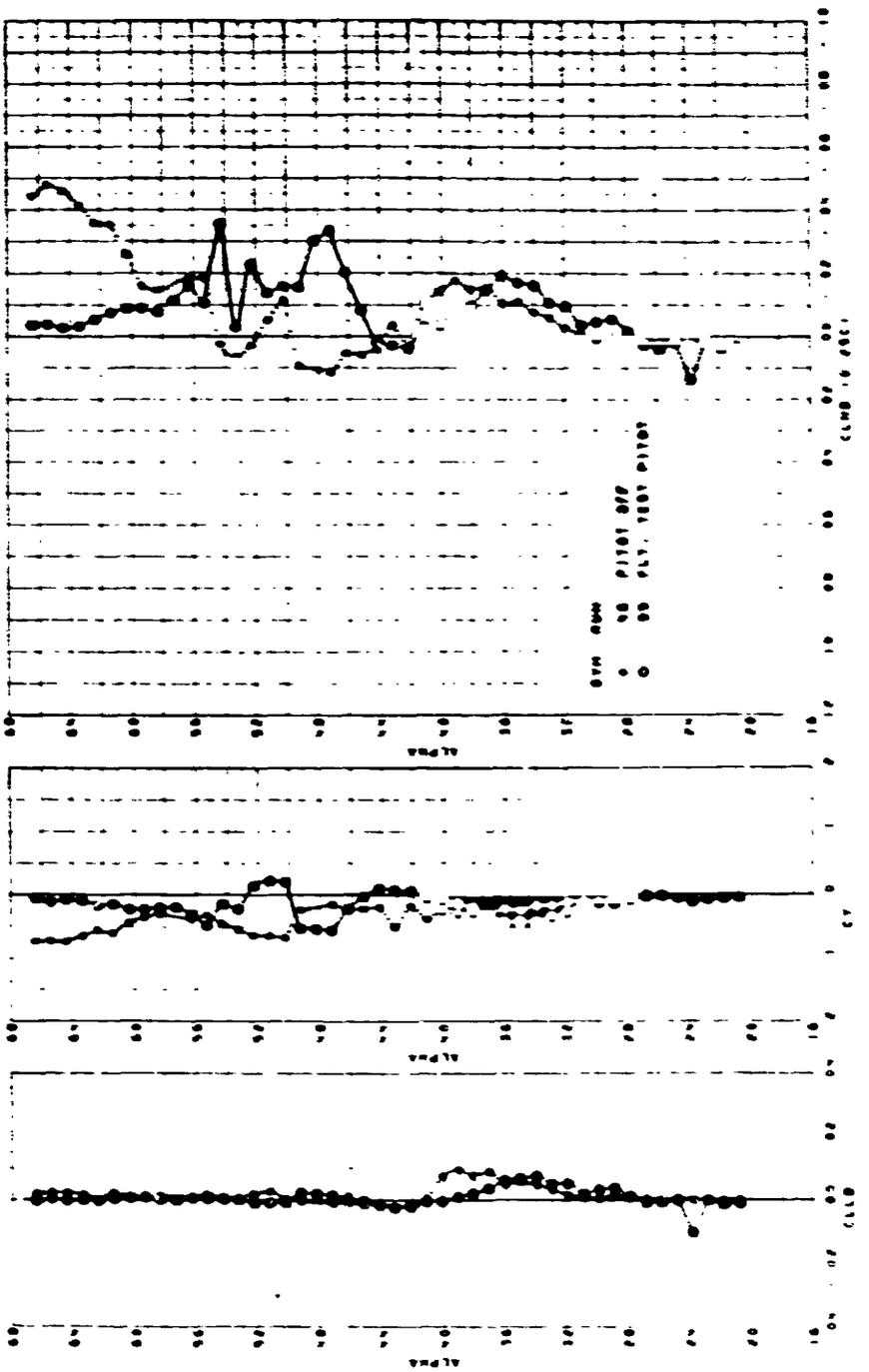

FIGURE 117. F-5F CLEAN CONFIGURATION. EFFECT OF FLIGHT TEST BOOM ON SHARK NOSE AT ZERO SIDESLIP, LAT/DIR DATA

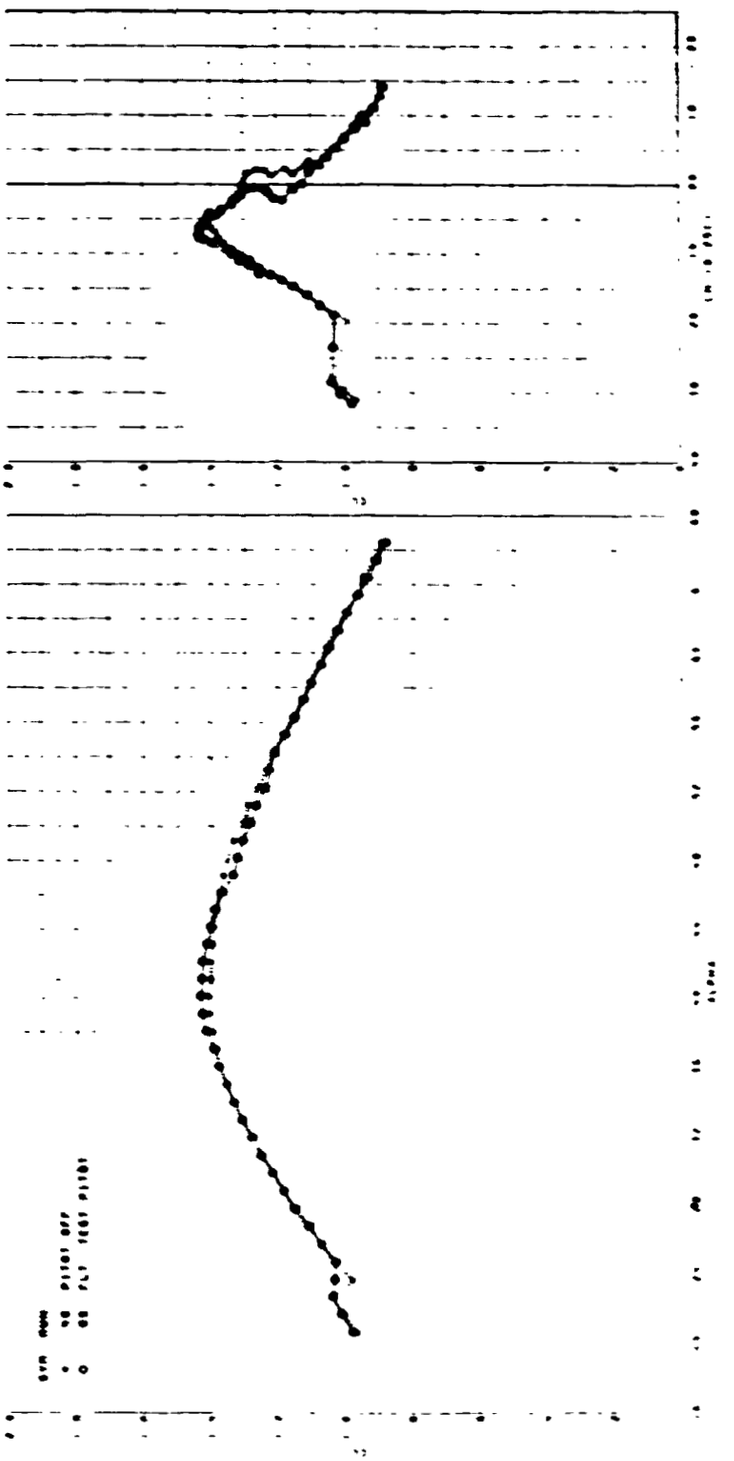

FIGURE 118. F-5F CLEAN CONFIGURATION. EFFECT OF FLIGHT TEST BOOM ON SHARK NOSE AT ZERO SIDESLIP, LIFT AND PITCH DATA

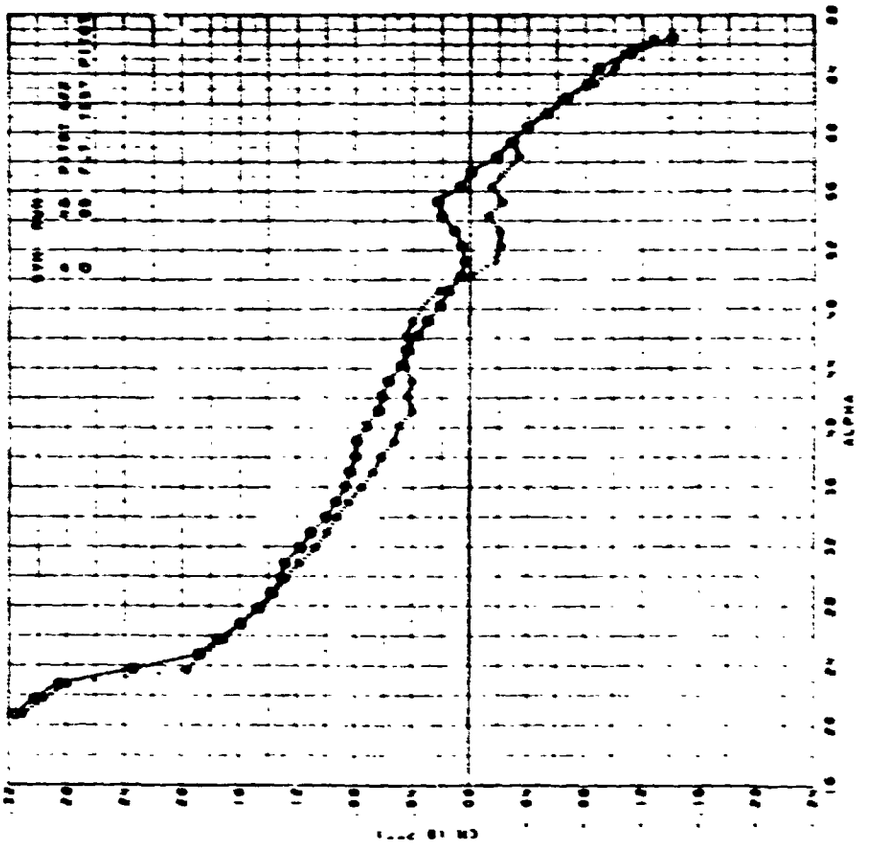

FIGURE 119. F-5F CLEAN CONFIGURATION. EFFECT OF FLIGHT TEST BOOM ON SHARK NOSE AT ZERO SIDESLIP, PITCHING MOMENT DATA

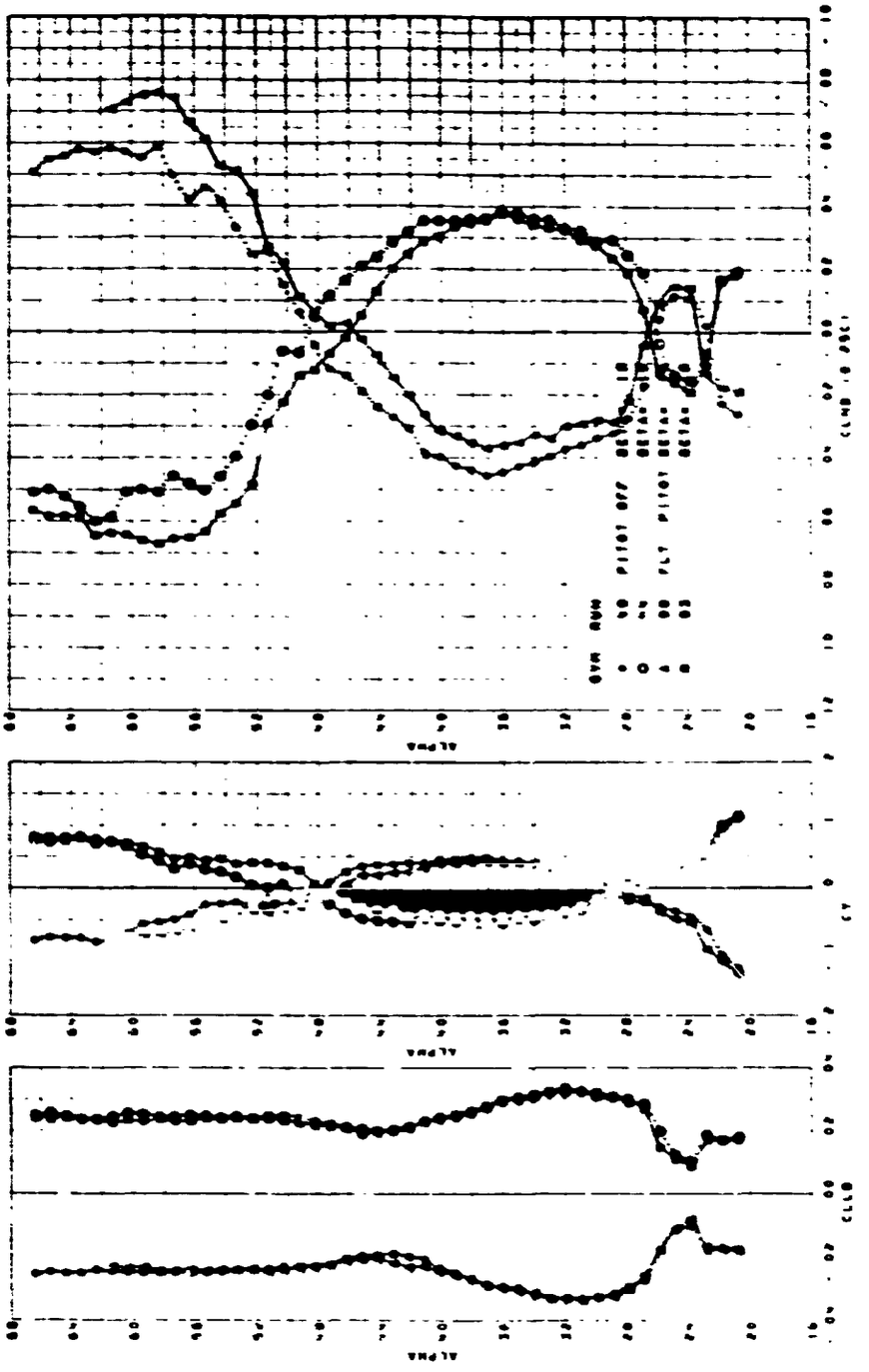

FIGURE 120. F-5F CLEAN CONFIGURATION. EFFECT OF FLIGHT TEST BOOM ON SHARK NOSE AT ±10° SIDESLIP, LAT/DIR DATA

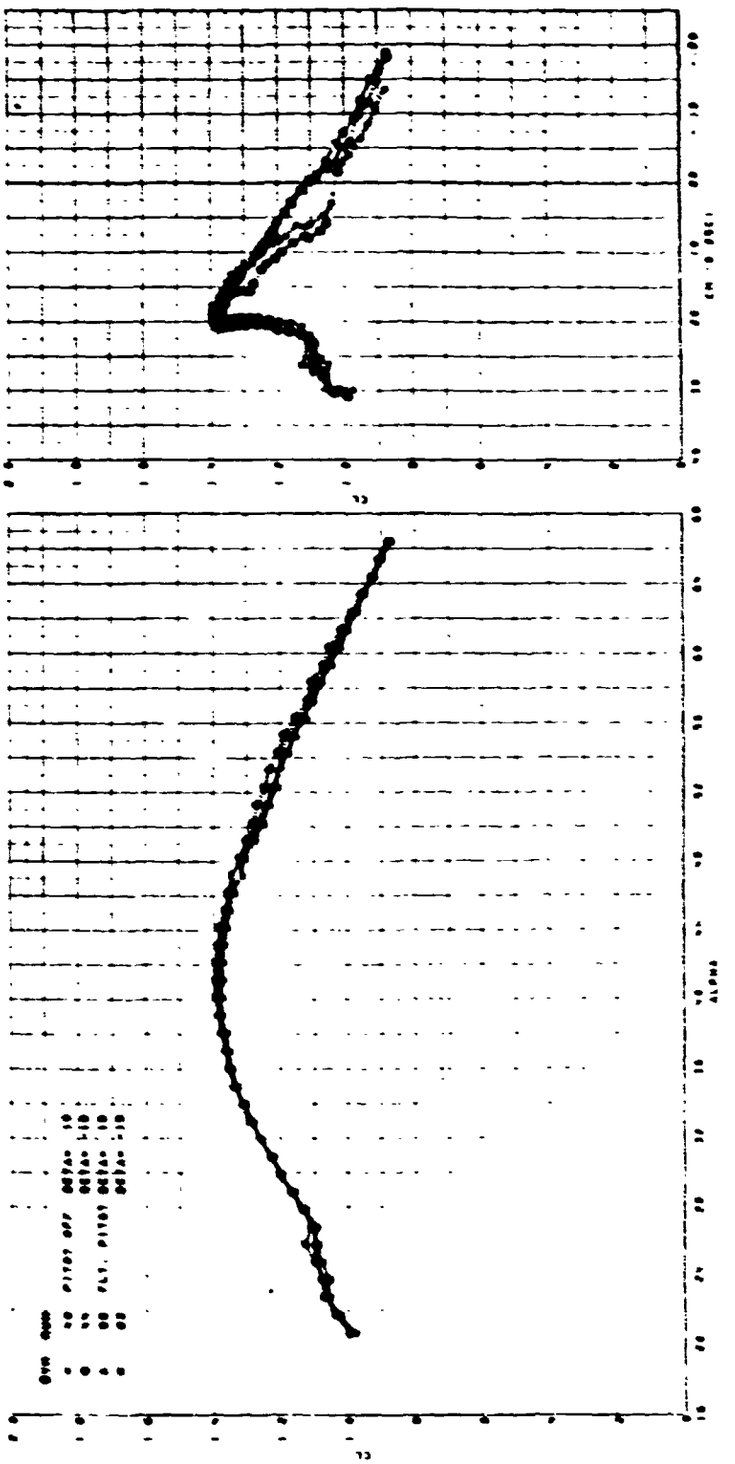

FIGURE 121. F-5F CLEAN CONFIGURATION. EFFECT OF FLIGHT TEST BOOM ON SHARK NOSE AT ±10° SIDESLIP, LIFT AND PITCH DATA

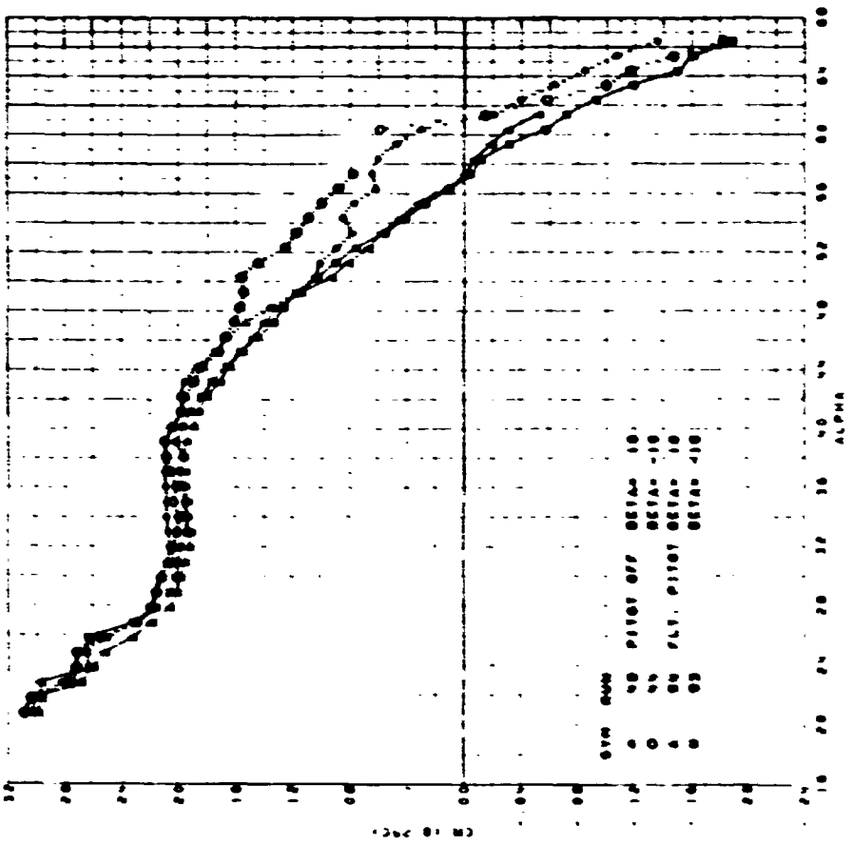

FIGURE 122. F-5F CLEAN CONFIGURATION. EFFECT OF FLIGHT TEST BOOM ON SHARK NOSE AT ±10° SIDESLIP, PITCHING MOMENT DATA

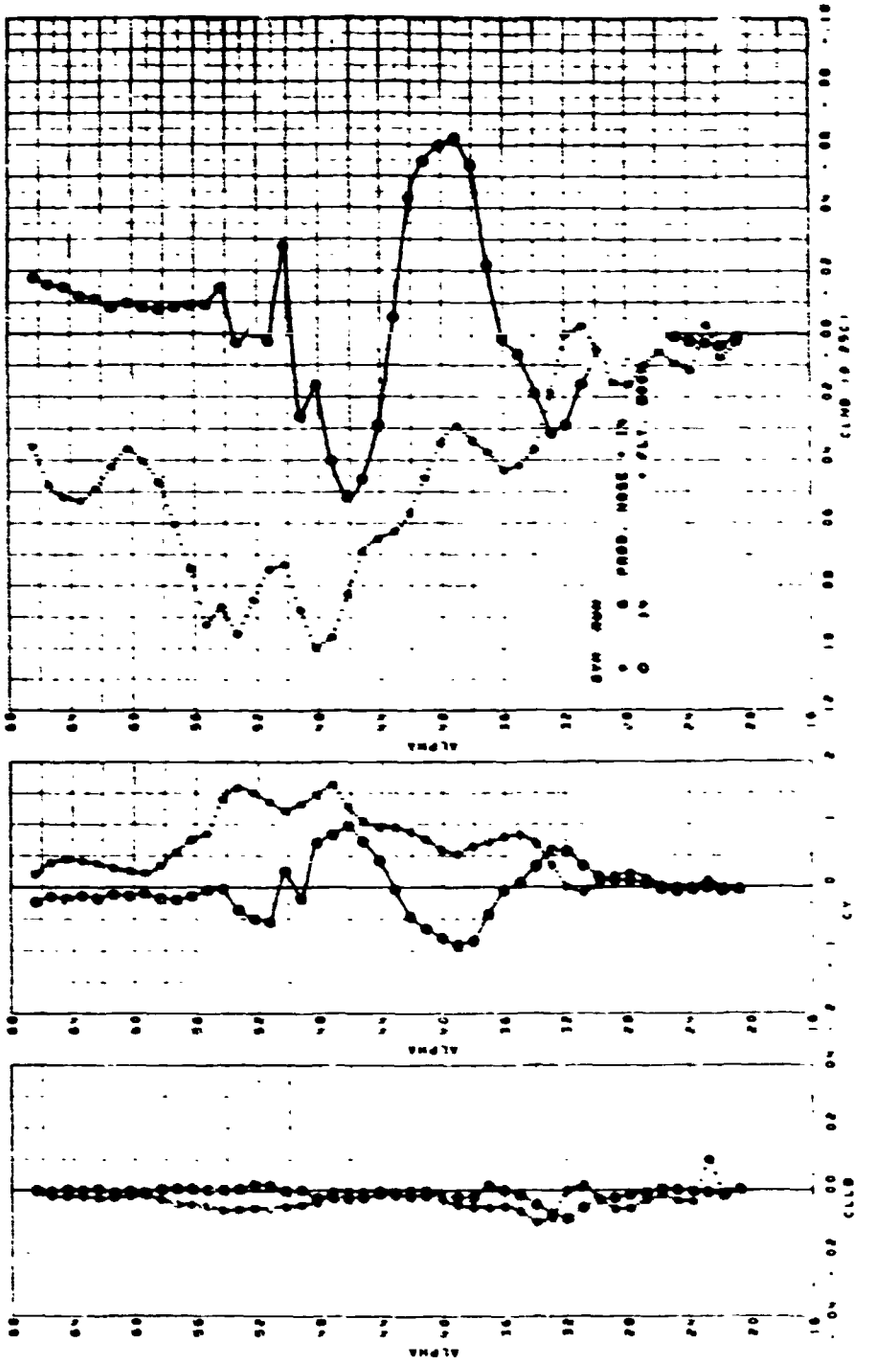

FIGURE 123. F-5F CLEAN CONFIGURATION. EFFECT OF FLIGHT TEST BOOM ON PRODUCTION NOSE AT ZERO SIDESLIP, LAT/DIR DATA

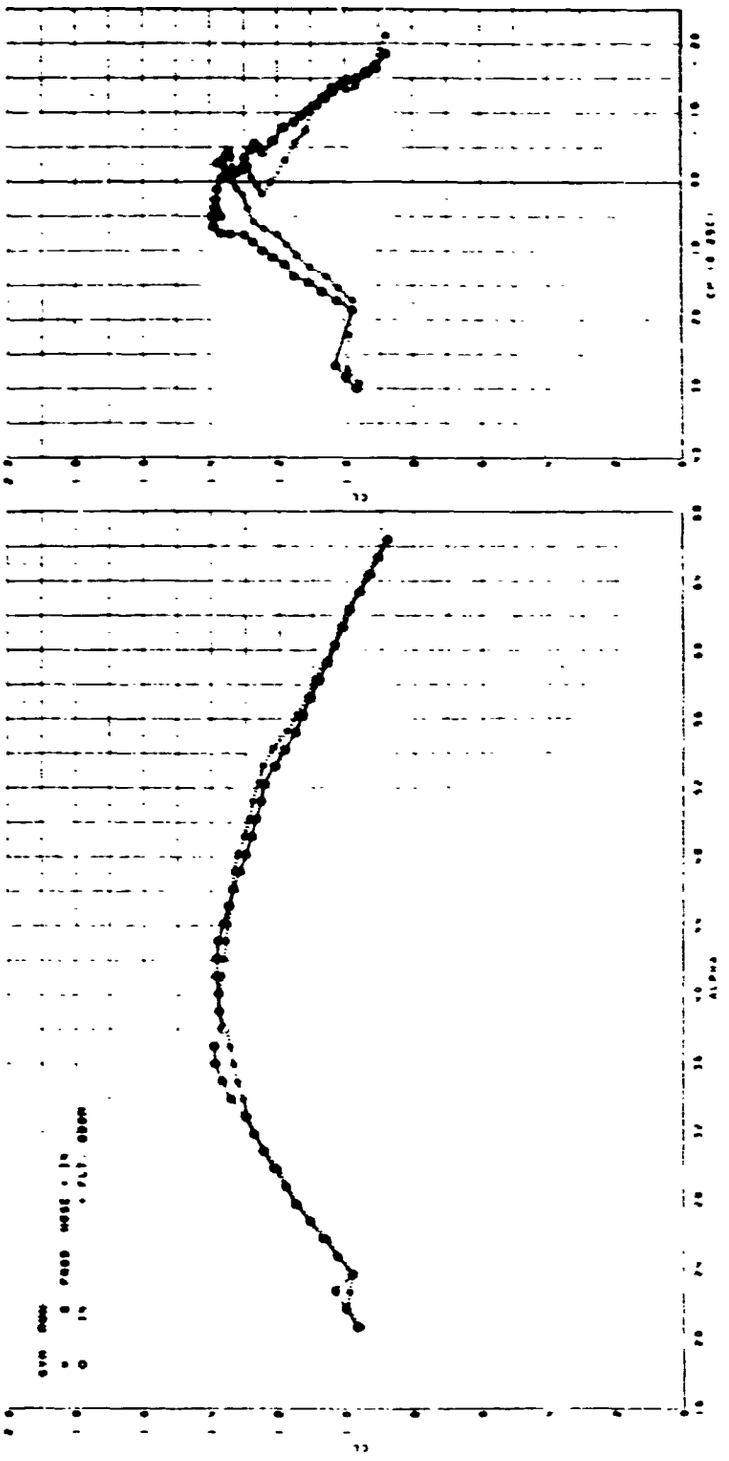

FIGURE 124. F-5F CLEAN CONFIGURATION. EFFECT OF FLIGHT TEST BOOM ON PRODUCTION NOSE AT ZERO SIDESLIP, LIFT AND PITCH DATA

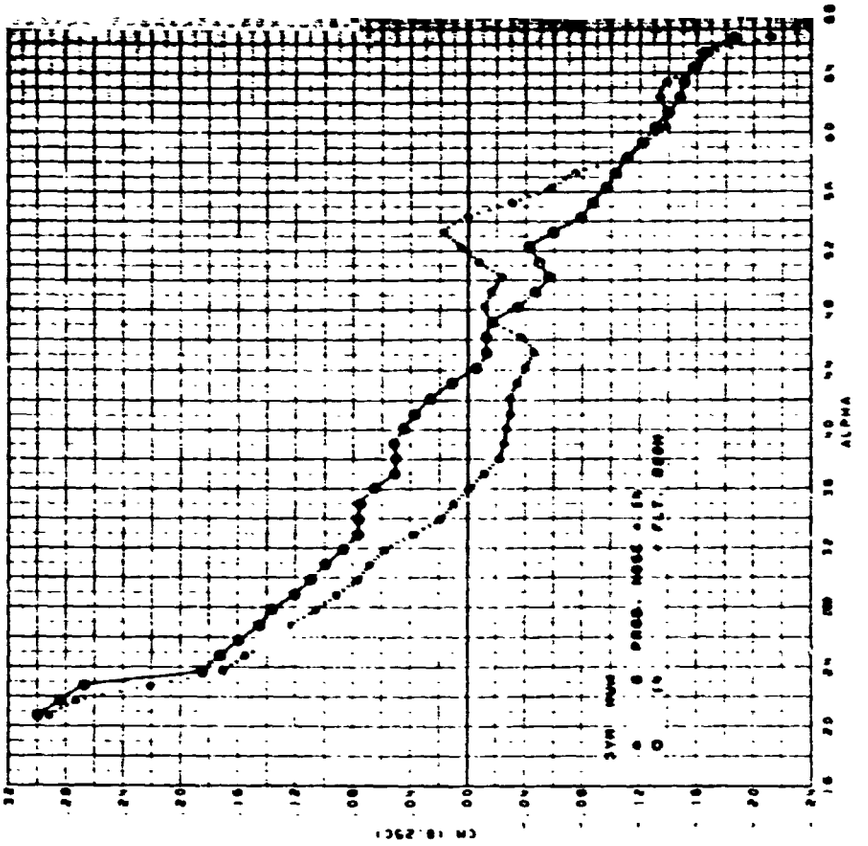

FIGURE 125. F-5F CLEAN CONFIGURATION. EFFECT OF FLIGHT TEST BOOM ON PRODUCTION NOSE AT ZERO SIDESLIP, PITCHING MOMENT DATA

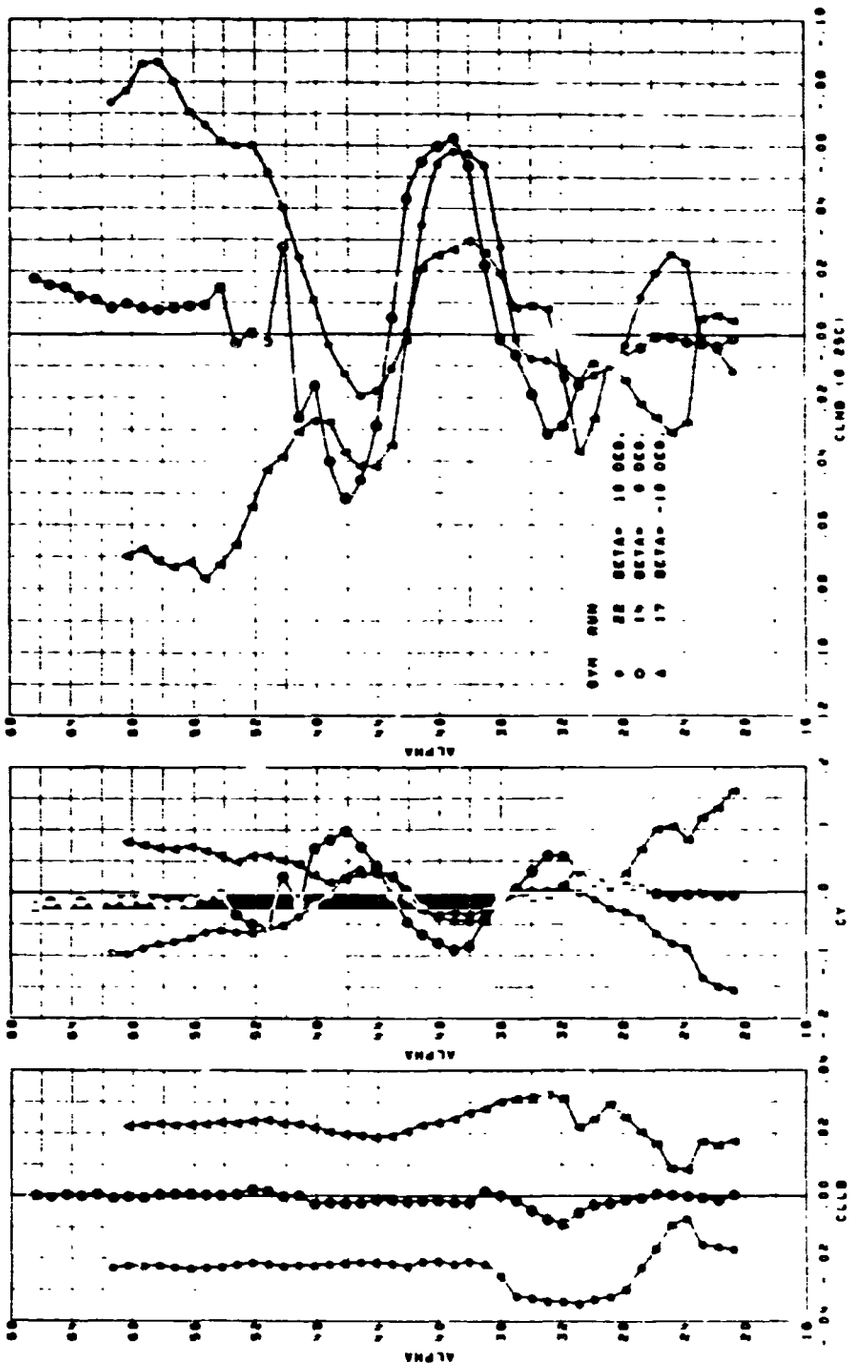

FIGURE 126. F-5F CLEAN CONFIGURATION. EFFECT OF FLT TEST BOOM ON PRODUCTION NOSE AT ±10° SIDESLIP, LAT/DIR DATA

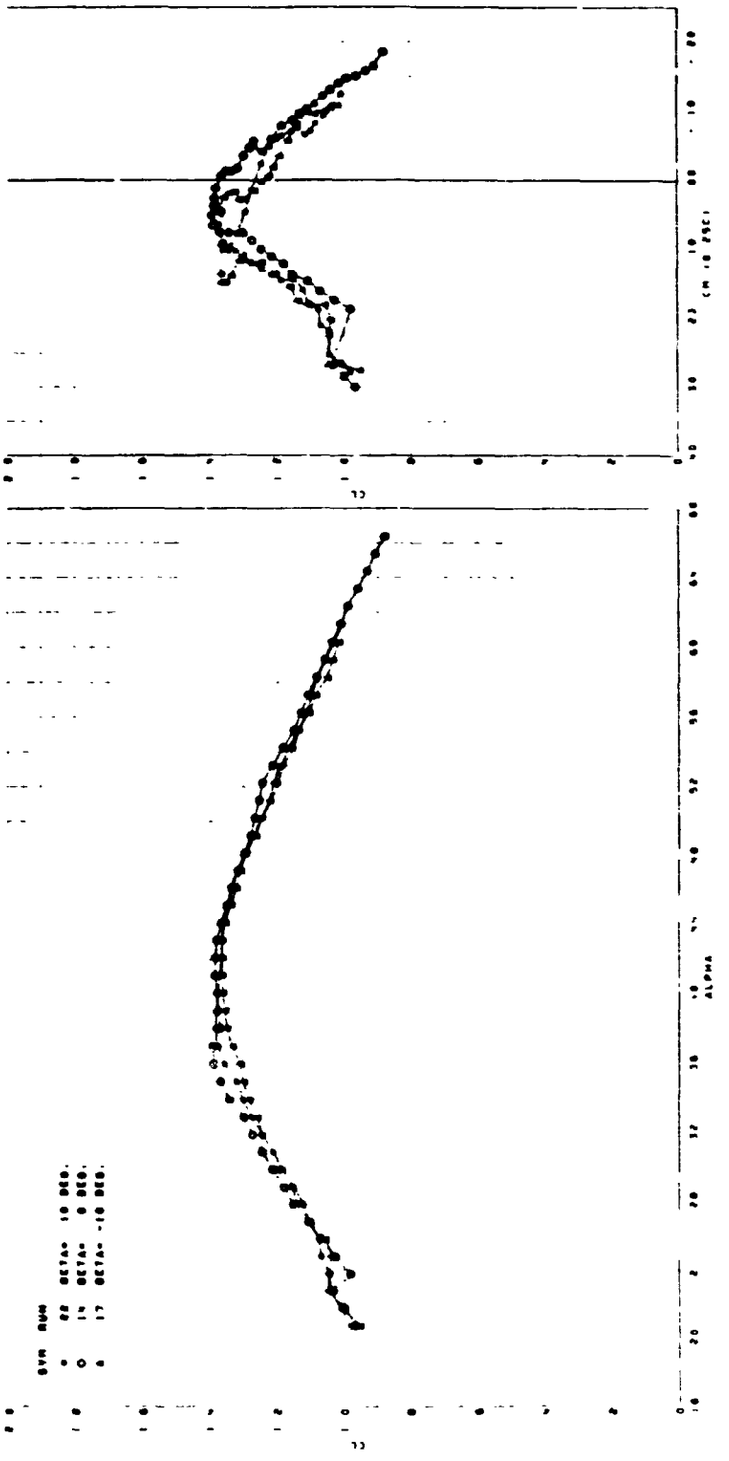

FIGURE 127. F-5F CLEAN CONFIGURATION. EFFECT OF FLIGHT TEST BOOM ON PRODUCTION NOSE AT ±10° SIDESLIP, LIFT AND PITCH DATA

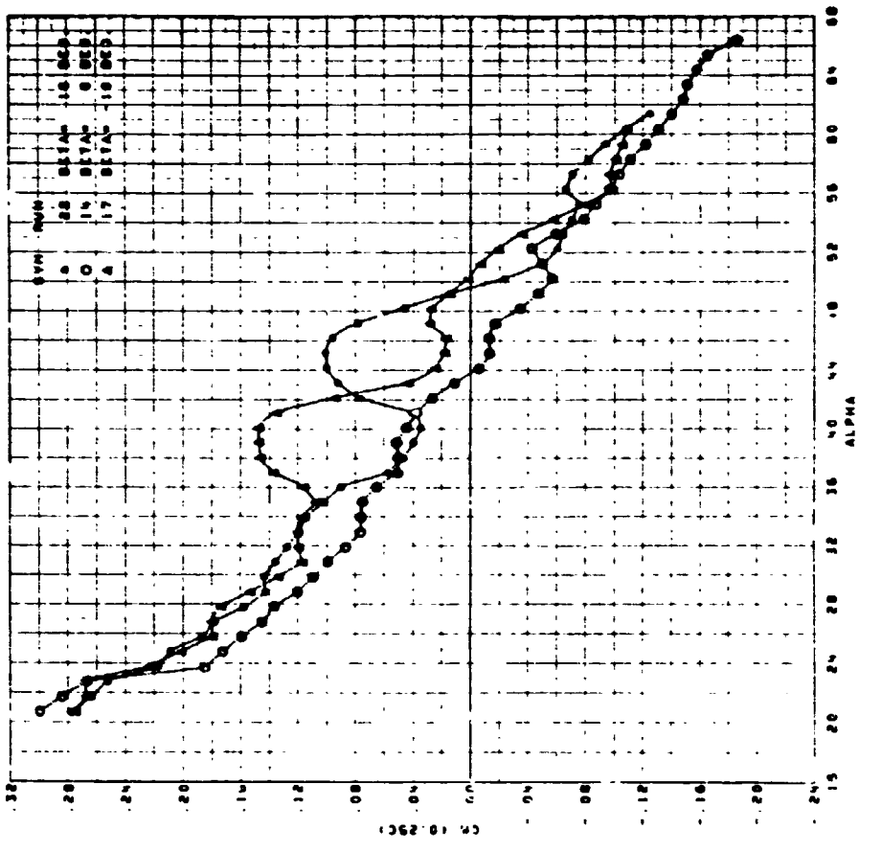

FIGURE 128. F-5F CLEAN CONFIGURATION. EFFECT OF FLIGHT TEST BOOM ON PRODUCTION NOSE AT ±10° SIDESLIP, PITCHING MOMENT DATA

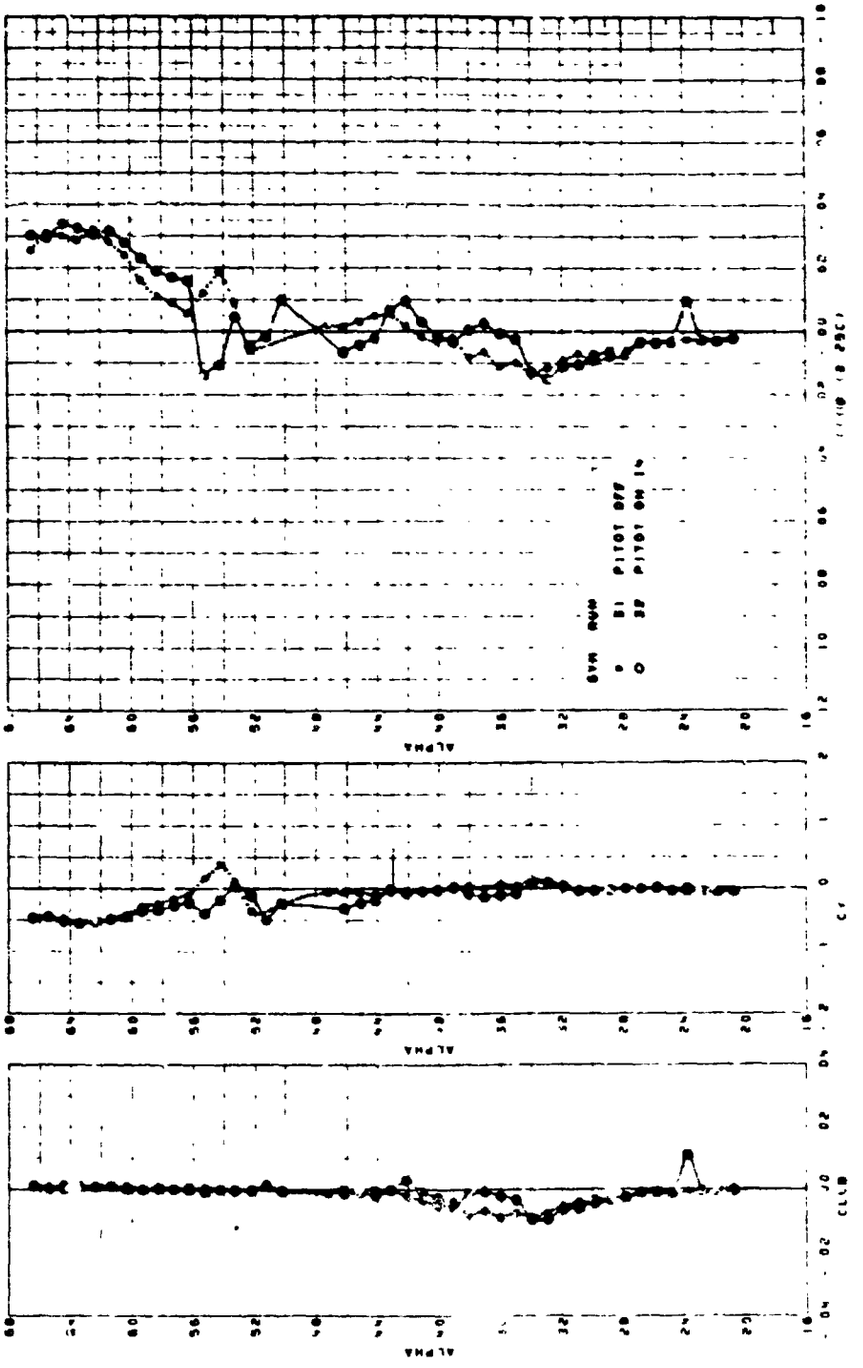

FIGURE 129. F-5F CLEAN CONFIGURATION. EFFECT OF PRODUCTION PITOT ON SHARK NOSE B29 AT ZERO SIDESLIP, LAT/DIR DATA

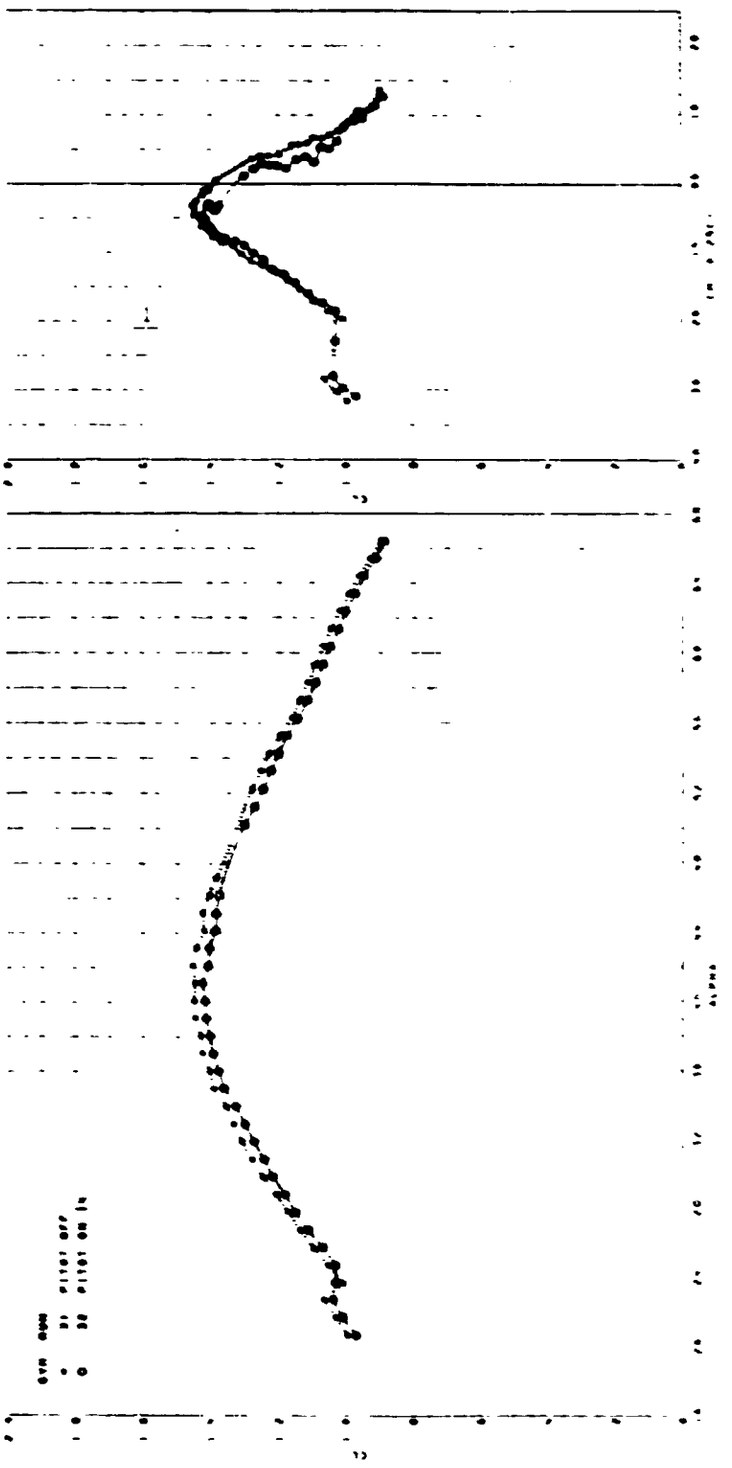

FIGURE 130. F-5F CLEAN CONFIGURATION. EFFECT OF PRODUCTION PITOT ON SHARK NOSE B29 AT ZERO SIDESLIP, LIFT AND PITCH DATA

C-3

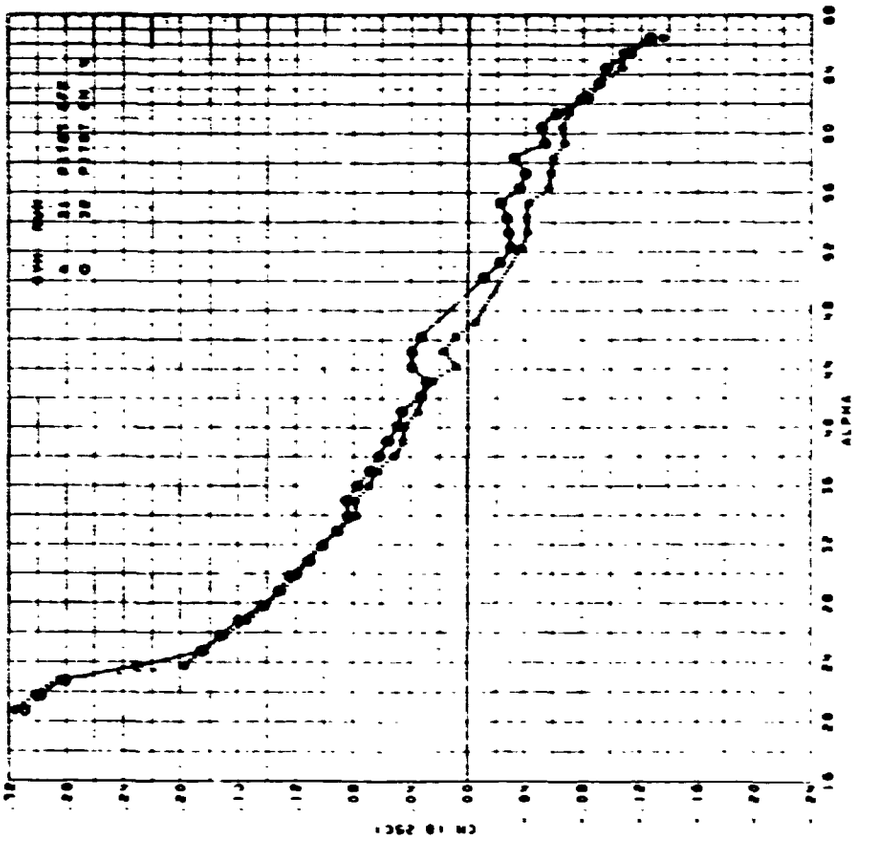

FIGURE 131. F-5F CLEAN CONFIGURATION. EFFECT OF PRODUCTION PITOT ON SHARK NOSE B29 AT ZERO SIDESLIP, PITCHING MOMENT DATA

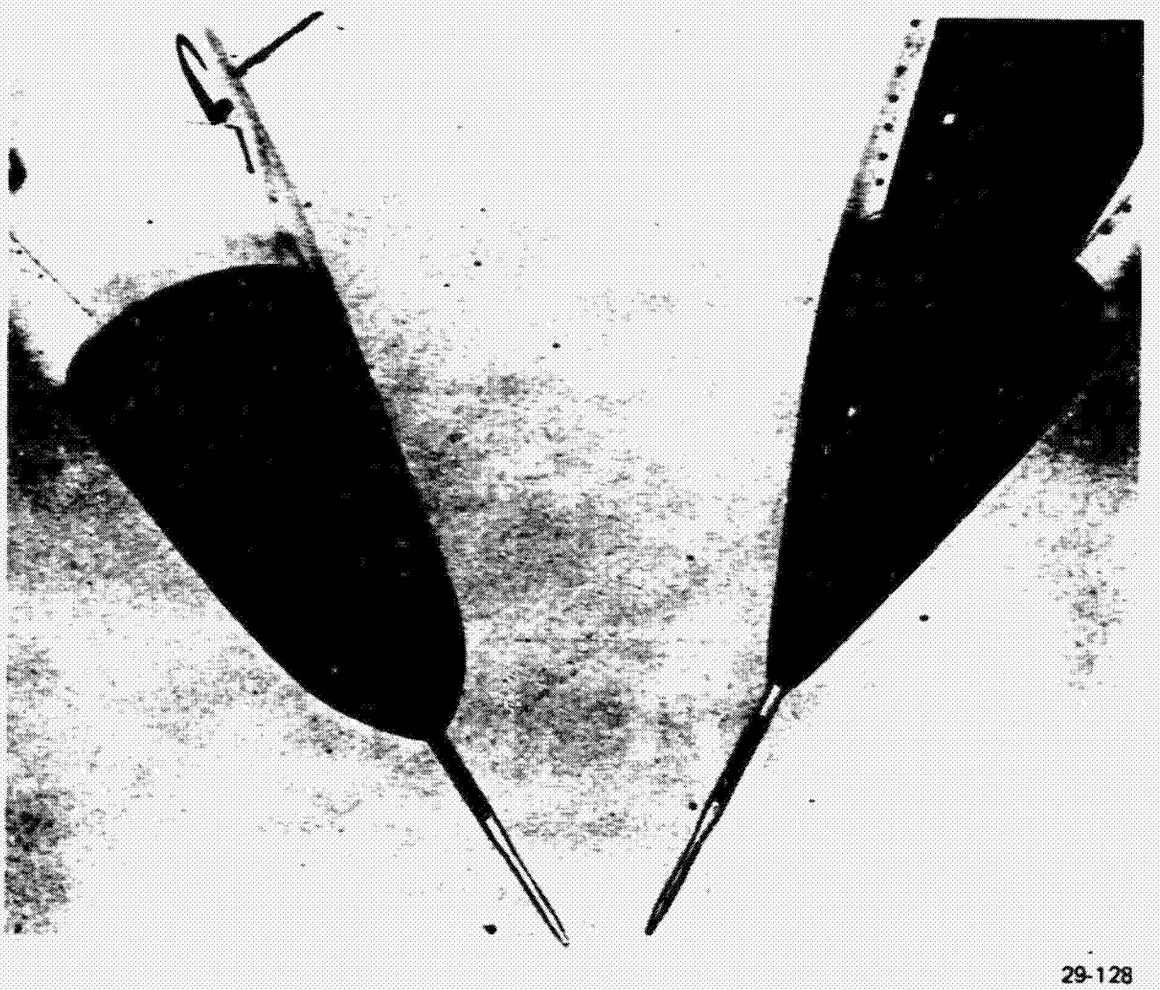

FIGURE 132. F-5F COMPARISON OF SHARK NOSE AND PRODUCTION NOSE

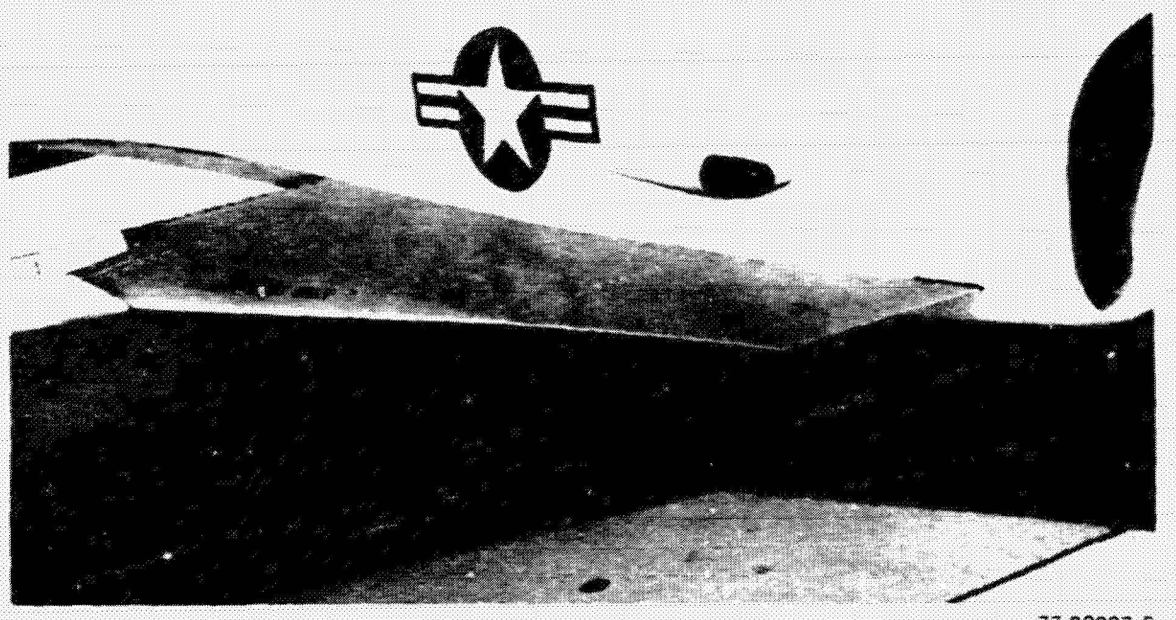

77-00927-5

FIGURE 133. W44 LEX INSTALLED ON F-5F AIRPLANE

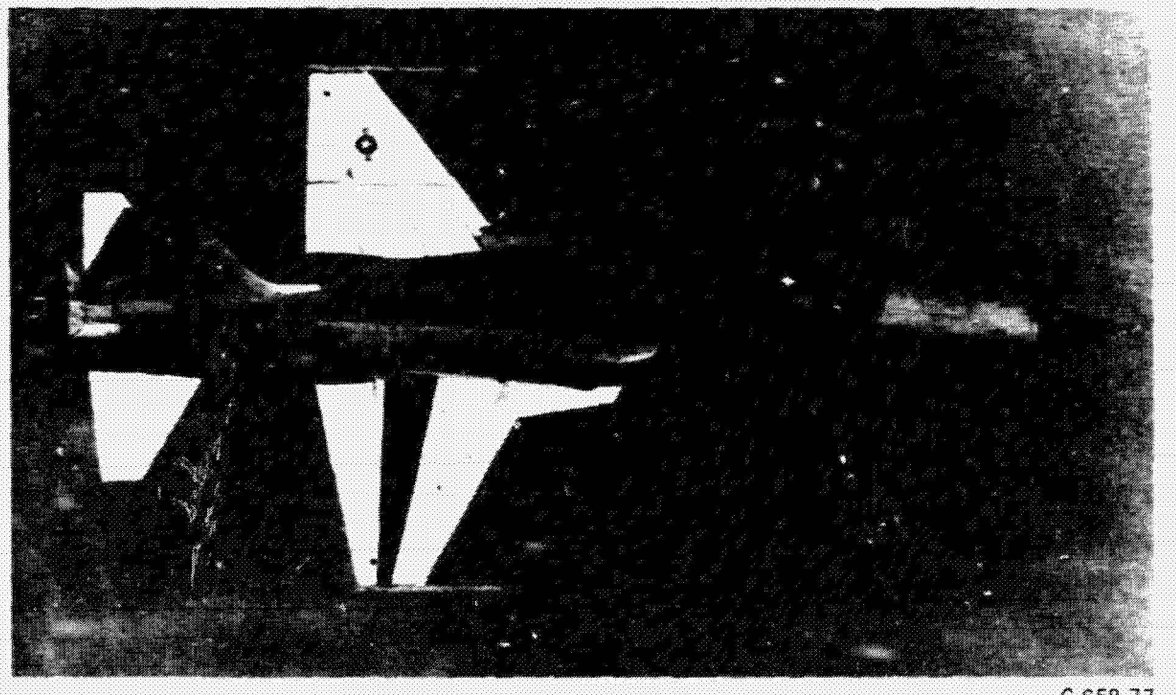

C-658-77

FIGURE 134. F-5F FLIGHT TEST AIRPLANE WITH SHARK NOSE AND W44 LEX INSTALLED

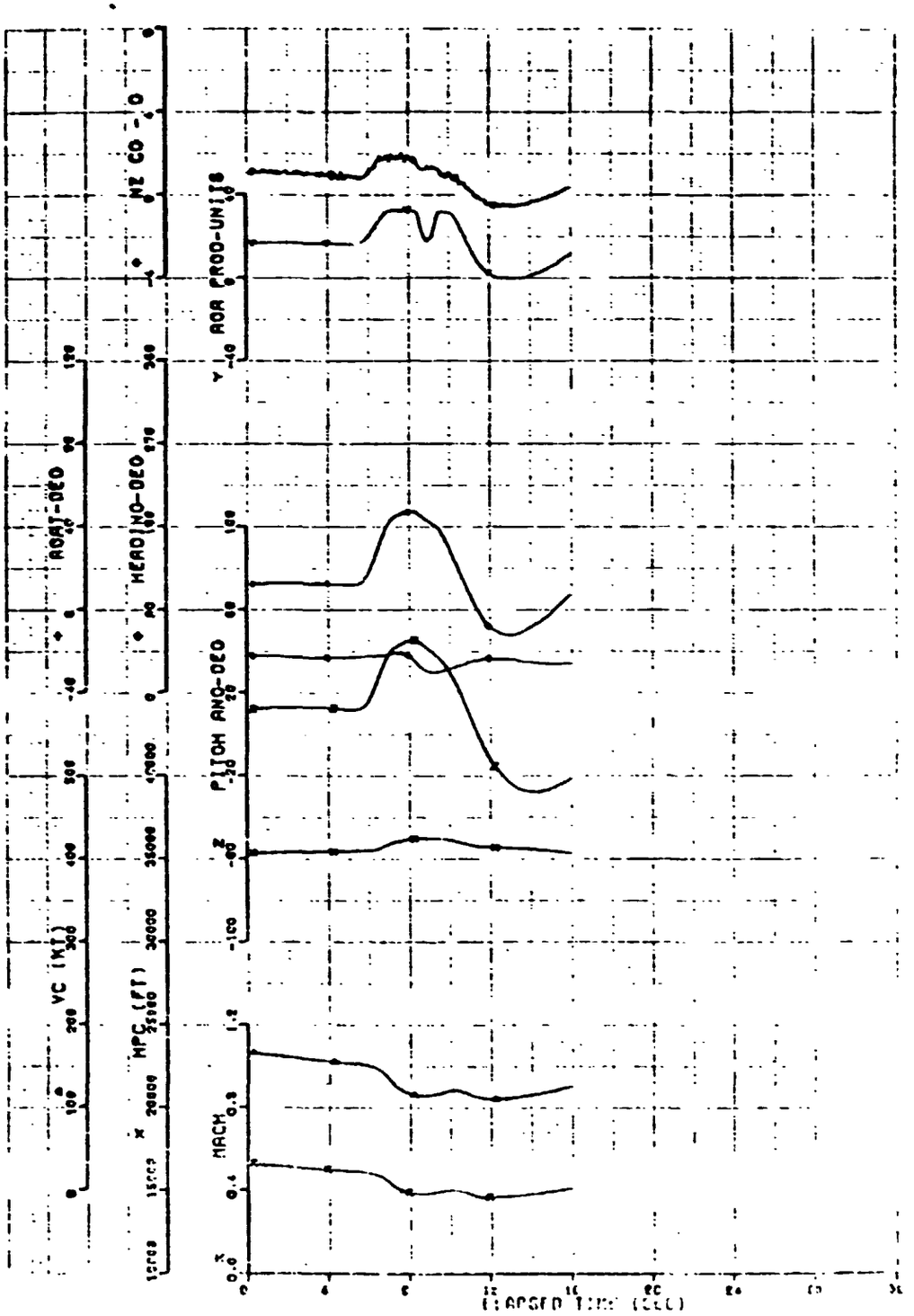

FIGURE 135. F-5F CLEAN CONFIGURATION. ABRUPT PULL UP
(Sheet 1 of 8)

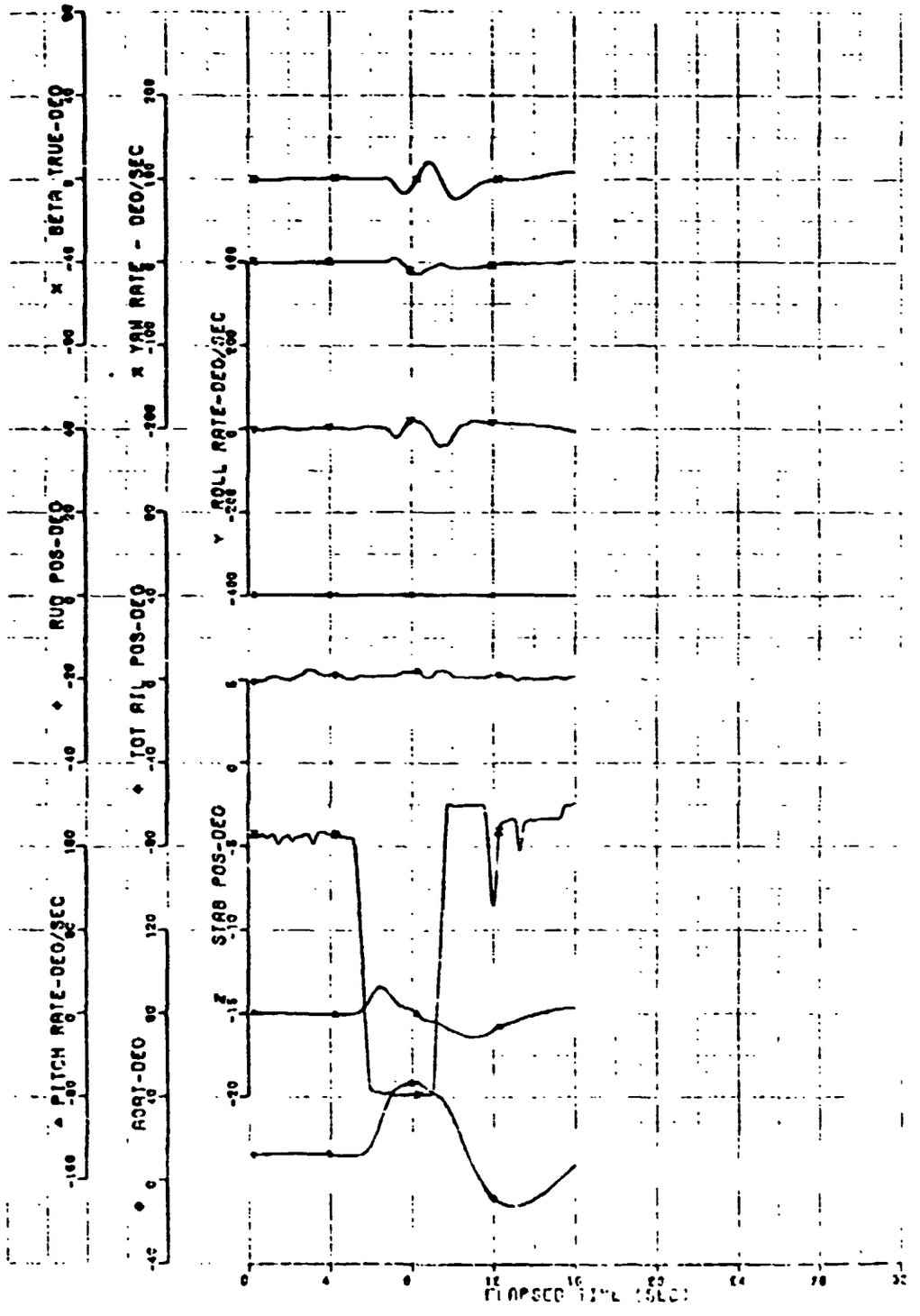

FIGURE 135. F-5F CLEAN CONFIGURATION. ABRUPT PULL UP
(Sheet 2 of 8)

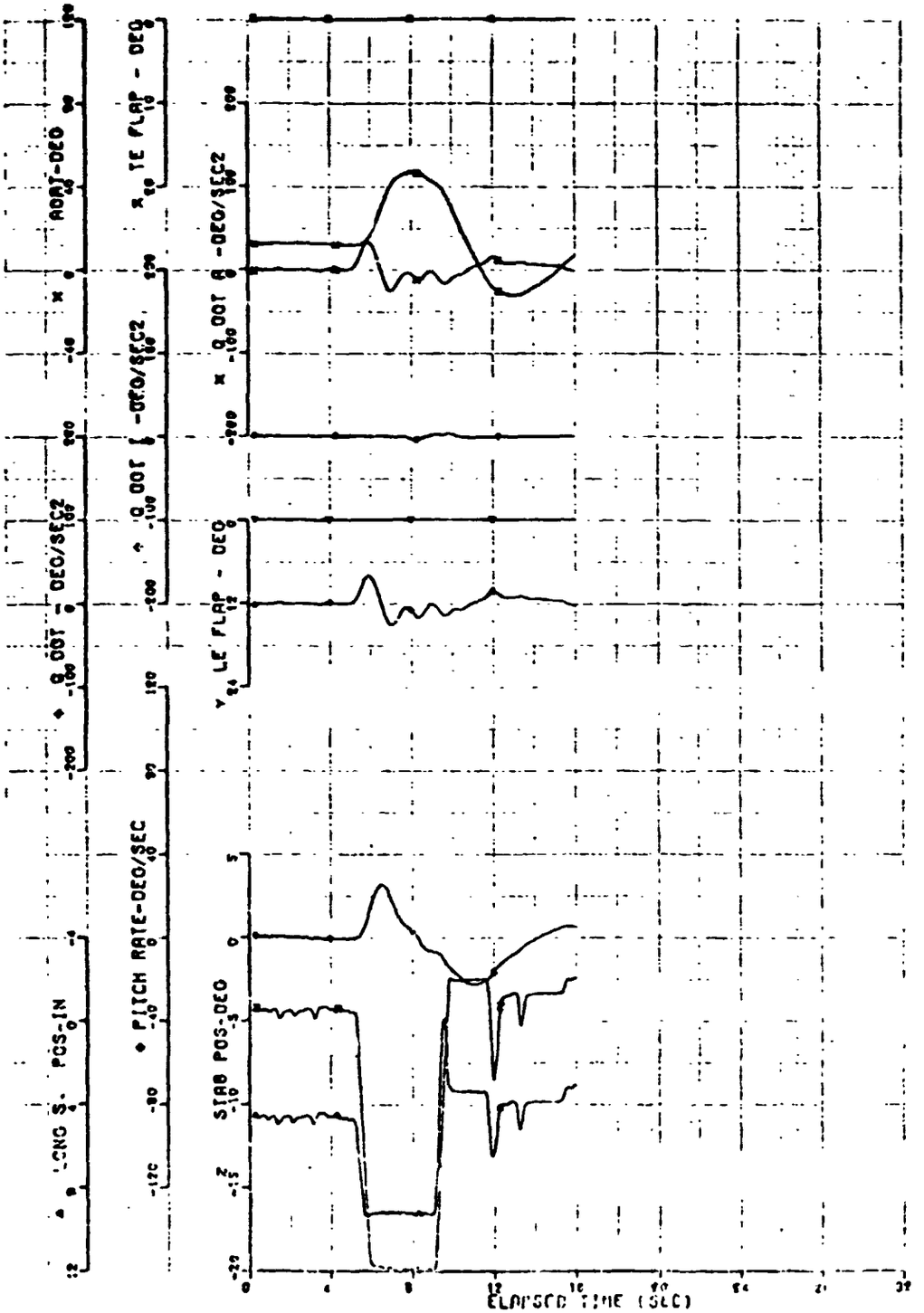

FIGURE 135. F-5F CLEAN CONFIGURATION. ABRUPT PULL UP
(Sheet 3 of 8)

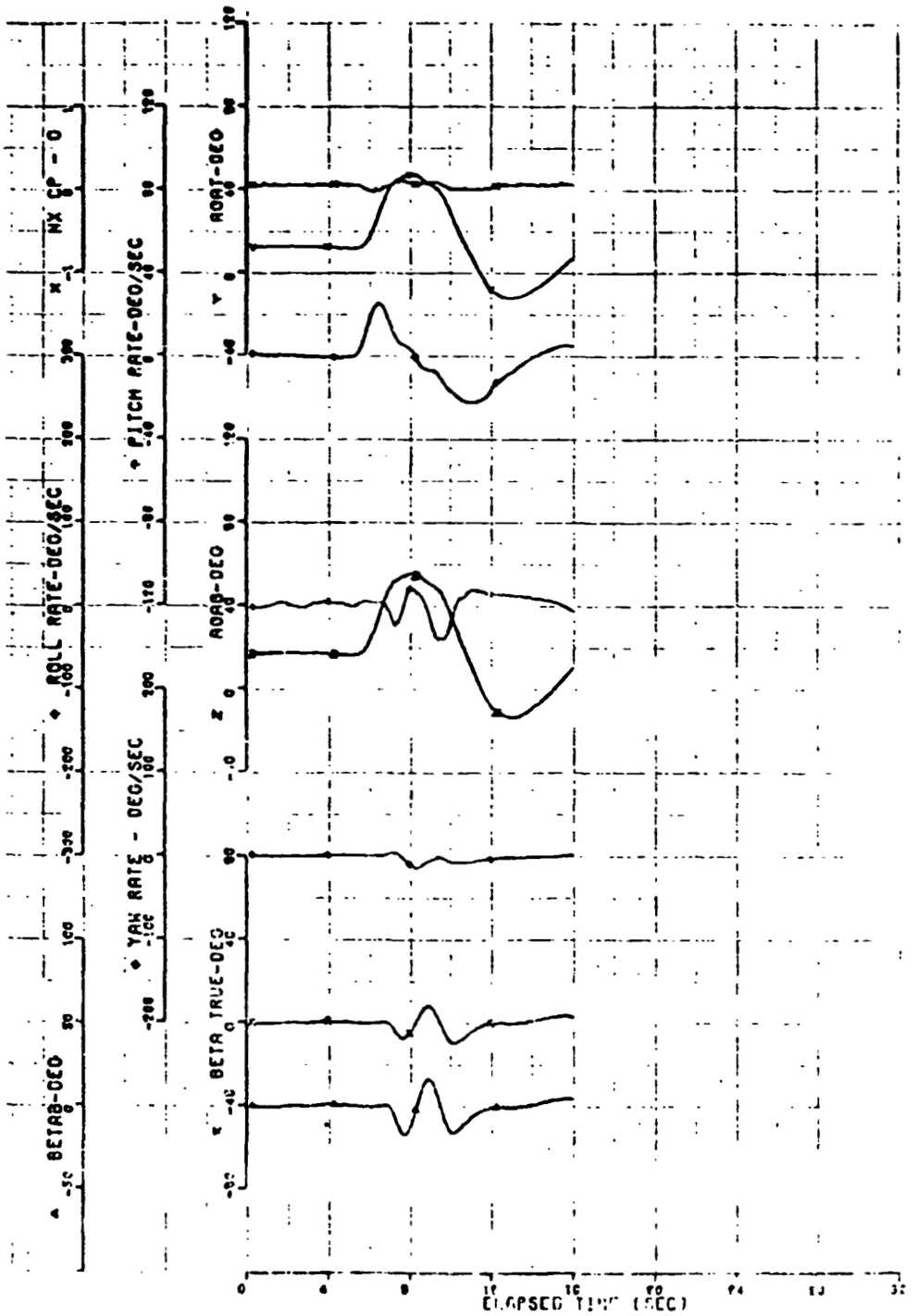

FIGURE 135. F-5F CLEAN CONFIGURATION. ABRUPT PULL UP
(Sheet 4 of 8)

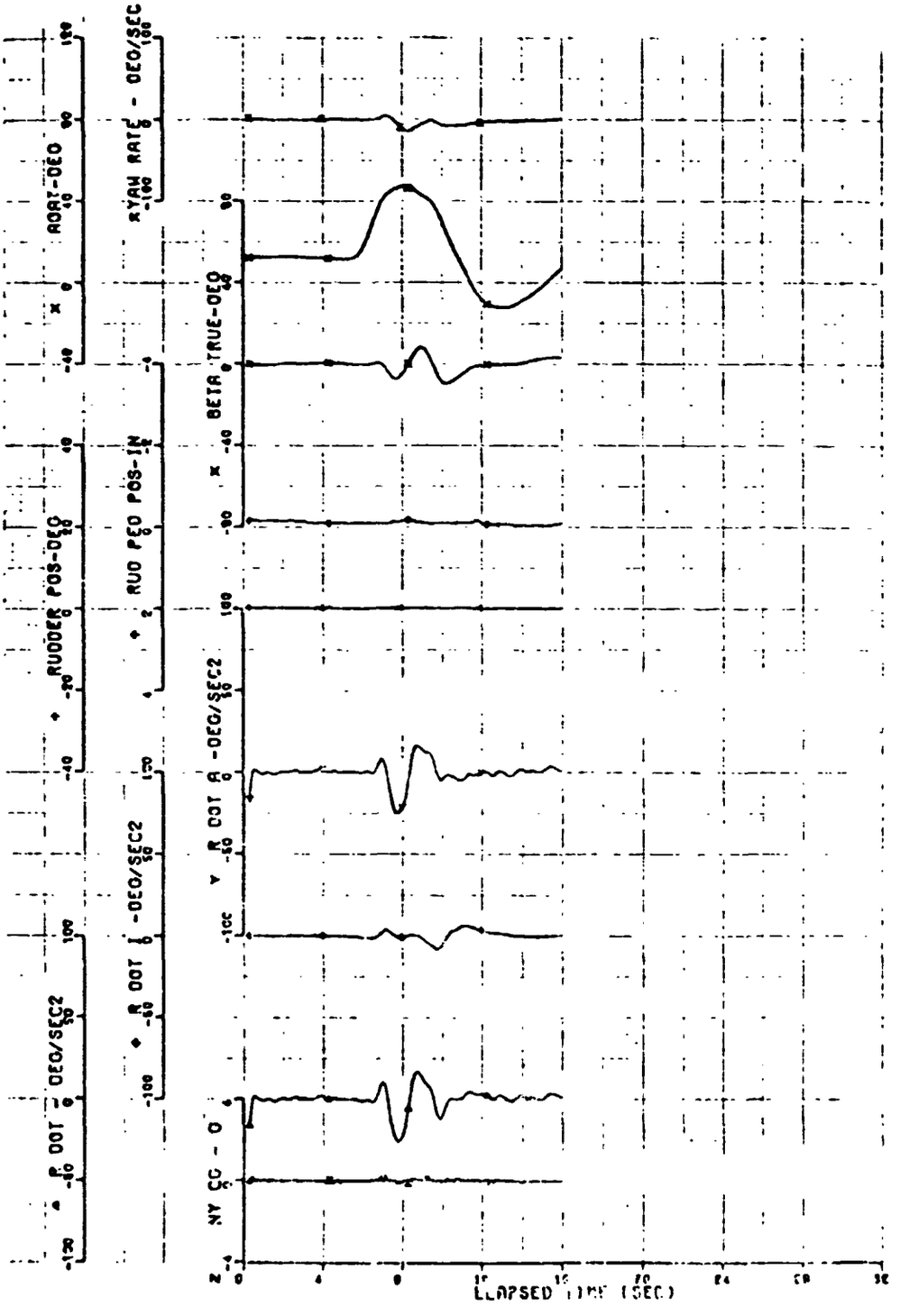

FIGURE 135. F-5F CLEAN CONFIGURATION. ABRUPT PULL UP
(Sheet 5 of 8)

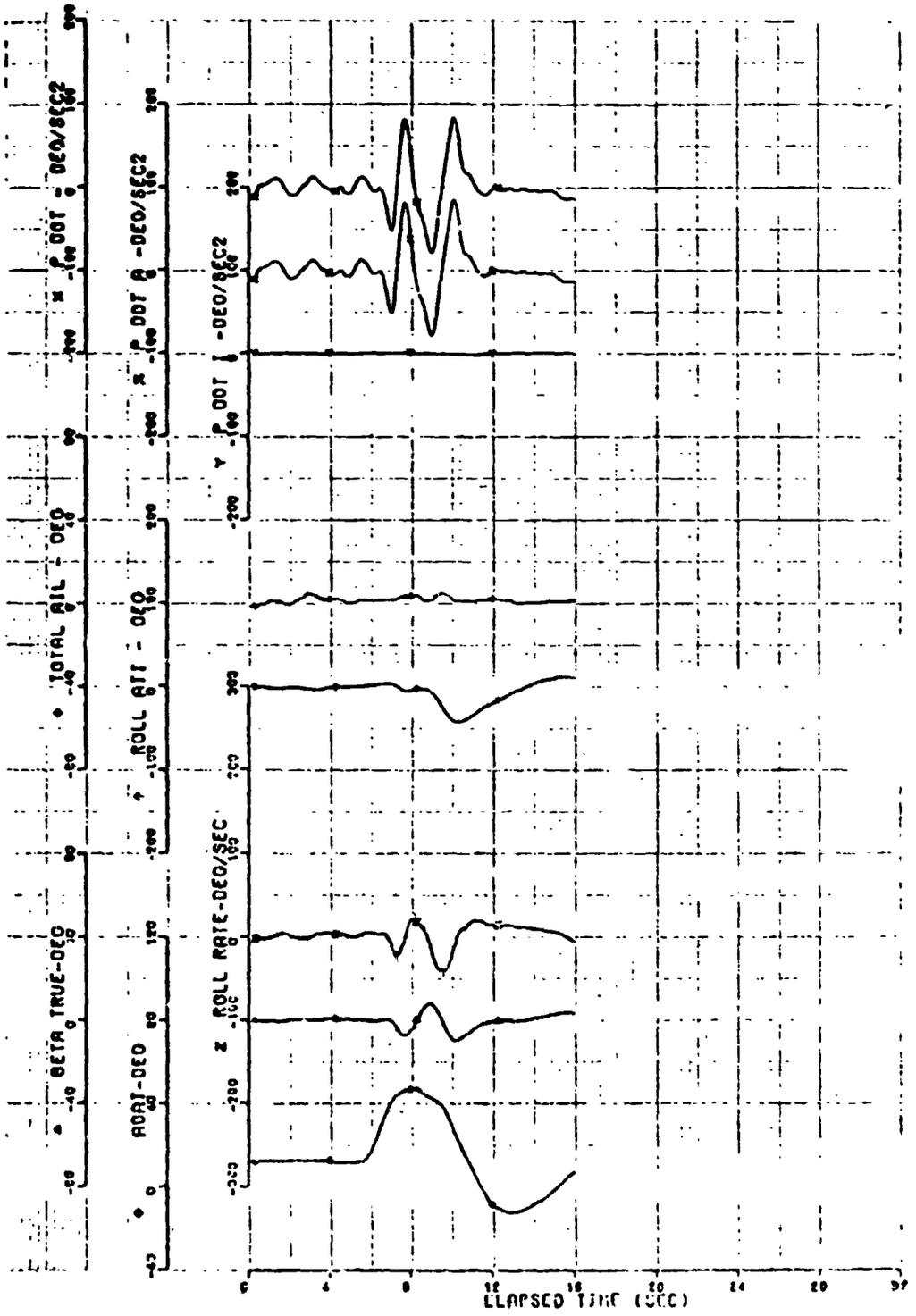

FIGURE 135. F-5F CLEAN CONFIGURATION. ABRUPT PULL UP
(Sheet 6 of 8)

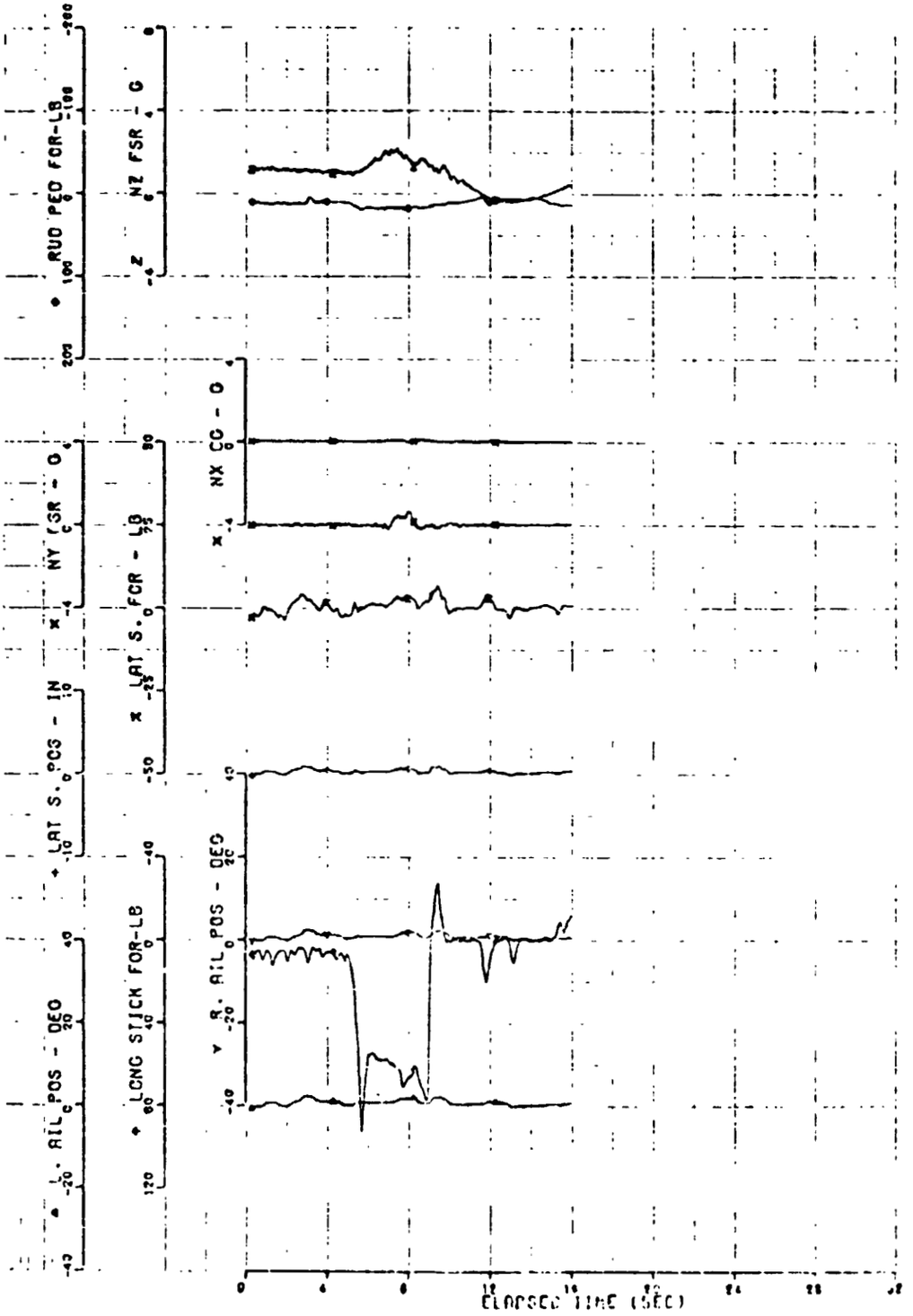

FIGURE 135. F-5F CLEAN CONFIGURATION. ABRUPT PULL UP
(Sheet 7 of 8)

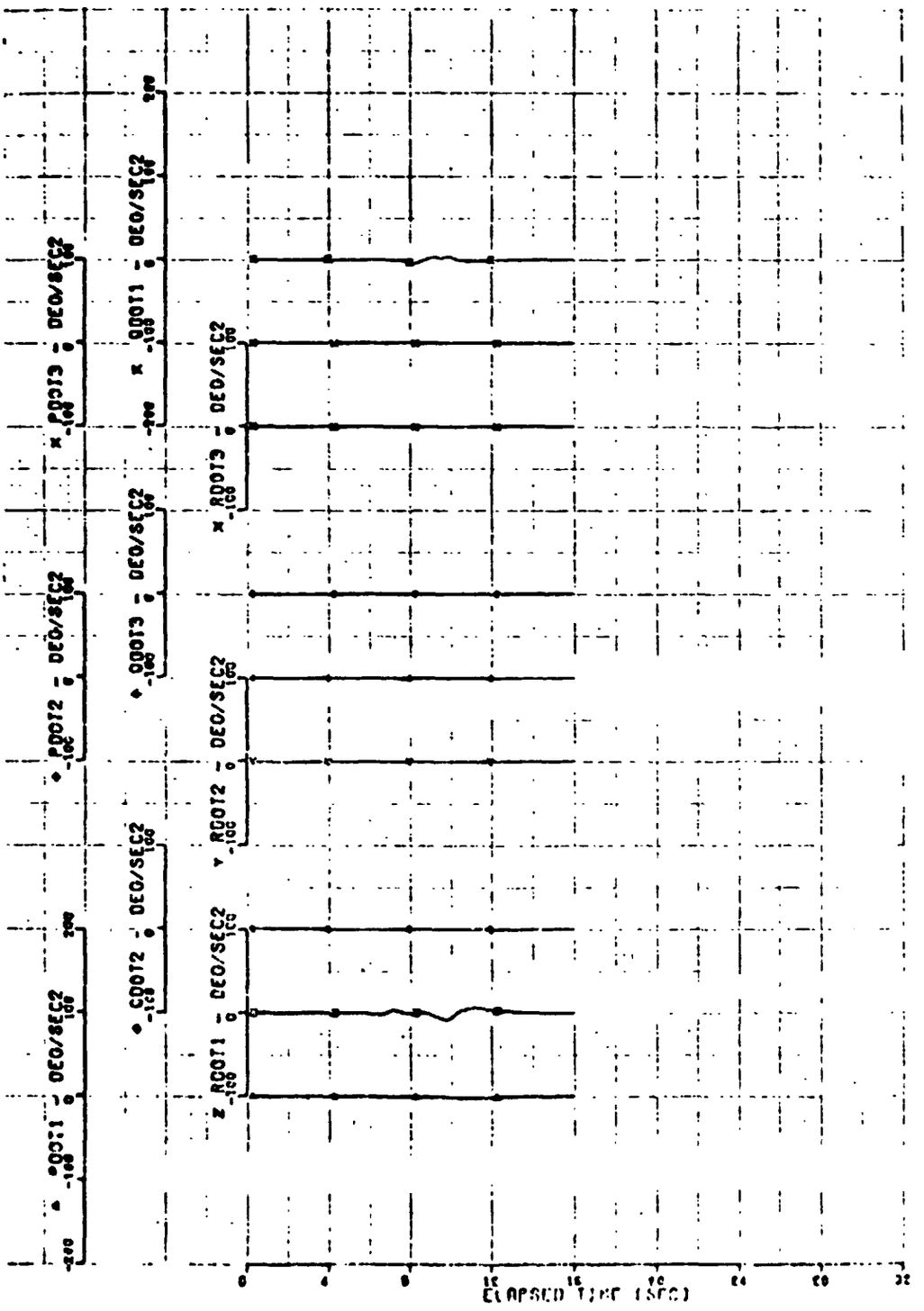

FIGURE 135. F-5F CLEAN CONFIGURATION, ABRUPT PULL UP
(Sheet 8 of 8)

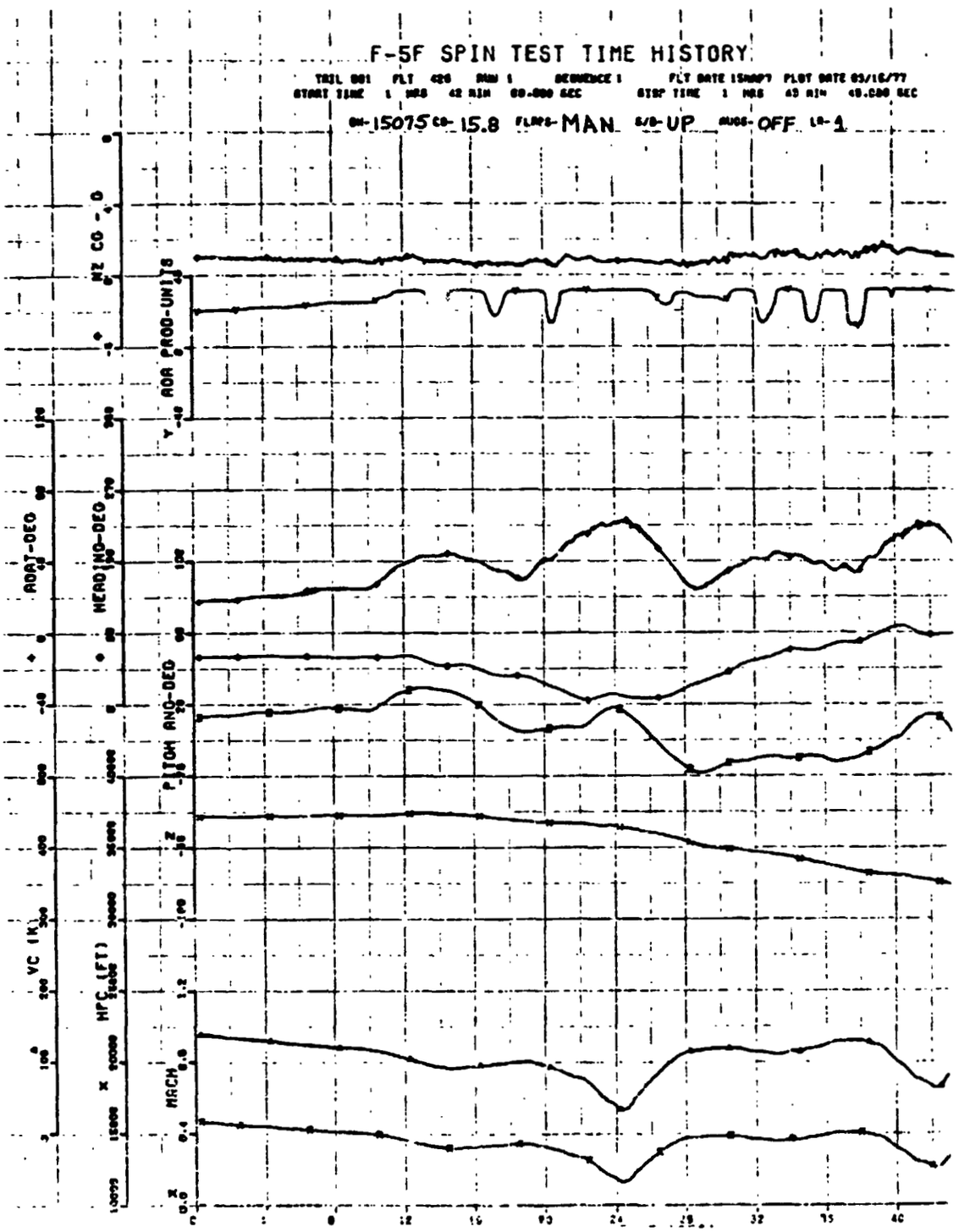

FIGURE 136. F-5F CLEAN CONFIGURATION. EXTENDED 1-g STALL
(Sheet 1 of 8)

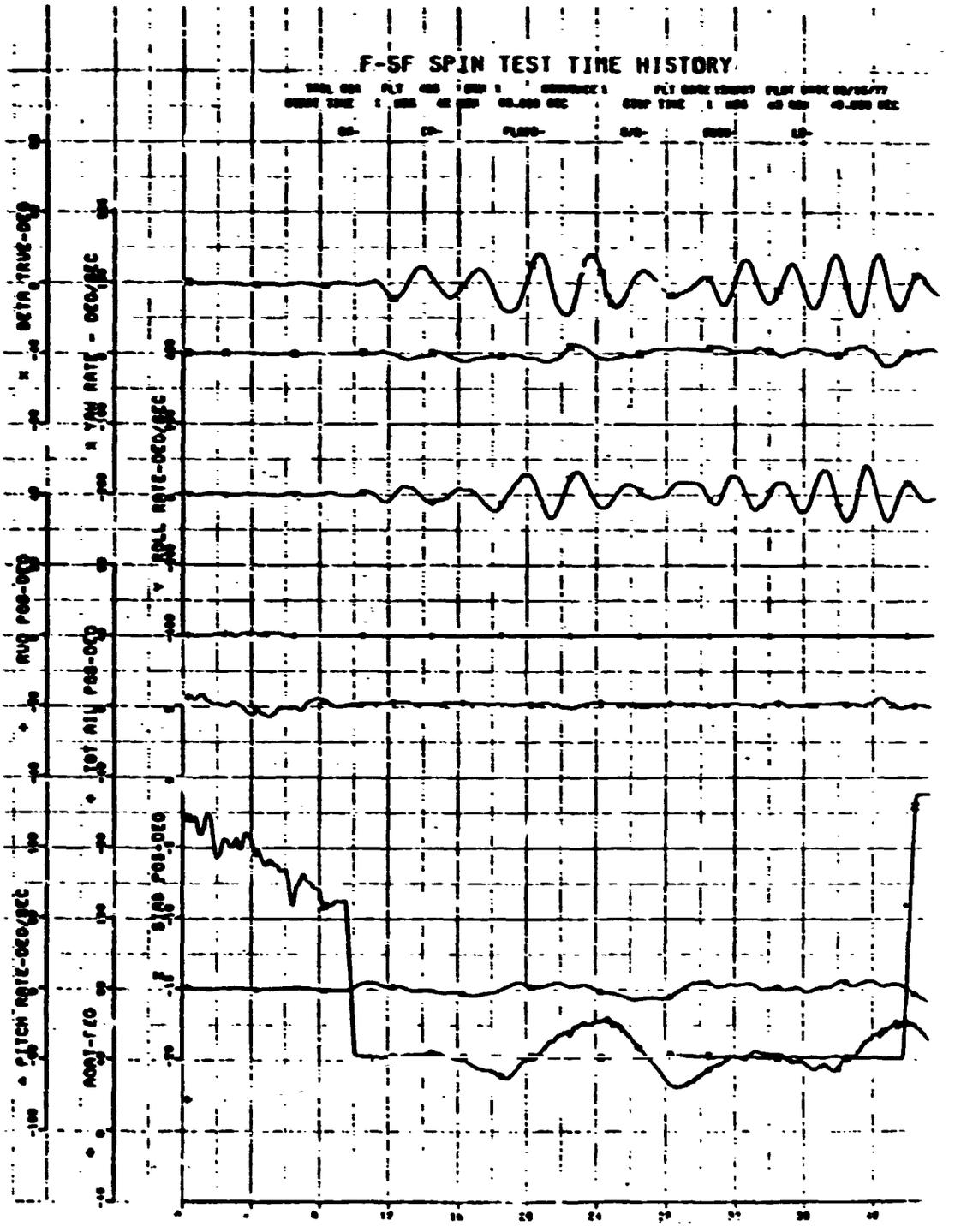

FIGURE 136. F-5F CLEAN CONFIGURATION. EXTENDED 1-g STALL
(Sheet 2 of 8)

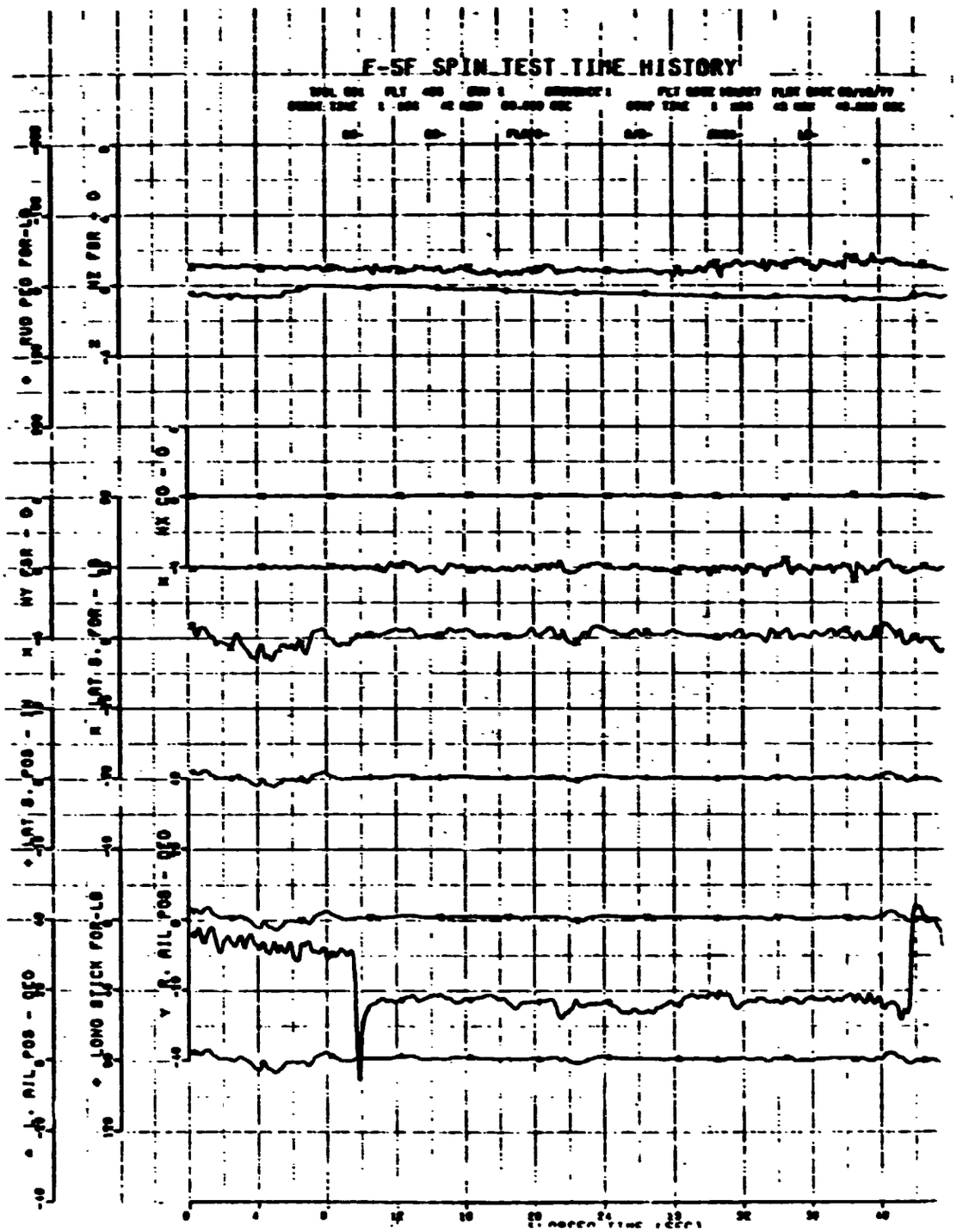

FIGURE 136. F-5F CLEAN CONFIGURATION, EXTENDED 1-g STALL
(Sheet 3 of 8)

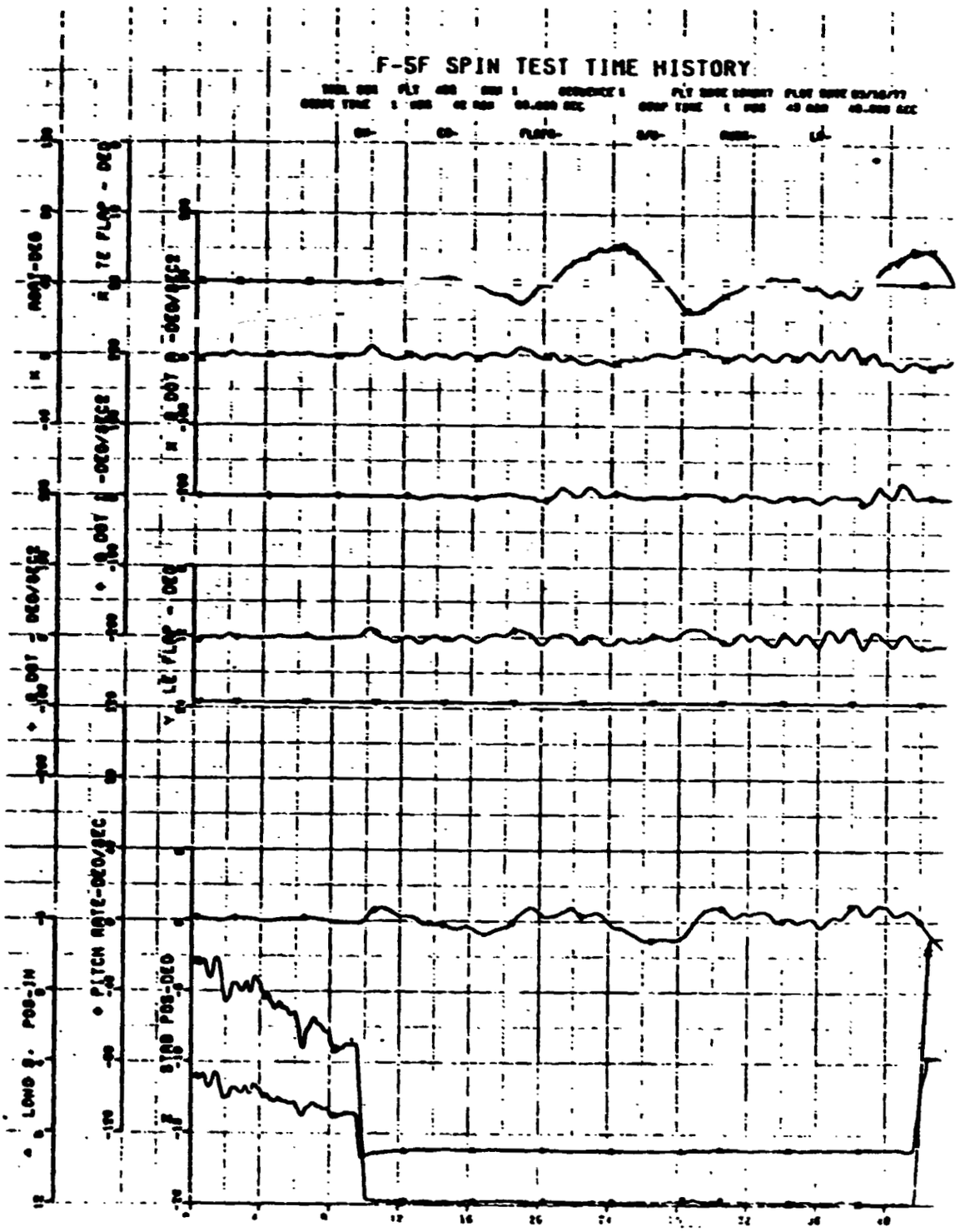

FIGURE 136. F-5F CLEAN CONFIGURATION. EXTENDED 1-g STALL
(Sheet 4 of 8)

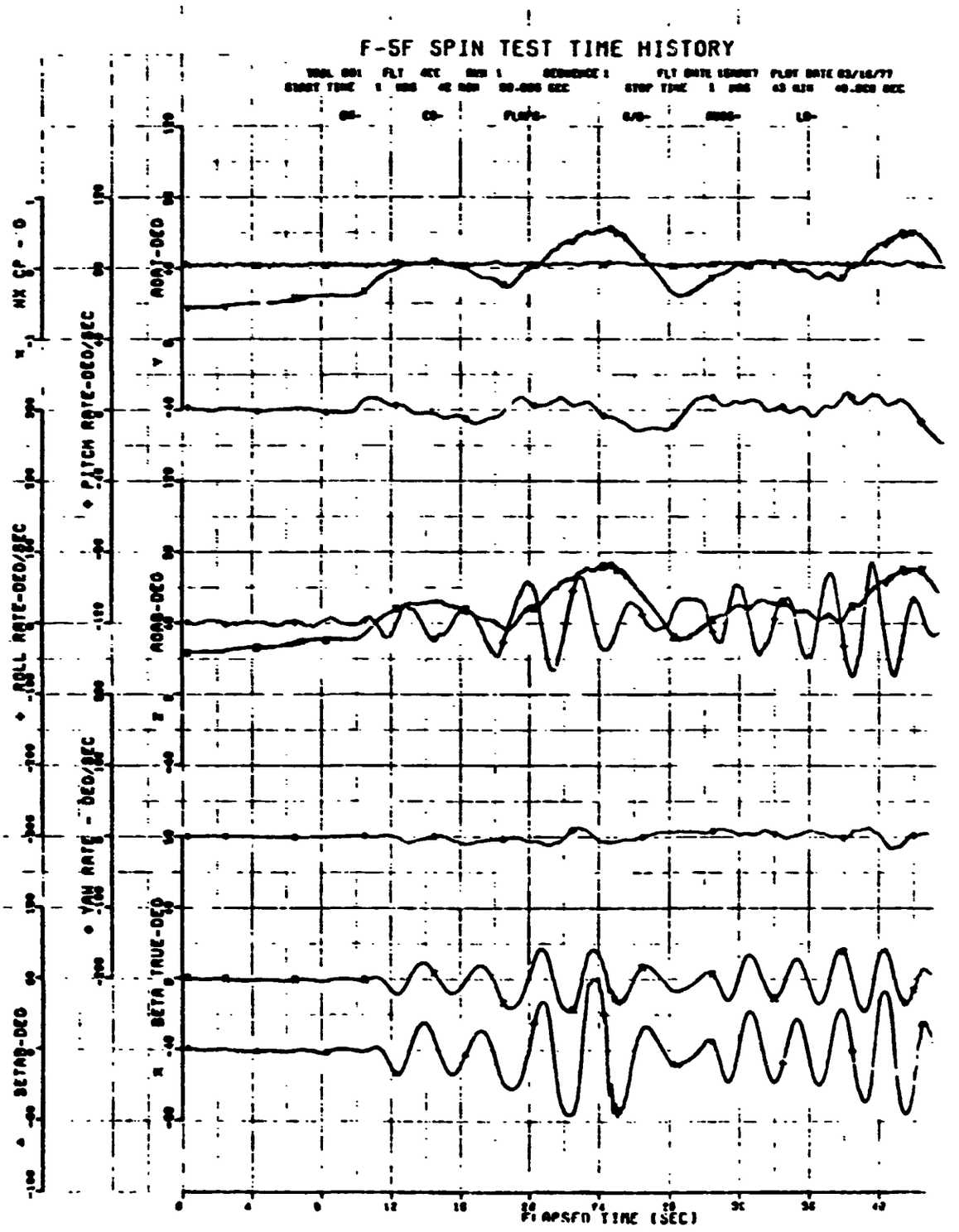

FIGURE 126. F-5F CLEAN CONFIGURATION. EXTENDED 1-g STALL
(Sheet 5 of 8)

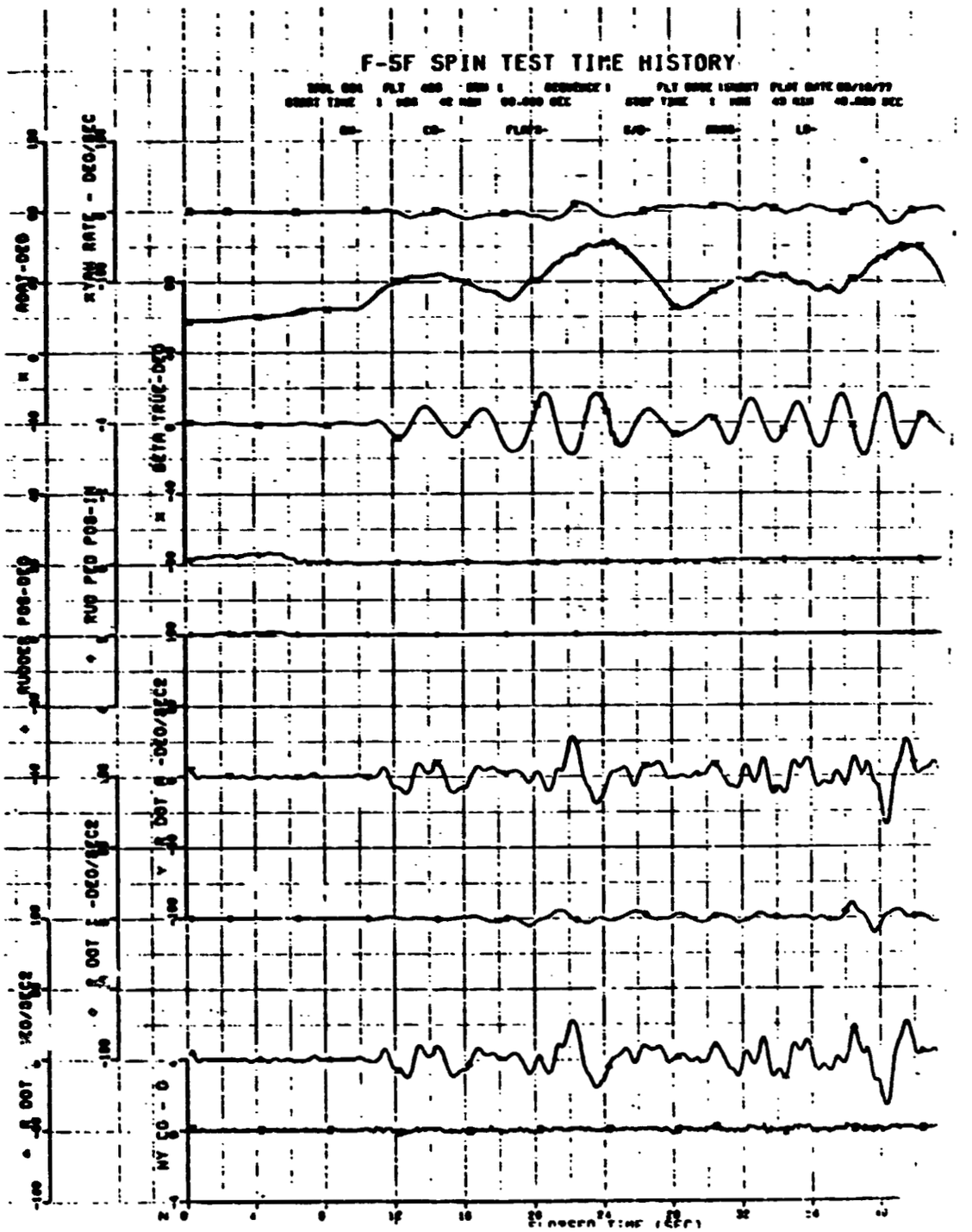

FIGURE 136. F-5F CLEAN CONFIGURATION. EXTENDED 1-g STALL
(Sheet 6 of 8)

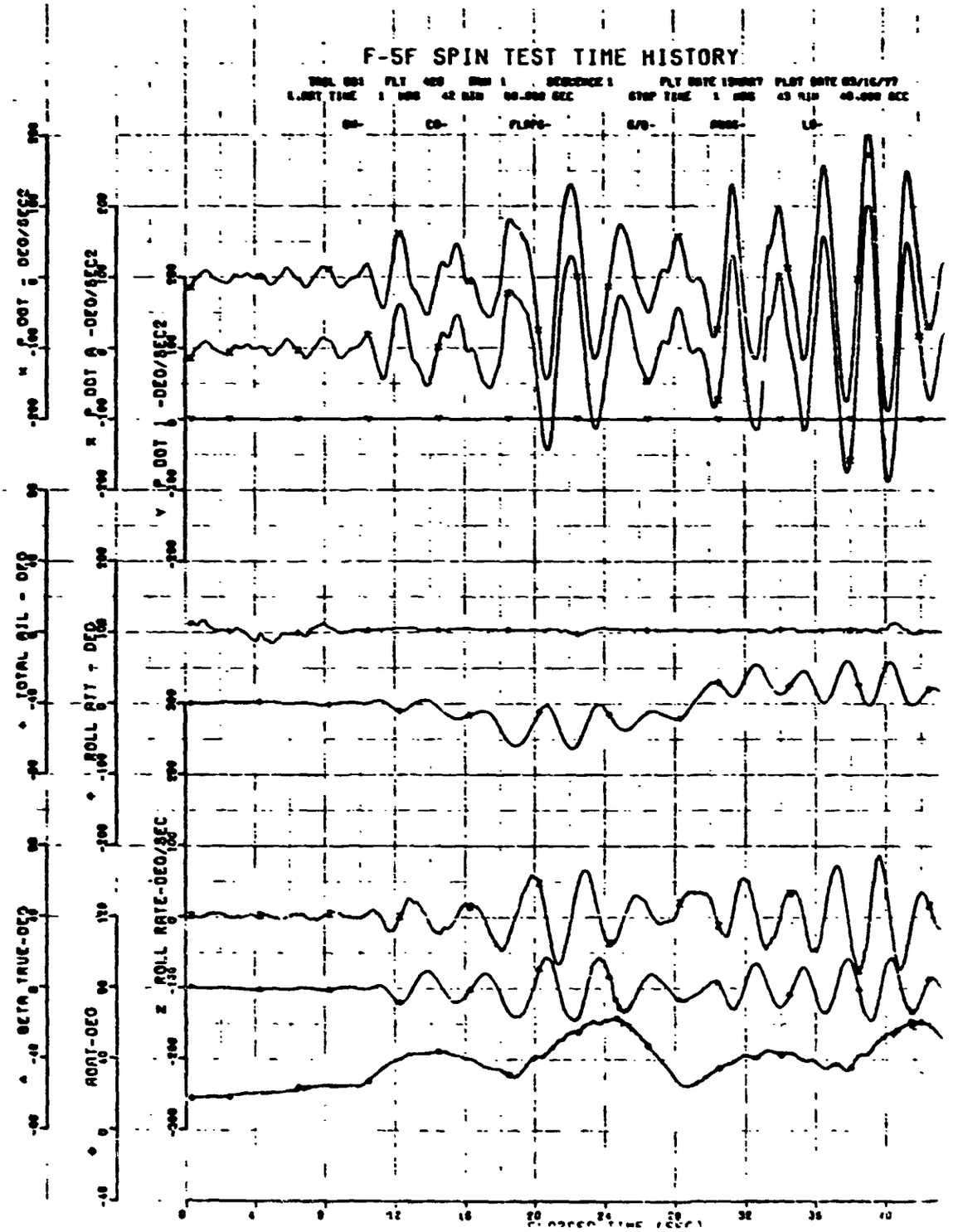

FIGURE 136. F-5F CLEAN CONFIGURATION. EXTENDED 1-g STALL
(Sheet 7 of 8)

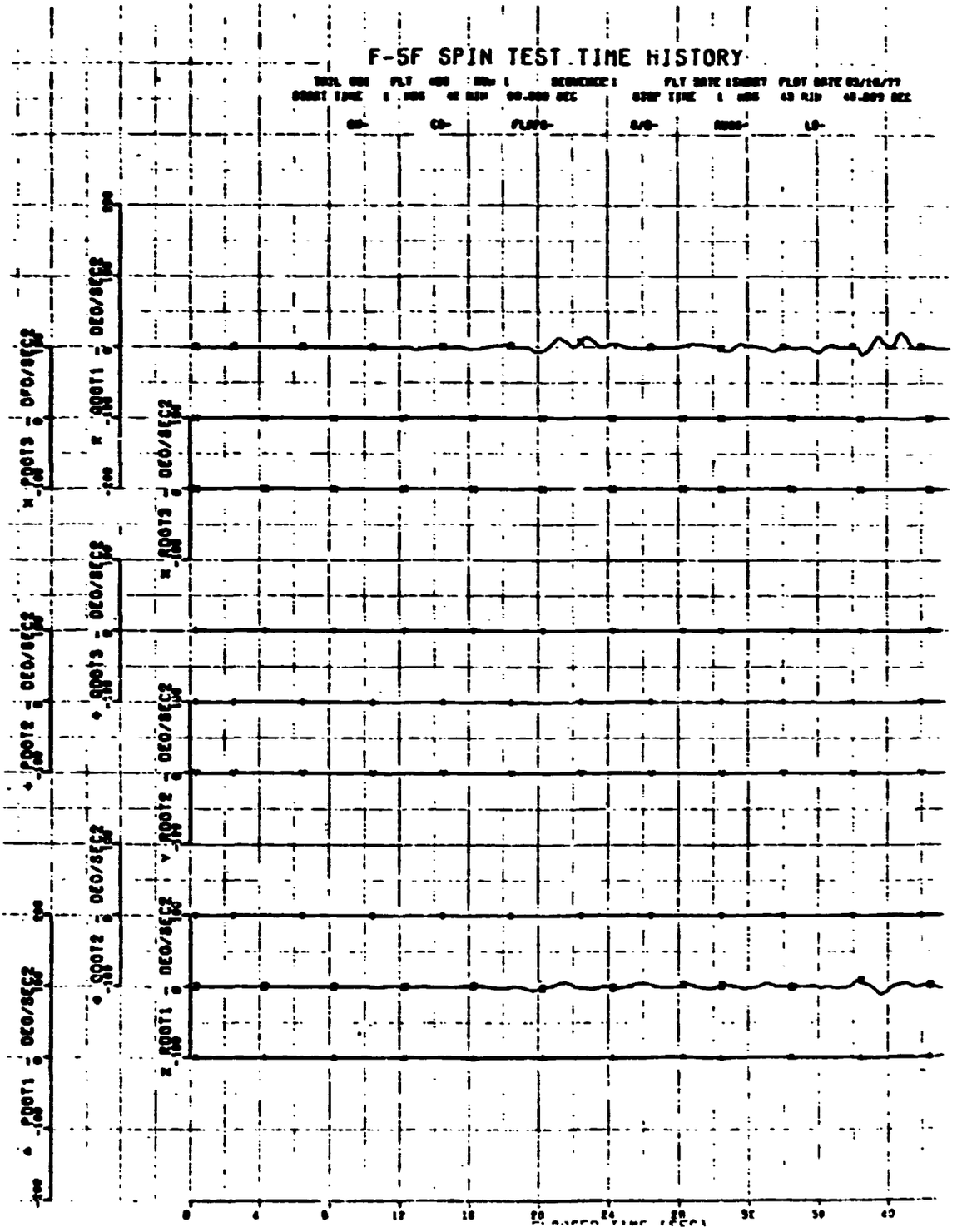

FIGURE 136. F-5 CLEAN CONFIGURATION. EXTENDED 1-g STALL
(Sheet 8 of 8)

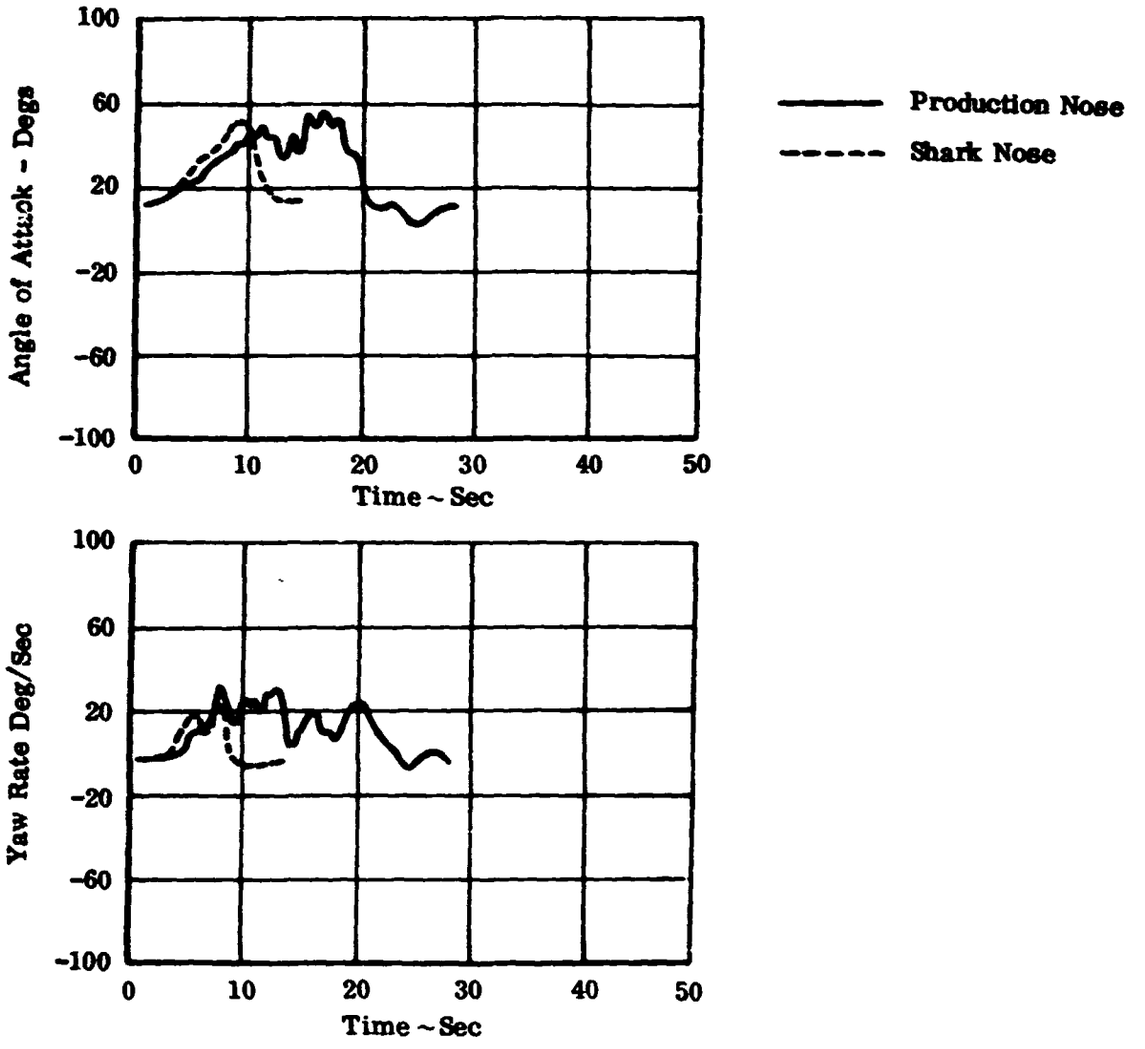

FIGURE 137. F-5F CLEAN CONFIGURATION. 2-g LEVEL DECEL (Sheet 1 of 2)

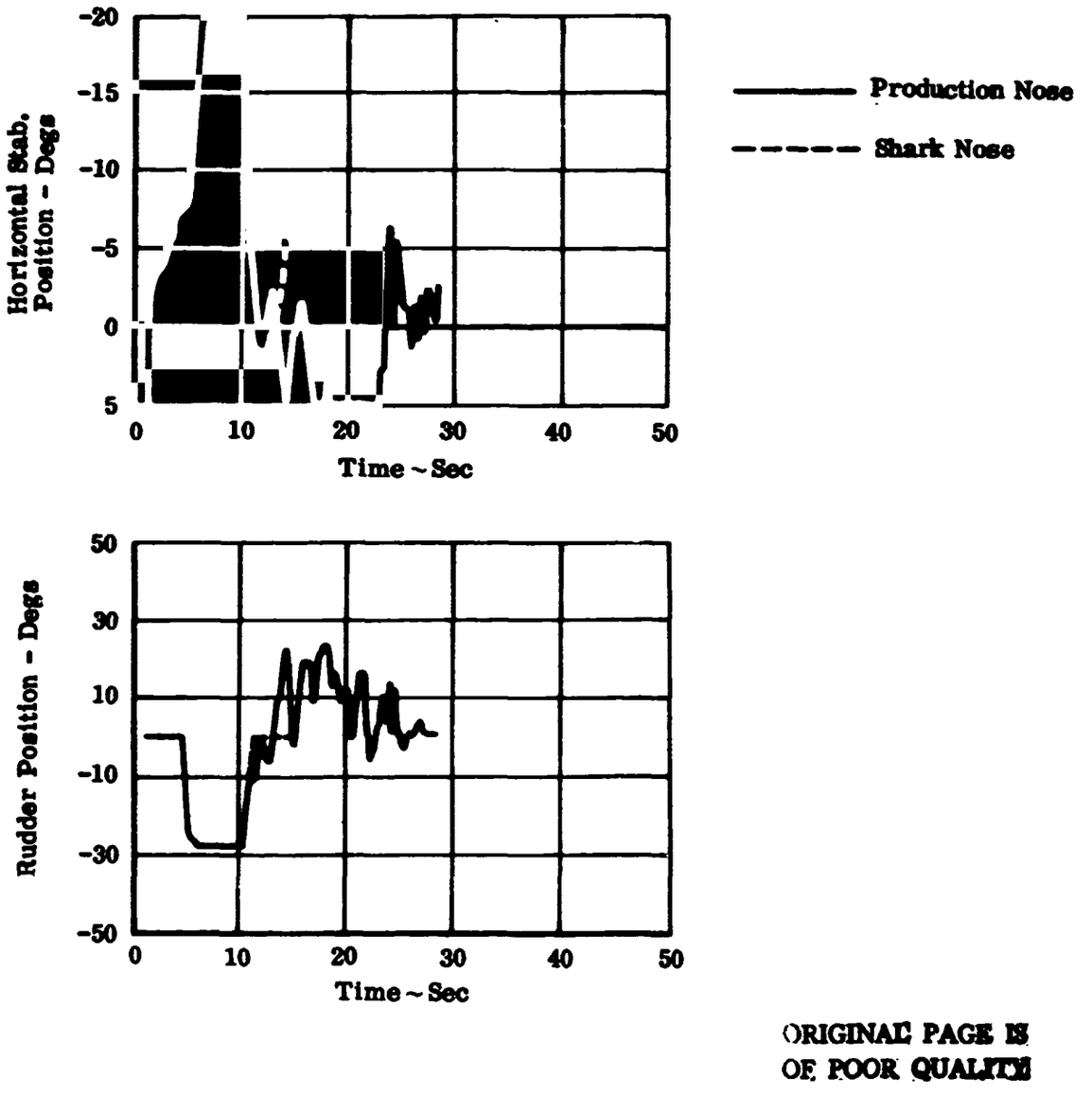

FIGURE 137. F-5F CLEAN CONFIGURATION. 2-g LEVEL DECEL (Sheet 2 of 2)

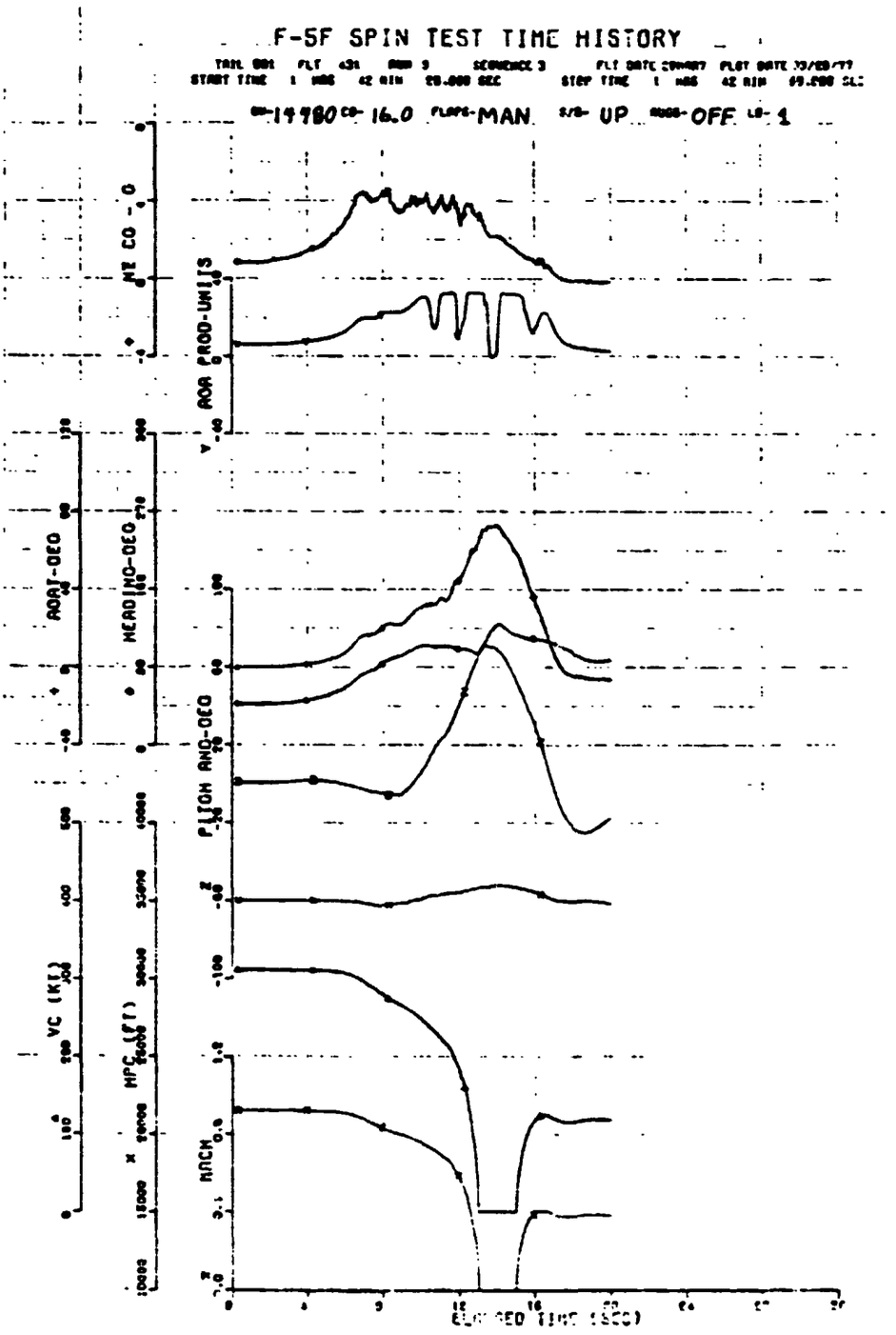

FIGURE 138. F-5F CLEAN CONFIGURATION. 4-g LEVEL DECEL AFT STICK AND RUDDER AT 20^{O} AOA (Sheet 1 of 8)

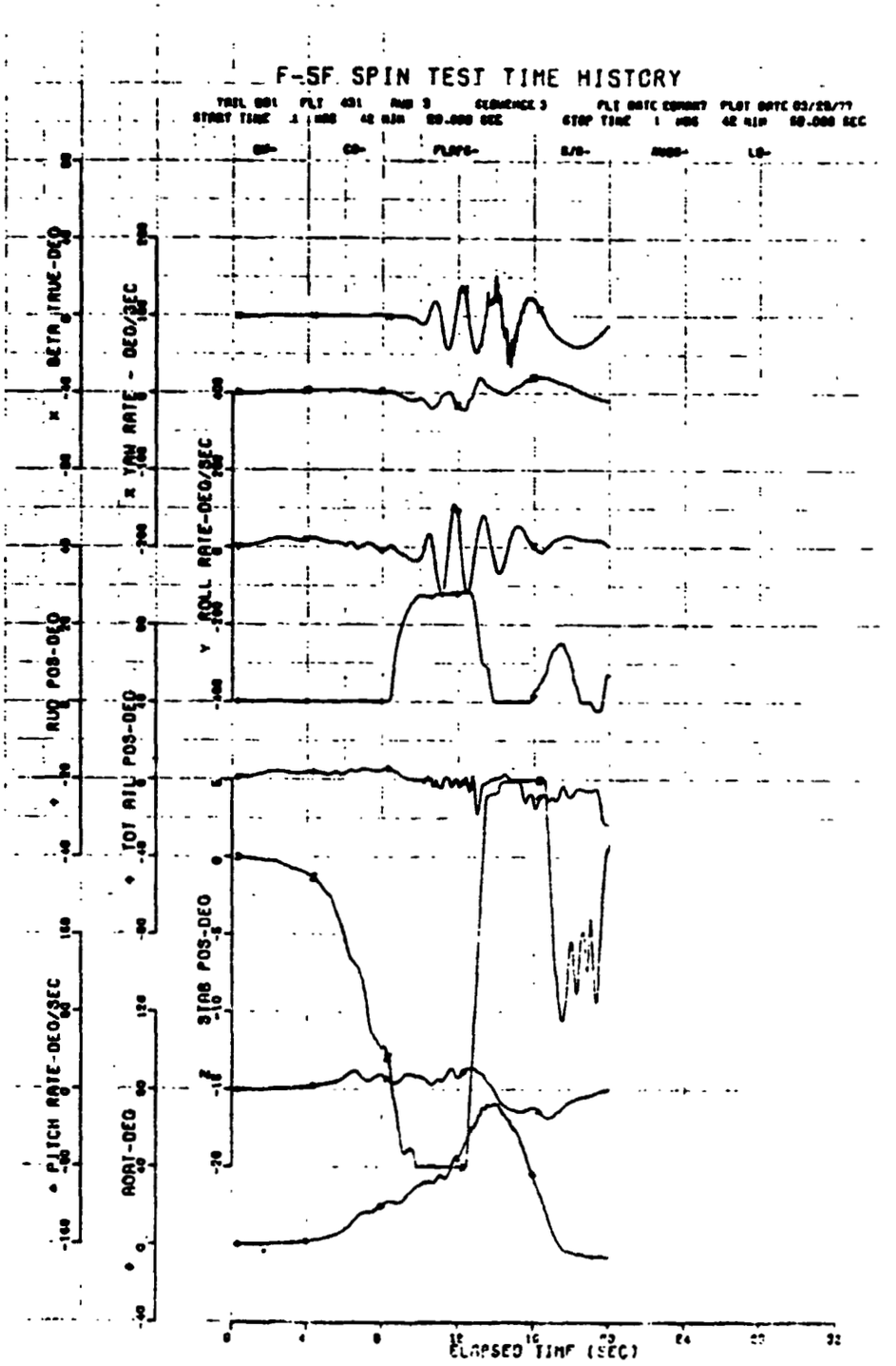

FIGURE 138. F-5F CLEAN CONFIGURATION. 4-g LEVEL DECEL AFT STICK AND RUDDER AT 20° AOA (Sheet 2 of 8)

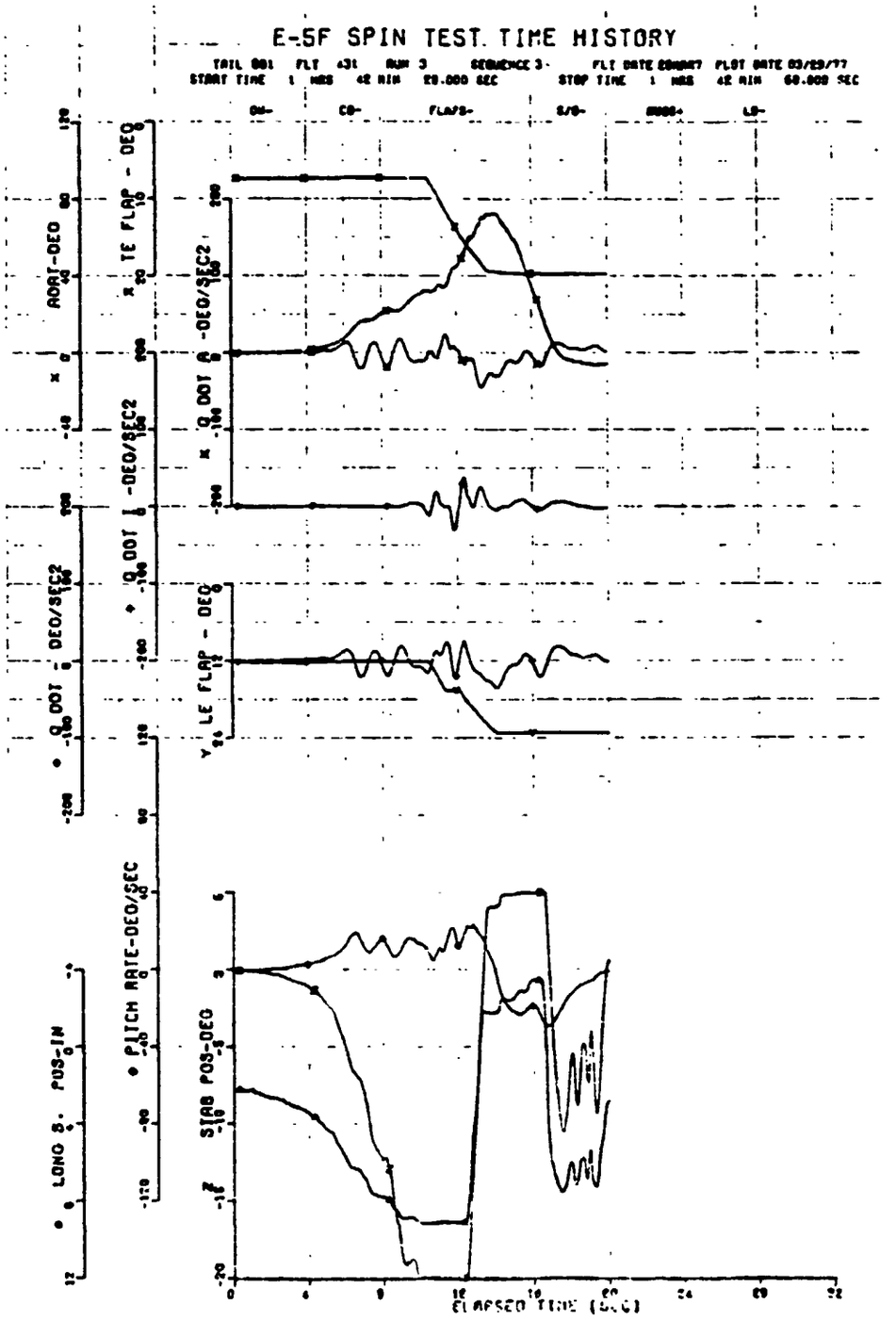

FIGURE 138. F-5F CLEAN CONFIGURATION. 4-g LEVEL DECEL AFT STICK AND RUDDER AT 20° AOA (Sheet 3 of 8)

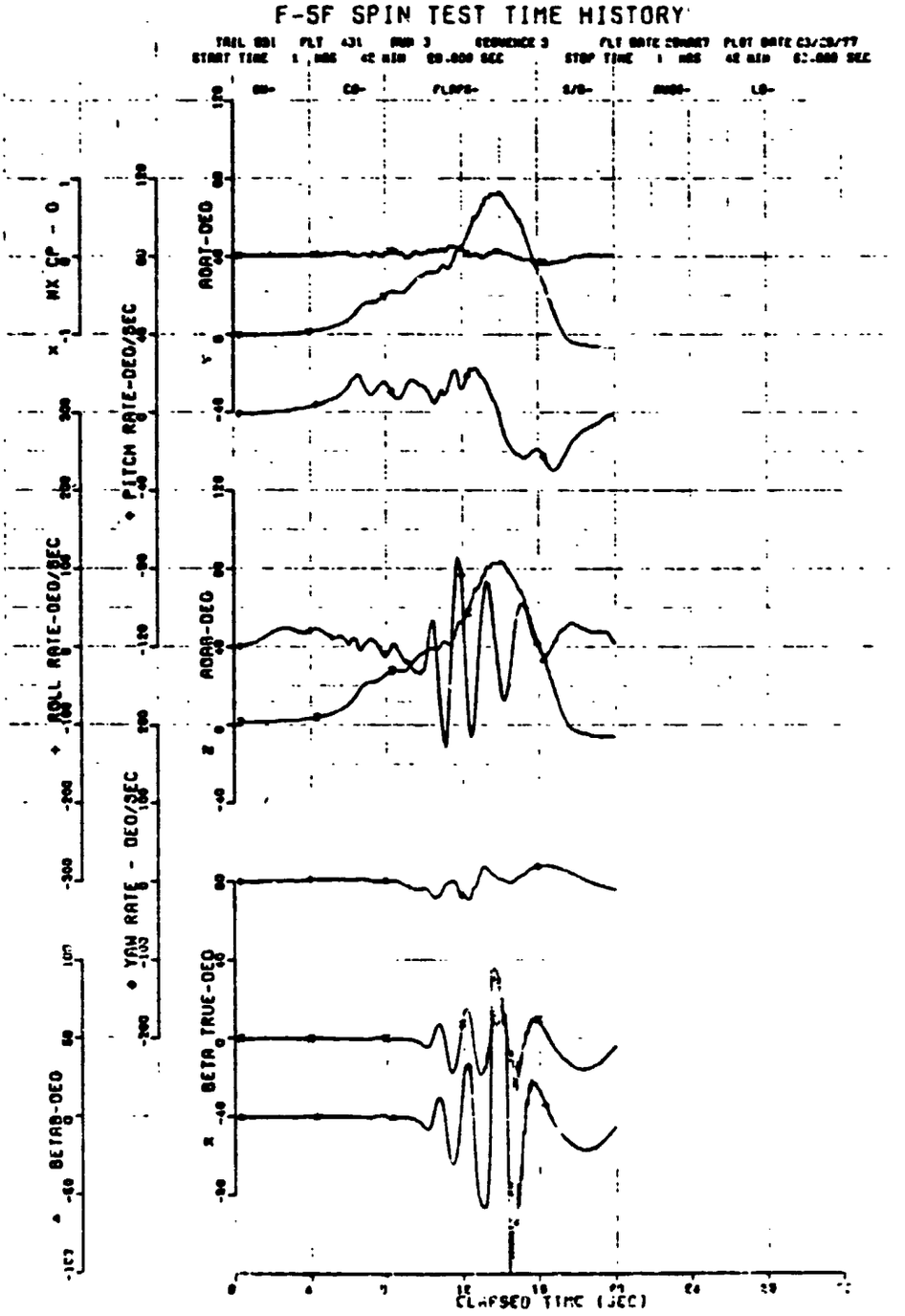

FIGURE 138. F-5F CLEAN CONFIGURATION. 4-g LEVEL DECEL AFT STICK AND RUDDER AT 20° AOA (Sheet 4 of 8)

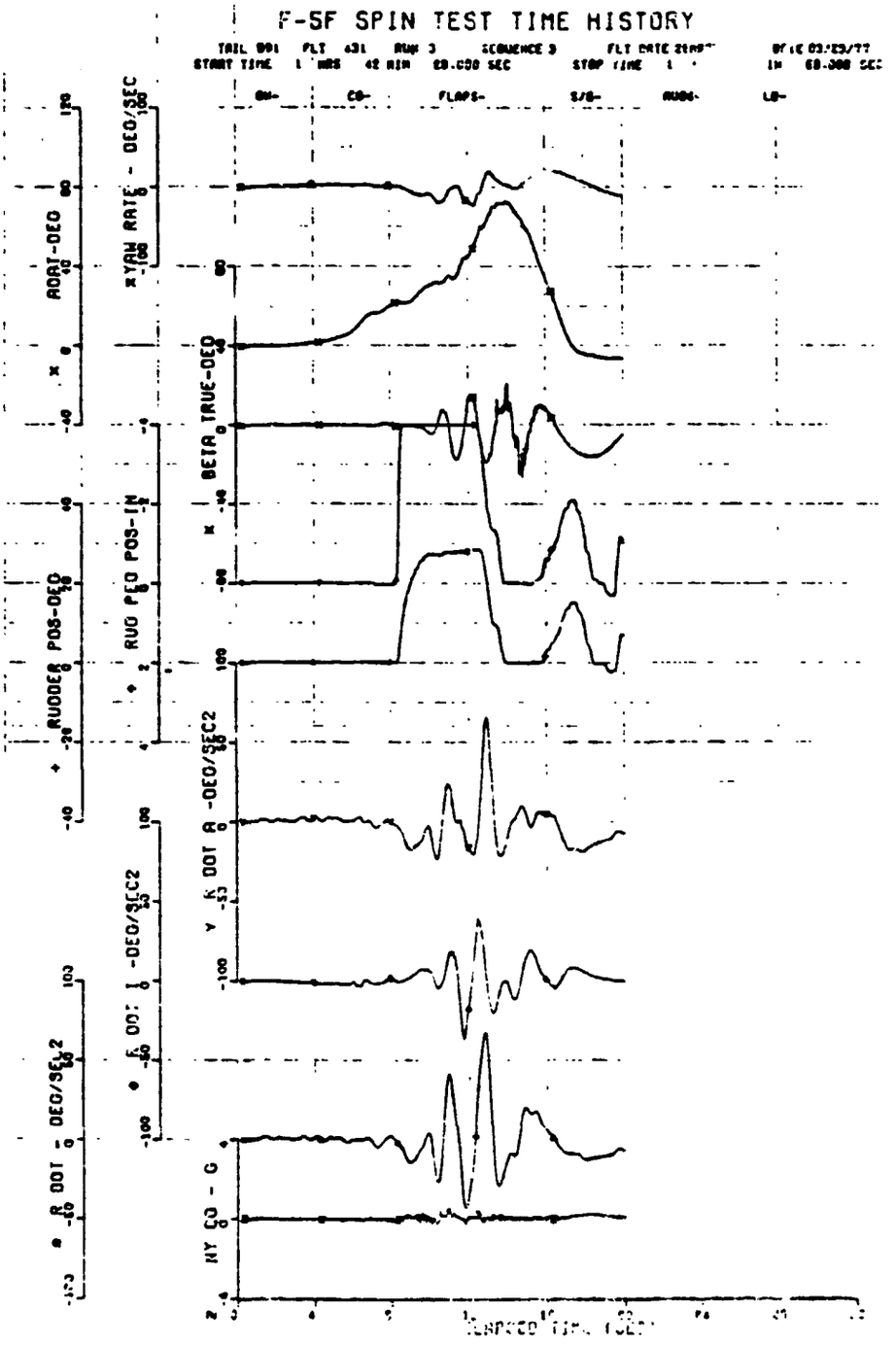

FIGURE 138. F-5F CLEAN CONFIGURATION. 4-g LEVEL DECEL AFT STICK AND RUDDER AT 20° AOA (Sheet 5 of 8)

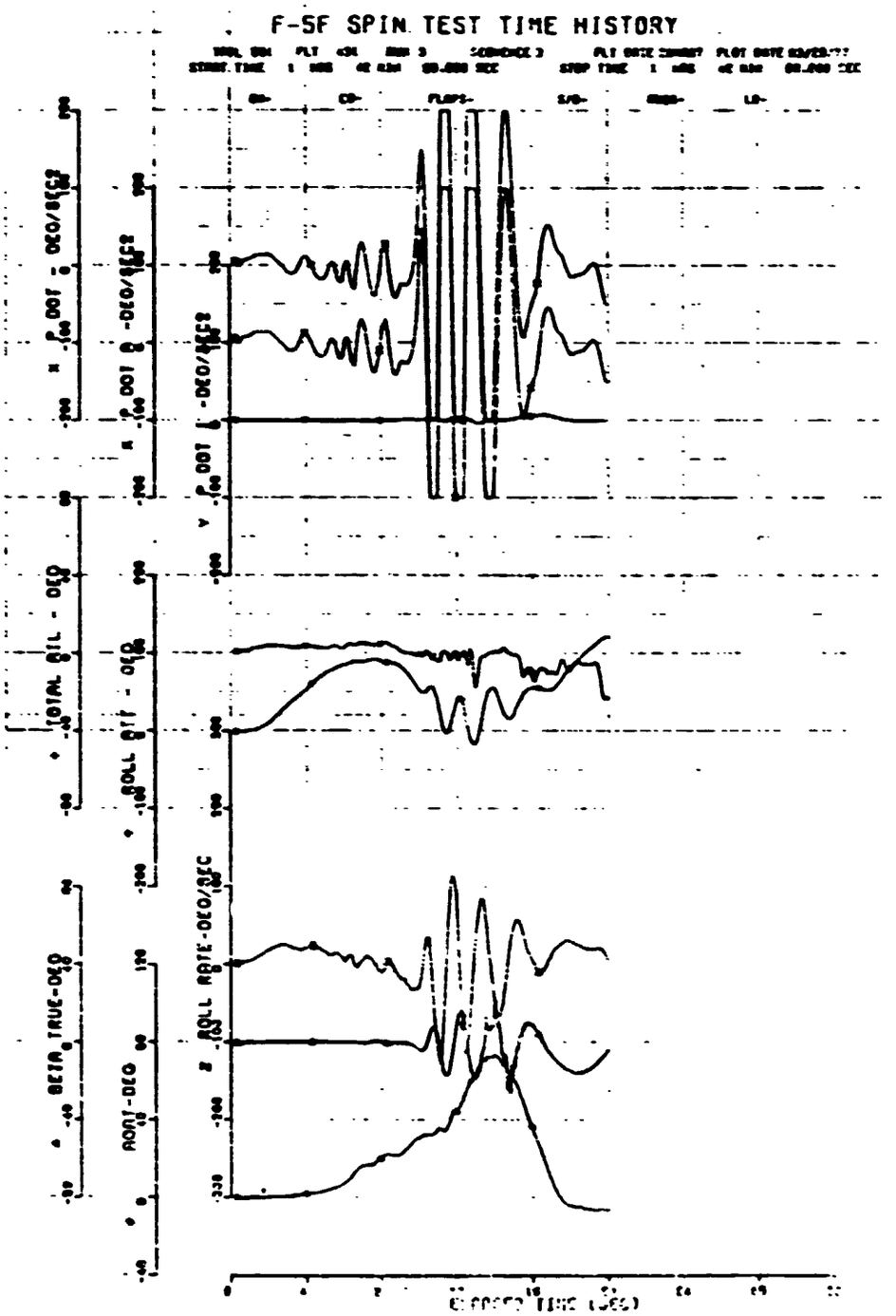

FIGURE 138. F-5F CLEAN CONFIGURATION. 4-g LEVEL DECEL AFT STICK AND RUDDER AT 20° AOA (Sheet 6 of 8)

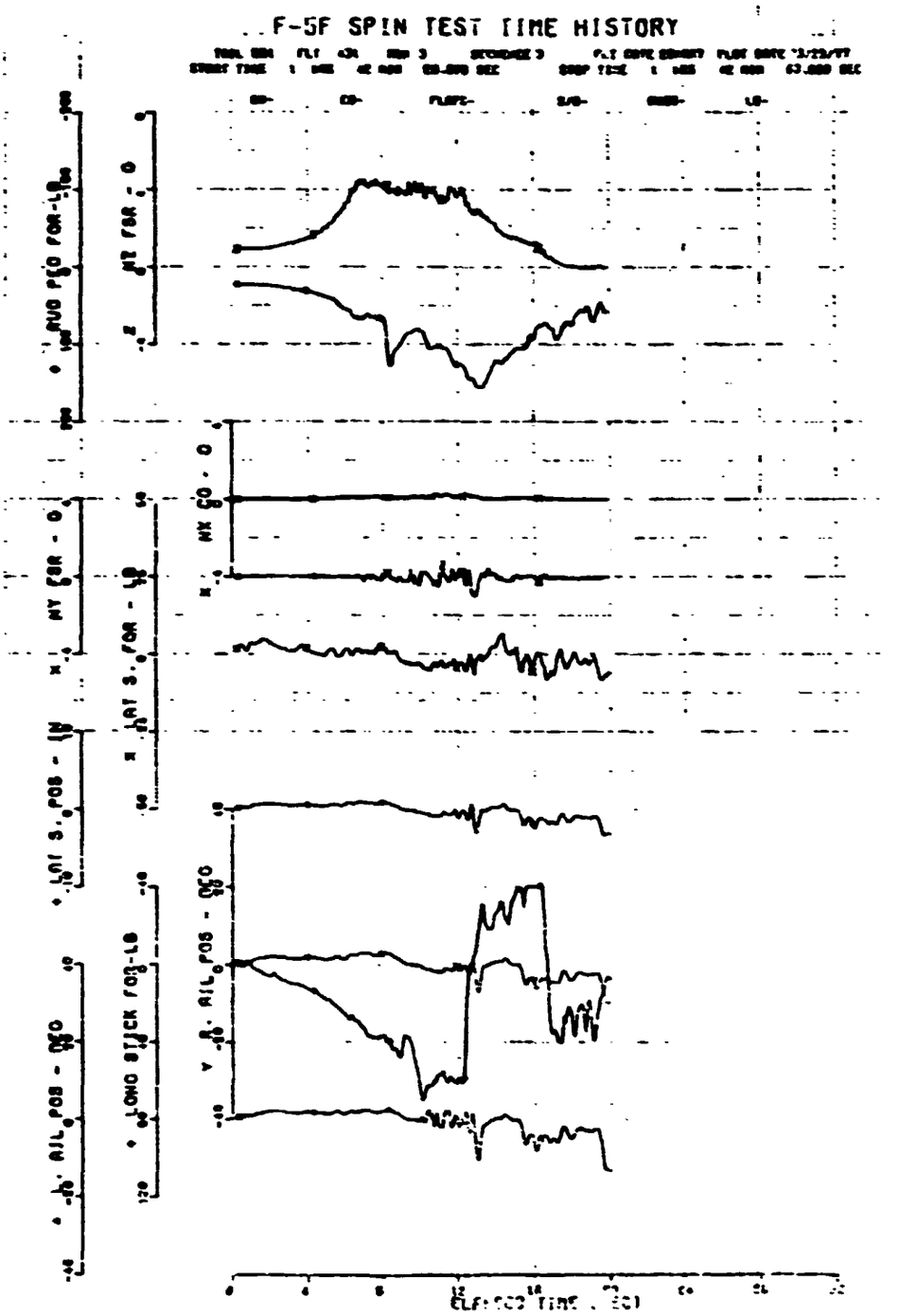

FIGURE 138. F-5F CLEAN CONFIGURATION. 4-g LEVEL DECEL AFT STICK AND RUDDER AT 20° AOA (Sheet 7 of 8)

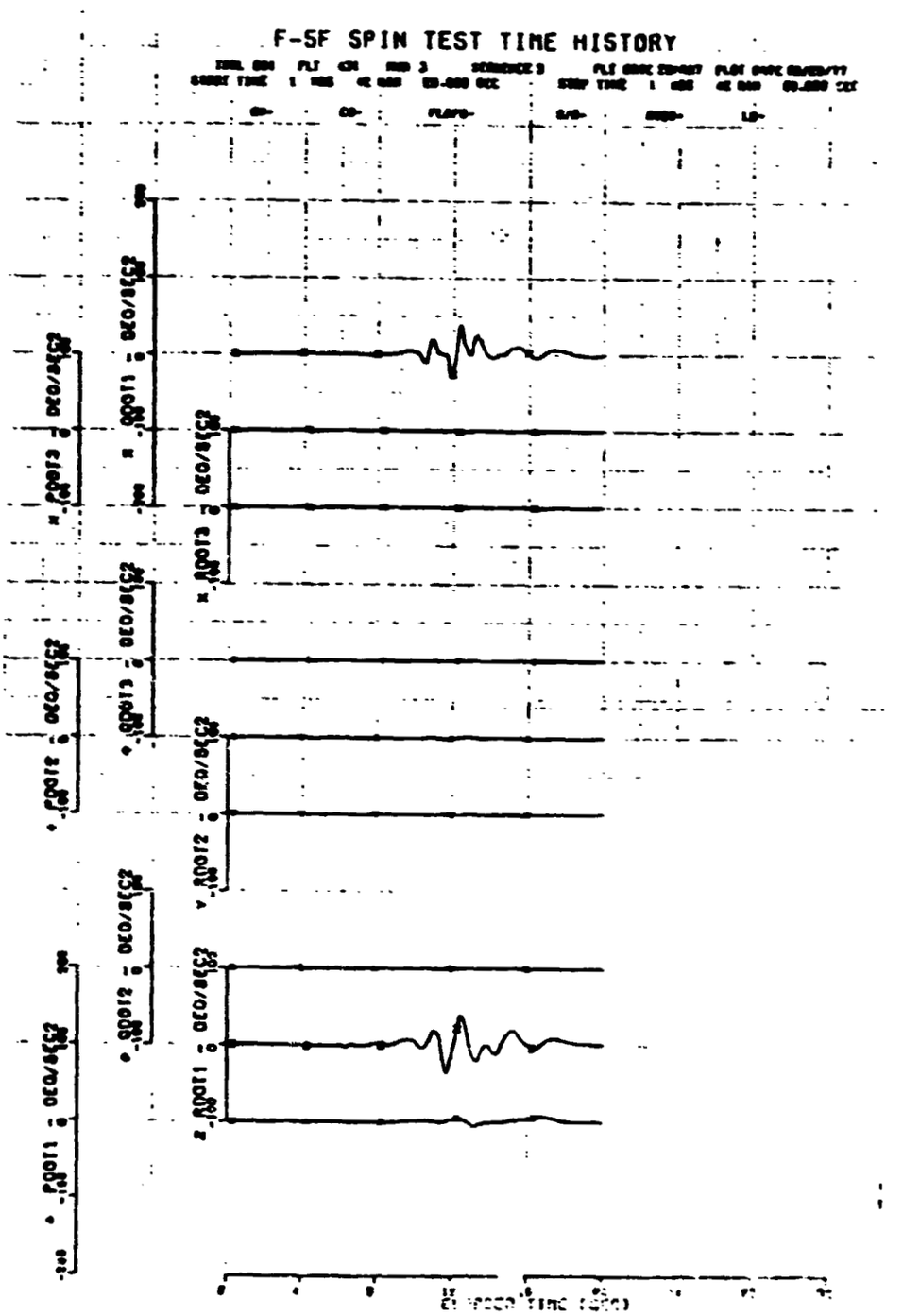

FIGURE 138. F-5F CLEAN CONFIGURATION. 4-g LEVEL DECEL AFT STICK AND RUDDER AT 20° AOA (Sheet 8 of 8)

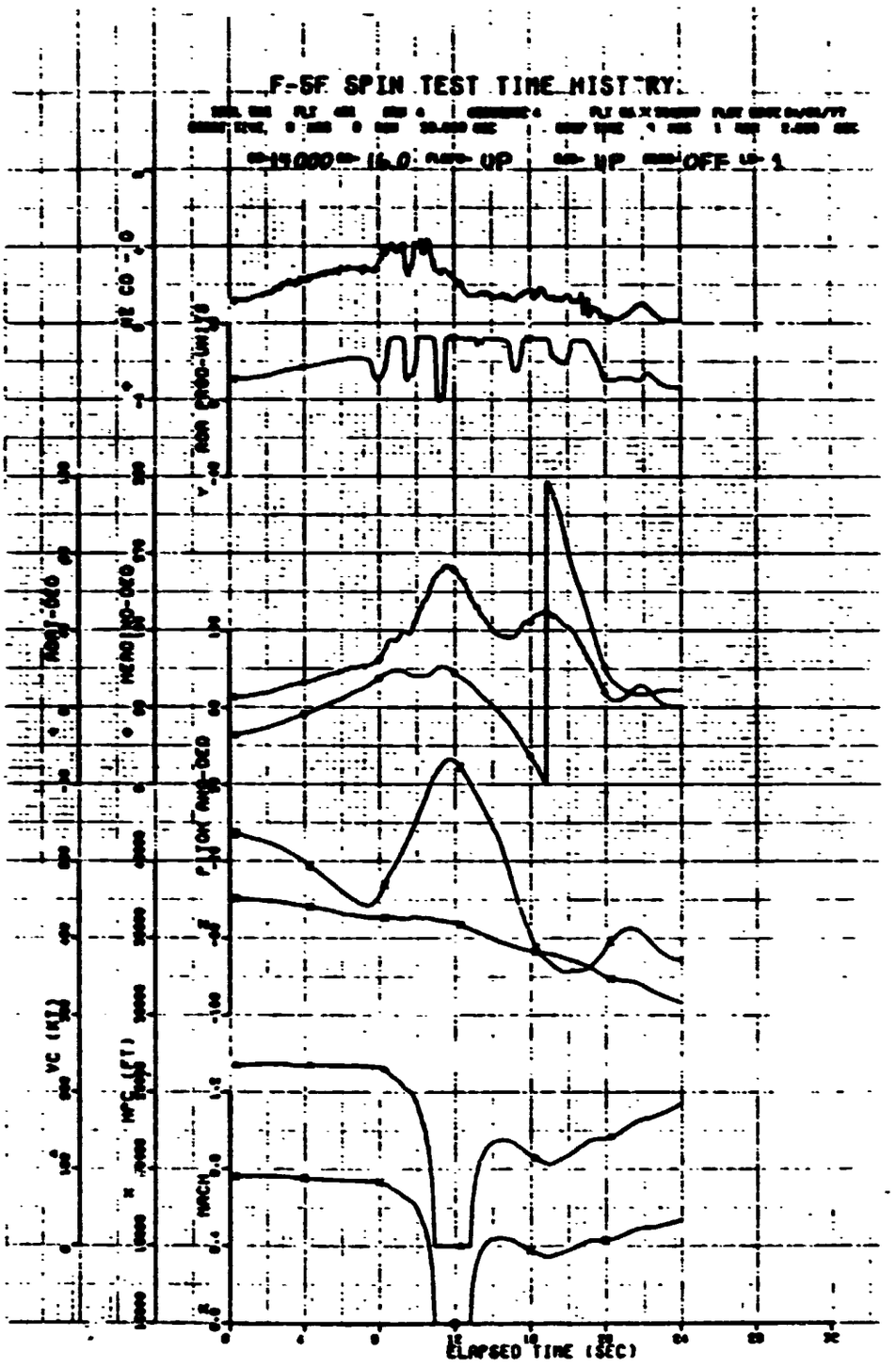

FIGURE 139. F-5F CLEAN CONFIGURATION. 240-kt WUT AFT STICK AND RUDDER AT 20° AOA (Sheet 1 of 8)

ORIGINAL PAGE IS
OF POOR QUALITY

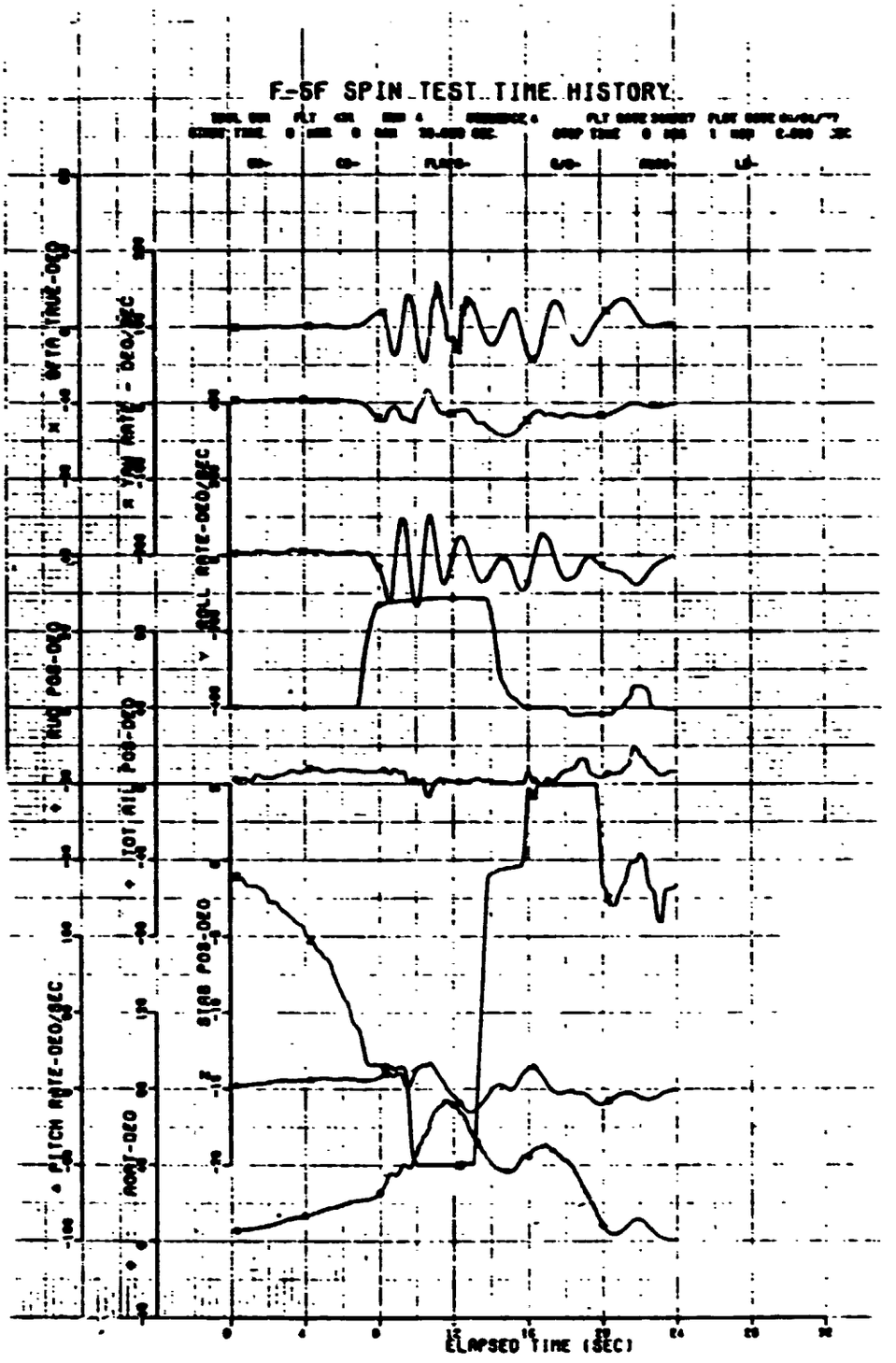

FIGURE 139. F-5F CLEAN CONFIGURATION. 240-kt WUT AFT STICK AND RUDDER AT 20° AOA (Sheet 2 of 8)

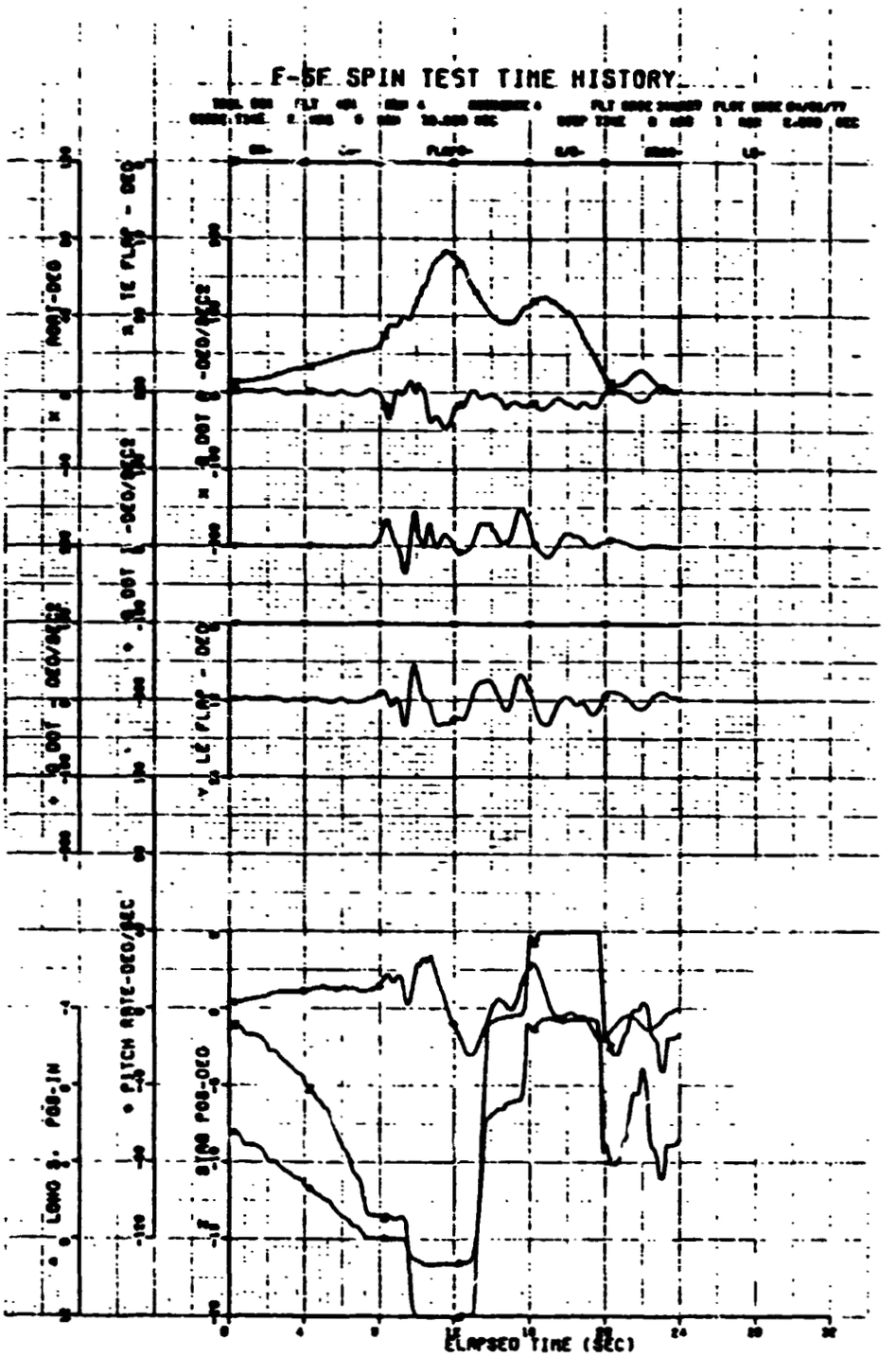

FIGURE 139. F-5F CLEAN CONFIGURATION. 240-kt WUT AFT STICK AND RUDDER AT 20° AOA (Sheet 3 of 8)

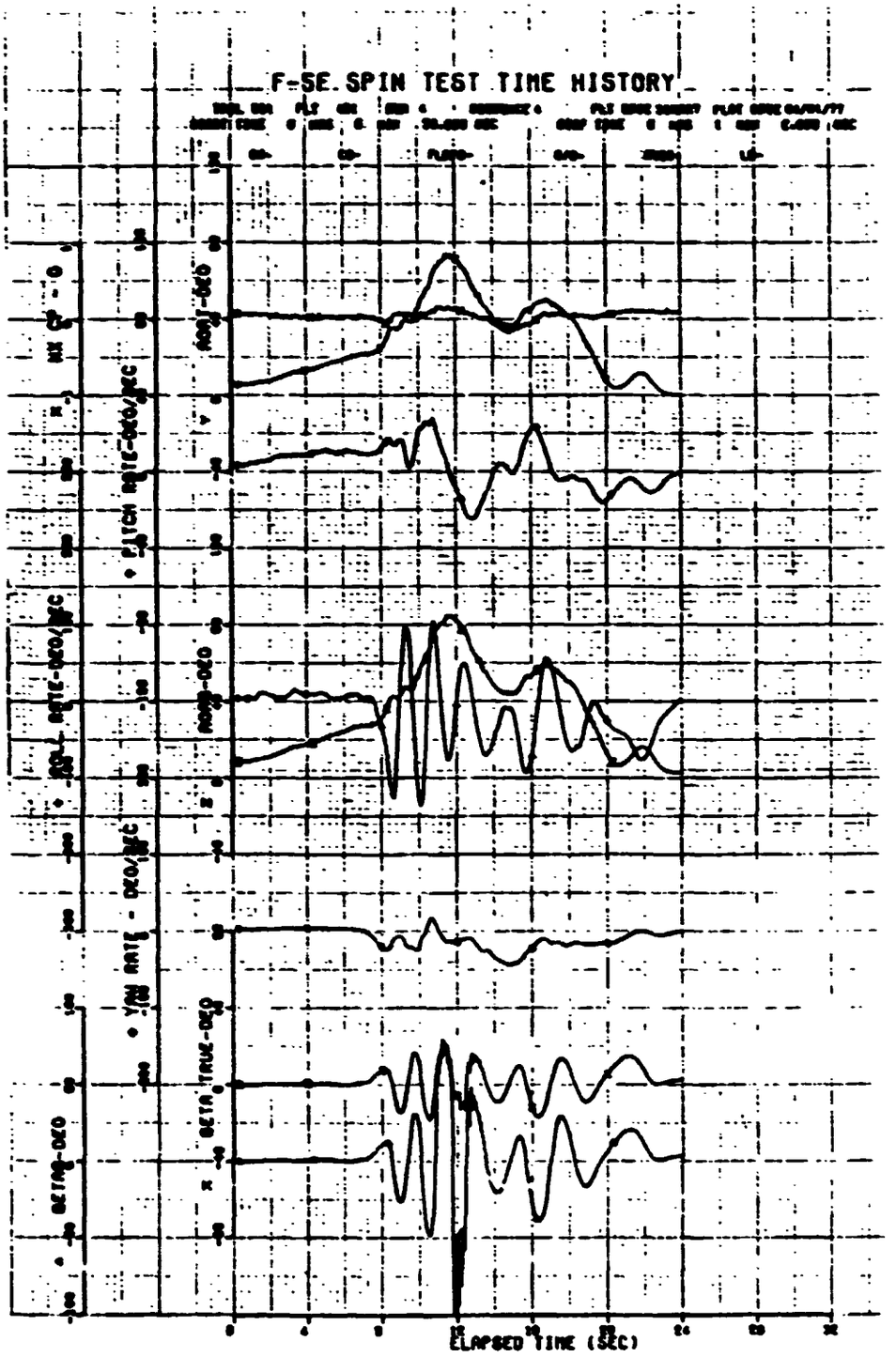

FIGURE 139. F-5F CLEAN CONFIGURATION. 240-kt WUT AFT STICK AND RUDDER AT 20° AOA (Sheet 4 of 8)

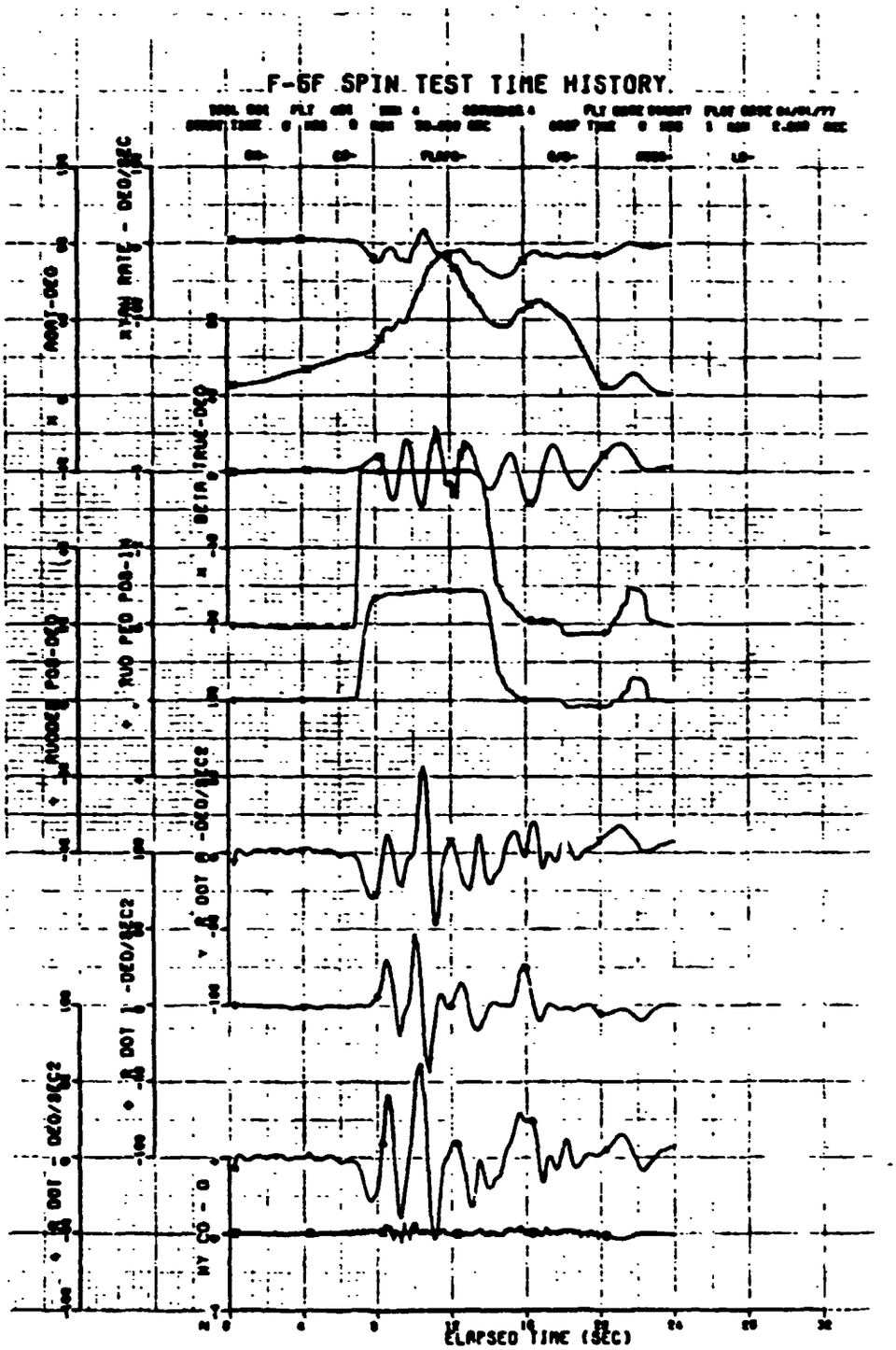

FIGURE 139. F-5F CLEAN CONFIGURATION. 240-kt WUT AFT STICK AND RUDDER AT 20° AOA (Sheet 5 of 8)

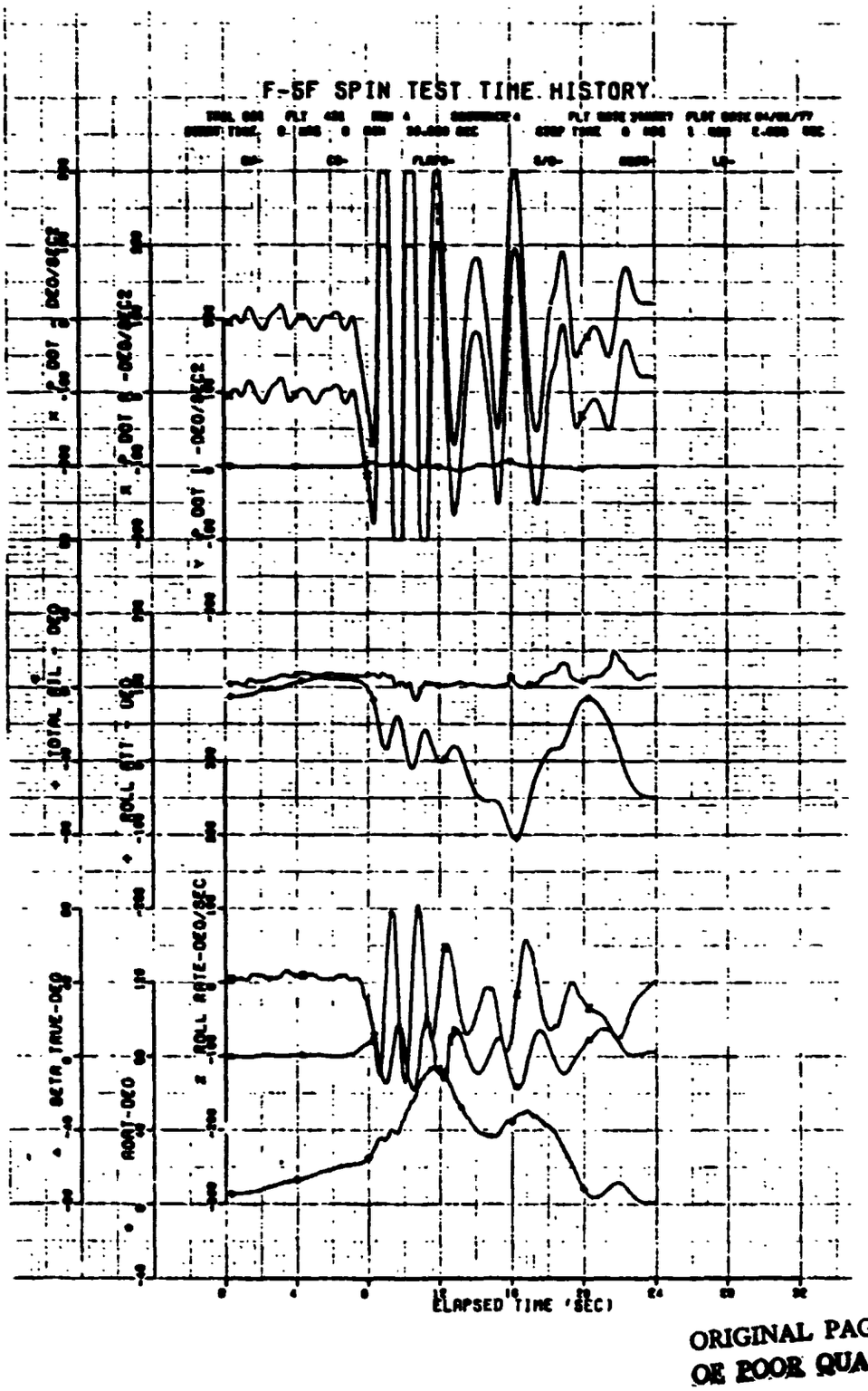

ORIGINAL PAGE IS
OF POOR QUALITY

FIGURE 139. F-5F CLEAN CONFIGURATION. 240-kt WUT AFT STICK AND RUDDER AT 20° AOA (Sheet 6 of 8)

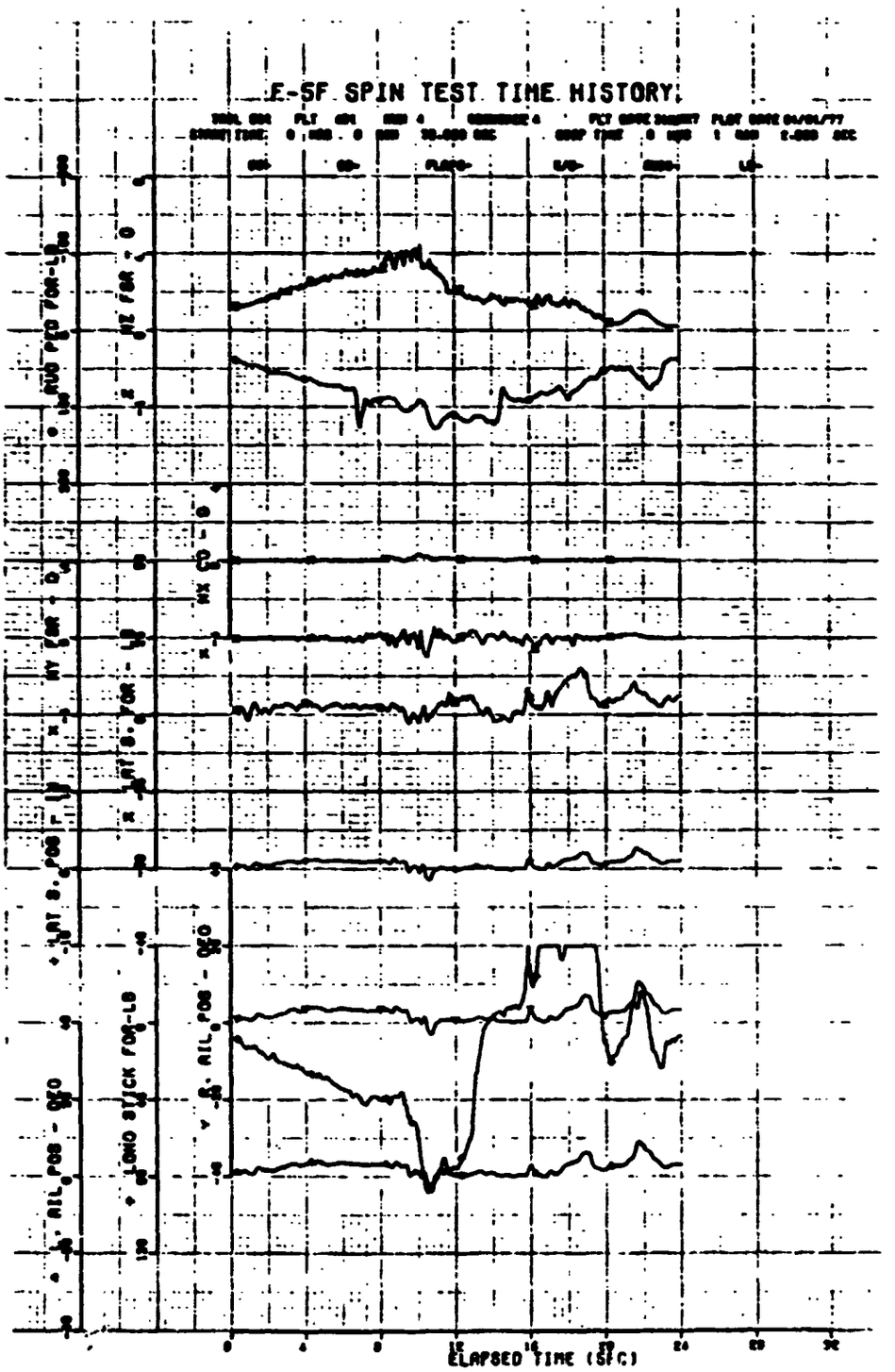

FIGURE 139. F-5F CLEAN CONFIGURATION. 240-kt WUT AFT STICK AND RUDDER AT 20° AOA (Sheet 7 of 8)

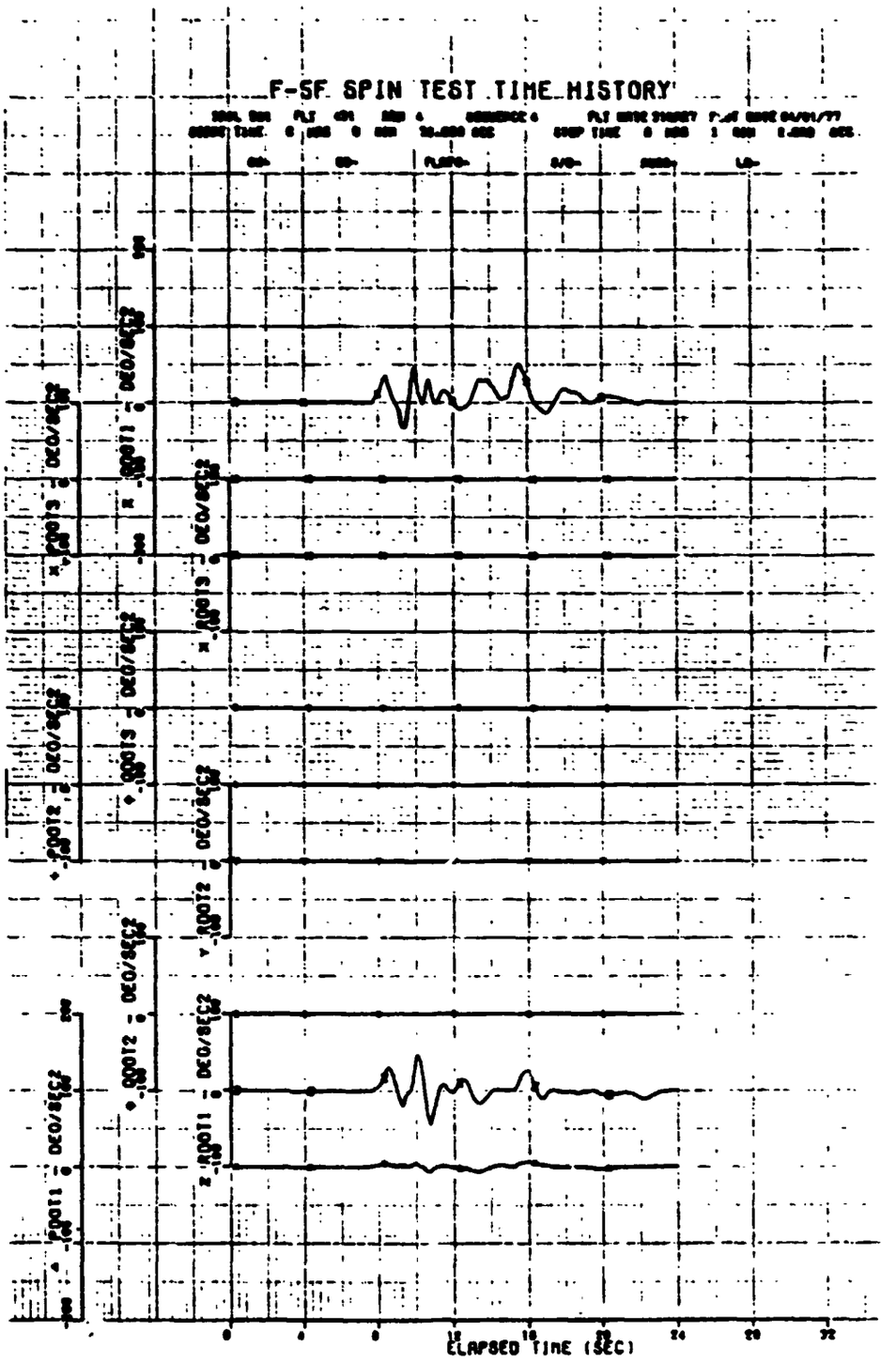

FIGURE 139. F-5F CLEAN CONFIGURATION. 240-kt WUT AFT STICK AND RUDDER AT 20° AOA (Sheet 8 of 8)

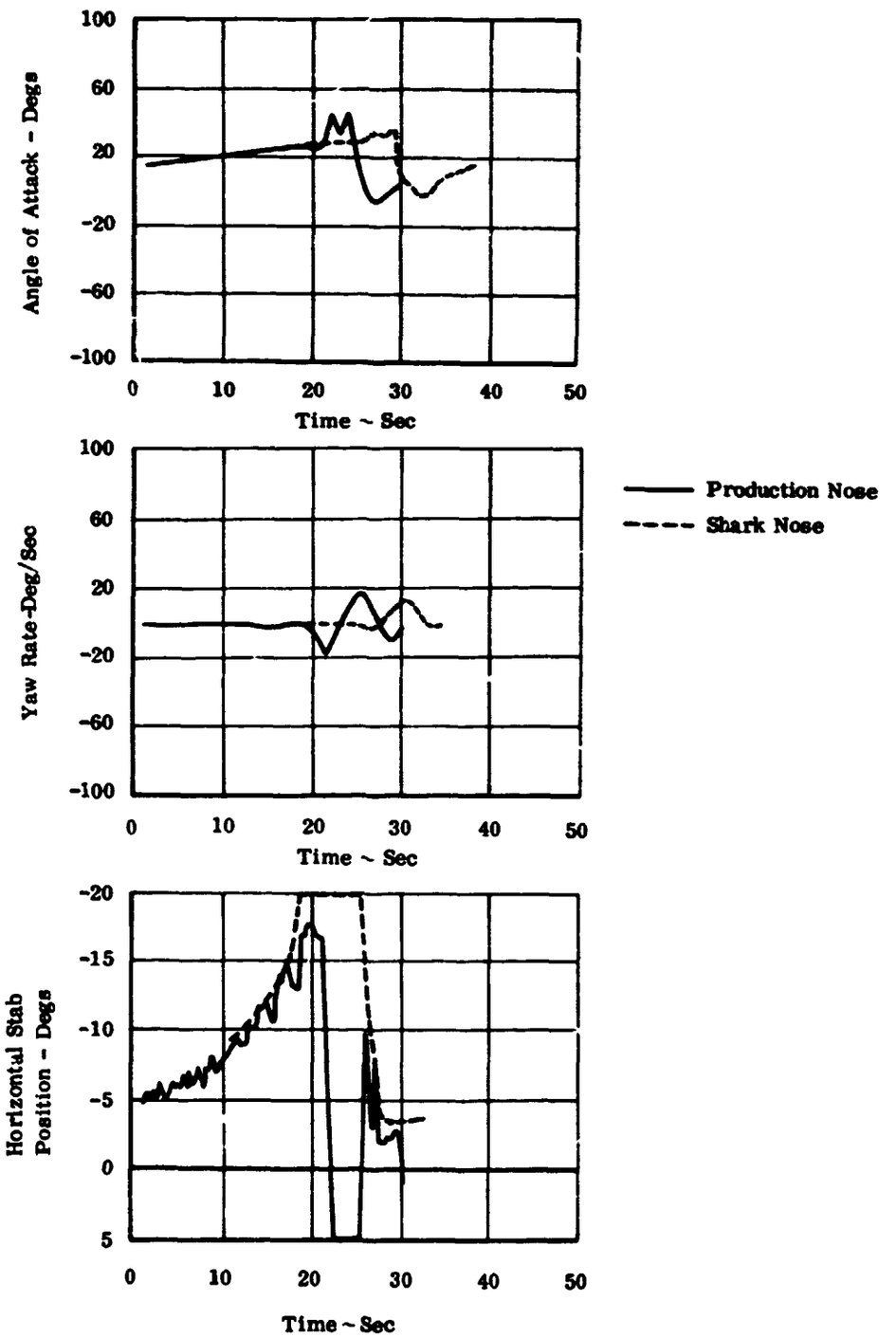

FIGURE 140. F-5F CENTERLINE TANK CONFIGURATION 1-g STALL

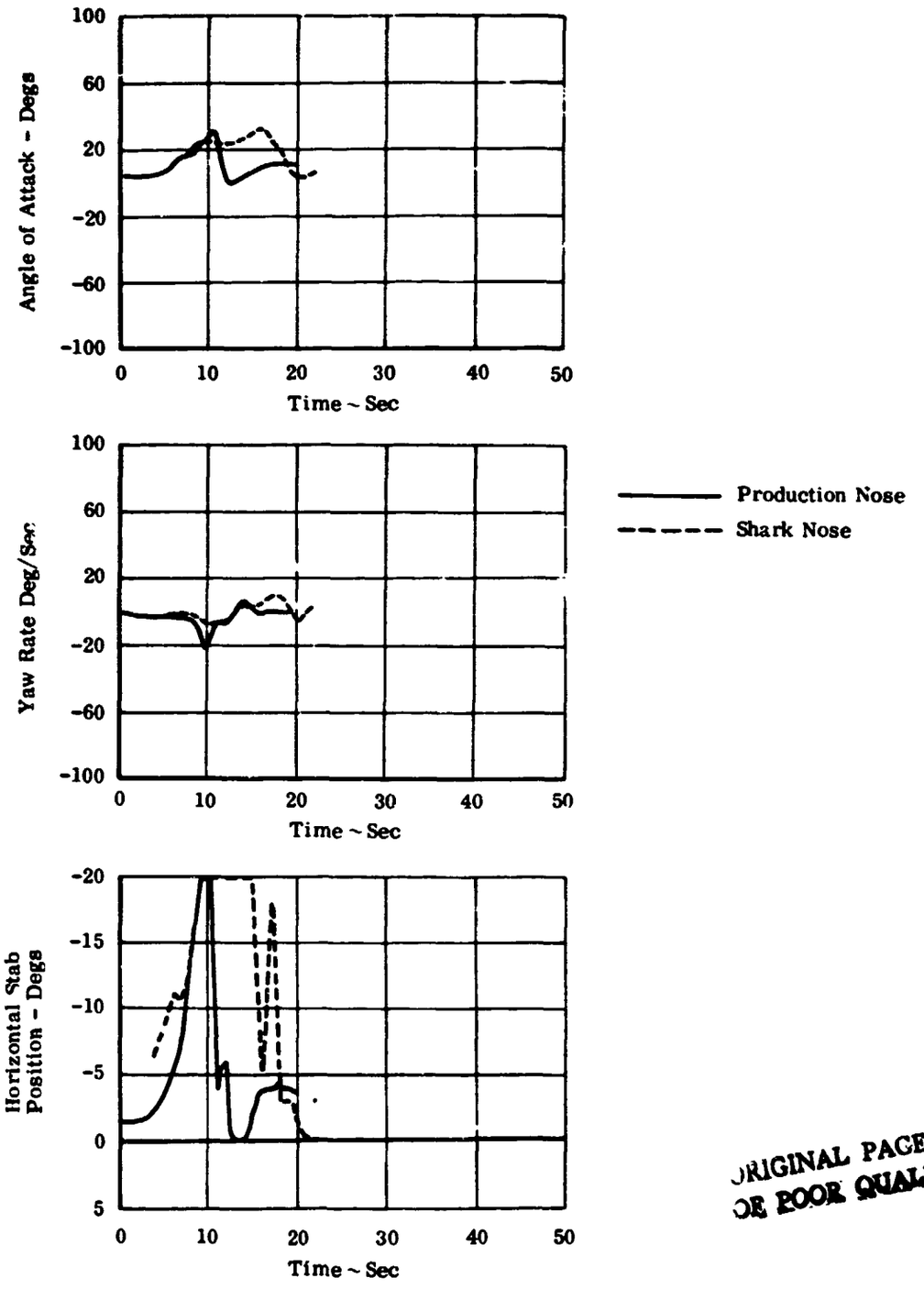

FIGURE 141. F-5F CENTERLINE TANK CONFIGURATION, 3-g LEVEL DECEL

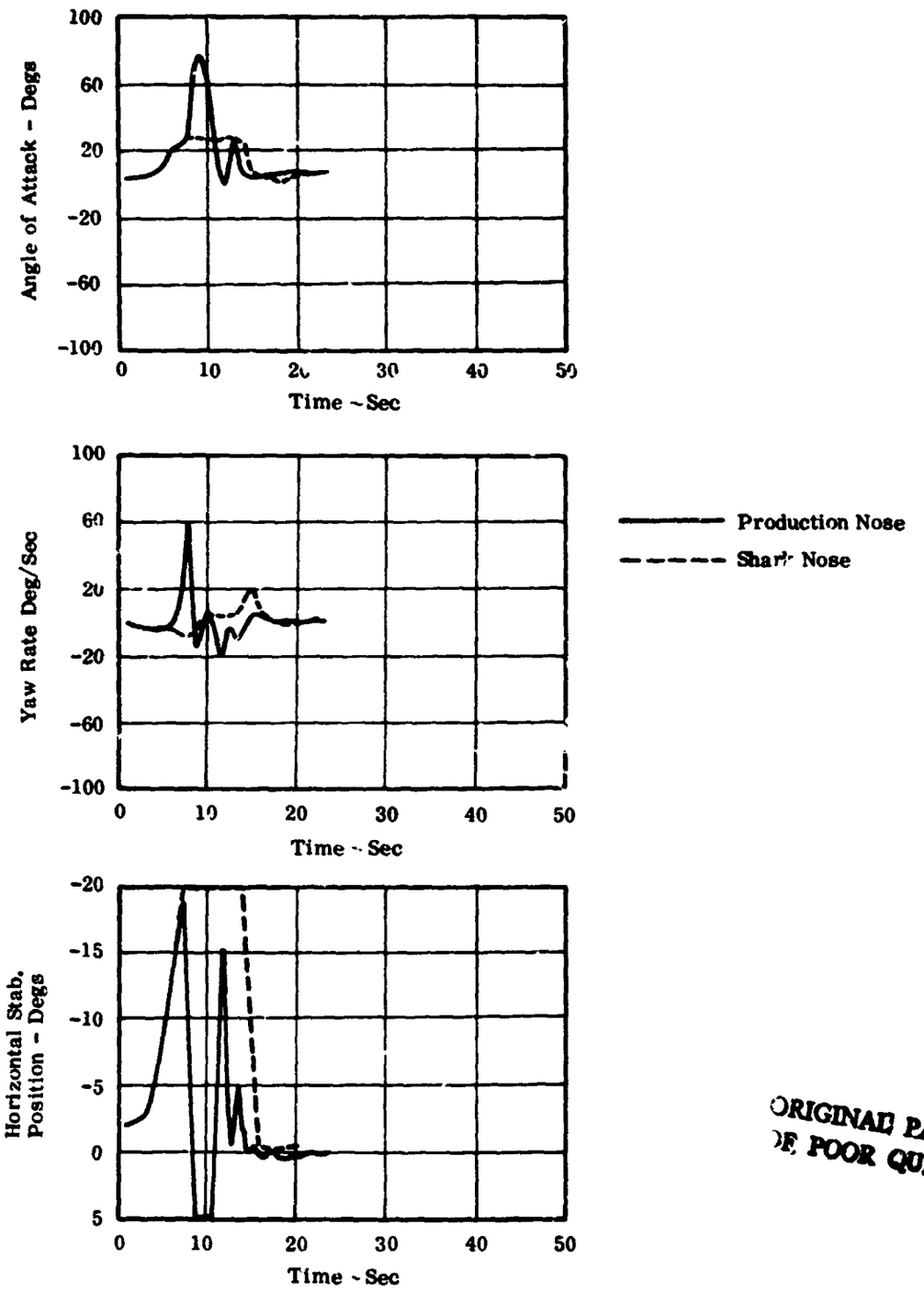

FIGURE 142. F-5F CENTERLINE TANK CONFIGURATION, 4-g LEVEL DECEL

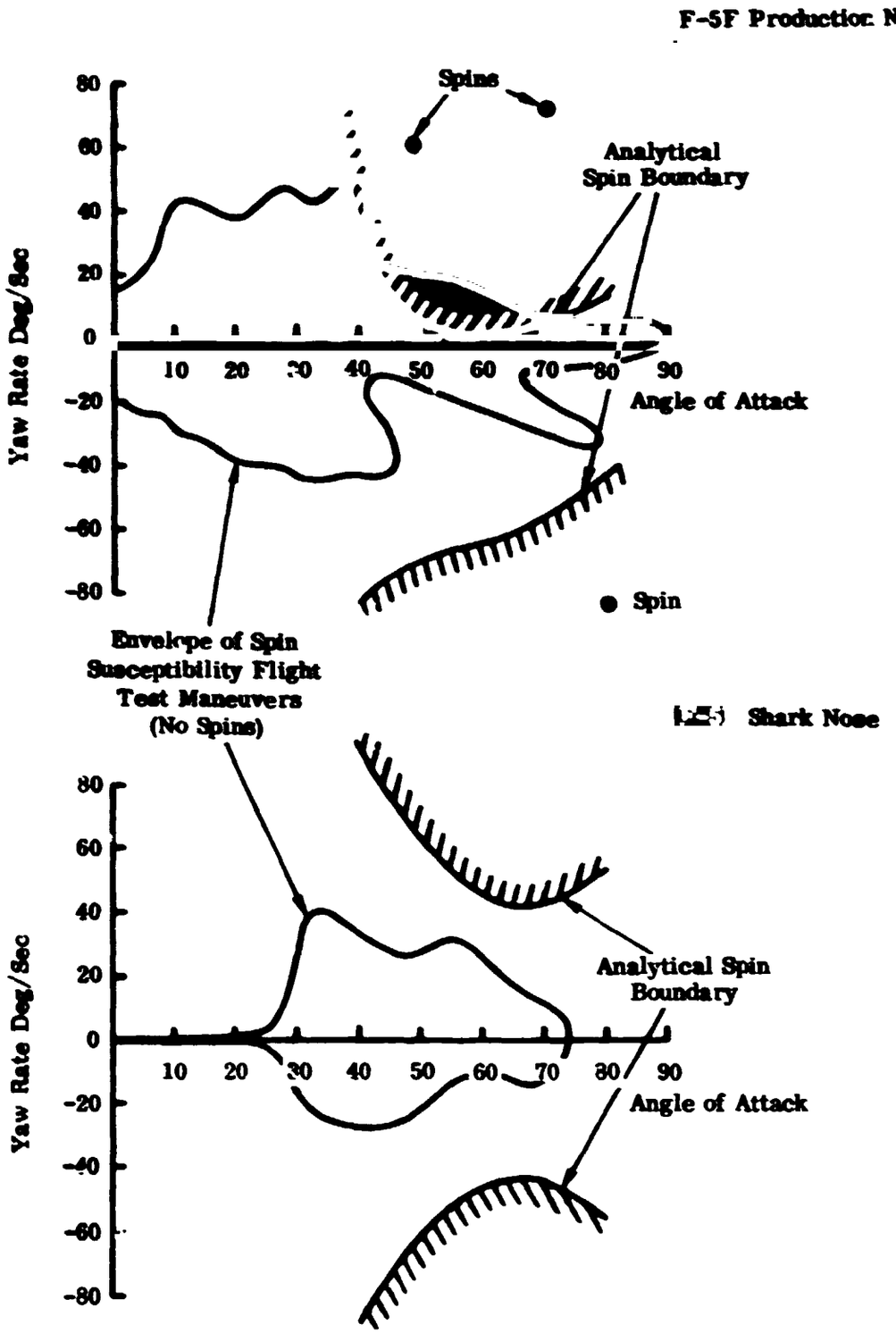

FIGURE 143. F-5F PRODUCTION NOSE AND SHARK NOSE ANALYTICAL SPIN AND FLIGHT TEST MANEUVER BOUNDARIES